AIRBORNE MEASUREMENT AND INTERPRETATION OF PEROXY RADICAL CONCENTRATIONS WITH A FOCUS ON THE OXIDATION MECHANISMS IN THE ASIAN FREE TROPOSPHERE

Dissertation zur Erlangung des akademischen
Grades des Doktor der Naturwissenschaften
an der Universität Bremen

(Dr. rer. nat.)

Volgelegt von

Midhun George
Institut für Umweltphysik
Fachbereich für Physik und Elektrotechnik
Universität Bremen
Bremen
Germany

Dedicated to my father, late Mr P. T. George

Index

Abstract

Hydroperoxyl (HO_2) and organic peroxy (RO_2, where R stands for any organic group) radicals are highly reactive molecules produced in the oxidation of many compounds in the troposphere. They participate in the catalytic cycle producing or destroying ozone (O_3) in the troposphere. Thus, HO_2 and RO_2 measurements provide unique information about the chemical processing of an air mass. Over the last decades, the understanding of the role of HO_2 and RO_2 in the chemical processes in the **p**lanetary **b**oundary **l**ayer (PBL) has improved through ground-based in-situ measurements. However, the number of unequivocal measurements of peroxy radicals in the free troposphere is still quite limited. Measurements from airborne platforms offer a unique opportunity to measure HO_2 and RO_2 together with other relevant trace gases to test and improve the understanding of their chemistry in the free troposphere.

During this doctoral study, an extensive set of airborne RO_2^* ($RO_2^* = HO_2 + \sum RO_2$, where RO_2 represents the organic peroxy radicals reacting with NO to produce NO_2) measurements in the PBL and free troposphere was acquired, analysed and interpreted. The RO_2^* measurements were made using the **Pe**roxy **R**adical **C**hemical **E**nhancement and **A**bsorption **S**pectrometer (PeRCEAS) developed at the **I**nstitut für **U**mwelt**p**hysik (IUP) of the University of Bremen. PeRCEAS has successfully deployed onboard the **H**igh **A**ltitude **LO**ng range research aircraft (HALO) in three research campaigns: the **O**xidation **M**echanism **O**bservations (OMO) Asia and the **E**ffect of **Me**gacities on the transport and transformation of pollutants on the **R**egional to **G**lobal scal**e**s (EMeRGe) field missions in Europe and Asia. The PeRCEAS instrument was characterised and calibrated under atmospherically representative conditions in the laboratory to assure data quality, reproducibility, accuracy and to define optimal operating conditions for the airborne measurements. PeRCEAS successfully measured RO_2^* in 33 HALO flights. RO_2^* mixing ratios of up to 120 pmole $mole^{-1}$ were measured in air masses having different origins, chemical compositions and physical conditions in Europe and Asia.

The RO_2^* measurements, the simultaneous measurements of other relevant trace gases, aerosol concentration, photolysis frequencies and other meteorological parameters were synergistically analysed to identify the chemical processes controlling the amount of RO_2^*. From the analysis, it was found that RO_2^* is primarily produced following the photolysis of ozone (O_3), formaldehyde (HCHO), glyoxal (CHOCHO), and nitrous acid (HONO) in the air masses investigated. The estimate for the contribution of O_3 photolysis to RO_2^* production rate is > 40 % in the PBL and < 40% in the free troposphere. This reduction is explained by the decrease in the water vapour concentration ($[H_2O]$) as a function of altitude.

Subsequently, the RO_2^* mixing ratios in the air masses measured during the EMeRGe in Asia and Europe campaigns were calculated assuming a **p**hotostationary **s**teady-**s**tate (PSS) for RO_2^*. The RO_2^* production from precursor photolysis, the loss through $HO_2 - HO_2$, $RO_2 - RO_2$ and $HO_2 - RO_2$ reactions, the hydroxyl radical (OH) and organic oxy-radicals (RO) loss during the radical interconversion, and HO_2 uptake on aerosol were considered for the calculation of RO_2^*. The calculations were constrained by the simultaneous measurements of photolysis frequencies, trace gas concentrations and aerosol particle number concentrations onboard HALO. Case studies confirmed the validity of the PSS assumption for air masses having different chemical compositions under different physical conditions. The RO_2^* calculated are generally in excellent agreement with the RO_2^* measurements.

An experimental budget analysis was performed to estimate the main loss processes of RO_2^* by introducing the RO_2^* measurements in the PSS equation. Except for the measurements inside pollution plumes with NO > 800 pmole mole^{-1} or aerosol particle number concentration > 800 particles cm^{-3}, the $HO_2 - RO_2$ and $HO_2 - HO_2$ were the dominant RO_2^* loss process during both EMeRGe Asia and Europe. The RO_2^* losses through HO_2 uptake on aerosol were higher in the pollution outflows measured in Asia than in Europe. This is attributed to the higher aerosol concentrations observed in the air masses probed during EMeRGe in Asia. The contribution from the HO_2 uptake on aerosol increases up to 60 % for an assumed aerosol uptake coefficient of 0.24 inside pollution plumes in Asia, where the aerosol particle number concentration is > 1000 particles cm^{-3}. In Europe, the OH – NO_x reactions were the dominant RO_2^* loss process in the pollution outflow. This finding is explained by the EMeRGe in Europe measurements being typically closer to anthropogenic emissions sources than in Asia, except for the case study of Taipei and Manila.

1

Introduction

Over the last decades, the advance in laboratory studies, field measurements, and model studies has led to a much better understanding of anthropogenic emissions and their impact on the chemical composition of the Earth's atmosphere. Phenomena such as the stratospheric ozone (O_3) depletion, the ozone hole, tropospheric pollution during summer and winter smog episodes and climate change demonstrate how harmful anthropogenic emissions are to life on Earth. The emission of the precursors of short-lived climate pollutants and long-lived greenhouse gases significantly affect air quality and the climate. Consequently, accurate knowledge of these trace gases and their photolysis, oxidation, and other reaction pathways are essential to improve the understanding of tropospheric chemistry and the mitigation strategies of the harmful anthropogenic emissions to achieve sustainability.

The chemical transformation of trace gases in the troposphere proceeds through a complex set of chemical reactions. The hydroperoxyl (HO_2) and organic peroxy (RO_2, where R stands for an organic group, typically an alkyl) radicals play a key role in tropospheric chemistry. During the day, they are produced following the oxidation of carbon monoxide (CO) and many volatile organic compounds (VOCs), as well as the photolysis of oxygenated volatile organic compounds (OVOCs). The reaction of HO_2 and RO_2 with nitrogen monoxide (NO) leads to nitrogen dioxide (NO_2) and either hydroxyl radical (OH) or organic oxy-radicals (RO) formation. The photolysis of NO_2 produces an oxygen atom and is the only source of O_3 in the troposphere. The RO formed often reacts with molecular oxygen (O_2) to generate HO_2 and OVOCs, i.e. aldehydes and ketones, which are oxidised by OH and/or photolysed to produce more HO_2 and RO_2. Dependent on the amount of NO_x (NO + NO_2) in the air mass, the catalytic cycles involving HO_2 and RO_2 produce or destroy O_3. The temperature-dependent equilibrium reactions of HO_2 and RO_2 with NO_2 form temporary reservoirs, a good example being peroxyacetyl nitrate (PAN; $CH_3COO_2NO_2$). These temporary reservoirs are convected, cooled, and transported. When descending, they are warmed and release HO_2, RO_2 and NO_2, which participate in chemical transformations far from the pollutant emission sources.

As inferred from the above, HO_2 and RO_2 play a role in determining the amounts and distributions of the oxidising agents like OH and O_3 in the troposphere and thus the oxidizing capacity of the troposphere. Consequently, knowledge about the spatial distribution and concentration of HO_2 and RO_2 is essential to test the current understanding of tropospheric chemistry. As HO_2 and RO_2 react rapidly with themselves and key tropospheric trace gases, their concentrations and mixing ratios are relatively small. Consequently, their measurement in the troposphere requires sensitive and accurate

instruments and techniques. Except for the method of freezing air and subsequent observation of HO_2 and RO_2 by **M**atrix **I**solation **E**lectron **S**pin **R**esonance technique (MIESR; Mihelcic et al., 1985), there are no direct measurements techniques for HO_2 or RO_2 which have been applied successfully in the field measurements. Alternatively, indirect measurement techniques like **Pe**roxy **R**adical **C**hemical **A**mplification (PeRCA), **L**aser **I**nduced **F**luorescence (LIF), **P**eroxy **R**adical **C**hemical **I**onization **M**ass Spectrometry (PerCIMS), and **E**thane **C**hemical **AMP**lifier (ECHAMP) have been developed and deployed in field campaigns. These measurement techniques convert HO_2 and RO_2 to other species, which can be detected and quantified more accurately.

In the last decades, ground-based measurements of HO_2 and RO_2 have been successfully made in a variety of environments (Monks et al., 1998, 2009 and references herein; Burkert et al., 2001a, b; Carslaw et al., 2002; Fleming et al., 2006a, b; Emmerson et al., 2007; Qui et al., 2007; Kanaya et al., 2007, 2012; Hofzumahaus et al., 2009; Andrés Hernández et al., 2009, 2010; Mao et al., 2010; Kukui et al., 2014; Lelieveld et al., 2018; Tan et al., 2017, 2018; Whalley et al., 2018, 2021; Lew et al., 2020). The majority of these measurements were made in field campaigns that studied different aspects of the chemistry in the lower troposphere, especially in the **p**lanetary **b**oundary **l**ayer (PBL). These studies tested the understanding of known oxidizing cycles by comparing the measurements with radical calculations from different photochemical models constrained with either measured or estimated radical precursors, photolysis frequencies and meteorological parameters. This approach led to different degrees of agreement between the measured and model results depending on the chemical mechanisms considered in the model, chemical and physical constraints applied to the simulations, and the chemical composition of the air masses investigated. Even though the differences between measured and modelled HO_2 and RO_2 were not entirely resolved, these case studies significantly improved the understanding and knowledge of the role of HO_2 and RO_2 in tropospheric boundary layer chemistry.

In contrast to the studies in the lower part of the PBL, the number of unequivocal measurements of peroxy radicals in the upper part of the PBL and the free troposphere is still quite limited. Campaigns involving the measurement of peroxy radicals and an adequate set of ancillary measurements of the trace gas composition and meteorological parameters are required to better understand oxidation processes during the transport and transformation of pollution plumes. Airborne measurements offer a unique opportunity to measure HO_2 and RO_2 in the upper part of the PBL and the free troposphere. However, the temporal and spatial variability in the chemical composition of the air masses makes the measurement from airborne platforms challenging. Robust instruments with high accuracy, sensitivity, and specificity are required to unequivocally identify and quantify potential spectral and chemical interferences (Green et al., 2002, 2006; Zanis et al., 2003; Clemitshaw, 2004 and references herein; Heard, 2006; and references herein; Stone et al., 2012 and references herein; Ren et al., 2012). In addition, each particular airborne platform has unique capabilities and limitations

(e.g., mechanical, electrical, and safety constraints), which significantly differ from one another. Similarly, the optimal operating conditions for the instruments are different onboard an aircraft to those used for ground-based or ship-board measurements. As a result, instruments for the airborne measurement of HO_2 and RO_2 must usually be designed and optimised for deployment on a specific aircraft platform.

Airborne measurements of HO_2 and RO_2 have been reported in a variety of environments in different parts of the world (Crawford et al., 1999; Faloona et al., 2000; Tan et al., 2001; Green et al., 2002; Cantrell et al., 2003a; Olson et al., 2006; Ren et al., 2008, 2012; Andrés-Hernández et al., 2009; Kartal et al., 2010; Martinez et al., 2010; Commane et al., 2010; Stone et al., 2011; Hornbrook et al. 2011). These airborne measurements were also compared with different photochemical models. The degrees of agreement between the measured and model results depend on the chemical mechanisms considered, chemical and physical constraints applied to the simulations, and the chemical composition of the air masses investigated (Stone et al., 2012).

1.1 Motivation

The overarching motivation of this research study is to improve the understanding of sources and sinks of HO_2 and RO_2 in the troposphere. To achieve this goal, the following are required:

a) accurate and extensive measurements of the total sum of peroxy radicals, collectively known as RO_2^* ($RO_2^* = HO_2 + \sum RO_2$, where RO_2 are those organic peroxy radicals reacting with NO to produce NO_2)

b) analysis of the chemistry taking place in the air masses observed during their transport and transformation.

The interpretation of the acquired observational data also aims to improve the current understanding of oxidation mechanisms and radical chemistry in the PBL and the free troposphere.

This research aims to significantly extend the limited number of RO_2^* measurements from different locations and atmospheric regions. The acquisition and interpretation of the data have taken advantage of the capabilities and the scientific payload of the **H**igh **A**ltitude **LO**ng range research aircraft (HALO; http://www.halo.dlr.de). RO_2^* measurements were carried out on board HALO in three airborne campaigns: the **O**xidation **M**echanism **O**bservations (OMO) Asia and the **E**ffect of **Me**gacities on the transport and transformation of pollutants on the **R**egional to **G**lobal scal**e**s (EMeRGe) in Europe and Asia. These are multi-institutional projects supported by the priority research program of the **D**eutsche **F**orschungs**g**emeinschaft (DFG), which facilitates the investigation of atmospheric processes using the HALO platform. The instrumentation deployed during these campaigns (see section 3.2) provides a unique opportunity to investigate chemical processes controlling RO_2^* concentration under different chemical compositions and physical conditions.

The **P**eroxy **R**adical **C**hemical **E**nhancement and **A**bsorption **S**pectrometer (PeRCEAS), designed and constructed by the scientists from the **I**nstitute für **U**mweltphysik **P**hysics (IUP) of the University of **B**remen (UB), was selected for the measurement of RO_2^* from HALO. PeRCEAS combines the PeRCA and **C**avity **R**ing-**D**own **S**pectroscopy (CRDS) techniques in a dual-channel instrument to measure the sum of OH + ∑RO + HO_2 + ∑RO_2, where RO_2 are those organic peroxy radicals reacting with NO to produce NO_2, in the free troposphere and lower stratosphere. Since the amount of OH and RO is much smaller than that of HO_2 and RO_2 in the atmosphere, PeRCEAS measures the sum of HO_2 and those RO_2 radicals that react with NO to make NO_2. During this doctoral research, the PeRCEAS instrument was transformed from the prototype (Hortsjann et al., 2014) to its final form (section 2.5 and George et al., 2020). The characterization, certification and deployment of PeRCEAS onboard HALO was also an essential part of the experimental phase of this doctoral research.

1.2 Scientific Objectives

Based on the scientific motivation described in section 1.1, the scientific objectives of this doctorate were chosen to be as follows:

- Characterization and optimization of the PeRCEAS instrument for airborne measurements through laboratory calibrations and characterization under atmospherically representative conditions.
- Acquisition of an accurate RO_2^* data set during the OMO Asia and EMeRGe field campaigns. This implies active participation in the instrumental deployment, adaptation, modification and calibration between measurement campaigns, as well as a thorough data quality control.
- Investigation of the processes controlling RO_2^* production and loss in the air masses encountered in the Asian troposphere using experimental data obtained during the campaigns.
- Comparison of RO_2^* production and loss processes in the air masses measured during EMeRGe in Asia and Europe.

1.3 Outline of the Dissertation

This dissertation comprises the above introduction and the following four chapters. The latter introduces and describes the research undertaken to achieve the aforementioned scientific objectives.

Chapter 2 provides a short review of the physics of the atmosphere and the chemistry relevant to this research. The known sources and sinks of RO_2^* in the atmosphere and RO_2^* measurement techniques are briefly explained and discussed afterwards. Finally, the PeRCEAS instrument and its configuration used in this study for the airborne measurement of RO_2^* are described in detail.

Chapter 3 describes the laboratory studies carried out: a) to identify and characterize the critical parameters affecting the accuracy and reproducibility of PeRCEAS measurements; and b) to

calibrate the PeRCEAS instrument. After that, the OMO Asia campaign and EMeRGe campaigns in Europe and Asia are briefly described together with the operating conditions selected for PeRCEAS during these campaigns.

Chapter 4 focuses on the presentation, analysis and interpretation of the airborne measurements of RO_2^* during the OMO Asia and EMeRGe campaigns. This involves the analysis of the RO_2^* and ancillary trace gas and photolysis frequencies synergistically to identify RO_2^* sources. Subsequently, RO_2^* concentration and mixing ratios are estimated using a **p**hotostationary **s**teady-**s**tate (PSS) approximation for RO_2^*.

The final chapter of the dissertation, chapter 5, summarises the research undertaken during this doctoral study and a set of conclusions obtained from the study. Two useful appendices follow Chapter 5. Appendix A-I contains the set of RO_2^* measurements from EMeRGe in Asia. Appendix A-II describes the derivation of the equation used for calculating RO_2^*. Details of the dataset and different model simulations used in this study are included in Appendix A-III and A-IV, respectively. Table A5 in Appendix A-V summarises the specifications of state-of-the-art instruments measuring peroxy radicals.

<div style="text-align: right">

2

</div>

Relevant Theoretical and Experimental Background

This chapter briefly describes the relevant aspects of the physics of the atmosphere, kinetics and photochemistry, and the role of free radicals in the troposphere. More detailed information can be found elsewhere (Egbert Boeker and Rienk Van Grondelle, 1994; Seinfeld and Pandis, 1997; Richard P. Wayne, 2000). The peroxy radical measurement techniques are also briefly introduced and explained in this chapter. The chapter ends with a detailed description of the technique and instrumentation used in this study for RO_2^* measurements, together with some results reported in previous studies.

2.1 Physics of the Atmosphere

The atmospheric temperature and pressure vary as a function of height, which results in changes in the physical and chemical process with height. The Earth's atmosphere is divided into different layers based on the average temperature profile (Figure 2.1).
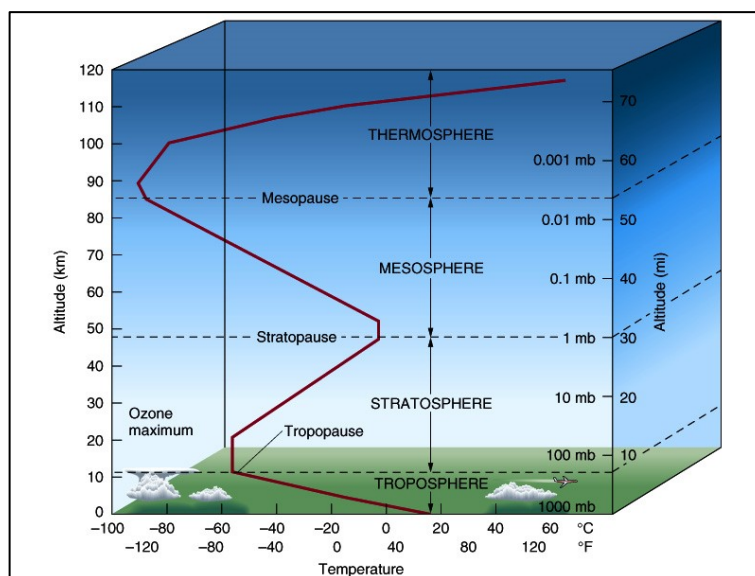
Figure 2.1 Vertical profiles of atmospheric temperature and pressure. The different atmospheric layers are also shown for visual support. (https://robertcarrollweather.files.wordpress.com/2014/11/ agburt01_09.jpg).

2.1.1 Vertical Profile of Temperature: Atmospheric Layers

Troposphere: The lowest layer of the atmosphere. It extends from the Earth's surface to the tropopause, which is at an average height of 18 km over the Equator and 8 km over the poles. The height of the tropopause depends on the latitude and time of the year. In the troposphere, temperature

decreases almost linearly with height due to the adiabatic cooling of rising air parcels heated by conduction from the sun-warmed Earth. The troposphere contains about 80% of the total mass of the atmosphere and is a region of ceaseless turbulence and mixing. The troposphere can be further divided into the **p**lanetary **b**oundary **l**ayer (PBL), extending from the Earth's surface up to 1 km, and the free troposphere, extending from about 1 km to the tropopause.

Stratosphere: The layer between the tropopause and the stratopause, which is at the height of 45 to 50 km. The stratosphere has a positive temperature gradient with increasing height. As a result, the vertical mixing in this layer is very low. The temperature profile in the stratosphere results from the solar UV radiation absorption by O_3.

Mesosphere: The layer between the stratopause and the mesopause. The temperature decreases with height due to adiabatic and radiative cooling until the mesopause, the coldest point in the atmosphere. Mesopause extends from 80 to 90 km. Rapid vertical mixing happens within this layer.

Thermosphere: The region with a positive temperature gradient with height situated above the mesopause. The absorption of short wavelength radiation by N_2 and O_2 results in this positive temperature gradient. The vertical mixing is rapid. The region of the upper mesosphere and lower thermosphere where ions are produced by photo-ionization is known as the ionosphere.

Exosphere: The region above 500 km, where molecules with sufficient energy can escape the Earth's gravitational field.

2.1.2 Vertical Profile of Pressure

The pressure in the atmosphere at each height is due to the weight of the air parcel located above. The atmospheric pressure at the surface of the Earth, known as the standard pressure, is 1015.13 hPa. If the mass density of air at a height z is given by $\rho(z)$, then the rate of change of pressure over a small height dz can be expressed as:

$$\frac{dP(z)}{dz} = -\rho(z)g \qquad\qquad\qquad \text{Eq. 2.1}$$

where g is the acceleration due to gravity. By applying the ideal gas law, Eq. 2.1 can be rewritten as

$$\frac{dP(z)}{dz} = \frac{M_{air} \cdot P(z)}{R \cdot T(z)} g \qquad\qquad\qquad \text{Eq. 2.2}$$

where M_{air} is the molecular weight of air (28.97 g mole^{-1}), $T(z)$ temperature at a height z, and R the universal gas constant 8.314 J mole K^{-1}.

Eq. 2.1 can be rewritten as:

$$\frac{d(\ln(P(z)))}{dz} = -\frac{1}{H_z} \qquad\qquad \text{Eq. 2.3}$$

where $H_z = \frac{R \cdot T(z)}{M_{air} \cdot g}$ is the characteristic length scale for the decrease of pressure with height.

The expression for P(z) can be simplified by considering the temperature to be approximately constant over dz.

$$\frac{P(z)}{P_0} = e^{-z/H} \qquad\qquad \text{Eq. 2.4}$$

where $H = \frac{RT}{M_{air}}$ is known as the scale height. It is the vertical distance over which the density and pressure fall by a factor of $1/e$.

Eq. 2.4 shows that the pressure decrease with height is approximately exponential. By considering the corresponding molecular weight (M_i), the concept of scale height can be applied to individual atmospheric species to find the partial pressure, $P_i(z)$. Heavy molecules tend to concentrate near the Earth's surface since the scale height is inversely proportional to the molecular weight. However, the separation based on molecular weight does not occur in the lower atmosphere due to rapid mixing. By considering a mean tropospheric temperature of 253 K, a scale height of 7400 m can be obtained.

2.1.3 General Atmospheric Circulation

Over the globe, the incoming solar radiation and the outgoing terrestrial radiation emitted by the Earth are nearly balanced when averaged over a year. When averaged over a latitude band, the incoming radiation is a surplus in the tropics, while a deficit of radiation is found in the Polar Regions. This is due to the outgoing terrestrial radiation being larger than the absorbed solar radiation in the poles. Atmospheric and oceanic transport processes account for this energy imbalance.

The intense incoming solar radiation leads to air rising in the equatorial region. The rising air cools, condenses, and forms a region of intense clouds and heavy precipitation. This area is called the **I**nter-**T**ropical **C**onvergence **Z**one (ITCZ). Tropical rain forests are found in this region. The ITCZ moves north and south during the year following the relative position of the Sun. Because the stratosphere is stable, rising air that reaches the tropopause moves poleward. By the time the air moving northward reached about 30°N, it had become a westerly wind (it is moving to the east) due to the Coriolis force. Due to the conservation of angular momentum, the poleward moving air increases speed. This increased speed and the Coriolis force are responsible for the subtropical jet. This poleward moving air piles up, forming high-pressure areas at the surface known as subtropical highs. Some of the air sinks toward the surface. Subsidence inhibits cloud formation, which is why many large deserts are near 30°N and 30°S. Once the sinking air reaches the ground, a part of it flows to the Equator, turning west due to the Coriolis force. This surface air forms the trade winds that blow

steadily from the northeast in the northern hemisphere and southeast in the southern hemisphere. This convection cell is known as the Hadley cell (http://cimss.ssec.wisc.edu/wxwise/class/gencirc.html, https://seos-roject.eu/oceancurrents/oceancurrents-c02-s02-p01.html).

Between 30° and 60° latitudes in both hemispheres, a new cell, known as the Ferrel Cell, takes over. This cell produces prevailing westerly winds at the surface within these latitudes. This is because some of the air sinking at 30° latitude continues travelling northward toward the poles and the Coriolis force bends it to the right (in the Northern Hemisphere). This still warm air at roughly 60° latitude approaches cold air moving down from the poles. With the converging air masses at the surface, the low surface pressure at 60° latitude causes air to rise and form clouds. Some of the rising warm air returns to 30° latitude to complete the Ferrel Cell. The two air masses at 60° latitude do not mix well and thereby form the polar front, separating the warm air from the cold air. Thus the polar front is the boundary between warm tropical air moving poleward and the colder polar air moving equatorward. The polar jet stream aloft is located above the polar front and typically flows from west to east. The polar jet is strongest in the winter because of the greater temperature contrast than during the summer. Waves along this front can pull the boundary north or south, resulting in local warm and cold fronts, which affect the weather at particular locations (https://mhsapes.weebly.com/44-45-reading.html).
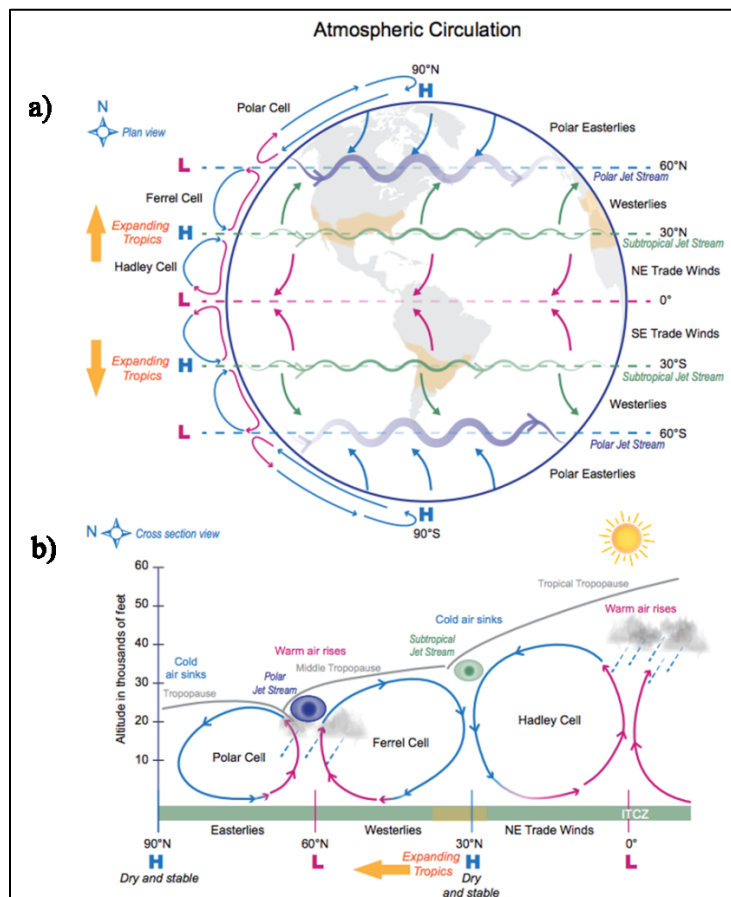

Figure 2.2: Schematic representations of general circulations in Earth's atmosphere. (a) plan, and (b) cross-section views (Figure source: NWS, National Weather Service, 2016).

Above 60° latitude, the polar cell circulates cold, polar air equatorward. The air from the poles rises at 60° latitude where the polar cell and the Ferrel cell meet, and some of this air returns to the poles completing the polar cell. Because the wind flows from high to low pressure and due to the effects of the Coriolis force, the winds above 60° latitude are prevailing easterlies (https://mhsapes.weebly.com/44-45-reading.html).

The Earth's heat engine not only moves heat from one part to another but also from the Earth's surface and lower atmosphere back to space. The flow of incoming and outgoing energy is the Earth's energy budget. In order to maintain a stable average temperature, the energy budget at the top of the atmosphere must balance. This state of balance is called radiative equilibrium (https://earthobservatory.nasa.gov/features/EnergyBalance/page4.php).

Bright ground surfaces like sea ice and snow together with the backscattering from the atmosphere (≈ 22 %) reflect 29 % of the incoming solar radiation back to space. This energy plays no role in Earth's climate system. Water vapour, dust and ozone in the atmosphere absorb almost 23 % of the incoming solar energy. The surface absorbs the rest, 48 % of the incoming radiation. So, to keep a stable temperature, the Earth system must radiate the absorbed 71 % of the incoming radiation back to space.

2.1.4 Troposphere – Stratosphere Exchange

Air transport across the tropopause plays an essential role in determining the chemical composition and hence the radiative properties of both the troposphere and stratosphere. One direct example is the ozone depletion in the stratosphere by the chlorofluorocarbons emitted at the Earth's surface. This exchange directly results from the wave-driven pumping from the extratropical troposphere. This pumping causes a steady ascent of air in the tropical stratosphere (Figure 2.3).
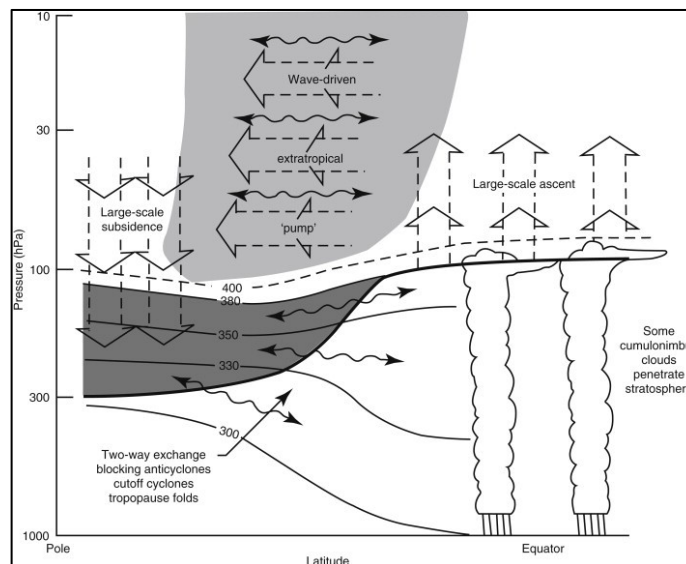

Figure 2.3: Dynamical aspects of stratosphere-troposphere exchange (Figure source: Holton et al., 1995).

2.1.5 Optical Properties of the Atmosphere

The Sun is the primary energy source of Earth. As shown in Figure 2.4, the energy in some spectral regions does not reach the Earth's surface due to the strong absorption by atmospheric gases. About 40 % of the solar energy is concentrated in the region between 400 to 700 nm, where the absorption is weak.

The interaction of electromagnetic radiation with molecules can be determined only by quantum mechanical calculations. In general, the molecules (like H_2O and O_3) with electric dipole moment interact strongly with electromagnetic radiation. The induced dipole in the CO_2 molecule makes an absorption band at 15µm, where the Earth emits most of its infrared radiation. This creates the so-called greenhouse effect.

The terrestrial long-wave infrared radiation emitted by the Earth's surface also has a window region from about 7µm to 13µm. Nearly 80 % of the terrestrial radiation in this region escapes to space. Most non-CO_2 greenhouse gases like O_3, methane (CH_4), Nitrous oxide (N_2O) and chlorofluorocarbons have a strong absorption band in this window region. Because of this, small changes in the concentration of these gases can produce significant changes in the net radiative flux.
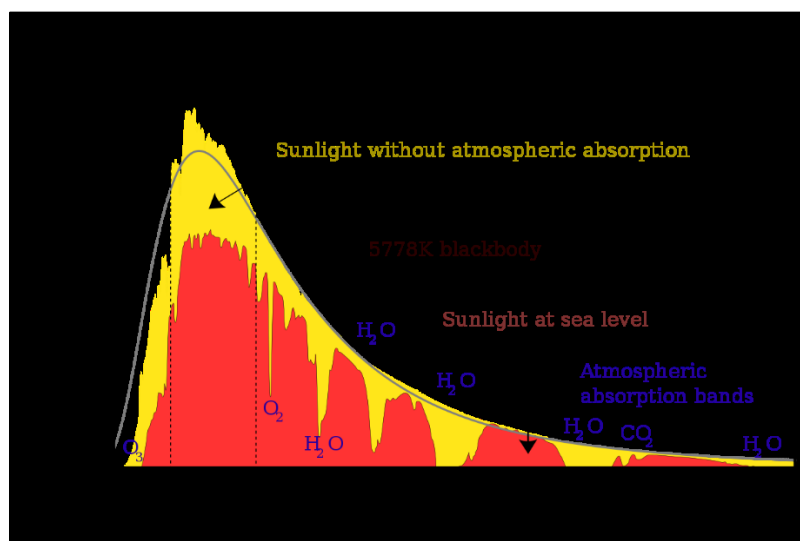
Figure 2.4: Solar spectral irradiance at the top of the atmosphere and sea level. (Figure source: https://commons.wikimedia.org/w/index.php?curid=24648395).

Due to the presence of clouds and aerosols in the atmosphere, $\approx$ 22 % of the incoming solar radiation is backscattered to space without being absorbed. This opposes the greenhouse effect and produces a cooling effect on the Earth's surface.

2.1.6 Chemical Composition of the Atmosphere

The Earth's atmosphere contains a mixture of several different gases in different amounts. The amounts of the most abundant gases are shown in Table 2.1. The percentage of permanent components does not vary from day to day and has little effect on the weather and other atmospheric processes.

The variable components, which make up far less than 1 % of the atmosphere, greatly influence weather and climate. Gases like water vapour, CO_2, CH_4, N_2O and sulphur dioxide (SO_2) absorb the infrared radiation emitted by the Earth's surface and warm the atmosphere. Without any traces of the so-called greenhouse gases, the Earth's atmosphere would be 303 K colder, which is too cold for life to exist on Earth. On the other hand, the increase in these gases causes global warming and affects the global energy balance. In addition to gases, the atmosphere also contains particulate matter such as dust and volcanic ash. These are highly variable and generally less persistent than gases. Nevertheless, they can sometimes remain in the atmosphere for an extended period (https://www.visionlearning.com/en/library/Earth-Science/6/Composition-of-Earths-Atmosphere/107/reading).

Even though the most abundant components are relatively inert molecules like N_2 and O_2, the Earth's atmosphere is a relatively efficient oxidizing medium. The presence of very reactive molecules with an unpaired electron in the outer (valence) shell, the so-called free radicals, is one of the main reasons for this. The most important free radical in the troposphere chemistry is the OH radical, which reacts with nearly every molecular species in the atmosphere. In addition, during the daytime, the HO_2 and RO_2 radicals also contribute to the oxidative capacity of the atmosphere. The nitrate (NO_3) radical and OH control the oxidation processes at night-time. Although less reactive than free radicals, ozone reacts with various compounds and participates in oxidation processes.

Table 2.1: Composition of the Earth's atmosphere (Data source: Atmospheric composition and Vertical Structure by Thomas W. Schlatter, book: Encyclopaedia of Aerospace Engineering 2010, chapter: Environmental Impact, Manufacturing and Operations Operational Environment).

Permanent Components		Variable Components	
Constituent	Mixing ratio (μmole mole^{-1})	Constituent	Mixing ratio (μmole mole^{-1})
Nitrogen (N_2)	780840	Water Vapour (H_2O)	0 to 40000
Oxygen (O_2)	209460	Carbon dioxide (CO_2)	399
Argon (Ar)	9340	Methane (CH_4)	1.8
Neon (Ne)	18.18	Nitrous oxide (N_2O)	0.320
Helium (He)	5.24	Ozone (O_3)	0.01 to 0.10
Hydrogen (H)	0.56	Particles (dust, soot, etc.)	0.01
Xenon (Xe)	0.09	Chlorofluorocarbons (CFC)	0.0002

2.2 Chemical Kinetics and Photochemistry

The gas-phase reactions occur when one or more molecules are converted to other molecules through bond breaking. For this, sufficient energy must be available to break chemical bonds. The minimum energy necessary for a reaction to take place is called activation energy, E_a. The E_a necessary for a reaction comes from either the collision of two or more gas molecules or the collision of a photon with a molecule. The molecules undergoing the chemical conversion during the reaction are called reactants, and the molecules produced at the end of the reaction are called products. The resultant product may have less (exothermic reaction, Figure 2.5b) or higher (endothermic reaction, Figure 2.5a) energy than the reactants. The energy released during an exothermic reaction is converted to heat, kinetic energy, and/or photons. Similarly, the energy absorbed during an endothermic reaction is given by heat, kinetic energy, and/or photons. A reaction involving two reactants and products is denoted as:
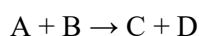
$$A + B \rightarrow C + D \hspace{4cm} R2.1$$
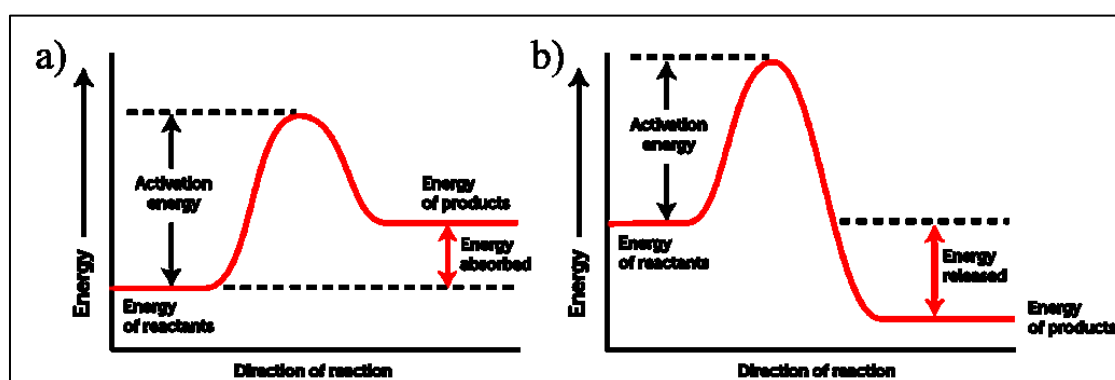
Figure 2.5: Potential energy surface along the reaction coordinate for an (a) endothermic and (b) exothermic reaction.

The rate of decrease of reactants or the rate of production of products in a reaction is known as the reaction rate. The reaction rate depends upon the rate coefficient (k) and the amount of reactant present. So the gas phase reactions can be further classified according to the number of reactants present as unimolecular, bimolecular, and termolecular reactions (Levine, 1995).

2.2.1 Unimolecular Reactions

The reactions involving only one reactant molecule are called unimolecular reactions. These reactions occur when a molecule lowers its energy by undergoing bond breaking. Thermal decomposition, cis-trans isomerization, ring-opening, and racemization are some examples of unimolecular reactions. Since the rate at which a substance decomposes depends on its concentration, unimolecular reactions are often first-order reactions and can be written as:

$$A \rightarrow B \hspace{4cm} R2.2$$

The rate of reaction R2.2 is given by

$$\frac{d[A]}{dt} = -k_{2.2}[A]$$

Eq. 2.5

k for a first-order reaction is given in units of s^{-1}.

A molecule might undergo a unimolecular reaction after getting excited by an incident photon with sufficient energy denoted by hv. These types of reactions are called photolysis reactions. The excitation of a molecule by a photon is denoted as:

$$AB + hv \rightarrow AB^*$$

R2.3

This excited state will result in one of the following processes:

Dissociation	$AB^* \rightarrow A + B$	R2.4
Direct reaction	$AB^* + C \rightarrow A + BC$	R2.5
Luminescence	$AB^* \rightarrow AB + hv$	R2.6
Collisional deactivation	$AB^* + M \rightarrow AB + M^*$	R2.7
Ionisation	$AB^* \rightarrow AB^+ + e^-$	R2.8
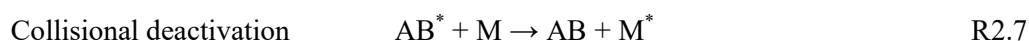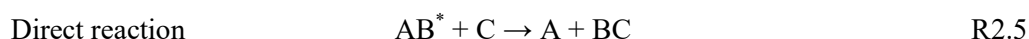
Photodissociation of a molecule occurs when the energy of the incident photon exceeds the binding energy of the particular chemical bond. Thus the excited species AB^* will have higher energy than the dissociation threshold of the molecule. Then the rate of the reaction is given as:

$$-\frac{d}{dt}[AB] = \frac{d}{dt}[A] = \frac{d}{dt}[B] = j_{2.3}[AB]$$

Eq. 2.6

where j is the photolysis frequency expressed in units of s^{-1}. The photolysis frequency of a particular molecule, j_x over a wavelength range from λ_1 to λ_2, is defined as:

$$j_x = \int_{\lambda_1}^{\lambda_2} \sigma(\lambda, T)\, \Phi(\lambda, T) I(\lambda) d\lambda$$

Eq. 2.7

where $\sigma(\lambda, T)$ is the wavelength and temperature-dependent absorption cross-section; $\Phi(\lambda, T)$ is the wavelength and temperature-dependent quantum yield for the reaction, and $I(\lambda)$ is the spectral actinic flux.

2.2.2 Bimolecular Reactions

The reactions involving the collision of two reactants are known as bimolecular reactions. The collision produces an activated complex that decomposes rapidly to either the original reactants or the products. An elementary bimolecular reaction can be written as:

$$A + B \rightarrow C + D \qquad\qquad\qquad R2.9$$

for which the rate expression is given by

$$-\frac{d}{dt}[A] = -\frac{d}{dt}[B] = \frac{d}{dt}[C] = \frac{d}{dt}[D] = k_{2.9}[A][B] \qquad\qquad Eq.\ 2.8$$

A special case of bimolecular reaction is the self-reaction of a reactant:

$$A + A = B + C \qquad\qquad\qquad R2.10$$

The corresponding rate equation is:

$$-\frac{1}{2}\frac{d}{dt}[A] = \frac{d}{dt}[B] = \frac{d}{dt}[C] = k_{2.10}[A]^2 \qquad\qquad Eq.\ 2.9$$

The k for bimolecular reactions is expressed in units of cm^3 molecules^{-1} s^{-1}.

In some cases, the products of a reaction might react together to get the reactants back. These reactions are called reversible reactions. Depending upon the physical parameters, reversible reactions will reach an equilibrium point where the concentrations of the reactants and products will no longer change. A reversible reaction is denoted by a double arrow pointing in both directions in a chemical equation. For example, a two reactant, two product equation is written as:

$$A + B \rightleftharpoons C + D \qquad\qquad\qquad R2.11$$

The forward and the backward reactions can be written separately as:

$$A + B \rightarrow C + D \qquad\qquad\qquad R2.12$$

and

$$C + D \rightarrow A + B \qquad\qquad\qquad R2.13$$

After the steady-state is reached,

$$k_{2.12}[A][B] = k_{2.13}[C][D] \qquad\qquad Eq.\ 2.10$$

from which an equilibrium constant, $k_{2.11}$ is defined for the two-way reaction R2.11 as:

$$K_{2.11} = \frac{[C][D]}{[A][B]} \qquad\qquad Eq.\ 2.11$$

The equilibrium constant is a thermodynamic quantity that only depends upon the free energies of molecules A, B, C and D.

2.2.3 Termolecular Reactions

The reactions in which the activated complex from the collision of reactants requires the collision with a third body M before decomposing into products are known as termolecular reactions. An elementary termolecular reaction involves the following steps.

$$A + B \rightarrow AB^*$$
R2.14

$$AB^* \rightarrow A + B$$
R2.15

$$AB^* + M \rightarrow AB + M^*$$
R2.16

The third body, M is an inert molecule (in the atmosphere, generally N_2 and O_2) that can remove the excess energy from AB^* and eventually dissipate it as heat. Common practice is to write the overall reaction as:

$$A + B + M \rightarrow AB + M \text{ or}$$

$$A + B \overset{M}{\rightarrow} AB$$
R2.17
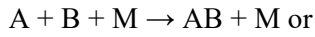
The rate of a three-body reaction is defined as the formation rate of AB by reaction R2.16 and is given by:

$$\frac{d}{dt}[AB] = k_{2.16}[AB^*][M]$$
Eq. 2.12

The excited complex AB^* has a very short lifetime and reacts through R2.15 or R2.16 as soon as it is produced. Therefore, we may assume that it is in a steady-state at all times, i.e., the production of AB^* is equal to the loss of AB^*.

$$k_{2.14}[A][B] = k_{2.15}[AB^*] + k_{2.16}[AB^*][M]$$
Eq. 2.13

Rearranging and substituting for $[AB^*]$ in Eq. 2.12:

$$-\frac{d}{dt}[A] = -\frac{d}{dt}[B] = \frac{d}{dt}[AB] = \frac{k_{2.14}k_{2.16}[A][B][M]}{k_{2.15}+k_{2.16}[M]}$$
Eq. 2.14

The equivalence between the production of AB and losses of A and B follows from the steady-state assumption for AB^*. [M] is typically taken as the number density of air molecules in the atmosphere.

Equation 2.14 is the general rate expression for a three-body reaction. There are two limits of interest. In the low-density limit where $[M] \ll k_{2.16}/k_{2.15}$ (called the low-pressure limit), Eq. 2.14 simplifies to:

$$-\frac{d}{dt}[A] = -\frac{d}{dt}[B] = \frac{d}{dt}[AB] = \frac{k_{2.14}k_{2.16}}{k_{2.15}}[A][B][M]$$
Eq. 2.15

In this case, the overall reaction rate depends linearly on [M]. One refers to $k_L = k_{2.14}k_{2.16}/k_{2.15}$ as the low-pressure limit rate constant. In the high-density limit $[M] \gg k_{2.16}/k_{2.15}$ (called the high-pressure limit), Eq. 2.14 simplifies to:

$$-\frac{d}{dt}[A] = -\frac{d}{dt}[B] = \frac{d}{dt}[AB] = k_{2.14}[A][B] \qquad \text{Eq. 2.16}$$

The rate of AB production is limited by the production of AB^* and is independent of [M]; M is in excess to ensure that all AB^* complexes stabilize to AB. Since the rate of reaction R2.14 determines the rate of the overall reaction, one refers to R2.14 in the high-pressure limit as the rate-limiting step for the production of AB, and $k_H = k_{2.14}$ as the high-pressure limit rate constant. Rewriting Eq. 2.14 in terms of k_L and k_H makes the two limits apparent:

$$-\frac{d}{dt}[A] = -\frac{d}{dt}[B] = \frac{d}{dt}[AB] = \frac{k_L[A][B][M]}{1 + \frac{k_L}{k_H}[M]} \qquad \text{Eq. 2.17}$$

The rate constant of a three-body reaction is sometimes given as one of the two limits identified by the units of k (cm^6 molecule^{-2} s^{-1} for the low-pressure limit and cm^3 molecule^{-1} s^{-1} for the high-pressure limit), indicating that the appropriate limit holds.

2.3 Atmospheric Free Radicals

Typically, the fastest reactions in the troposphere involve at least one free radical species. Many tropospheric free radical reactions have zero activation energy. Free radicals have at least one unpaired electron. This results in having relatively high enthalpies and Gibbs free energies for them. They are much more reactive than non-radical species whose electrons are paired. Often, species with an odd number of electrons are free radicals, and those with an even number are non-radicals. An important exception to this rule is atomic oxygen, which has 8 electrons but two unpaired valence shell electrons in its "triplet" $O(^3P)$ ground state ($2s^2\ 2p_x^2\ 2p_y^1\ 2p_z^1$) and is, therefore, a free radical, more precisely a biradical. Atomic oxygen with all electrons paired ($2s^2\ 2p_x^2\ 2p_y^2$) is in a higher-energy "singlet" $O(^1D)$ state. It is more reactive than $O(^3P)$.

Since free radicals have high enthalpies and Gibbs free energies, their formation from non-radical species is generally endothermic; i.e. an external energy source is required to form a free radical. In the atmosphere, this energy is generally supplied by sunlight.

non-radical + hν → radical + radical
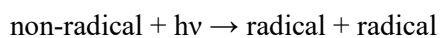
The production of free radicals initiates radical reaction chains, which are propagated by subsequent reactions of free radicals with non-radical species:

radical + non-radical → radical + non-radical
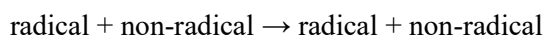
A free radical and non-radical species reaction must always produce a free radical to conserve the total odd number of electrons. The free radical produced in the atmosphere reacts with another non-radical, propagating a chain of reactions. A non-radical species produced by a reaction involving free radicals may subsequently photolyse to produce additional free radicals during the propagation chain. This photolysis is called a branching reaction as it accelerates (or "branches") the chain by increasing the pool of free radicals. Due to the critical importance of solar radiation in initiating radical-assisted chain mechanisms in the atmosphere, these mechanisms are often referred to as photochemical processes.

The free radicals are lost by reactions between free radicals leading to non-radical products or on the surfaces (heterogeneous loss processes), for example, on aerosols. Termination through radical–radical reactions is generally slower than propagation reactions because of the low concentration of free radicals in the atmosphere. On the other hand, the heterogeneous loss process depends on the actual aerosol loading, the effective surface area, phase and compounds present in the particles, and relative humidity.

The free radicals influence the atmospheric composition through their central function in controlling the **o**xidative **c**apacity of the **a**tmosphere (OCA). The oxidation in the troposphere is of crucial importance because the troposphere contains the bulk of atmospheric mass and gases that are generally emitted at the surface. Since H. Levy II (1971) found a route for the formation of OH radicals in the troposphere and suggested that they could be a significant sink for CO, the free radicals have been recognised as the cleaning agents of the atmosphere. OH, by far, is the most effective scavenger in the troposphere during the daytime. It is the primary oxidant for CO, VOCs, hydrogen sulphide (H_2S) and SO_2. The oxidation of CO and VOCs by OH produces peroxy radicals, HO_2 and RO_2, which significantly contribute to the OCA during the daytime. HO_2 and RO_2 are very much intertwined with OH through oxidation processes in the atmosphere, as summarised in figure 2.6. Even though not as reactive as OH, HO_2 and RO_2 play a vital role in the photochemical formation of oxidizing agents like ozone, peroxides and organic nitrites. This initiates the degradation and removal of most oxidisable trace gases. The self–reaction of HO_2 produces hydrogen peroxide (H_2O_2), an important oxidant in cloud droplets. The NO_3 radical takes over the role of hydroxyl and peroxy radicals as the dominant oxidant in the atmosphere at night. NO_3 are mainly formed by the reaction of NO_2 with O_3. Due to the fast photolysis of NO_3 by sunlight, the concentration is negligibly small during the daytime.

2.3.1 Peroxy Radicals

HO_2 and RO_2 participate in catalytic cycles, which produce and destroy O_3, as shown in figure 2.6. The photolysis of NO_2 is the primary source of O_3 in the troposphere.
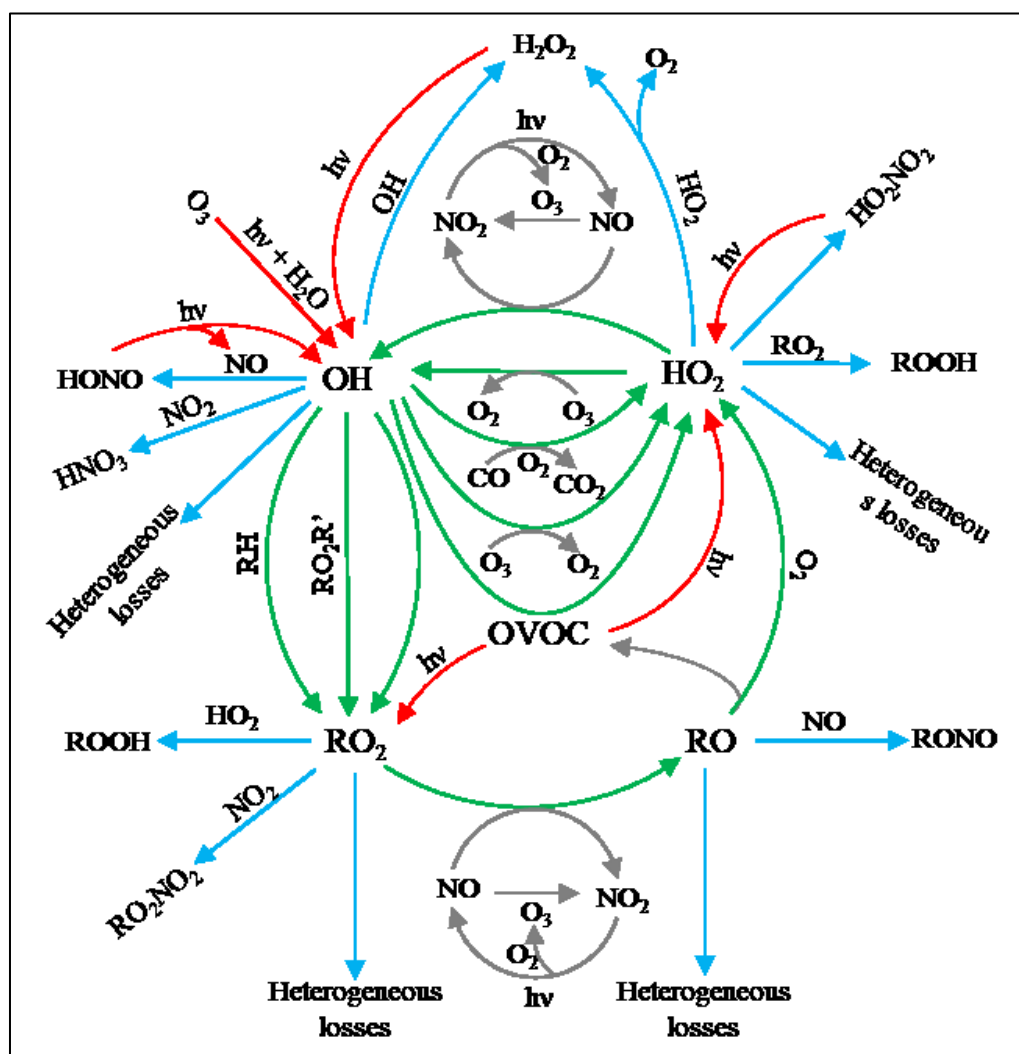
Figure 2.6: Schematic representation of reactions of relevance for the OCA involving OH and RO_2^*. The red, blue, and green arrows indicate radical production, loss, and catalytic cycles, respectively.

$$NO_2 + hv \ (< 320 \ nm) \rightarrow O(^3P) + NO \qquad\qquad R2.18$$

$$O(^3P) + O_2 + M \rightarrow O_3 + M \qquad\qquad R2.19$$

The NO produced in R2.18 and O_3 produced in R2.19 reacts to produce NO_2 and O_2.

$$NO + O_3 \rightarrow NO_2 + O_2 \qquad\qquad R2.20$$

These three reactions make a null cycle. The O_3 budget is controlled by the additional NO_2 formation and O_3 losses through the following RO_2^* reactions:

$$HO_2 + NO \rightarrow OH + NO_2 \qquad\qquad R2.21$$

$$RO_2 + NO \rightarrow RO + NO_2 \qquad\qquad R2.22$$

$$RO + O_2 \rightarrow HO_2 + carbonyl \ products \qquad\qquad R2.23$$

$$HO_2 + O_3 \rightarrow OH + 2O_2 \qquad\qquad R2.24$$

$$OH + O_3 \rightarrow HO_2 + O_2 \qquad\qquad R2.25$$
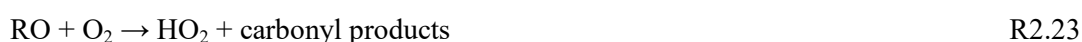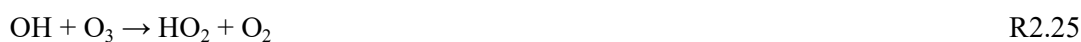
When the $[NO] > \frac{k_{2.24}}{k_{2.21}} [O_3]$, the NO_2 producing reactions R2.21 and R2.22 will dominate over the O_3 consuming reaction R2.24. This extra NO_2 produced changes the NO to NO_2 ratio and eventually results in O_3 production through R2.18 and R2.19. On the other hand, when $[NO] < \frac{k_{2.24}}{k_{2.21}} [O_3]$, the O_3 is consumed through R2.24 and R2.25.

2.3.2 Sources of $RO_2{}^*$

      The following reactions produce HO_2 and RO_2 in the troposphere and lower stratosphere:

- Oxidation of CO by OH:

$$OH + CO \overset{O_2}{\rightarrow} HO_2 + CO_2 \qquad\qquad R2.26$$

- Oxidation of CH_4 by OH followed by the reaction between methyl radical and O_2:

$$CH_4 + OH \rightarrow CH_3 + H_2O \qquad\qquad R2.27$$

$$CH_3 + O_2 + M \rightarrow CH_3O_2 + M \qquad\qquad R2.28$$

- Oxidation aldehydes by OH. The oxidation of formaldehyde (HCHO) is given as an example:

$$HCHO + OH \rightarrow CHO + H_2O \qquad\qquad R2.29$$

$$CHO + O_2 \rightarrow HO_2 + CO \qquad\qquad R2.30$$

- Oxidation of peroxides by OH. The oxidation of H_2O_2 and methyl peroxide (CH_3O_2H) are given as an example:

$$H_2O_2 + OH \rightarrow HO_2 + H_2O \qquad\qquad R2.31$$

$$CH_3O_2H + OH \rightarrow CH_3O_2 + H_2O \qquad\qquad R2.32$$
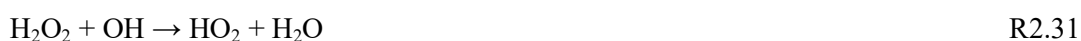
- Photolysis of aldehydes. The photolysis of the simplest aldehyde (HCHO) is given by:

$$HCHO + h\nu\ (\lambda < 340\ nm) \rightarrow H_2 + CO \qquad\qquad R2.33$$

$$H_2 + OH \rightarrow H_2O + H \qquad\qquad R2.34$$

$$H + O_2 + M \rightarrow HO_2 + M \qquad\qquad R2.35$$

$$HCHO + h\nu\ (\lambda < 340\ nm) \rightarrow H + CHO \qquad\qquad R2.36$$
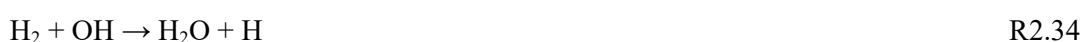
R2.36 is followed by R2.30.

- Ozonolysis of alkenes. The ozonolysis of the simplest alkene (i.e., ethylene) is given by:

$$CH_2 = CH_2 + O_3 \rightarrow HCHO + [H_2COO]^*$$ 　　　　　　　　R2.37

The HCHO produced acts as a source of HO_2 by R2.29 + R2.30, R2.33 + R2.34 + R2.35 and R2.36. $[H_2COO]^*$ is called the "Criegee intermediate", which decomposes, forming H, HCHO and OH with a total radical yield of approximately 0.45 (Atkinson and Aschmann, 1993; Paulson and Orlando et al., 1996). The exact reaction mechanism is specific for each alkene.

- Oxidation of some organic species by NO_3:

$$NO_3 + RH \rightarrow HNO_3 + R$$ 　　　　　　　　　　　　R2.38

$$R + O_2 + M \rightarrow RO_2 + M$$ 　　　　　　　　　　　　R2.39

Since the NO_3 concentration during daytime is very low, the contribution from reactions involving NO_3 is only significant at night-time.

2.3.3 Sinks of $RO_2{}^*$

The following reactions act as a direct sink of $RO_2{}^*$:

$$HO_2 + OH \rightarrow H_2O + O_2$$ 　　　　　　　　　　　　R2.40
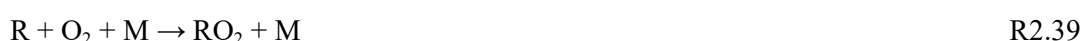
$$HO_2 + HO_2 + M \rightarrow H_2O_2 + O_2$$ 　　　　　　　　　R2.41

$$HO_2 + CH_3O_2 \rightarrow CH_3O_2H + O_2$$ 　　　　　　　　　R2.42

$$CH_3O_2 + CH_3O_2 \rightarrow 2CH_3O + H_2O$$ 　　　　　　　　R2.43

The peroxides formed through reactions R2.41 and R2.42 might undergo washout leading to $RO_2{}^*$ loss or get oxidised by OH through R2.31 and R2.32, leading to $RO_2{}^*$ formation. The peroxides might also undergo photolysis leading to OH and other $RO_2{}^*$ precursor formations, further producing $RO_2{}^*$.

$$H_2O_2 + h\nu \rightarrow OH + OH$$ 　　　　　　　　　　　　R2.44

$$CH_3O_2H + h\nu \rightarrow HCHO + H + OH$$ 　　　　　　　　R2.45

The reaction of OH formed from R2.21, R2.24, and R2.44 with NO and NO_2 results in nitrous acid (HONO) and nitric acid (HNO_3) formation, respectively.

$$OH + NO \xrightarrow{M} HONO$$ 　　　　　　　　　　　　R2.46

$$OH + NO_2 \xrightarrow{M} HNO_3$$ 　　　　　　　　　　　　R2.47

The HNO$_3$ formed results in OH consumption and effectively acts as a peroxy radical sink during the radical interconversion. In contrast, the HONO produced in R2.46 might undergo washout and transport acting as a peroxy radical or undergo photolysis and produce OH back.

HONO + hν (λ ≤ 400 nm) → OH + NO   R2.48

The loss rate of HO$_2$ (D$_{het}$) through uptake on small particles (submicrometer) is described by:

$$D_{het} = \frac{\omega[ASA]\gamma}{4}[HO_2]$$ Eq. 2.18

where ω is the mean molecular speed of HO$_2$ (ω = 43725 cm s^{-1} at 298 K), ASA is the total aerosol surface area, and γ is the aerosol uptake coefficient. Previous kinetic studies about the HO$_2$ uptake on aerosol (Mozurkewich et al., 1987; Hanson, 1992; Gershenzon et al., 1995; Bedjanian et al., 2005; Remorov et al., 2002; Thornton and Abbatt, 2005; Taketani et al., 2008, 2009, 2010) showed that the uptake coefficient (γ) for single-component particles depends upon the phase and relative humidity of the particle. For particle-containing water, the reported γ varies between 0.1 and 0.2 at 45 % to 75 % relative humidity. In the case of dry particles with 20 % to 53 % relative humidity, γ is < 0.01 to 0.05. In addition, the presence of transition metal ions (Cu and Fe) in the aerosol acts as catalysts for the heterogeneous uptake of HO$_2$ and thereby increases γ (Jacob, 2000). Taketani et al., 2012, reported measurements of HO$_2$ uptake coefficients in two sites in North China Plane with regional-scale air pollution. The value varied between 0.09 and 0.4 depending on the components in the aerosol. In previous studies, different values have been used for γ to account for the loss of HO$_2$ through uptake on aerosol (references herein).

2.4 Peroxy Radical Measurement Techniques

The HO$_2$ and RO$_2$ concentrations in the atmosphere are small because of their high reactivity. Consequently, their measurement requires sensitive and accurate techniques. Except the Matrix Isolation-Electron Spin Resonance (Mihelcic et al., 1985), the Bromide Chemical Ionization Mass Spectrometry (Veres et al., 2015) and chemical ionization–atmospheric pressure interface–time-of-flight (CI-APi-TOF) mass spectrometry (Junninen et al., 2010; Jokinen et al., 2012; Rissanen et al., 2014), there are no other direct measurement techniques of HO$_2$ or RO$_2$ in air. Most commonly used are indirect methods, in which peroxy radicals are chemically converted into other molecules that can be detected and quantified more accurately. In this section, well-established peroxy radical measurement techniques are briefly discussed.

2.4.1 Matrix Isolation-Electron Spin Resonance (MIESR)

MIESR is the first reported technique for directly measuring peroxy radicals (Mihelcic et al., 1985, 1990, 1993). The air samples are collected on a gold-coated cold finger kept at 77 K in a

vacuum D_2O-ice matrix during the measurement. These samples are then analysed in laboratory conditions using the Electron Spin Resonance (ESR) technique to obtain a spectrum due to the unpaired electron of radicals. This spectrum is fitted with reference spectra to determine the concentration of individual species (Mihelcic et al., 1990). NO_2, NO_3, HO_2, $CH_3C(O)O_2$ and the sum of the organic peroxy radicals can be measured by this technique. MIESR enables the discrimination of HO_2 from RO_2. The long sampling time required, over 20-30 min, makes it unsuitable for monitoring fast variations in the air mass.

2.4.2 Laser Induced Fluorescence (LIF)

The LIF instrument samples ambient air by expansion into a low-pressure volume, where OH in the sampled air is detected spectroscopically by laser-excited fluorescence at 308 nm. This concept is also known as Fluorescence Assay with Gas Expansion, FAGE (Hard et al., 1984). By adding NO in excess to the sampled air mass, HO_2 is converted to OH (R2.21). Thereby the sum of OH and HO_2 in the sampled air mass is measured by LIF as OH. Using two measurement channels or modes, with and without NO, the LIF instrument can separately determine OH and HO_2. The RO_2 radicals from alkenes, such as isoprene and other aromatics, are partly detected in the HO_2 modus and might interfere in air masses with a significant amount of biogenic VOCs (Fuchs et al. 2011).

The ROxLIF instrument reported in Fuchs et al., 2008 can measure OH, HO_x (OH + HO_2) and RO_x (OH+ HO_2 + RO +RO_2) using a two-stage chemical conversion scheme at reduced pressure with a flow reactor. For the RO_2 measurement, excess reagent gases (CO and NO) are added to convert RO_2 into HO_2 in the flow reactor. The added NO converts RO_2 to HO_x, while CO converts HO_x to HO_2. For the HO_2 measurement, only CO is added to convert all the HO_x into HO_2, thus avoiding major radical losses by OH reactions such as wall losses. This is followed by the chemical conversion of HO_2 to OH in a downstream low-pressure chamber, which is measured using the LIF technique. The OH present in the sampled air is measured in a separate channel without adding reagent gases. This allows simultaneous measurement of OH along with alternating RO_x and HO_x measurements. However, the HO_x measurement might have some interference from RO_2. This can be reduced below 20 % by reducing the reaction time and/or the NO concentration in the detection cell. This leads to a decrease in the HO_2 detection limit. The ROxLIF technique is very sensitive, with a detection limit signal-to-noise ratio around 0.1 pmole mole^{-1} of HO_2 or RO_2 at a time resolution of 1 minute.

2.4.3 Peroxy Radical Chemical Amplifier (PeRCA)

The chemical amplification technique (Cantrell and Stedman, 1982; Hastie et al., 1991) has been used to measure the total sum of peroxy radicals, collectively known as RO_2^*, (RO_2^* = OH + ΣRO + HO_2+ ΣRO_2), by the amplified conversion into NO_2 in a flow reactor and subsequent detection of the NO_2 produced. The conversion into NO_2 is achieved by adding an excess amount of reagent

gases (NO and CO) to the sampled air. Due to the low concentration of OH and RO molecules compared to peroxy radicals in the atmosphere, the PeRCA technique gives the sum of HO_2 and those RO_2, which react with NO to form NO_2. Larger RO_2, which do not react with NO and thereby do not contribute to the total O_3 budget, are not detected by the PeRCA technique. So the PeRCA measurements give an accurate quantification of peroxy radicals which controls the O_3 budget. Figure 2.7 shows a simplified illustration of the chemistry in a PeRCA flow reactor.
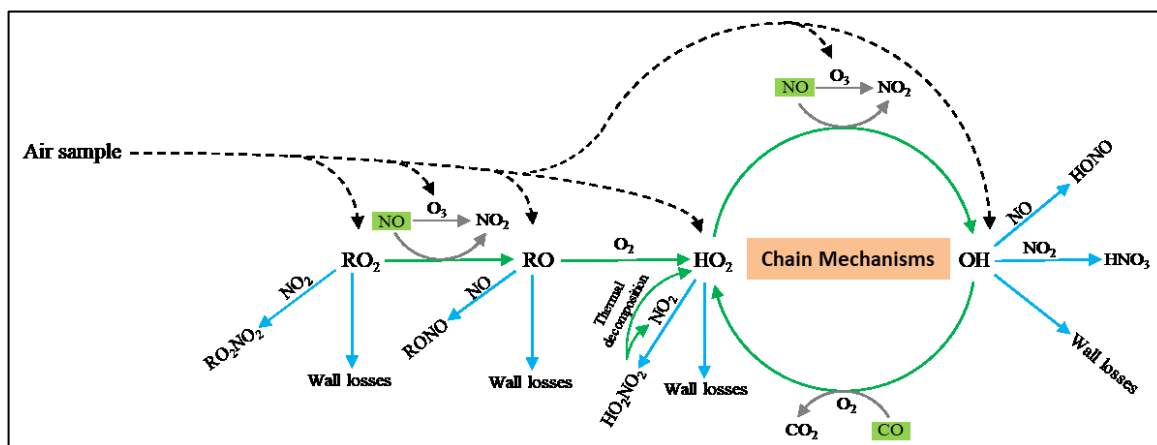

Figure 2.7: Simplified illustration of the amplification cycle and the main loss reactions of PeRCA. The reagent gases are marked with green background. The radical amplification and loss reactions are indicated with green and blue arrows, respectively. The grey colour indicates other important reactions taking place inside the reactor.

The NO_2 reaching the detector connected to a PeRCA flow reactor is the sum of the background NO_2 and the amplified amount of NO_2 produced from RO_2^* in the sampled air. The background NO_2 is the sum of ambient NO_2 in the sampled air, NO_2 produced from the reaction of ambient O_3 with the reagent gas NO (R2.20), and NO_2 produced from the thermal decomposition of peroxy nitrates (e.g. PAN), and peroxynitric acid (PPN) in the flow reactor. Accurate measurement of the background NO_2 is necessary to discriminate the NO_2 produced from the amplified conversion. The background NO_2 is measured by adding N_2 to the flow reactor instead of CO to suppress the chain mechanism. By considering this, the RO_2^* is calculated from the difference in NO_2 (ΔNO_2) concentration in the sample flow after passing through the flow reactors with and without the amplification, i.e., with and without the addition of CO. The amount of RO_2^* from a PeRCA system is given by:

$$[RO_2^*] = \frac{\Delta[NO_2]}{eCL}$$

Eq. 2.19

Where eCL is the conversion factor of RO_2^* into NO_2, known as **e**ffective **c**hain **l**ength.

Since the rate of chain propagation reaction (R2.26) is directly proportional to the amount of reagent gas CO, the eCL increases with the amount of CO added to the reactor (Ashbourn et al., 1998; Reichert et al., 2003; Sadanaga et al., 2004). Unlike CO, NO participates in both the chain carrier (R2.21) and chain termination (R2.46) reactions (Hastie et al., 1991; Mihele et al., 1999). These NO

reactions determine the eCL at different NO concentrations added to the sample flow for a constant CO concentration. The rate of titration of the sampled O_3 by NO to form NO_2 also depends on the concentration of NO and the time for reaction before reaching the detector. The eCL is also affected by the sample flow velocity due to the wall losses at the inlet before the addition of CO. This wall loss is directly proportional to the residence time and increases with decreasing sample flow velocity. Several studies have shown that the eCL of a PeRCA reactor decreases with inlet humidity (Mihele and Hastie, 1998; Mihele et al., 1999). It has been partially characterised by Stöbener, 1999; Reichert, 2000; Burkert et al., 2001; Salisbury et al., 2002. Reichert et al. (2003) conducted experimental studies and numerical simulations to accurately define the main processes involved and postulated this as the effect of HO_2 water clusters formation acting as an extra loss process by reducing the $HO_2 - NO$ (R2.21) reaction.

To account for the fast variations of RO_2^* and background NO_2 during ambient measurements, continuous monitoring of both amplified and background NO_2 signals is necessary. This can be achieved by different reactor-detector configurations:

i) a single flow reactor – single detector combination, where the reagent gas flows into the inlet are alternated periodically between NO + N_2, the so-called 'background mode', and NO + CO, the so-called 'amplification mode', which suppresses or allow the chain mechanism respectively. This method has been successfully demonstrated in many previous studies (Cantrell et al., 1984; Hastie et al., 1991; Cantrell et al., 1993, Carslaw et al., 1997; Penkett et al., 1997; Andrés Hernández et al., 2001; Burkert et al., 2001a, b; Burkert et al., 2003; Green et al., 2002; Li et al., 2009, Liu et al., 2009). This technique cannot account for the background variations during the amplification mode and the RO_2^* variations during the background mode. This increases the uncertainty in the retrieved RO_2^*. The uncertainty can be reduced by reducing the time in each mode.

ii) a two flow reactor – single detector combination, where one reactor works in amplification mode and the second one in background mode. The reactor connected to the detector is alternated periodically to account for the background variations (Cantrell et al., 1996; Sadanaga et al., 2004; Miyazaki et al., 2010). This method monitors background variations much more efficiently than a single reactor – single detector method. Still, fast variations of O_3 and NO_2 in the sampled air mass will increase the uncertainty of the retrieved data set (Cantrell et al., 1996).

iii) a two flow reactors – two detector combination, where one reactor – detector line is working in amplification mode and the second reactor detector line is working in the background mode continuously (Cantrell et al., 1996; Liu et al., 2014; Chen et al., 2016). This method offers the possibility to retrieve RO_2^* at the exact resolution as the NO_2 measurement. The continuous background and amplification mode monitoring accurately discriminates NO_2 produced from the amplified conversion during any background variations. Since the amplified NO_2 signal from one

detector is compared with the background NO_2 from another detector, the quality of the retrieved ΔNO_2 and thereby of the RO_2^* data mainly depends on the measurement accuracy and the variations in sensitivity to NO_2 from each detector. So, any malfunction present only in one detector increases the error in the retrieved RO_2^*.

iv) a two flow reactor – two detector combination, where both reactors alternate between amplification and background mode out of phase to one another. Thus, during the first part of the measurement cycle, the first reactor and detector are in amplification mode, while the second reactor and detector are in background mode. In the second part of the cycle, the first reactor and detector are in background mode, while the second reactor detector are in amplification mode (Green et al., 2006; Fleming et al., 2006a, b, Kartal et al., 2010; Horstjann et al., 2014; Wood et al., 2014; George et al. 2020). This method continuously measures the amplification and background modes while reducing all the uncertainties arising from differences in the measurement channels.

Over the years, several techniques have been reported for the accurate detection of NO_2 produced in a chemical amplifier.

i) Chemiluminescence: The NO_2 is measured using the chemiluminescence reaction between NO_2 and a luminol solution (3-aminophthalhydrazide: $C_8H_7N_3O_2$) (Cantrell et al., 1984; Hastie et al., 1991; Cantrell et al., 1993, Carslaw et al., 1997; Penkett et al., 1997; Andrés Hernández et al., 2001; Burkert et al., 2001a, b; Burkert et al., 2003; Green et al., 2002, 2006; Fleming et al. a, b, 2006; Li et al., 2009; Kartal et al., 2010). The photons produced are measured using a photodiode/photomultiplier tube from which the actual number concentration of NO_2 is calculated. The luminol detector sensitivity reduces with increasing NO. The response of the detector changes depending upon the amount of reagent gas NO added to the inlet. To account for this, the luminol detector requires an additional NO_2 offset to assure its linear response, especially at low ambient O_3 concentrations (Clemitshaw et al., 1997). The luminol based detectors also have interferences for impurities like $Ni(CO)_4$ and $Fe(CO)_6$ in the reagent gas CO stored in nickel coated iron cylinders. In addition, the luminol–based instruments are prone to instrumental drift, which increases the necessity for periodic calibration of the NO_2 detector sensitivity.

ii) Laser Induced Fluorescence: The NO_2 detection is based on the fluorescence of excited NO_2 (Sadanaga et al., 2004; Miyazaki et al., 2008; Miyazaki et al., 2010). A second harmonic of the solid-state pulsed Nd:YAG laser is used as a light source for NO_2 excitation. The photons produced in the fluorescence decay are used to calculate the actual number concentration of NO_2. Fluorescence quenching and the collision quenching of the excited NO_2 molecules might reduce the accuracy of the measurements (Sadanaga et al., 2004; Miyazaki et al., 2008). In addition, accurate knowledge of the Nd:YAG laser power is necessary to correct the variations in the fluorescence due to laser power drift.

iii) Cavity Ring-Down Spectroscopy: In CRDS (O'Keefe and Deacon, 1988; Atkinson, 2003; Brown, 2003; Berden and Engel, 2010 and references herein), the time decay of the intensity of monochromatic electromagnetic radiation trapped inside a low-loss high finesse optical cavity defined by two or more high reflective mirrors (R > 99.99 %) is measured. The concentration of NO_2 is calculated from the decay times of the light pulse to $1/e^{th}$ of its initial value, the so-called ring-down time, for a resonator containing (τ) or not containing (τ_0) NO_2. Since the actual laser intensity is not necessary to determine NO_2, this technique is inherently independent of source power fluctuations. The drift in τ_0 manly due to changes in the cavity finesse and temperature might add uncertainties to the NO_2 measurement.

iv) Cavity Phase Shift Spectroscopy (CAPS): This technique also makes use of a low-loss high finesse optical cavity defined by two or more high reflective mirrors (Herbelin et al., 1980; Engeln et al., 1996; Kebabian et al., 2005 and references herein). The concentration of NO_2 is calculated from the phase shift difference of the electromagnetic radiation reaching the detector from a resonator coupled with a square or a sine wave modulated continuous light source containing (υ_0) or not containing (υ_1) NO_2.

v) Incoherent Broad Band Cavity Enhanced Spectroscopy (IBBCAS): A high-finesse optical cavity is coupled with a broadband incoherent light source, enabling high-sensitivity measurement of multispecies. The NO_2 molecules are identified by applying a **D**ifferential **O**ptical **A**bsorption **S**pectroscopy (DOAS) type data processing algorithm to the measured broadband absorption spectra (Fiedler et al., 2003; Langride et al., 2006; Varma et al., 2009; Thalman et al., 2010 and references herein)

2.4.4 Peroxy Radical Chemical Ionization Mass Spectrometry (PerCIMS)

In the PerCIMS method (Cantrell et al., 2003, Edwards et al., 2003), also known as ROxMas (ROx Chemical Conversion/Chemical Ionisation Mass Spectrometry) (Reiner et al., 1997; Hanke et al., 2002), the peroxy radicals in the sampled air mass are chemically amplified and converted into H_2SO_4 by replacing CO with SO_2 as a reagent in a PeRCA flow reactor. The H_2SO_4 formed is converted into HSO_4^- ion by adding NO_3^- (nitrate ion), which is subsequently detected by mass spectrometry. Figure 2.8 shows the conversion reaction in a PerCIMS instrument.

Separate measurement of HO_2 and $HO_2 + \sum RO_2$ is achieved by varying the concentration of NO relative to O_2 to favour or suppress the RO conversion to HO_2 (Edwards et al., 2003; Hornbrook et al., 2011).
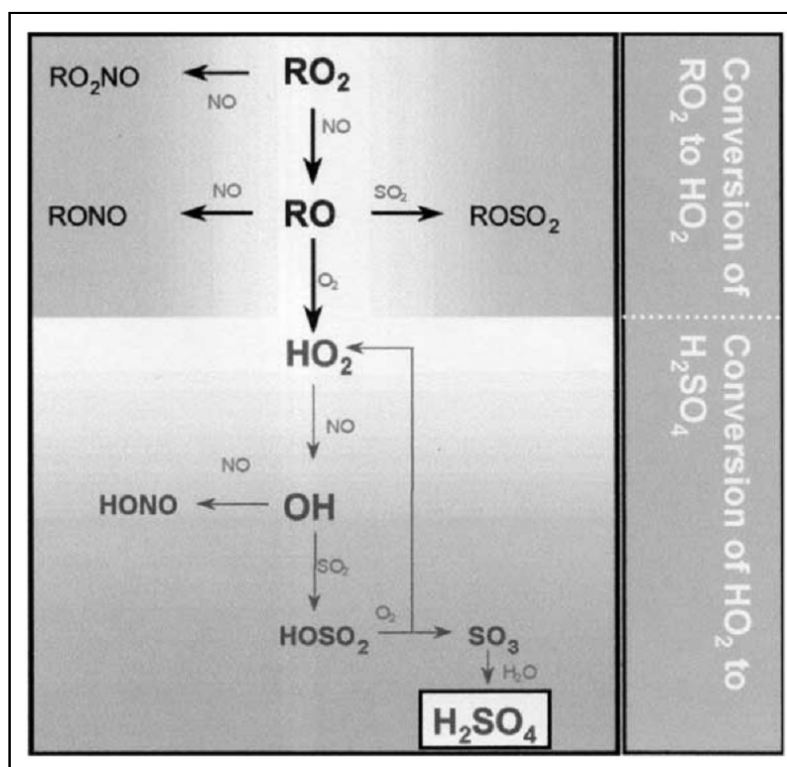
Figure 2.8: Simplified illustration of the conversion mechanism of simple organic peroxy radicals, RO_2 to HO_2 in a PerCIMS flow reactor (Figure source: Hanke et al., 2002).

2.4.5 Ethane Chemical Amplifier (ECHAMP)

Wood et al. (2017) introduced a new chemical amplifier, Ethane CHemical AMPlifier (ECHAMP), that uses ethane (C_2H_6) rather than CO to convert RO_2^* to NO_2. The net amplification cycle in an ECHAMP flow reactor is given by:

$$C_2H_6 + 2O_2 + 2NO_2 \rightarrow CH_3CHO + H_2O + 2NO_2 \qquad\qquad R2.49$$
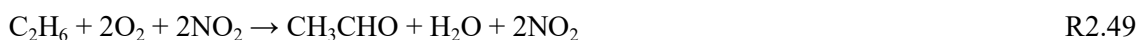
The replacement of the toxic reagent CO with C_2H_6 reduces the risk and simplifies the safety requirements of the chemical amplifier. The amplification factor of ECHAMP is almost seven times lower than that of the CO-based amplifiers under dry conditions. The difference decreases as the relative humidity increases (Wood et al., 2017).

2.4.6 Bromide Chemical Ionization Mass Spectrometry (Br-CIMS)

To overcome the limitations of indirect measurement techniques, Veres et al. (2015) developed a relatively new approach for direct detection of HO_2 radicals by a CIMS instrument using iodide as the primary ion. Sanchez et al. (2016) proposed for the first time the use of Br^- (Br-CIMS) and showed that the most promising ionization technique is detecting the bromide cluster. In this method, the sampled air is mixed with a Br^- reagent, which results in the $Br^-(HO_2)$ adduct formation. The subsequent detection of $Br^-(HO_2)$ adduct is achieved by a **h**igh-**r**esolution **t**ime-**of**-**f**light **c**hemical **i**onization **m**ass **s**pectrometer (HR-ToF-CIMS) and a quadrupole CIMS. Even though

the technique shows no significant interference from NO_x, HCHO, SO_2, or O_3 in the sampled air, the temperature and humidity dependence might increase the uncertainty of the measurements.

In a further study, Albrecht et al. (2019) compared the measurement of the Br-CIMS technique with the LIF measurements in controlled atmospheric chamber experiments. A good agreement between these two techniques was observed except for measurement under a high amount of some VOCs loading. Further experiment and characterization are still required to fully quantify the interferences before using this technique for field measurements.

2.4.6 Chemical Ionization–Atmospheric Pressure interface–Time-of-Flight Mass Spectrometry (CI-APi-ToF MS)

Recent developments in mass spectrometry have improved the resolution and sensitivity of mass spectrometers, facilitating the measurement of low concentrations of atmospheric OVOCs (Junninen et al., 2010; Jokinen et al., 2012; Rissanen et al., 2014). CI-APi-ToF MS consists of a **c**hemical **i**onisation (CI) system, and a **t**ime-**o**f-**f**light mass spectrometer (ToF) coupled to an **a**tmospheric **p**ressure **i**nterface (APi). The ionisation of the sample gas occurs in the CI-system at ambient pressure through proton transfer with the nitrate (NO_3^-), acetate (CH_3COO^-), lactate ($CH3CH(OH)COO^-$) or pyruvate ($CH3C(O)COO^-$) ions (Berndt et al., 2016). APi guides the chemically ionised sample gas into the ToF mass spectrometer, where they are separated according to their mass to charge ratio (m/z). Berndt et al., 2016 showed that when acetate (CH_3COO^-), lactate ($CH3CH(OH)COO^-$) and pyruvate ($CH3C(O)COO^-$) ions are used for the chemical ionisation, RO_2 produced from the ozonolysis and oxidation of α-pinene and β-pinene can be measured using a CI-APi-ToF MS.

2.5 PeRCEAS Instrument

The PeRCEAS instrument, which combines the PeRCA and the CRDS techniques in a dual-channel instrument to measure RO_2^*, has been used to acquire all the RO_2^* data analysed in this work. The core of the PeRCEAS airborne instrument (Figure 2.9) are the **DU**al channel **A**irborne peroxy radical Chemica**l** Amplifi**er** (DUALER) inlet installed inside a pylon, located on the outside of the HALO fuselage, and two CRDS NO_2 detectors mounted in a rack inside the cabin. The prototype was reported in Hortsjann et al. (2014), and further optimization and characterization in the laboratory for airborne measurements made during this research are presented in George et al. (2020).

Figure 2.9: Schematic diagram of the PeRCEAS instrument. MFC: mass flow controllers, PR: pressure regulator, P: Pressure sensor, T/RH: Temperature and relative humidity sensor, NO/N$_2$: a mixture of NO in N$_2$, and SA: synthetic air.

2.5.1 DUALER Inlet

The DUALER inlet consists of one pre-chamber and two PeRCA flow reactors (Figure 2.10). The pre-chamber is necessary to keep the pressure inside the flow reactor constant during airborne measurements to preserve the chemical conversion irrespective of outside pressure. As mentioned in section 2.4.3, in the flow reactors, RO$_2$* in the sampled air is converted into an amplified amount of NO$_2$ in the presence of the excess reagent gases NO and CO.

In the DUALER, the sampled air enters the pre-chamber, which is at a lower pressure than outside, through an orifice in a truncated cone, i.e. a nozzle. The temperature, pressure and relative humidity of the sample are measured at the pre-chamber. The air is pumped through the two flow reactors and a bypass line from the pre-chamber. A mixture of CO or N$_2$ and NO are added at the upper addition point in the flow reactors. At the lower addition point, a flow of N$_2$ or CO is added to each reactor. The two flow reactors work in alternating measurement modes (amplification and background modes) out of phase with one another. Four three-way solenoidal valves (Type QE 622, operation range 0-1 bar, Staiger GmbH) allow the CO/N$_2$ flows to be switched simultaneously but out of phase with one another from the upper to the lower or lower to upper addition point for each reactor. The reagent gases enter the reactor through eight circular distributed 1 mm holes. This results in rapid mixing of the sampled air and reagent gases. The flows from each reactor pass through a 5 μm

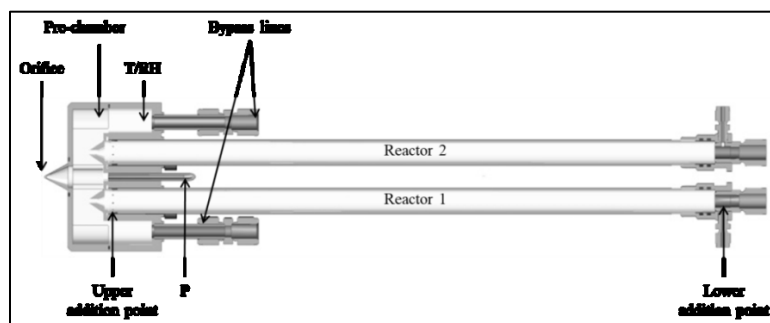PTFE membrane filter (Whatman[TM], GE Healthcare Life Sciences) and enter separate CRDS NO_2 detectors.

Figure 2.10: Schematic drawing of the DUALER inlet. P: Pressure sensor, T/RH: Temperature and relative humidity sensor.

Two versions of DUALER, i.e., DUALER I and DUALER II, were designed, built and calibrated at IUP-UB. After the first field deployment of DUALER I, the inner dimensions of the pre-chamber were further optimised to reduce wall losses and turbulence in the pre-chamber, and DUALER II was designed. In DUALER II, the volume of the pre-chamber was increased by extending its vertical extent, and the length of the truncated cone on top of the reactors was reduced by 3 mm. In addition, the volume of the reactors was increased to 130.5 ml from the 112 ml in DUALER I. These changes resulted in a higher eCL and improved pressure stability during the flight in DUALER II as compared to DUALER I. Figure 2.11 shows the upper part of both DUALER I and DUALER II.
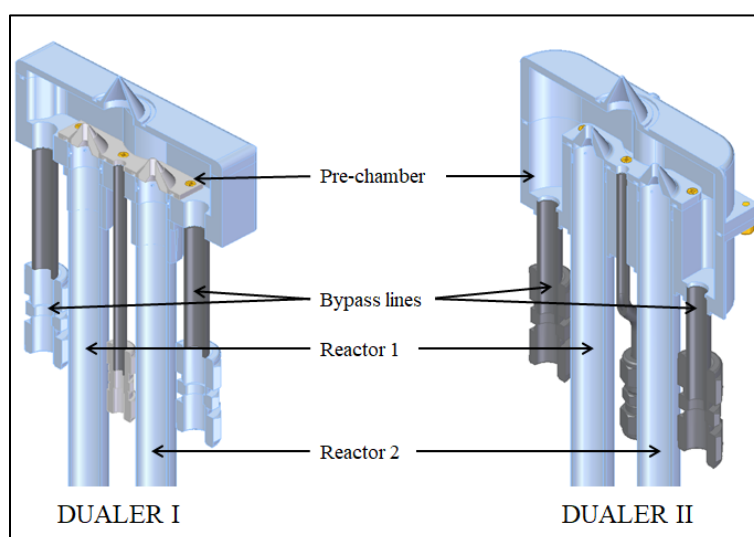

Figure 2.11: Graphical 3D representation of the upper part of the DUALER I and DUALER II inlets. Pre-chamber volume DUALER I = 75.25 cm^3; reactor volume DUALER I = 112 cm^3; pre-chamber volume DUALER II = 119.57 cm^3; reactor volume DUALER I = 130.5 cm^3.

2.5.2 NO_2 Detector

The CRDS based detectors measure the time decay of the electromagnetic radiation trapped inside an optical cavity. Provided that dominant light extinction in the cavity at the operating

wavelength is from NO_2, the $[NO_2]$ is determined from the time decay using Eq. 2.20 (O'Keefe and Deacon, 1988; Atkinson, 2003; Brown, 2003; Berden and Engel, 2010).

$$\sigma_{NO_2}[NO_2] = \alpha_{NO_2} = \frac{n}{c_0}\left(\frac{1}{\tau} - \frac{1}{\tau_0}\right) \qquad\qquad \text{Eq. 2.20}$$

where σ_{NO_2} is the wavelength-dependent absorption cross-section of NO_2, α_{NO_2} the absorbance, n the refractive index of air, c_0 the speed of light in vacuum, τ the ring-down time in the presence of NO_2 in the optical cavity and τ_0 the ring-down time without NO_2. The $\Delta[NO_2]$ in PeRCEAS is calculated from the difference in the ring-down times of the background and amplification modes of operation by substituting and rearranging equation Eq. 2.20. If τ_0 and the total scattering do not change substantially during two consecutive sampling modes, then:

$$\sigma_{NO_2}\,\Delta[NO_2] = \Delta\alpha = \alpha_2 - \alpha_1 = \frac{n}{c_0}\left(\frac{1}{\tau_2} - \frac{1}{\tau_1}\right) \qquad\qquad \text{Eq. 2.21}$$

where α_1 and α_2 are the absorbance during background and amplification modes of operation, τ_1 and τ_2 are the ring-down time during background and amplification modes.

As shown in Figure 2.12, the NO_2 detector houses a 100 mW continuous wave multimode diode laser (Stradus 405, wavelength ≈ 408 nm, max output power 100 mW, Vortran Laser Technology Inc.). The laser is aligned to a V-shape cavity using two motorised alignment mirrors (0.5" aluminium mirrors, Thorlabs BB05-E02, mounted on Newport 8885 Picomotor Actuated Pint-Sized Center Mounts). These mirrors enable the correction of any misalignment of the optical elements with respect to the optical cavity. The misalignments generally arise from vibration or mechanical shocks during transport, installation or in-flight measurement. Three glued-in highly reflective mirrors (reflectivity, R = 99.995%, diameter, d = 0.5", the radius of curvature, roc = 100 cm, AT Films, USA) on the side of a Teflon coated aluminium cuboid form the V-shape cavity of 100 cm^3 volume. The cavity is fixed to the 19" outer case by steel springs to reduce mechanical vibrations. All the optical elements are fixed to the cavity to make the entire optical system vibration-free. Two vacuum-sealed cleaning windows are situated on the top part of the cavity, which are opened to clean the high reflective mirrors. The output from the two back mirrors of the optical cavity is directed towards a Silicon (Si) photodiode detector (type HCA-S, bandwidth 2 MHz, gain 5 × 105 VA^{-1}, Femto Messtechnik GmbH) using two fixed 0.5" front silvered aluminium mirrors and one motorised 1" front silvered aluminium mirror. A 9:1 beam splitter is used to reflect 10 % of the resonator output towards a beam camera (BM-USB-SP907-OSI, Ophir Spiricon Europe GmbH) to monitor the beam profile during alignment procedures and for test purposes. This simplifies the identification of misalignments or loss of performance of the optical system. The laser diode is temperature stabilised at 303 K by an in-built Peltier element. The laser base plate is kept at 298 K using an external Peltier element (type CP-031, Te Technology Inc.) to improve the efficiency of the in-built Peltier element in the laser. The laser output is modulated using a TTL switch-off signal generator (designed and built by

Stachl Elektronik GmbH). The switch-off signal is generated when the cavity output measured by the photodiode reaches 100 mV. Under normal working conditions, the laser modulation frequency is between 650 and 800 Hz.

The gas flow from each of the DUALER reactors enters the corresponding optical cavity through the centre, exits at both ends through NPT-threaded connections and then passes through the pressure (HCX Series, Sensortechnics GmbH), temperature (AD22100, Analog Devices, Inc), relative humidity (HIH-4000-001, Honeywell Sensing and Control) sensors and a flow meter (mass flow controller, Bronkhorst®) placed inside the 19" detector case.

The 19" outer case also houses a temperature sensor to measure the temperature inside the case, a DAQ (data acquisition) distribution board (BNC-2110, National Instruments), a power supply distribution board, two fans, necessary cables and gas flow components. Three identical interchangeable detectors (hereafter named Abbé: AB; Fraunhofer: FH; and Fresnel: FR) have been constructed and characterised at the IUP-UB, of which two are always simultaneously deployed in measurement campaigns. During the measurement, each DUALER reactor is connected to a specific detector. From here onwards, the combination of reactor 1 with the corresponding detector is called system 1, and the combination of reactor 2 with the corresponding detector is called system 2.
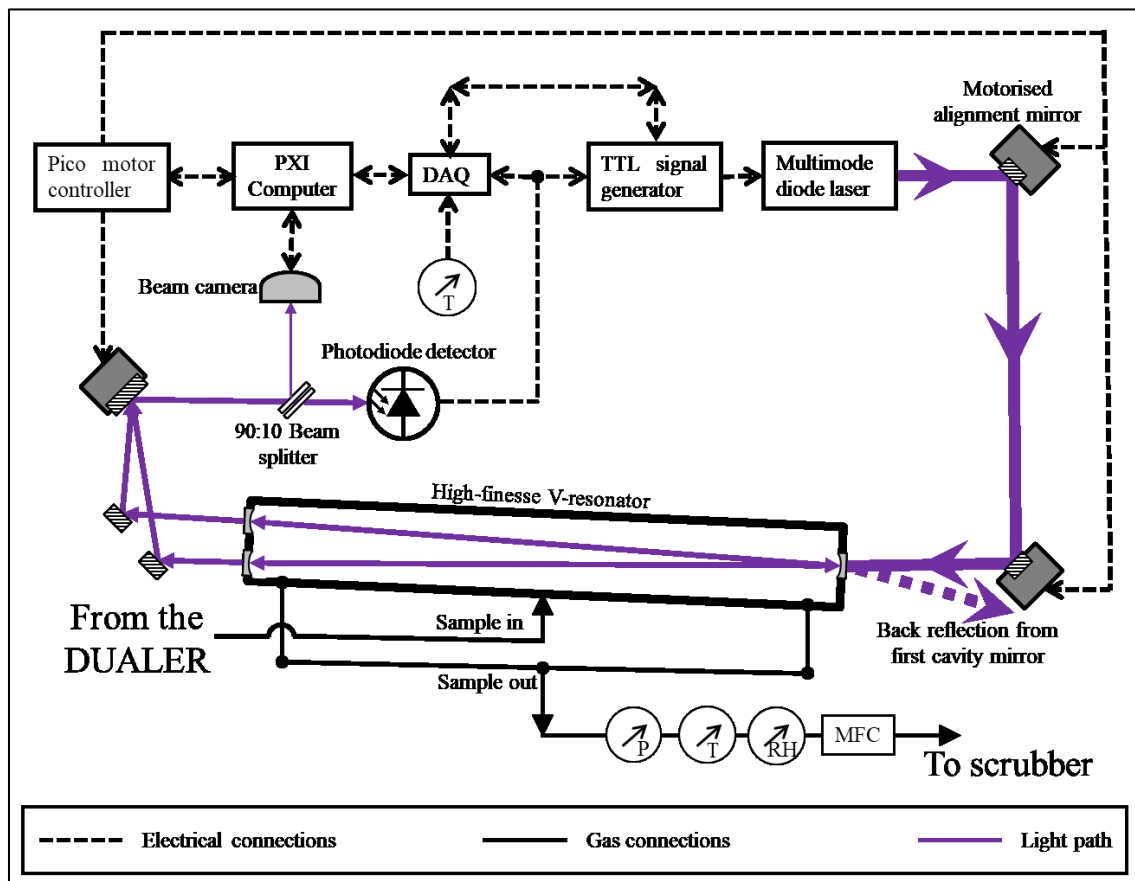

Figure 2.12: Schematic of a PeRCEAS NO_2 detector. MFC: mass flow controllers, P: Pressure sensor, T: Temperature sensor, RH: relative humidity sensor, DAQ: data acquisition distribution board.

2.5.3 Airborne Configuration on HALO

The two NO_2 detectors are mounted in the customised HALO 19" rack (outer dimension 170 cm × 65 cm × 55 cm; total mounted weight 118 kg), shown in figure 2.13. The rack also contains the main power supply distribution, a 15" touch screen monitor (VISAM GmbH), an electronic distribution unit (designed and built by Stachl Elektronik GmbH), a PXI-8840 computer (processor intel i7-5700EQ @ 2.60 GHz processor; 8 GB RAM; 500 GB SSD hard drive, National Instruments), a picomotor controller, two Peltier temperature controllers (type MPT 10000, Wavelength Electronics), one pressure and ten mass flow controllers (Bronkhorst GmbH), necessary gas connections, tubing and electrical connections. The bottom of the rack holds a drawer (figure 2.14) which houses a 0.5 L 5000 µmole mole^{-1} NO in N_2 gas cylinder, the corresponding pressure regulator and a NO_2 scrubber (Iron^{2+} sulfate heptahydrate, i.e., $FeSO_4 \cdot 7H_2O$, Honeywell).
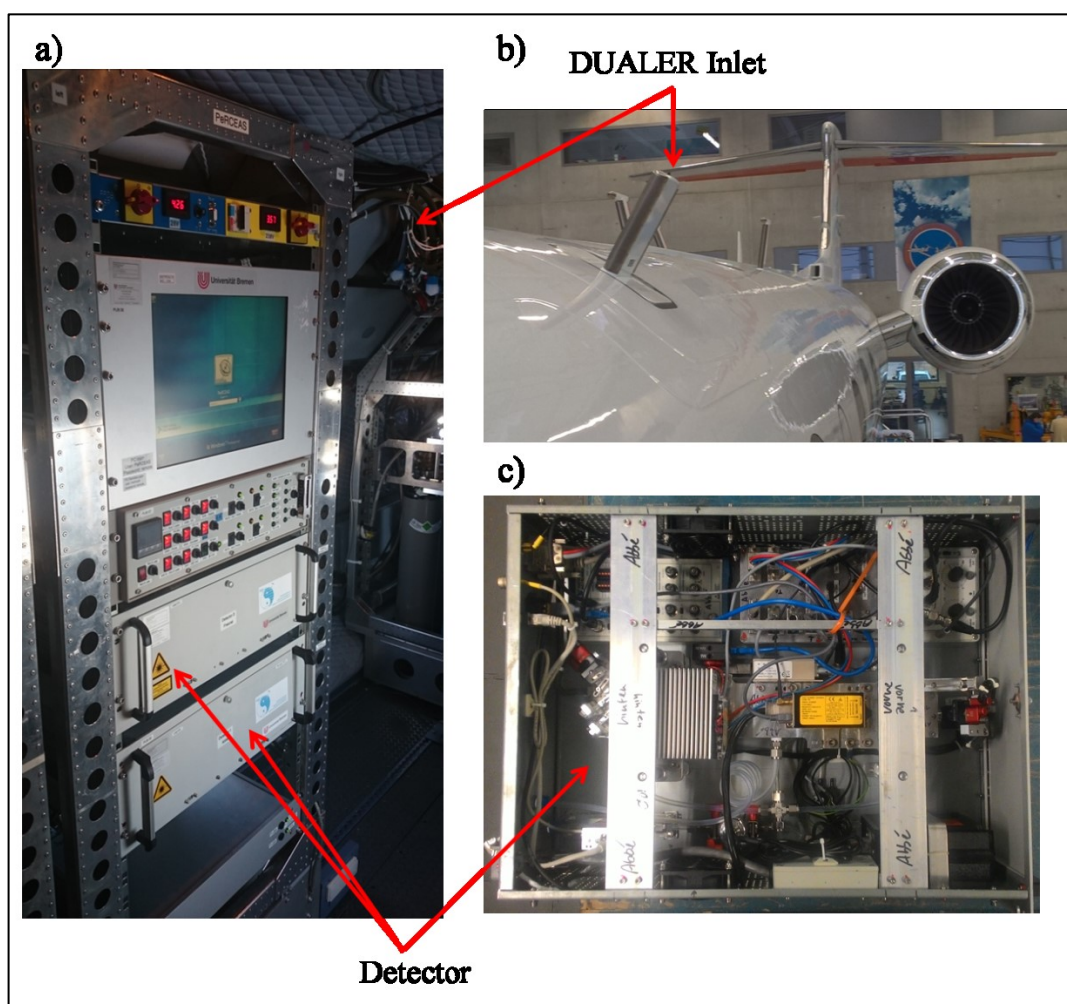

Figure 2.13: a) PeRCEAS main rack, b) DUALER inlet mounted on the HALO fuselage, and c) CRDS detector.

Figure 2.14: Detail of the Gas Bottle Drawer located at the bottom of the PeRCEAS rack.

The DUALER inlet is connected to the main rack through an aperture plate. The pressure in the DUALER inlet, reagents and sample gas flows are controlled by Bronkhorst pressure regulators and mass flow controllers situated in the main rack. These pressure regulators and mass flow controllers, in turn, are controlled by the PXI computer through serial com port communication. The photodetector signal and the laser modulation pulse from both detectors are measured at 1 M samples s^{-1} using separate PXI-6132 cards. All other sensor data such as pressure, temperature and humidity are measured with one PXI-6129 DAQ card at 1 sample s^{-1}. A custom-built LabVIEW program controls, displays and saves all the measurements. The program calculates the real-time ring-down time in 1 Hz from the individual ring-down times averaged over one second. Generally, the individual ring-down times are deleted after averaging, except in the case of sensitivity studies. Thus, the measurement of NO_2 is typically made at 1 Hz.

After the NO_2 detectors, the sampled air passes through a NO_x scrubber, i.e., activated charcoal pellets to adsorb NO_x (Donau Carbon GmbH), and a CO scrubber filled with Pt/Al pellets heated to a temperature above 373 K for the conversion of CO into CO_2 (figure 2.15). After scrubbing, the air is exhausted to the main aircraft exhaust through the scroll pump (Scrollvac SC 30 D, Oerlikon Leybold Vakuum), which is also used for air sampling in PeRCEAS. Due to the space and weight limitation of the main rack, the scrubber unit is placed in a separate rack near the PeRCEAS main rack. The scroll pump is directly mounted on the aircraft floor. A check valve (Swagelok) is installed between the pump and the aircraft exhaust to prevent the flow of exhaust air into PeRCEAS in case of any malfunction.
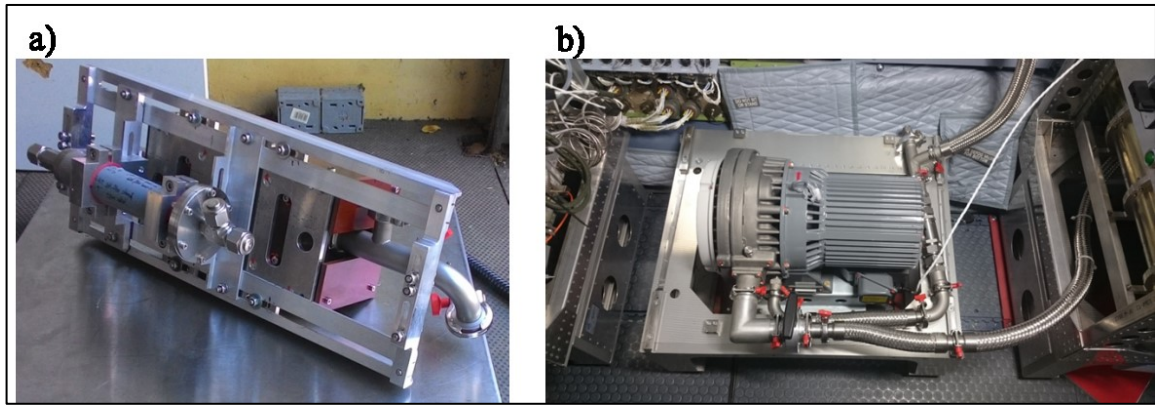
Figure 2.15: Details of the PeRCEAS peripherals: a) gas scrubber unit; b) scroll pump.

The N_2 gas required for the PeRCEAS operation is supplied from a 10 L N_2 gas cylinder (99.99% N_2, Air Liquide) placed in a separate rack. Additionally, a 10 L synthetic air cylinder (20.5% O_2 in N_2, Air Liquide) is also placed in this rack and connected to PeRCEAS for τ_0 measurements.

CO is a toxic and flammable gas with a lower explosive limit (LEL) in the air of 12.5% v v^{-1} at room temperature and atmospheric pressure (Zabetakis, 1965). LEL is the minimum concentration necessary to support the gas combustion along with an ignition source such as a spark or flame. Therefore the CO necessary for the operation of PeRCEAS is supplied from a 2 L CO bottle (Air Liquide) placed inside a vacuum-sealed secondary containment, the so-called GSBX (Gassicherheitsbehälter). The GSBX is certified to carry dangerous gases onboard HALO and is equipped with the following elements (figure 2.16):

i) Pressure reducers to keep the pressure in the CO gas lines at 1.8 bar.

ii) Solenoidal valves to cut off the CO flow in the case of emergency.

iii) Manometers to identify pressure changes inside the GSBX due to CO leaks.

iv) A safety valve to release CO to the aircraft exhaust in the case of a leak inside the GSBX.

v) Critical orifices to limit the flow towards PeRCEAS to 120 ml min^{-1}.

vi) A mechanical valve to close the CO cylinder entirely without opening the GSBX.

vii) An electronic interface for remote monitoring and operation.

The GSBX is installed in the same rack as the scrubber unit. In addition to storing the CO cylinder inside GSBX, the safety concept onboard includes five CO sensors placed at different positions in the aircraft cabin to identify CO leaks and a CO flow cut-off switch in the cockpit for the pilots.
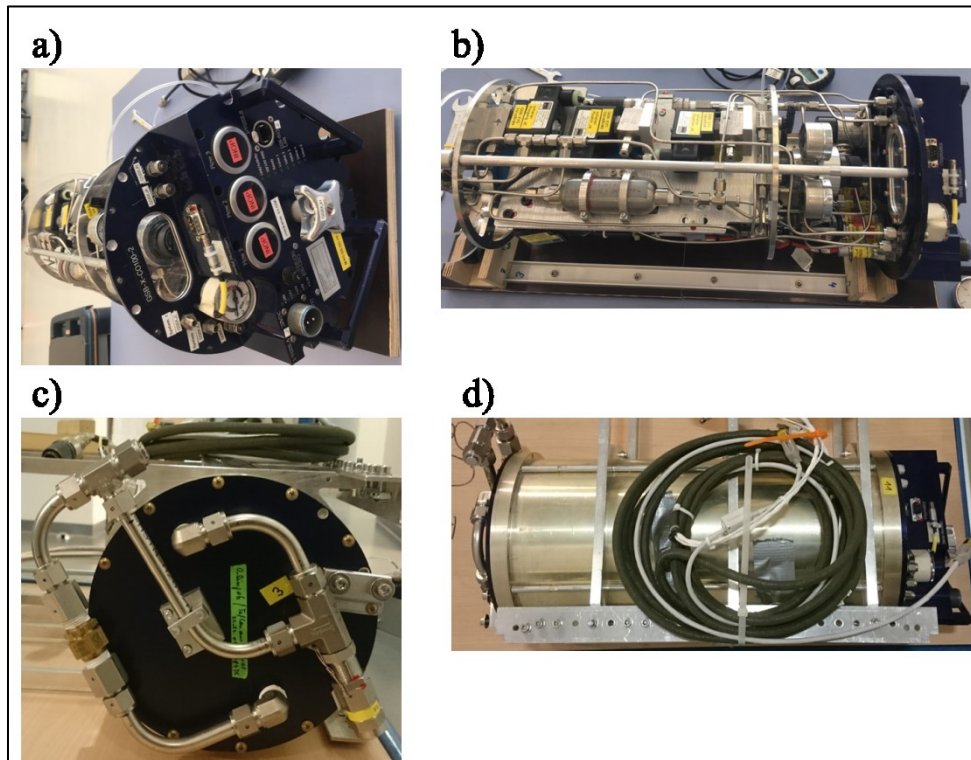
Figure 2.16: HALO GSBX secondary containment: a) front view; b) top view of the internal parts; c) detail of burst valve and exhaust pipes in the back; d) top view with the vacuum-sealed container.

3

Experimental Studies

The laboratory characterisation and optimisation of the PeRCEAS instrument and airborne measurements conducted during this doctoral study are presented in this chapter. The chapter describes a series of laboratory experiments carried out to characterise the PeRCEAS instrument under airborne measurement conditions and the critical parameters influencing PeRCEAS measurements. The chapter also discusses the capability of PeRCEAS to retrieve RO_2^* during rapid background changes and the sensitivity of the measurements based on laboratory studies. The results from these laboratory studies are published in George et al., 2020. These laboratory studies enhanced the interpretation of the field measurements carried out during the international airborne campaigns: OMO-Asia and EMeRGe in Europe and Asia. The chapter ends with a detailed overview of these three measurement campaigns.

3.1 Laboratory Characterisation

The optimal PeRCEAS operating conditions for different expected airborne scenarios were determined through thorough laboratory characterisation during this study. In addition, pre and post-campaign laboratory characterisations were made to check and quantify changes in eCL and the NO_2 sensitivity of the detector. The post-campaign study also focused on calibrations under the unique measurement conditions encountered during the campaigns. This section gives an insight into the laboratory calibrations, the inflight performances, and the critical parameters influencing PeRCEAS measurements.

3.1.1 NO_2 Detector

Provided that the NO_2 absorption is the dominant process leading to light extinction at ~ 408 nm in the optical cavity of each detector, the absorption coefficient can be calculated from Eq. 2.20. Under stable measurement conditions, only σ_{NO_2}, τ and τ_0 might differ from one detector to another due to differences in the laser emission spectrum, mirror reflectivity and alignment of the optical cavity.

The effective σ_{NO_2} for each PeRCEAS NO_2 detector has been determined by using the convolution of the σ_{NO_2} from Vandaele et al. (2002) with the normalised laser spectra from each corresponding detector. The values obtained have been verified by regular sampling of known NO_2 mixtures in synthetic air (SA).

The PeRCEAS lasers are kept at the maximum 100 mW power to achieve the best Gaussian profile for the emission and are digitally modulated during operation. The laser emission spectrum is measured periodically in the laboratory using a calibrated spectrometer (AvaSpec-ULS2048x64; 295-535 nm grating; 0.132 nm resolution) to verify the long-term spectral stability. The comparison of spectra obtained for the three PeRCEAS detectors together with the high-resolution NO_2 spectrum reported by Vandaele et al. (2002) is shown in Figure 3.1.

By integrating σ_{NO_2} under the normalised laser spectrum, the effective σ_{NO_2} are calculated to be $6.0 \pm 0.3 \times 10^{-19}$, $6.3 \pm 0.3 \times 10^{-19}$ and $6.4 \pm 0.3 \times 10^{-19}$ cm^2 molecule^{-1} for AB, FH, and FR detectors, respectively. The errors are calculated from the 2σ variation of 1 hour average spectrum of laser emission measured at 10 Hz and the error reported for the high-resolution NO_2 spectra.

In addition, the effective σ_{NO_2} is also calculated by sampling known mixtures of NO_2 from commercial gas cylinders (Air Liquide, 9.89 ± 0.2 µmole mole^{-1} NO_2 in SA) under controlled laboratory conditions, as shown in figure 3.2. According to Eq. 3.1, the effective σ_{NO_2} is $1/c_0$ times the slope of the $1/\tau$ versus the $[NO_2]$ plot.

$$\frac{1}{\tau_x} = c_0 \sigma_{NO_2} [NO_2]_x + \frac{1}{\tau_0} \qquad \text{Eq. 3.1}$$
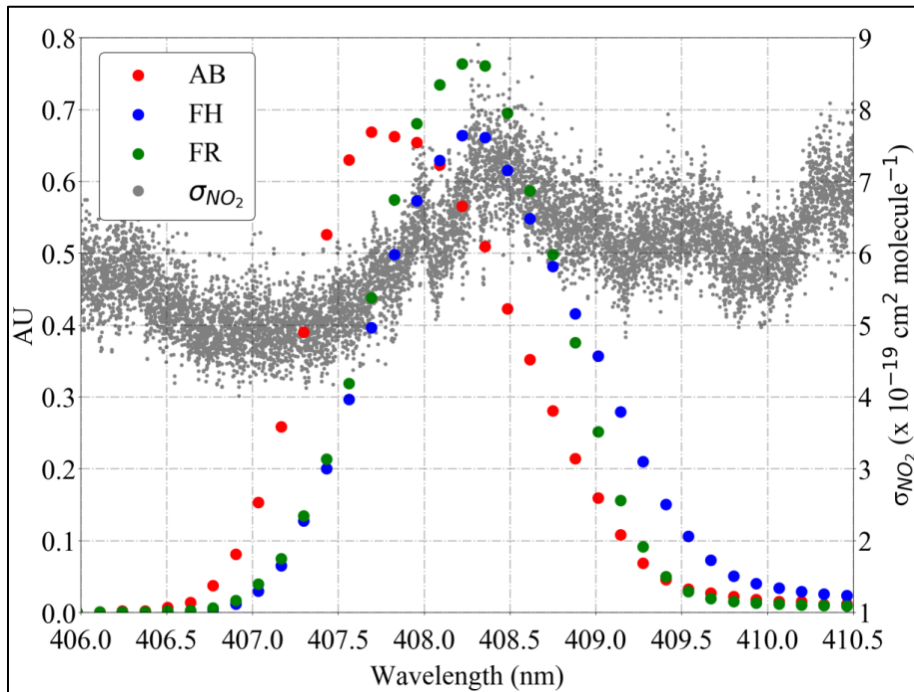

Figure 3.1: Emission spectrum of the lasers used by the three PeRCEAS detectors (large dots) AB: Abbé (red); FH: Fraunhofer (blue); and FR: Fresnel (green). The high resolution σ_{NO_2} at 294 K from Vandaele et al. (2002) is also depicted for comparison (small dots).
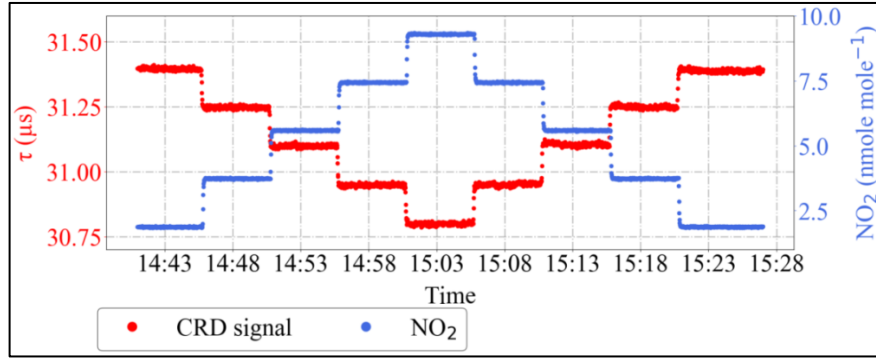
Figure 3.2: PeRCEAS measurement of known NO_2 mixing ratios in SA using the FH detector at 200 hPa and 500 ml min^{-1} sample flow. The blue dots show the sampled NO_2 mixing ratio, and the red show the corresponding ring-down time measured.

The result of applying Eq. 3.1 to the PeRCEAS detectors at 200 hPa is depicted in figure 3.3. The obtained effective σ_{NO_2} agrees within 5 % to the values derived by integrating σ_{NO_2} under the normalised laser spectrum as described above. The y-intercept in figure 3.3 corresponds to $1/\tau_0$ values which are different for each detector. These variations are attributed to slight differences in the mirror reflectivity and the overall alignment of the optical cavities. Under laboratory conditions τ_0 is not expected to vary significantly for a particular detector.
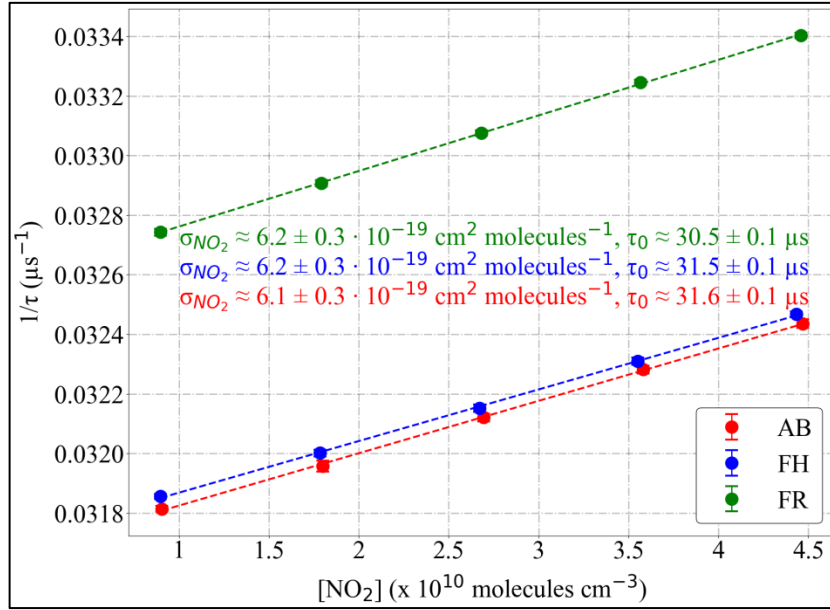
Figure 3.3: Effective absorption cross-section, σ_{NO_2}, obtained from NO_2 calibrations carried out at 200 hPa detector pressure for the PeRCEAS detectors: AB (red), FH (blue) and FR (green). The corresponding linear fits are also depicted as dashed lines.

An Allan variance (Allan, 1966; Werle et al., 1993) study has been applied to the ring-down time of each detector to estimate the limit of detection. Given a time series of N elements and a total measurement time of $t_{acq} = f_{acq} \times N$, where f_{acq} is the frequency of acquisition, the Allan variance is defined as:

$$\sigma_x^2(\tau) = \frac{1}{2} \langle \, (x_{i+1} - x_i)^2 \, \rangle_\tau \qquad \text{Eq. 3.2}$$

where x_i is the mean over a time interval of length $\tau = f_{acq} \times m$; and m is the number of elements in a selected interval. The use of $\langle \ldots \rangle$ denotes the arithmetic mean. The square root of the Allan variance is the Allan deviation. The Allan deviation for any given integration time determines the limit of detection (LOD) for random noise. The Allan variance plot of PeRCEAS detectors when measuring 5.6 nmole mole^{-1} NO_2 at 200 hPa and 296 K is shown in Figure 3.4. As can be seen, the optimal averaging time for the three PeRCEAS detectors is in the range of 20 s to 50 s. The minimum (2σ) detectable NO_2 mixing ratio is < 40 pmole mole^{-1} for FH and FR (1.96×10^8 molecules cm^{-3} for these measurement conditions) and < 60 pmole mole^{-1} (3.153×10^8 molecules cm^{-3} for these measurement conditions) for AB. The LOD for NO_2 (LOD_{NO_2}) is therefore estimated to be 60 pmole mole^{-1}. Slow temperature drifts over longer averaging times impact both the laser and the resonator characteristics. This behaviour is observed for averaging times longer than 60 s, as indicated by the increase in the Allan variance.
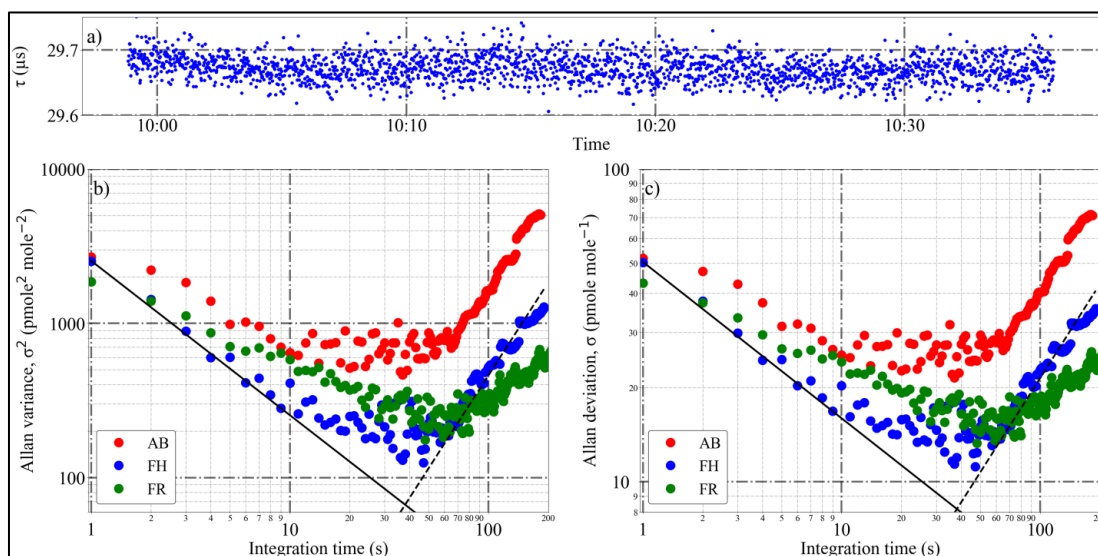

Figure 3.4: Allan variance analysis of PeRCEAS measurements: a) 40 minutes of data from detector FH used for the calculations, b) Allan variance, and c) Allan deviation when 5.6 nmole mole^{-1} of NO_2 at 200 hPa and 296 K is sampled by the PeRCEAS detectors: AB (red), FH (blue), and FR (green). The theoretical behaviour of random noise and slow drifts are also shown by the solid and dashed lines, respectively.

In addition to random noise, systematic noise in the measurement arises from the instability of the laser and or that of the detector response over the modulation time. This is decisive for the overall accuracy of the RO_2^* determination. As mentioned in section 2.5.2, the ΔNO_2 concentrations are calculated from the detector signals using Eq. 2.21. This assumes that the variation of τ_0 has a negligible impact over two consecutive sampling modes.

Temperature changes of the detector affect (i) the laser emission, both its amplitude and wavelength, and (ii) the mode matching between laser and detector, and consequently τ_0. The effect of variations in τ resulting from changes in room or HALO cabin air temperatures on the accuracy and precision of ΔNO_2 determination was investigated through a series of laboratory experiments. For this,

modulated concentrations of NO_2 in the sample flow were generated by alternating between two selected NO_2 concentrations once per minute. The temperature of the CRDS detector (T) and τ were then measured. Temperature gradients over a time t, i.e. $\Delta T/\Delta t$, were induced by controlled changes in the room temperature. The detector temperature was measured by using a temperature sensor within the detector housing close to the photodiode. Figure 3.5 shows the effect of introducing temperature perturbations in a modulated NO_2 signal between 11.5 and 12.1 nmole mole^{-1} measured at 200 hPa and 296 K. As seen in the figure, the temperature perturbation affects both the precision and accuracy of the retrieved ΔNO_2. For temperature gradients up to $\Delta T/\Delta t \approx 7$ K h^{-1} the experimental precision of the ΔNO_2 determination (2σ) remains within 150 pmole mole^{-1} (7.3×10^8 molecules cm^{-3} at 200 hPa and 296 K).
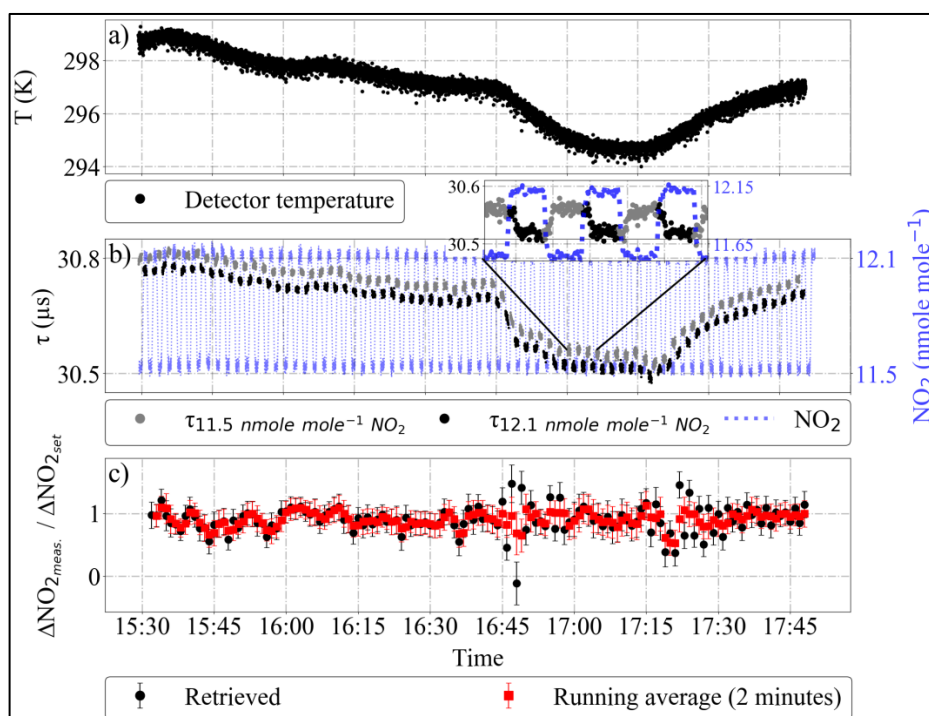

Figure 3.5: Effect of varying room temperature on the ring-down time τ and the ΔNO_2 accuracy. Panel (a): detector temperature, (b): τ for a modulated NO_2 flow and the corresponding NO_2 mixing ratios, and (c): ratio of the measured to the set ΔNO_2. The error bars in panel (c) are estimates of the total uncertainty of the retrieved ΔNO_2. The inset in panel (b) magnifies three modulation cycles. The first 20 s of the signal after a change in the NO_2 mixing ratio are not used in the analysis to avoid the transition time between stable mixing ratios.

3.1.2 DUALER Inlet

The eCL of a PeRCA reactor depends on the physical and chemical losses of RO_2^* in the inlet, defined by the measurement conditions such as the inner surface of the flow reactor, the amount of reagent gases added, the temperature, pressure, and water number concentration. Accurate knowledge of the eCL of each particular reactor under specific measurement conditions is necessary for the retrieval of RO_2^* from ΔNO_2 using Eq. 2.19. This is achieved in the laboratory by using a modified version of the RO_2^* source (Figure 3.6) reported by Reichert et al. (2003) and Kartal et al. (2010).

The RO_2^* are produced using water photolysis (Schultz et al., 1995), as described by Reichert et al. (2003). For PeRCEAS, the flow reactor providing a known amount of HO_2 or RO_2^* is placed inside a pressure chamber, having a vacuum-sealed connection to the DUALER inlet (Figure 3.7). The photolysis of H_2O leads to an OH and a hydrogen (H) atom (R3.1). The hydrogen atom formed reacts with O_2 in a three-body reaction to make HO_2 (R2.37). The addition of CO is used to convert OH to HO_2 through R2.28. Alternatively, the addition of a hydrocarbon (RH) leads to the production of RO_2 through reactions R2.29 and R2.30.
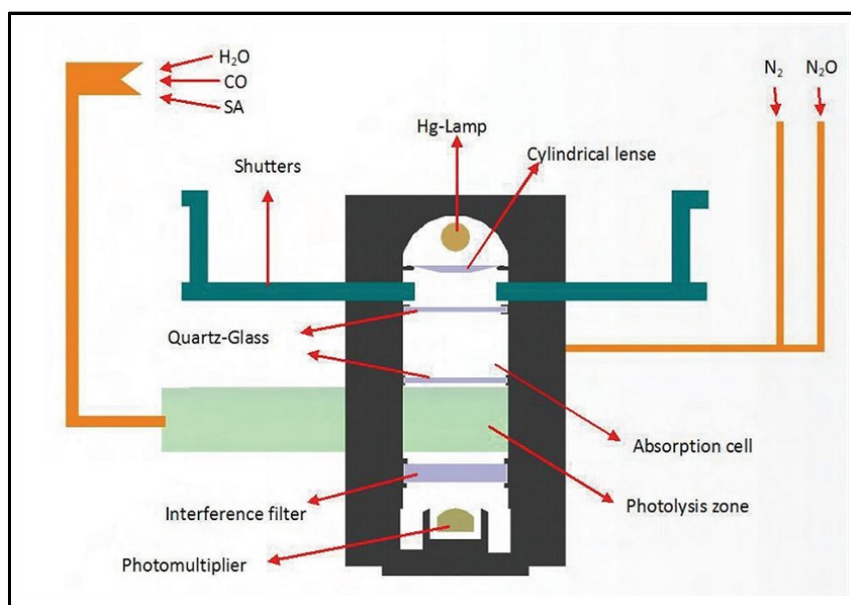

Figure 3.6: Schematic of the RO_2^* source (Figure source: Kartal, 2009).
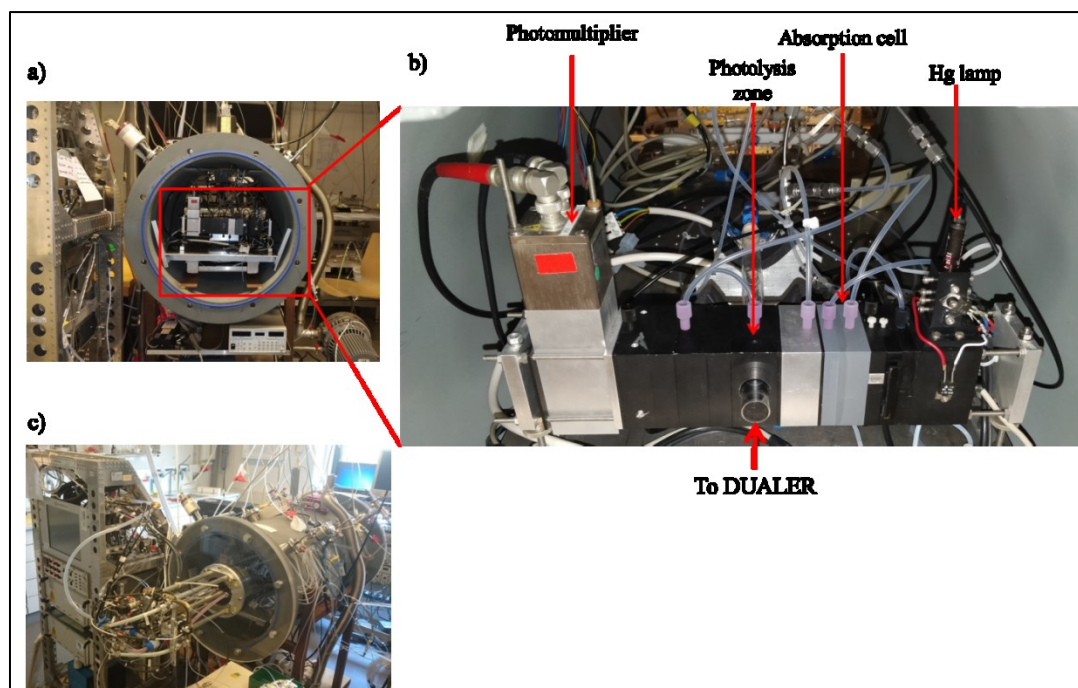

Figure 3.7: DUALER laboratory calibration setup: a) RO_2^* source inside the pressure chamber, b) zoomed-in view of the RO_2^* source, and c) DUALER connected to the RO_2^* source inside the pressure chamber.

$H_2O + h\nu \ (\lambda = 184.9 \ nm) \rightarrow H + OH$ R3.1

For the HO_2 configuration, the HO_2 concentrations are calculated using the following equation:

$$[HO_2] = \frac{\sigma_{H_2O}^{184.9nm}}{\sigma_{O_2}^{184.9nm}} \times \frac{[H_2O]}{[O_2]} \times [O_3]$$ Eq. 3.3

The value for the absorption cross-section of H_2O at 184.9 nm, $\sigma_{H_2O}^{184.9nm} = 7.14 \pm 0.2 \times 10^{-20} \ cm^2$ molecules^{-1} is taken from Cantrell et al. (1997) and Hofzumahaus et al. (1997). The O_2 effective cross-section $\sigma_{O_2\,eff}^{184.9nm}$ is determined experimentally for any particular calibration Hg lamp and the measurement conditions, according to Hofzumahaus et al. (1997) and Creasey et al. (2000).

HO_2 and 1:1 HO_2:CH_3O_2 mixtures are generated at controlled pressures within the expected airborne concentration ranges by adding 0.35% of CO or CH_4, respectively, to the humidified air. The HO_2 and RO_2^* mixing ratios are changed every ten minutes and stepwise from 8 pmole mole^{-1} to 150 pmole mole^{-1} using a customised LabVIEW™ program. The PeRCEAS eCL is determined as the slope of measured NO_2 versus set HO_2 or RO_2^* mixing ratios. Figure 3.8 shows an example of the calculated eCL from 6 calibrations carried out over six months. The results of experiments conducted under similar experimental conditions are reproducible, as indicated by the small spread of the data points in Figure 3.8.
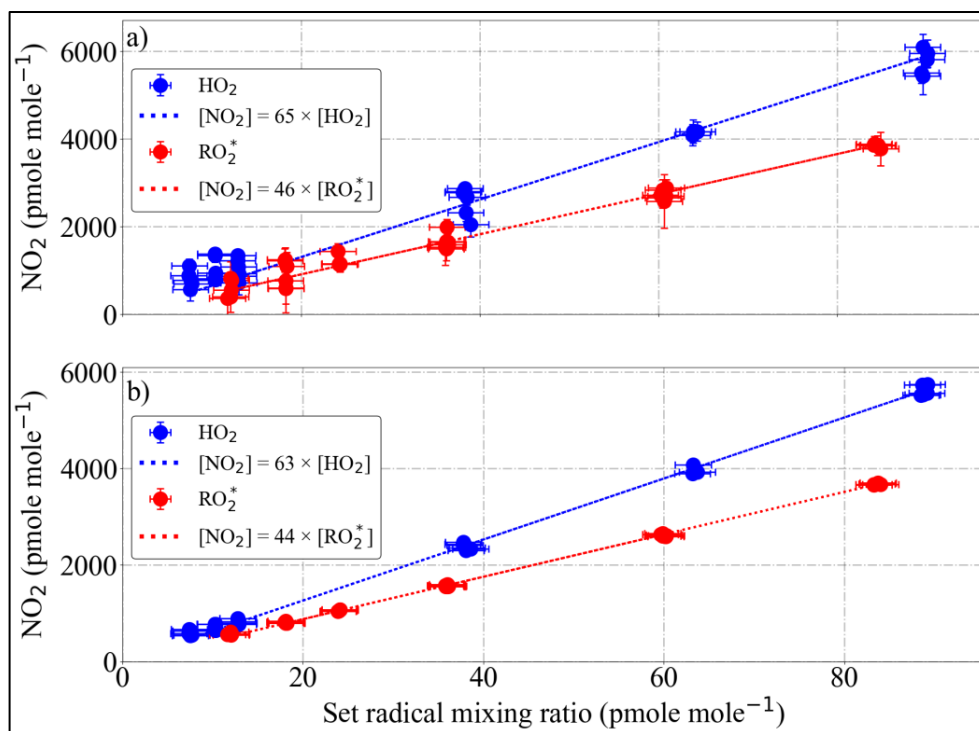
Figure 3.8: Experimental eCL determination of the DUALER II reactors from a series of 6 calibrations with HO_2 (in blue) and 1:1 HO_2:CH_3O_2 radical mixture (in red) mixing ratios generated at 300 hPa inlet pressure, and NO reagent gas added to achieve a mixing ratio of 30 µmole mole^{-1} within the inlet.

The value of the eCL depends on i) the concentration of the NO added as reagent gas, ii) the inlet pressure, and iii) the humidity of the sampled air. The effects were studied separately in detail.

i)   Reagent gas NO

In Figure 3.9, the eCL obtained experimentally for PeRCEAS as a function of [NO] reagent gas at inlet pressures between 200 and 350 hPa are depicted. As expected, the eCL decreases with an increase in NO concentration due to the terminating reactions forming HONO and CH_3ONO, the latter also causing the eCL to be lower for the 1:1 HO_2:CH_3O_2 radical mixture. The eCL values increase with increasing pressure for a constant NO number concentration. This is due to the increase in the CO number concentration with pressure as the CO mixing ratio was kept at 9 % irrespective of the inlet pressure to match the safety regulations.
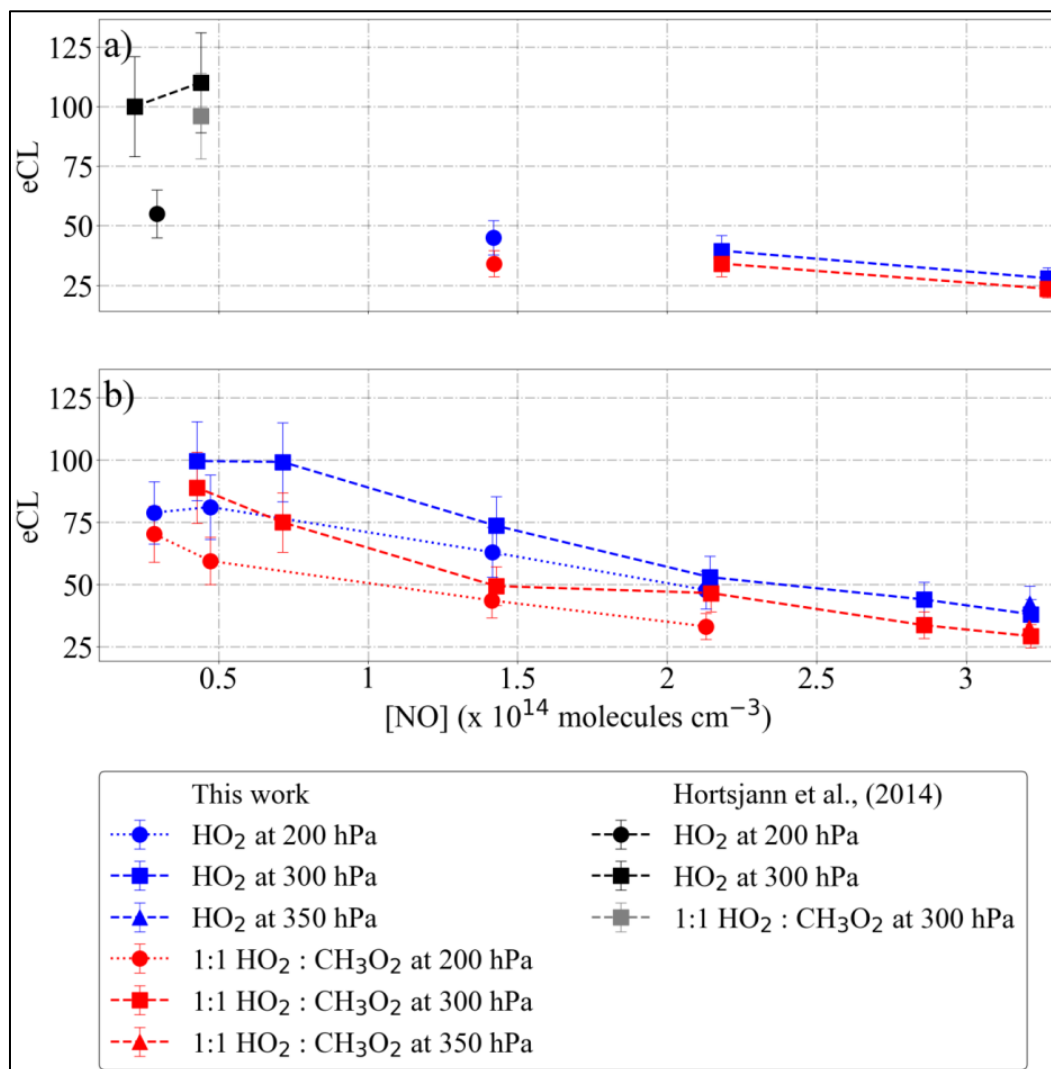
Figure 3.9: Variation of eCL with NO under laboratory conditions for DUALER I and DUALER II. The RO_2^* source is kept at 500 hPa while the inlet pressure varies between 200 and 350 hPa. For comparison, the values from Hortsjann et al. (2014) are also depicted.

A simple chemical box model was developed using the Kintecus software (Ianni, 2013, 2017; http://www.kintecus.com) to simulate the RO_2^* amplification in the DUALER inlets. The model comprises two consecutive modules to simulate the pre-chamber and the reactors separately. The first module considers RO_2^* terminating reactions on the pre-chamber surface before adding the reagent gases. The second module includes the relevant amplification and terminating reactions in the reactor,

as listed in Table 3.1. The rate coefficients used are taken from Burkholder et al., 2015. The first module is initialised either with 50 pmole mole^{-1} HO$_2$ (6.07 × 10^8 molecules cm^{-3} at 500 hPa) or a 50 pmole mole^{-1} HO$_2$ plus 50 pmole mole^{-1} CH$_3$O$_2$ mixture. The second module is initialised with the RO$_2$* output of the first module and calculates the eCL at different inlet pressures for a series of NO concentrations with 9 % CO. An initial O$_3$ mixing ratio of 3 nmole mole^{-1} at 500 hPa is also introduced in the model to account for the O$_3$ produced in the RO$_2$* source.

Table 3.1: Reactions used in a box model for the eCL simulation in the DUALER inlet.

Amplification reactions	k (cm^{3}molec^{-1}s^{-1})	k_0 (cm^{6}molec^{-2}s^{-1})	n	k_∞ (cm^{3}molec^{-1}s^{-1})	m
HO$_2$ + NO → NO$_2$ + OH	8.0 × 10^{-12}				
CO + OH $\xrightarrow{M}$ HOCO		5.9 × 10^{-33}	1.0	1.1 × 10^{-12}	-1.3
HOCO + O$_2$ → HO$_2$ + CO$_2$	2.0 × 10^{-12}				
CO + OH $\xrightarrow{M}$ H + CO$_2$	1.5 × 10^{-13}				
H + O$_2$ $\xrightarrow{M}$ HO$_2$		4.4 × 10^{-32}	1.3	7.5 × 10^{-11}	-0.2
CH$_3$O$_2$ + NO → CH$_3$O + NO$_2$	7.7 × 10^{-12}				
CH$_3$O + O$_2$ → CH$_2$O + HO$_2$	1.9 × 10^{-15}				
Termination reactions					
OH + NO $\xrightarrow{M}$ HONO		7.0 × 10^{-31}	2.6	3.6 × 10^{-11}	0.1
OH + NO$_2$ $\xrightarrow{M}$ HNO$_3$		1.8 × 10^{-30}	3.2	2.8 × 10^{-11}	0.0
OH + NO$_2$ $\xrightarrow{M}$ HOONO		1.0 × 10^{-32}	3.9	4.2 × 10^{-11}	0.5
CH$_3$O + NO $\xrightarrow{M}$ CH$_3$ONO		2.3 × 10^{-29}	2.8	3.8 × 10^{-11}	0.6
OH + HO$_2$ → H$_2$O + O$_2$	1.1 × 10^{-10}				
HO$_2$ + CH$_3$O$_2$ → CH$_3$OOH + O$_2$	5.2 × 10^{-12}				
OH + OH $\xrightarrow{M}$ H$_2$O$_2$		6.9 × 10^{-31}	1.0	2.6 × 10^{-11}	0.0
OH + HONO → H$_2$O + NO$_2$	4.5 × 10^{-12}				
CH$_3$O$_2$ + CH$_3$O$_2$ → CH$_3$O+ CH$_3$O+ O$_2$	3.5 × 10^{-13}				
HO$_2$ + HO$_2$ → H$_2$O$_2$ + O$_2$	1.4 × 10^{-12}				
HO$_2$ + NO$_2$ $\xrightarrow{M}$ HO$_2$NO$_2$		1.9 × 10^{-31}	3.4	4.0 × 10^{-12}	0.3
HO$_2$ (g) → HO$_2$ (s)	0.97				
CH$_3$O$_2$ (g) → CH$_3$O$_2$ (s)	0.74				
Other reactions					
O$_3$ + NO → O$_2$ + NO$_2$	1.9 × 10^{-14}				
CH$_3$COO$_2$NO$_2$ → CH$_3$COO$_2$ + NO$_2$	2.52 × 10^{16} e$^{(-1353/T)}$				
CH$_3$COO$_2$ + NO$_2$ $\xrightarrow{M}$ CH$_3$COO$_2$NO$_2$		9.7 × 10^{-29}	5.6	9.3 × 10^{-12}	1.5
CH$_3$COO$_2$ + NO → CH$_3$ + CO$_2$+ NO$_2$	2.0 × 10^{-11}				
CH$_3$+ O$_2$ + M → CH$_3$O$_2$+ M		4.0 × 10^{-31}	3.6	1.2 × 10^{-12}	1.1

According to sensitivity studies, the amount of O$_3$ used for initialising the model does not affect the eCL value calculated. As in previous work (Kartal, 2009; Chrobry, 2013), the RO$_2$* wall loss

rates (k_w) in the DUALER reactors are estimated by using the expression from Murphy et al. 1987 and Hayman, 1997 for a cylindrical reactor:

$$k_w = 1.85 \left(\frac{v^{1/3} D^{2/3}}{d^{1/3} L^{1/3}} \right) \left(\frac{S}{V} \right)$$
Eq. 3.4

where S is the surface area in cm^2, V the volume in cm^3, L the length and d the diameter of the flow tube in cm, v the velocity of the gas in cm s^{-1}, and D is the diffusion coefficient, calculated to be D_{HO_2} = 0.21 and $D_{CH_3O_2}$ = 0.14 in cm^2 s^{-1}. Using Eq. 3.4, values for $k_{w_{HO_2}}$ and $k_{w_{CH_3O_2}}$ are estimated to be 0.97 and 0.74 s^{-1}, respectively, for the DUALER reactors at a pressure of 300 hPa. The k_w for the pre-chamber cannot be calculated by Eq. 3.4 due to its complex geometry and flow dynamics. Consequently, different values of k_w are used in module 1 to account for RO_2^* losses in the pre-chamber matching the eCL obtained experimentally. Figure 3.10 shows the eCL obtained experimentally for the DUALER II at 300 hPa inlet pressure, 500 ml min^{-1} sample flow and different NO mixing ratios added to the inlet. The best agreement between modelled and experimental data is obtained for the k_w calculated in the reactor using Eq. 3.4, and 64 % HO_2 and 54 % CH_3O_2 radical losses in the pre-chamber. This agrees with previous results reported by Kartal et al. (2010) for a similar configuration. Table 3.2 summarises the simulated PeRCEAS sensitivity for the HO_2 and CH_3O_2 detection for different NO mixing ratios in the reactor at 300 hPa. Up to 10 µmole $mole^{-1}$ NO ([NO] = 7.29 × 10^{13} molecules cm^{-3} at 300 hPa and 298 K), the difference in sensitivity remains within the PeRCEAS uncertainty.
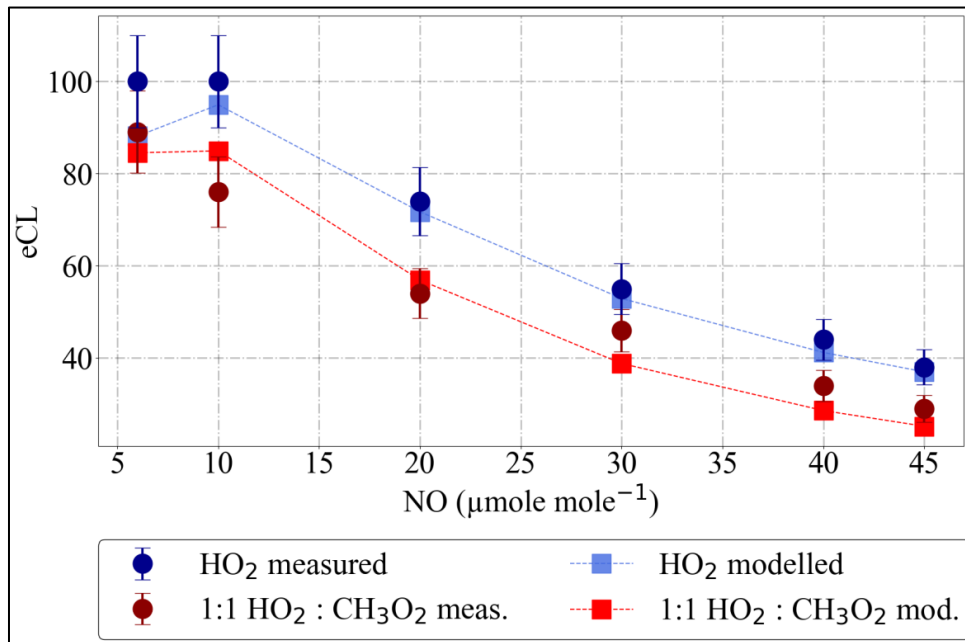
Figure 3.10: PeRCEAS eCL values retrieved experimentally at 300 hPa for HO_2 (blue circles) and a 1:1 HO_2:CH_3O_2 radical mixture (red circles) for different NO mixing ratios in DUALER II. Modelled eCL values obtained for the same conditions are also depicted (blue and red squares) for comparison. The simulations use calculated values of $k_{w_{HO_2}}$ = 0.97 s^{-1} and $k_{w_{CH_3O_2}}$ = 0.74 s^{-1}, and assume 64 % HO_2 and 54 % CH_3O_2 radical losses in the pre-chamber.

In the case of a $HO_2:CH_3O_2$ mixture, Eq. 2.19 can be written as:

$$\Delta[NO_2] = eCL_{HO_2} \times [HO_2] + eCL_{CH_3O_2} \times [CH_3O_2] \qquad \text{Eq. 3.5}$$

$$\frac{\Delta[NO_2]}{eCL_{HO_2}} = [HO_2] + \alpha \times [CH_3O_2] \qquad \text{Eq. 3.6}$$

The ratio of $eCL_{CH_3O_2}$ to eCL_{HO_2} is defined as α. Estimated values of α from modelling and measurements are given in Table 3.2.

Table 3.2: PeRCEAS eCL simulated at 300 hPa for HO_2, CH_3O_2 and a 1:1 $HO_2:CH_3O_2$ mixture (eCL_{mix}).

NO (μmole mole^{-1})	[NO] molecules cm^{-3}	$eCL_{CH_3O_2}$ modelled	eCL_{mix}/eCL_{HO_2} measured	eCL_{mix}/eCL_{HO_2} modelled	$\alpha = eCL_{CH_3O_2}/eCL_{HO_2}$
6	4.37E+13	93.5	0.89	0.97	1.04
10	7.29E+13	85.3	0.76	0.90	0.89
20	1.46E+14	46.8	0.73	0.79	0.65
30	2.19E+14	27.3	0.84	0.74	0.52
40	2.91E+14	17.7	0.77	0.70	0.43
45	3.28E+14	14.7	0.76	0.68	0.40

ii) Inlet pressure

The PeRCEAS operating pressure is kept constant and below ambient pressure to preserve the RO_2^* chemical conversion in the inlet during the flight. However, the $\Delta P = P_{ambient} - P_{inlet}$ varies at different flight altitudes, leading to physical losses and humidity changes in the pre-chamber. These may significantly affect the eCL, as reported in previous work by Kartal et al., 2010.

To evaluate this effect for PeRCEAS, different ΔPs were experimentally generated by changing the pressure in the pressure chamber while keeping inlet conditions like pressure, mixing ratios of the reagent gases (NO, CO and N_2), sampling gas velocity (sample flow) and relative humidity invariable. Figure 3.11 shows the variation of the eCL for 10 and 45 μmole mole^{-1} NO within a pressure range of 50 hPa $\leq \Delta P \leq$ 600 hPa. As shown in the figure, the eCL variation remains within 10 % except for ΔP values < 100 hPa. As the ΔP decreases, the total flow through the inlet pre-chamber also decreases, which increases the sample retention time in the pre-chamber. Increasing the retention time of the sample in the pre-chamber favours wall losses. This might lead to variations in the relative importance of terminating processes (wall losses versus chemical reactions) with the sample velocity through the pre-chamber (Kartal et al., 2010). Consequently, $\Delta P = 100$ hPa is defined as the minimum operating pressure for PeRCEAS airborne measurements. Since the ambient pressure at 12000 m is approximately 200 hPa, PeRCEAS can measure up to 12000 m with an inlet pressure of 100 hPa.
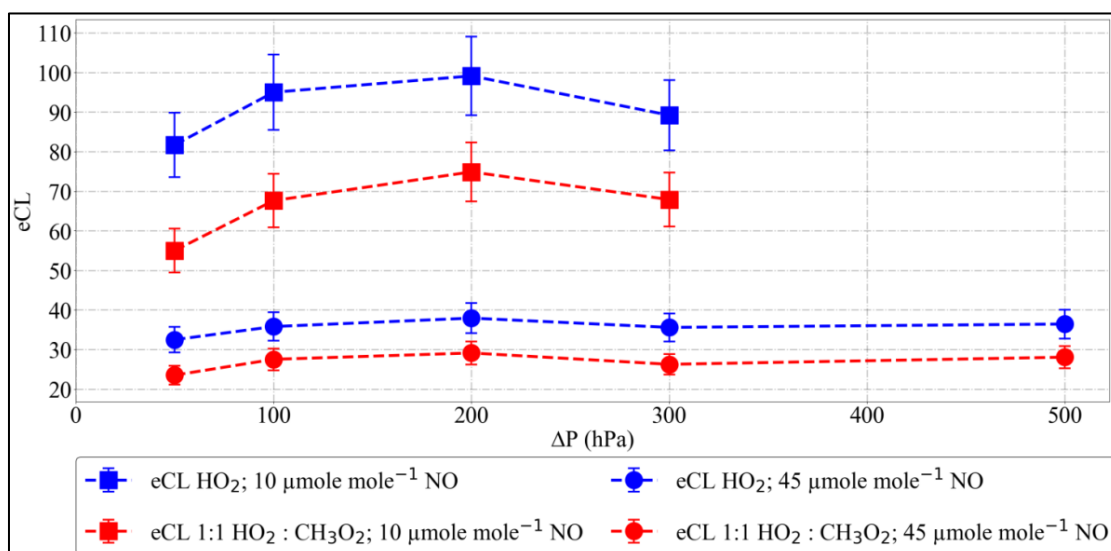
Figure 3.11: Dependency of eCL on ΔP ($\Delta P = P_{ambient} - P_{inlet}$) as determined for PeRCEAS under controlled laboratory conditions for 10 (squares) and 45 (circles) μmole mole^{-1} NO and 300 hPa inlet pressure. The error bars represent the 1σ deviation of identical calibrations at each ΔP.

iii)   The humidity of the air sampled

The effect of variations in the sampled air humidity on the eCL (Mihele and Hastie, 1998; Mihele et al., 1999) was also investigated. In a previous work, Reichert et al., 2003 confirmed the dependency of the eCL on the relative humidity for ground-based measurements reported by Mihele and Hastie (1998) by investigating the eCL variation as a function of relative humidity for 293 K and 303 K at standard pressure, i.e., almost doubling the absolute water concentration. According to the results from Reichert et al., 2003, the effect of [H$_2$O] on eCL decreases with the operating temperature.

During airborne measurements, the DUALER inlet pressure is kept at $\leq$ 300 hPa for all measurement conditions to reduce the dependency of eCL on ambient [H$_2$O]. The pressure reduction reduces [H$_2$O] in the inlet up to 3 times compared to the ambient. This reduced [H$_2$O] effect on the eCL has been investigated for different added reagent gas NO mixing ratios at 295 K and 300 hPa inlet pressure. The results obtained and the values from Reichert et al., 2003 are shown in Figure 3.12. Since Reichert et al., 2003 used 3.3 μmole mole^{-1} NO at 1000 hPa, the [NO] is similar to the 10 μmole mole^{-1} NO at 300 hPa. As shown in Figure 3.12, the eCL dependency on [H$_2$O] reduces with an increase in the [NO] reagent gas added to the inlet and is in good agreement with the result presented in Reichert et al., 2003.
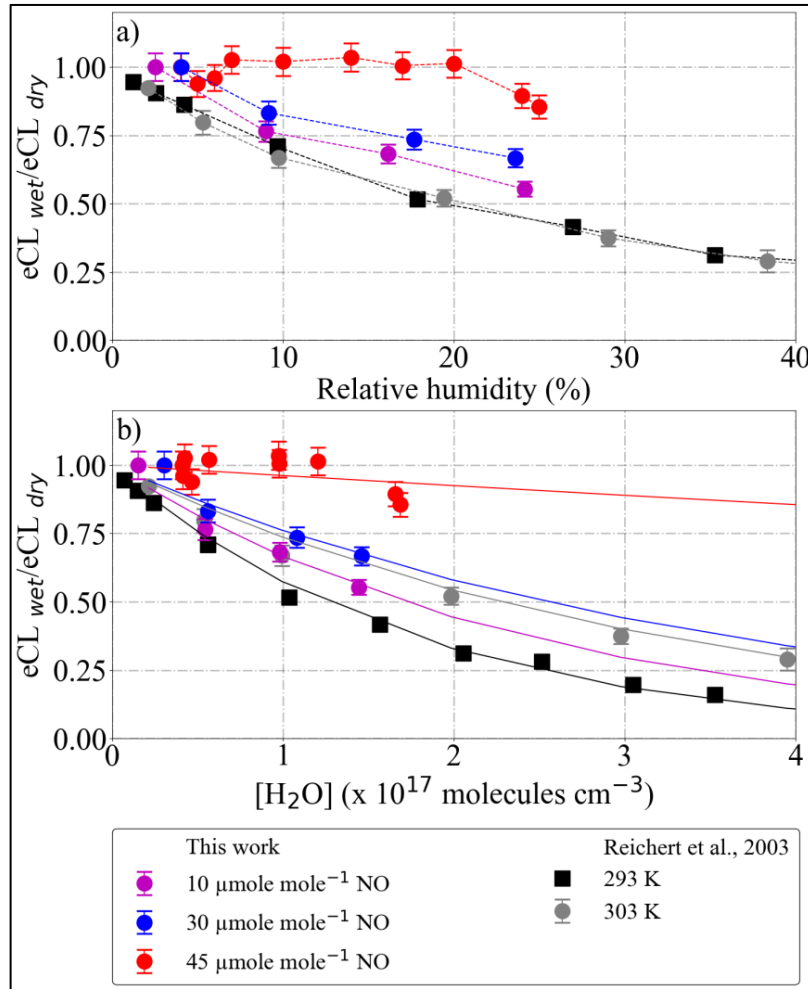
Figure 3.12: Dependency of PeRCEAS eCL on a) inlet humidity, and b) [H₂O], at constant sample flow, ΔP, [CO] and [N₂], measured at 300 hPa inlet pressure. Depicted are the results for adding 10 (magenta), 30 (blue), and 45 (red) µmole mole^{-1} NO mixing ratios (respectively 7.29×10^{13}, 2.19×10^{14} and 3.28×10^{14} molecules cm^{-3}) in the sample flow. The values from Reichert et al., 2013 obtained for adding 3.3 µmole mole^{-1} NO at standard pressure (8.12×10^{13} molecules cm^{-3}) are also plotted for comparison.

This result is explained considering the resistance model described in Hastie et al., 1991 and Reichert et al., 2003. The chain length (CL) of a PeRCA reactor can be expressed using a resistance model as follows:

$$\frac{1}{CL} = \left(\frac{1}{CL_{HO_2}} + \frac{1}{CL_{OH}} \right)$$

Eq. 3.7

$$\frac{1}{CL} \approx \frac{1}{P_{NO_2}} \cdot \left(\frac{\sum HO_2 \text{ removal rates}}{\sum HO_2 \text{ propagating rates}} + \frac{\sum OH \text{ removal rates}}{\sum OH \text{ propagating rates}} \right)$$

Eq. 3.8

If only the predominant processes are considered:

$$\frac{1}{CL} \approx \frac{1}{P_{NO_2}} \cdot \left(\frac{k_{w_{HO_2}} + k_{other\ losses}}{k_{NO+HO_2} \cdot [NO]} + \frac{k_{w_{OH}} + k_{HONO} \cdot [NO]}{k_{CO+OH} \cdot [CO]} \right)$$

Eq. 3.9

51

where P_{NO_2} is the probability of RO_2^* conversion into NO_2, $k_{w_{HO_2}}$ and $k_{w_{OH}}$ are the wall losses of HO_2 and OH, respectively, k_{NO+HO_2} is the rate constant for NO_2 production from the $HO_2 - NO$ reaction, k_{HONO} is the rate constant for HONO formation from the $OH - NO$ reaction, and k_{CO+OH} is the rate constant for HO_2 formation from the $OH - CO$ reaction. $k_{other\,losses}$ represents all other losses of HO_2, such as the HO_2 water clusters, which are formed in the presence of H_2O and do not react with NO, as postulated by Reichert et al., 2003.

As [NO] increases, the rate of the chain termination termolecular reaction of OH with NO making HONO and the rate of the propagation reaction between HO_2 and NO increases. As a result, CL_{OH} decreases and CL_{HO_2} increases with an increase in [NO]. Due to this, CL begins to be dominated by CL_{OH}, which is independent of water vapour. The result of adding 45 µmole mole^{-1} (3.28×10^{14} molecules cm^{-3}) NO to the inlet at 300 hPa indicates that variations in the sample humidity do not lead to additional uncertainty in the RO_2^* retrieval as the PeRCEAS eCL remains invariable within the experimental error up to $[H_2O] \sim 1.4 \times 10^{17}$ molecules cm^{-3}. Increasing the reagent gas NO also changes the PeRCEAS sensitivity to HO_2 and RO_2 due to the higher rate constant of organic nitrites formation, which terminates the RO_2 chain reactions (see Table 3.2).

The solid lines in Figure 3.12.b result from applying the least square fit to each measurement condition using Eq. 3.10. The fit parameters are given in Table 3.3 and are later used to correct eCL during ambient measurements.

$$eCL_{wet} = eCL \times A^{([H_2O] \times 10^{-16})} \qquad\qquad \text{Eq. 3.10}$$

Table 3.3: Fit parameters from Figure 3.12.b.

	NO (molecules cm^{-3})	Temperature (K)	A
This work	7.29×10^{13}	298	0.960
	2.19×10^{14}	298	0.973
	3.28×10^{14}	298	0.996
Reichert et al., 2013	8.12×10^{13}	293	0.946
	8.12×10^{13}	303	0.970

3.1.3 Operating Conditions

In PeRCEAS, both systems measure in background and amplification mode in an alternating manner out of phase with one another (Figure 3.13). This enables the continuous monitoring of both background NO_2 and the NO_2 produced from RO_2^* through chemical amplification. The uncertainties

due to differences in the detector sensitivity and the NO_2 scrubber efficiency in the inlet are reduced significantly through this method. A complete measurement cycle of each system consists of one background and one amplification measurement mode. The time taken for one complete measurement cycle is defined as a modulation time. The time selected for the measurement in either amplification or background mode is called the mode time. The ΔNO_2 for each detector is calculated from the ring-down time of two consecutive modes using Eq. 2.21. Provided that the mode time is adequately selected, the RO_2^* retrieved per measurement cycle shall be identical in both systems, as the two reactors are operated out of phase with one another. Therefore, the final RO_2^* data is calculated as the mean of the RO_2^* determined from the ΔNO_2 and eCL of both systems for a given measurement cycle. This makes the RO_2^* time resolution to be equal to the mode time. Modulation and mode times are selected empirically. The optimised values are a compromise between the time taken for the detector signal to stabilise and the temporal variability of the chemical composition of the air probed. Using the results from the sensitivity and calibration studies done for detectors and DUALER, a 60 s mode time and a 120 s modulation time are selected. This provides an optimal signal to noise ratio for ΔNO_2 and a 2σ error $< 3.15 \times 10^8$ molecules cm^{-3}. From the 60 s mode time, the first 20 s are removed during the RO_2^* retrieval to account for the small pressure pulse arising from the switching between modes. The time lag arising from the time taken for the sample flow between the point of switching and the CRDS detectors is typically less than 8 s.

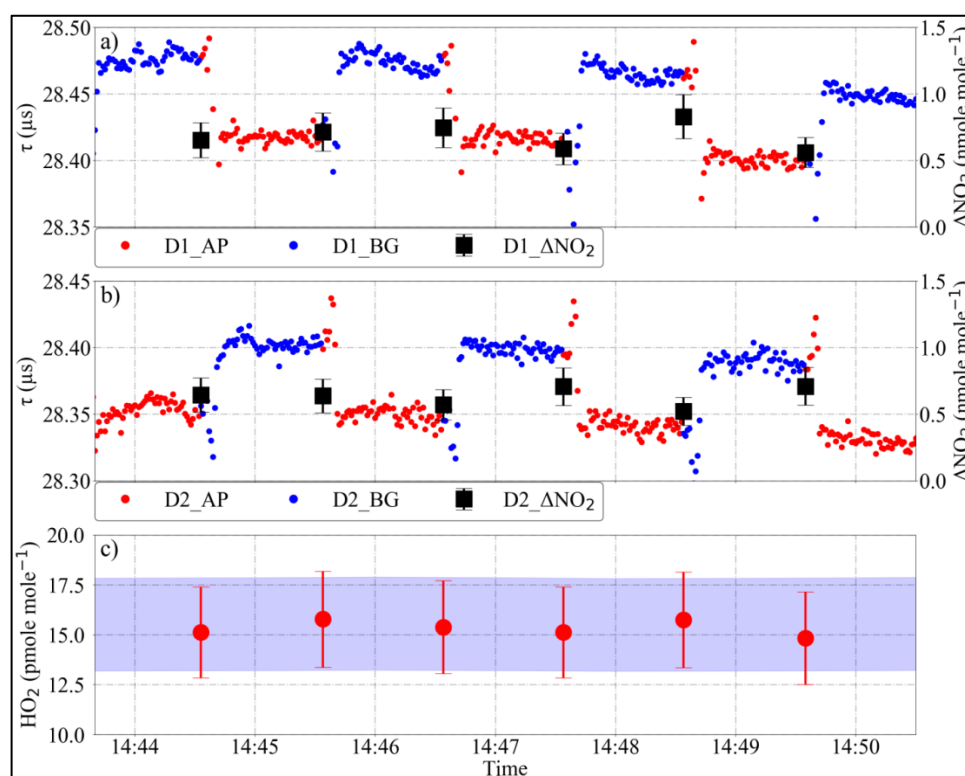Figure 3.13: PeRCEAS measurement cycle: a) and b) show the ring-down time of detector one (D1) and two (D2) in both amplification (AP mode) and background (BG mode) modes and the retrieved ΔNO_2. The ΔNO_2 and the respective eCL of each reactor are used to retrieve the HO_2 mixing ratio in c). The blue shading in c) corresponds to the 2σ uncertainty of the HO_2 mixing ratio produced in the source.

Sample and reagent gas flows have different and related impacts on the sensitivity of the PeRCEAS measurements. The rate of the sample flows determines the residence time in different parts of the flow system, which in turn determines the reaction time for the conversion of RO_2^* to NO_2, the titration of the O_3 in the sampled ambient air, and the thermal decomposition of PAN and PNN to produce NO_2 interfering signals. Interferences are minimised by short residence times, facilitated by a rapid flow. Conversely, the RO_2^* to NO_2 conversion rate in the DUALER is determined by the concentration of CO and NO reagent gases added. Since CO is a toxic and flammable gas, CO mixing ratio was limited to 9 % v v^{-1} for all measurement conditions to meet the safety requirements in the aircraft. On the other hand, sample flow, amount of reagent gas NO, and pressure in the DUALER are selected for each deployment of PeRCEAS. This ensures maximum chain length and complete conversion of ambient O_3 into NO_2 while keeping interferences as low as possible at different ambient conditions.

Table 3.4 shows the residence time of the sampled air mass in PeRCEAS for different sample flows and inlet pressures. The residence time between the upper and lower addition points is defined as the reactor residence time. In the same way, the residence time between the upper addition point and the detector is defined as the total residence time. To get maximum eCL, the amplification chain reactions have to be completed within the reactor residence time. In a previous study of a similar PeRCA inlet, Kartal (2009) showed that the chain reaction requires 1.88 s to be completed under 200 hPa inlet pressure and 3 µmole $mole^{-1}$ NO reagent gas. As the NO increases, the chain termination is faster due to the reactions forming HONO and organic nitrites. As a result, the time required for the chain reaction reduces with an increase in NO.

Increasing NO will also facilitate the O_3 titration to NO_2. Since NO is always added at the upper addition point irrespective of the measurement mode, the total residence time is available for the O_3 titration. Figure 3.14 depicts the O_3 decay simulated for 100 and 200 nmole $mole^{-1}$ O_3 sampled, i.e. $5 \times 10^{11} - 1.7 \times 10^{12}$ molecules cm^{-3} at 200 and 300 hPa, respectively. The titration is assumed to be completed for a rest of $[O_3] = 5 \times 10^7$ molecules cm^{-3}. These results agree with a series of laboratory measurements made at 300 hPa for DUALER II with a sample flow of 500 mL min^{-1}, as shown in Figure 3.15. After 8 s, the O_3 is titrated out for NO mixing ratios above 10 µmole $mole^{-1}$ added to the sample flow at the conditions investigated (i.e. $[NO] = 4.83 \times 10^{13}$ and 7.29×10^{13} molecules cm^{-3} at 200 and 300 hPa, respectively).

Table 3.4: Sample residence times in PeRCEAS for different sample flows and pressures. Reactor residence time: residence time between upper and lower addition points in each reactor; total residence time: residence time between upper addition point in each reactor and the corresponding detector. The inner volumes up to the detector are 132 cm^3 in DUALER I and 220 cm^3 in DUALER II.

DUALER I						
Inlet pressure (hPa)	Reactor residence time (s)			Total residence time (s)		
	300 ml min^{-1}	500 ml min^{-1}	1000 ml min^{-1}	300 ml min^{-1}	500 ml min^{-1}	1000 ml min^{-1}
300	6.55	3.93	1.96	7.82	4.69	2.35
200	4.36	2.62	1.31	5.21	3.13	1.56
160	3.49	2.10	1.05	4.17	2.50	1.25
100	2.18	1.31	0.65	2.61	1.56	0.78
80	1.75	1.05	0.52	2.09	1.25	0.63
50	1.09	0.65	0.33	1.30	0.78	0.39
DUALER II						
Inlet pressure (hPa)	Reactor residence time (s)			Total residence time (s)		
	300 ml min^{-1}	500 ml min^{-1}	1000 ml min^{-1}	300 ml min^{-1}	500 ml min^{-1}	1000 ml min^{-1}
300	7.73	4.64	2.32	13.18	7.91	3.95
200	5.15	3.09	1.55	8.79	5.27	2.64
160	4.12	2.47	1.24	7.03	4.22	2.11
100	2.58	1.55	0.77	4.39	2.64	1.32
80	2.06	1.24	0.62	3.51	2.11	1.05
50	1.29	0.77	0.39	2.20	1.32	0.66
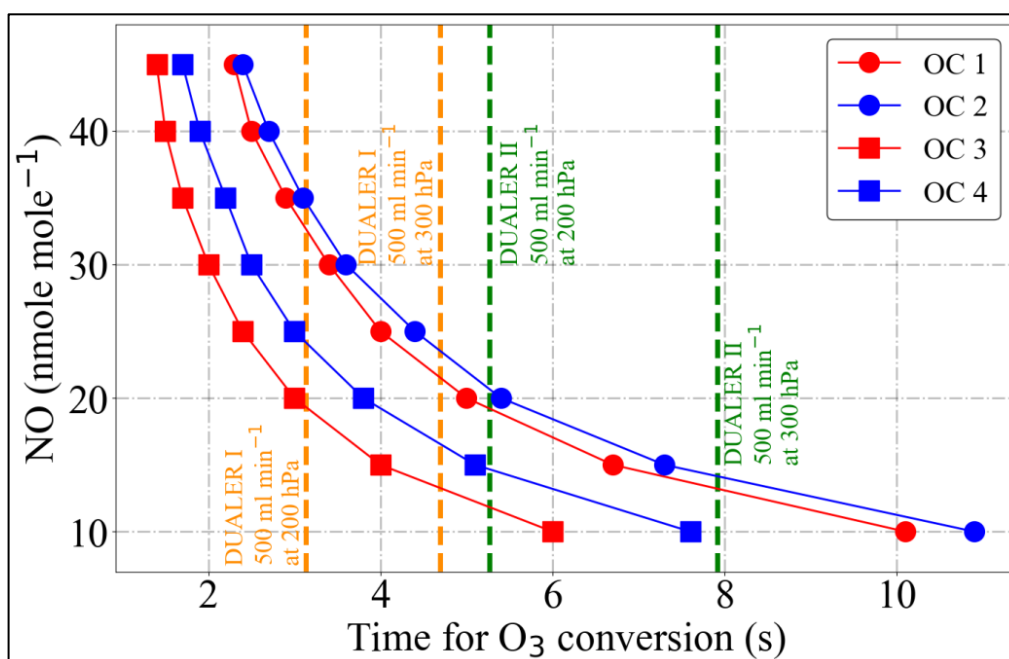
Figure 3.14: Time evolution of the O_3 decay for different NO mixing ratios added at the PeRCEAS reactors as simulated by a box model for 200 and 300 hPa for different operating conditions (OC) 1: 100 nmole $mole^{-1}$ O_3 at 200 hPa inlet pressure; OC 2: 200 nmole $mole^{-1}$ O_3 at 200 hPa inlet pressure; OC 3: 100 nmole $mole^{-1}$ O_3 at 300 hPa inlet pressure; OC 4: 200 nmole $mole^{-1}$ O_3 at 300 hPa inlet pressure. The sample residence times for 500 ml min^{-1} sample flow in the DUALER I and II are also depicted for reference.

Figure 3.15: PeRCEAS measurement of O_3 mixing ratios up to 100 nmole mole^{-1} for different [NO] added in DUALER II. NO is scaled in µmole mole^{-1} and molecules cm^{-3}. The O_3 conversion is completed when the ratio $NO_{2\ measured}$ / $O_{3\ set}$ reaches unity. R 1: PeRCEAS reactor 1 (blue squares); R 2: PeRCEAS reactor 2 (red circles).

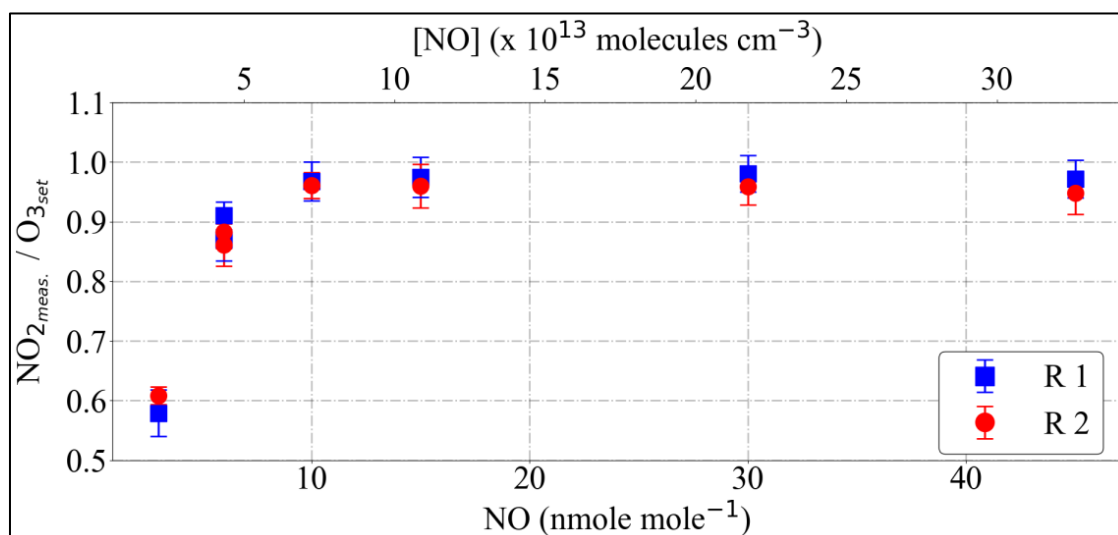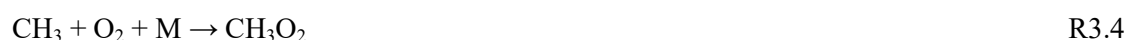Under a rapidly changing background, the RO_2^* determination might be affected by the thermal decomposition of Peroxyacyl nitrates ($RC(O)OONO_2$) such as PAN and PPN. This effect depends on the temperature and the sample residence times between the gas addition points in the DUALER (Table 3.4). To evaluate this effect, the production of RO_2^* from the thermal decomposition of 1 nmole mole^{-1} PAN at different temperatures and pressures has been simulated. The results obtained with a box model (Ianini, 2003), including the reactions:

$$CH_3COO_2NO_2 \rightarrow CH_3COO_2 + NO_2 \qquad \text{R3.2}$$

$$CH_3COO_2 + NO \rightarrow CH_3 + CO_2 + NO_2 \qquad \text{R3.3}$$

$$CH_3 + O_2 + M \rightarrow CH_3O_2 \qquad \text{R3.4}$$

are depicted in figure 3.16. The rate coefficients used are taken from Burkholder et al., 2015. The [CH_3O_2] produced does not vary significantly at the pressures investigated for the same temperature. As the temperature of the PeRCEAS reactors during flight generally remains under 290 K, this source of RO_2^* interference is considered to be negligible for most operating conditions. The thermal stability of the PAN analogues is similar to that of PAN, but they are usually at much lower concentrations than PAN in the atmosphere. Therefore, they are also assumed to be a negligible source of error.
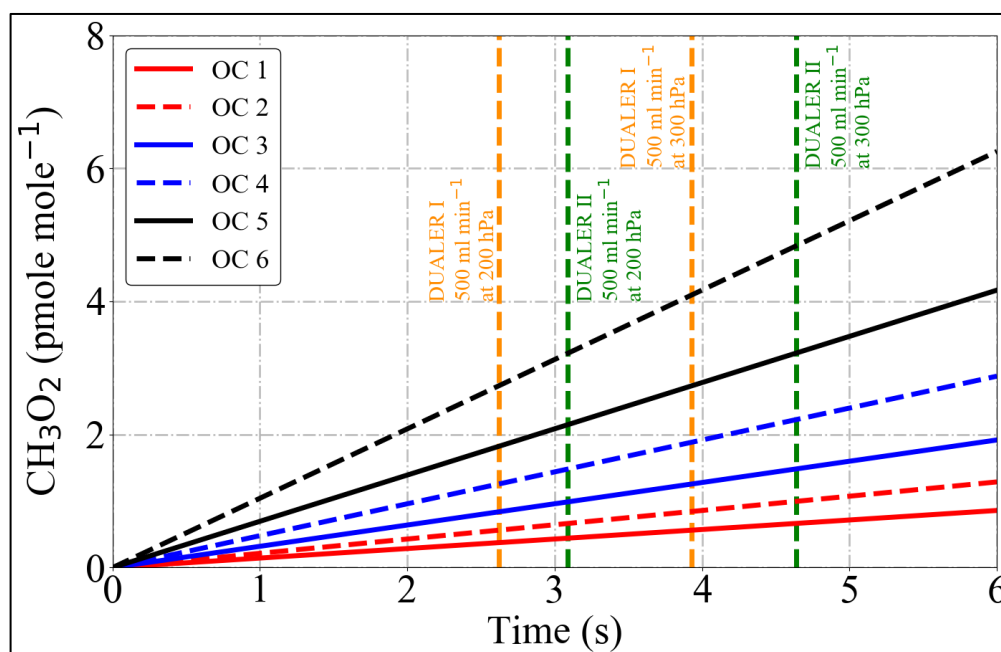
Figure 3.16: CH_3O_2 radical production from the thermal decomposition of 1 nmole mole^{-1} PAN as simulated by a box model between 288 and 298 K at 200 and 300 hPa. OC 1: 288 K and 300 hPa; OC 2: 288 K and 200 hPa; OC 3: 293 K and 300 hPa; OC 4: 293 K and 200 hPa; OC 5: 298 K and 300 hPa; OC 6: 298 K and 200 hPa. The sample residence times for 500 ml min^{-1} sample flow in the DUALER I and II are also depicted for reference.

3.1.4 RO_2^* Retrieval Procedure

As explained in section 2.4.3, the RO_2^* retrieval using the PeRCA technique requires a continuous and accurate knowledge of the background NO_2 variation. Compared to ground-based measurements, airborne measurements might have rapid background variations due to the relative motion of the aircraft with respect to the air mass. In this context, the reliability of the PeRCEAS RO_2^* retrieval technique to effectively remove short-term background variations was investigated in the laboratory. The O_3 mixing ratio in the sampled air was varied in a controlled manner between 3 and 30 nmole mole^{-1} in different steps while keeping the HO_2 mixing ratio at 16 ± 2 pmole mole^{-1}. The DUALER I inlet was stabilised at 200 hPa, and all other parameters like chamber pressure, mixing ratios of the reagent gases (30 µmole mole^{-1} NO, 9 % CO and 9 % N_2), the sample flows (500 ml min^{-1}), and relative humidity (< 3 %) were controlled and held constant.

As shown in figure 3.17, the ΔNO_2 calculated from both detector signals remains around 700 pmole mole^{-1} for a constant O_3 mixing ratio, which is eCL times the HO_2 set value (i.e., $\approx 43 \times 16$ pmole mole^{-1}). O_3 variations within one minute lead to opposite deviations in the ΔNO_2 calculated for each system from 700 pmole mole^{-1}. This causes the HO_2 calculated from each system to deviate in the same manner from the actual value. Because the two reactors are operated out of phase with one another, the final HO_2 data determined as the mean of HO_2 calculated from each detector cancel out the variations in their respective ΔNO_2.

The ΔNO_2 calculated over 1 minute has a standard deviation of the order of the variation of O_3, as shown in the retrieved ΔNO_2 plot in figure 3.17. In the case of short term background O_3 variations up to 30 nmole mole^{-1}, the set HO_2 mixing ratio of 16 pmole mole^{-1} (7.8×10^7 molecules cm^{-3} at 200 hPa and 298 K) is successfully retrieved with a maximum deviation of 6 pmole mole^{-1} (2.9×10^7 molecules cm^{-3} at 200 hPa and 298 K). The error in the retrieved HO_2 data results from the 15 % uncertainty of the eCL and the background NO_2 variation within one minute caused by the change in O_3. This result is valid for all the background signal variations during a real-time measurement and proves the robustness of the DUALER approach for the retrieval of RO_2^* even with rapid changes in the sampled air mass.
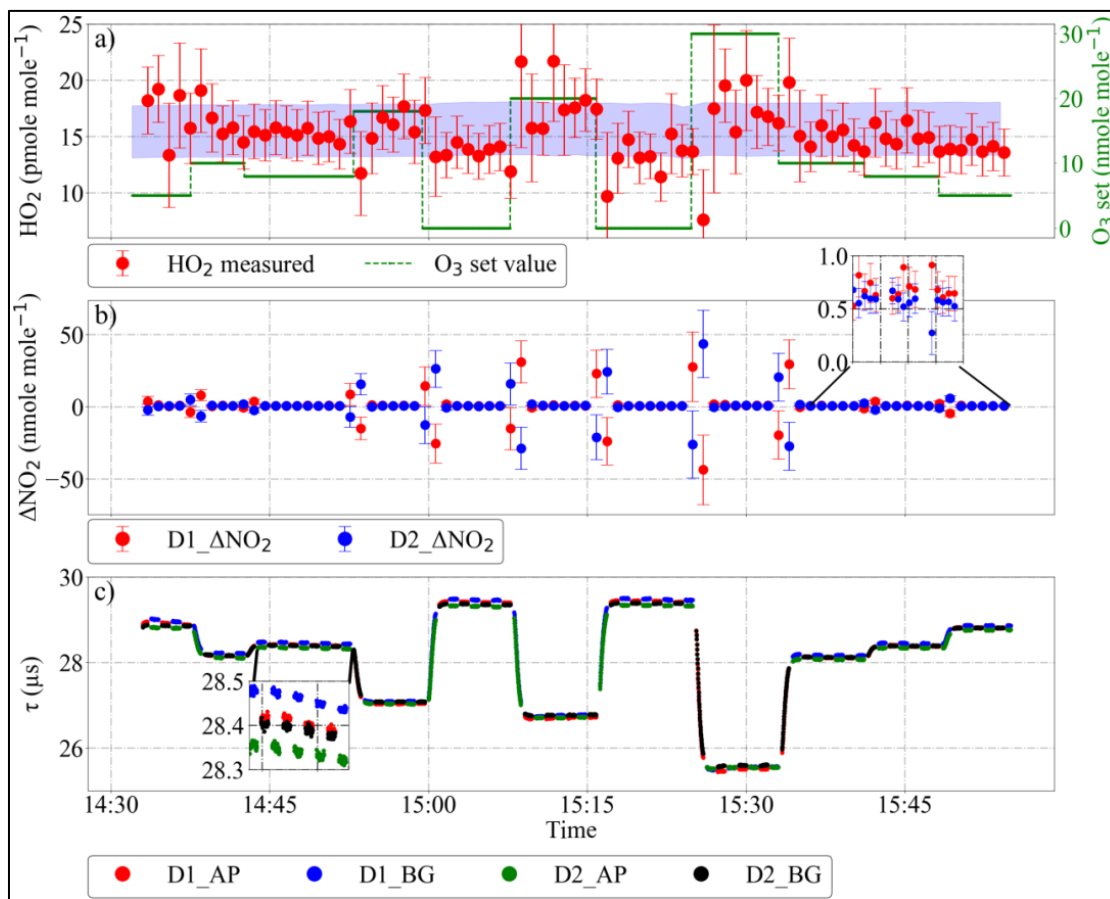
Figure 3.17: HO_2 retrieval under controlled O_3 variations using DUALER I. Panel: a) retrieved HO_2 and O_3 variation. The blue shaded area in a) shows the HO_2 produced in the source (15 %, i.e. 2σ, uncertainty); b) ΔNO_2 retrieved from detector 1 (red) and detector 2 (blue); c) ring-down time from both detectors. D1: detector 1; D2: detector 2; AP: amplification mode, BG: background mode. The inset in panels b) and c) magnifies corresponding plots.

3.1.5 Detection Limit and Accuracy

The PeRCEAS lower limit of detection for RO_2^* ($LOD_{RO_2^*}$) is calculated by dividing the LOD_{NO_2} by the corresponding eCL for each measurement condition set in the laboratory. Provided that LOD_{NO_2} is 90 pmole mole^{-1} NO_2 (3.15×10^8 molecules cm^{-3} at 200 hPa and 296 K), 3σ over 1 minute, as mentioned in section 3.1.1, the $LOD_{RO_2^*}$ varies between 1 and 3.5 pmole mole^{-1} for the eCL values

expected under prevailing conditions in the free troposphere. The $LOD_{RO_2^*}$ can additionally be determined from the eCL calibration curves at different measurement conditions, according to

$$LOD_{RO_2^*} = \frac{3 \times S_a}{m} \qquad \qquad \text{Eq. 3.11}$$

where S_a is the standard deviation of the y-intercept and m is the slope of the measured NO_2 versus set HO_2 from the calibration curve, as in Figure 3.8. For controlled laboratory conditions, the $LOD_{RO_2^*}$ is 6.2×10^6 molecules cm^{-3} (≤ 2 pmole $mole^{-1}$ in all conditions investigated for DUALER I and DUALER II).

The generation of RO_2^* described in section 3.1.2 has a precision < 3 pmole $mole^{-1}$ (2σ). Based on the experimental reproducibility of RO_2^* calibrations, the eCL precision is ≤ 3 % under all conditions investigated. In addition to this, the experimental determination of eCL has a 15 % uncertainty, dominated by the 10 % uncertainty of both $[O_3]$ and $\sigma_{O_2\,eff}^{184.9nm}$ determinations using the current calibration setup (Creasy et al., 2000; Kartal et al., 2009). Other errors associated with the determination of $[H_2O]$ (0.05 %), $[O_2]$ (0.5 %) and the $\sigma_{H_2O}^{184.9nm}$ literature value (1.4 %) are significantly lower compared to the uncertainty of $[O_3]$ and $\sigma_{O_2\,eff}^{184.9nm}$.

As described in section 3.1.1, the σ_{NO_2} used for the retrieval of NO_2 from the ring-down signal has an uncertainty of 5 %. Therefore, the NO_2 measurements from the PeRCEAS CRDS detectors are expected to have 5 % uncertainty under stable laboratory conditions.

Considering these uncertainties, the RO_2^* retrieval using Eq. 2.19 has an overall uncertainty of < 16 % for all conditions investigated in the laboratory.

Conversely, the in-flight PeRCEAS detector signals can be significantly affected by instabilities in the following physical and chemical parameters:

i)   Dynamic pressure at the inlet: Even though the DUALER inlet pressure is constantly kept below the ambient pressure, sudden changes in dynamic pressure experienced by the inlet might induce pressure fluctuations. Depending upon the variation rate (< 10 hPa with 60 s), the inlet pressure regulator might take several seconds to adjust the pressure back to a stable set value. The pressure fluctuations in the inlet propagate to the detector and cause signal instabilities due to the change in the number of molecules inside the detector. Since the pressure fluctuations are not the same in both detectors, the signal instabilities cannot be accounted for during the final RO_2^* retrieval. Pressure fluctuations in the reactor also affect the eCL due to the termolecular reactions involved in the amplification and loss mechanisms. These variations in the eCL further increase the uncertainty in the final RO_2^* retrieval. In addition to this, the pressure fluctuation affects the sample flow stability, which changes the residence time of the sampled air mass (Table 3.4) and thereby the O_3 titration and PAN decomposition. The uncertainties due to the dynamical pressure

fluctuations are nonlinear and cannot be quantified during the RO_2^* retrieval. The data points expected to be affected by pressure fluctuations are marked with a flag during the analysis.

ii) Temperature inside the aircraft: The temperature variations in the HALO cabin might increase the noise in the NO_2 measurements. This increases the uncertainty of ΔNO_2 and thereby increases the uncertainty in the retrieved RO_2^*. The in-flight temperature in the HALO cabin remains reasonably constant (< 298 K). However, during the instrumental preparation on the ground before the flight, the cabin temperature may increase up to 313 K. This affects the stability of the ring-down time signal and thereby the accuracy of the reference measurements.

iii) Mechanical vibration: The airborne measurements are expected to have higher noise than laboratory conditions even under stable pressure and temperature due to the mechanical vibrations experienced by the instrument during the flight. Even though PeRCEAS detectors are equipped with steel springs to absorb mechanical vibrations, the vibration of the aircraft under turbulent conditions might affect the performance of the CRDS detectors and increase the noise. In extreme cases, the cavity might get misaligned entirely due to the relative motion of optical parts under heavy vibrations.

iv) Variation in the chemical composition: Even though the continuous measurement of both signal and background account for fast variations in the chemical composition of the sampled air mass, the uncertainty of the RO_2^* retrieval increases with changes occurring within a mode time (section 3.1.4).

Therefore, the in-flight error in the RO_2^* measurement is calculated by considering the uncertainty of the RO_2^* under laboratory conditions (16 %) and the background variation in the signal within a mode time, as discussed in section 3.1.4. Furthermore, changes in the HO_2 to RO_2 ratio affect the accuracy of the PeRCEAS retrieval of RO_2^*. As described in section 3.1.2, the PeRCEAS sensitivity for HO_2 and CH_3O_2 depends on the concentration of the reagent gas NO added to the reactor. Therefore, the effect of changes in the HO_2 to RO_2 ratio in the air mass on the accuracy of PeRCEAS retrieval varies with operating conditions (see Table 3.2).

The current sensitivity of PeRCEAS on HALO is competitive with similar airborne peroxy radical instruments. Table A.5 in appendix A-V summarises the specifications of state-of-the-art instruments for the airborne measurement of peroxy radicals. Ground-based instruments are also included for comparison. Due to physical and chemical operating conditions differences, a direct comparison between methods is challenging and only possible for time resolution and detection limits related to well-defined and controlled measurement conditions. As mentioned in chapter 2, MIESR, though the only direct measurement technique of high precision, is not suitable for airborne measurements and is difficult to implement in field campaigns. LIF based instruments have a better detection limit but are subject to interferences from RO_2 in the sample (Fuchs et al., 2011).

3.2 Flight Deployment

As part of the research undertaken, the PeRCEAS instrument was successfully deployed and measured the sum of peroxy radicals, i.e. RO_2^* ($RO_2^* = HO_2 + \sum RO_2$) in 33 mission flights during the airborne campaigns **O**xidation **M**echanism **O**bservations (OMO) Asia and **E**ffect of **Me**gacities on the transport and transformation of pollutants on the **R**egional to **G**lobal scal**e**s (EMeRGe). The optimal operating conditions for each campaign were determined based on the laboratory calibration prior to the campaign. During the campaign, the instrument was calibrated before and after each flight on the ground to identify potential mechanical and electrical malfunctions and detector miss alignments. Post campaign laboratory calibrations were made to check the instrumental stability and variation in the sensitivity.

The maintenance and calibration on the ground and the inflight operations were also part of the research undertaken during this doctoral study. The final RO_2^* data were retrieved using a program in Python language developed during this doctoral study using the procedure mentioned in section 3.1.4. After quality assessment based on sample air temperature and humidity, operating pressure, detector temperature, and laser beam profile, the final version of the data set was uploaded to the HALO database.

3.2.1 OMO Asia Campaign

The OMO is a multi-institutional project belonging to the priority research program of the **D**eutsche **F**orschungs**g**emeinschaft (DFG) to investigate atmospheric processes using the HALO platform. OMO involves the Max Planck Institute for Chemistry, Mainz; the Research Centre Jülich; the Institut für Physik der Atmosphäre (IPA), DLR Oberpfaffenhofen, Munich; the Research Centre Karlsruhe; the Universities of Bremen, Heidelberg, and Wuppertal..

The quasi-stationary anticyclone formed during the Asia summer monsoon uplifts natural and anthropogenic air pollutants into the upper troposphere and are transported downstream. During the transport, the pollutants are partly removed by wet deposition or transformation into soluble gases or involved in chemical processing. In this context, OMO Asia tries to understand these mechanisms by focusing on the key aspects like oxidation processes, radical chemistry, the efficiency of convective cloud transport, deposition, and the impact of long-distance transport of air pollution on air quality and climate change. The radiation, water vapour, species that are emitted by natural and anthropogenic sources (NMVOC and their isotopes, CH_4, NO_x, CO, SO_2), short-lived free radicals that initiate and propagate photo-oxidation processes (OH, HO_2, RO_2, BrO), longer-lived oxidants (O_3), reaction intermediates (OVOC including aldehydes, ketones), and products that can be removed from the atmosphere by deposition processes (acids, peroxides) were measured during the field campaign (https://www.mpic.de/3599603/OMO).

The OMO Asia mission took place in July and August 2015. A total of 111 flight hours were carried out during 19 flights (Figure 3.18), with 90 % of the flight tracks in the upper troposphere (9000 – 15000 m) over the Mediterranean, the Arabian Peninsula, and the Indian Ocean. HALO was based alternately at Paphos in Cyprus and Gan in the Maldives with refuelling stops at the Bahrain airport. The flight tracks were made to measure the air mass from the western part of the anticyclone, where the emission from South Asia is expected after about 1 to 2 weeks of chemical processing (Lelieveld et al., 2018, Tomsche et al., 2019). Table 3.5 summarises the flight time and the flight routes carried out during the field campaign. The flights are named OMO-FN, where OMO stands for the OMO mission, and FN are two digits for the flight number. The instrumentation used during OMO onboard the HALO aircraft is summarised in Table 3.6. Further information about OMO Asia mission can be found on the following websites: http://www.halo.dlr.de/science/missions/omo/omo.html; https://www.mpic.de/3599603/OMO.

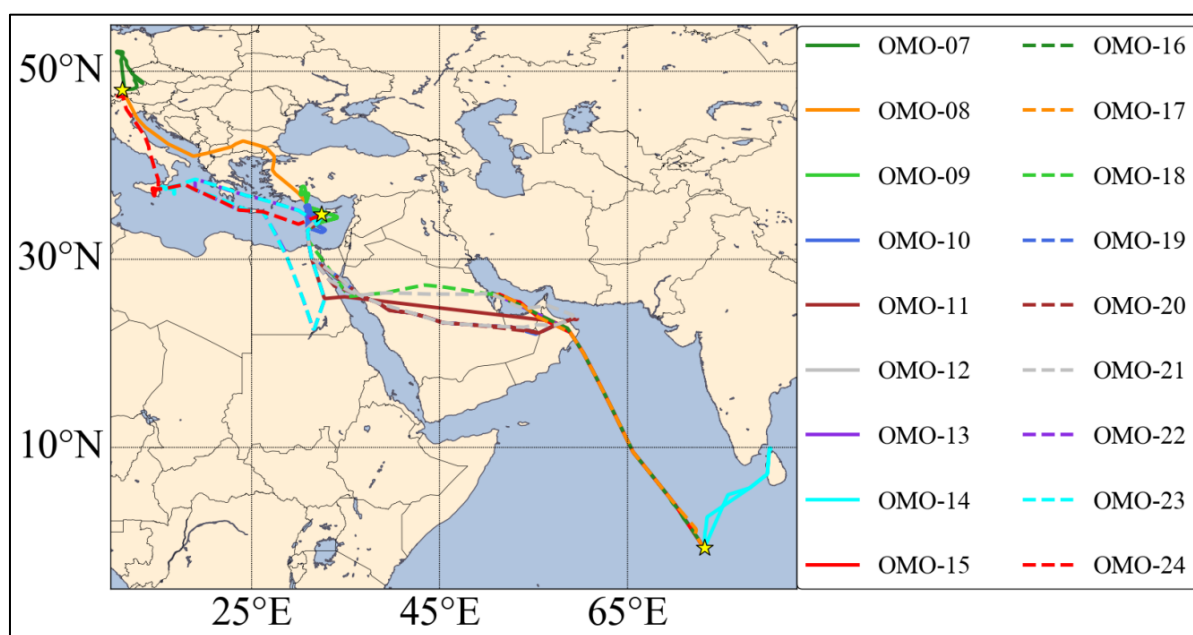Figure 3.18: OMO Asia flight tracks. The HALO bases at DLR in Oberpfaffenhofen, Paphos in Cyprus, and Gan in the Maldives are indicated by a yellow star for reference.

In addition to the measurement of RO_2^* from PeRCEAS, other in-situ measurements and basic aircraft data from HALO are also used in this study. Details of the corresponding dataset from the instruments listed in Table 3.6 are given in appendix A-III.

Table 3.5: Details of the HALO flights carried out during OMO Asia.

Flight number	Day/ Month	Start/End time (UTC)	Main scientific objectives	Flight route
OMO-06	13/07	09:35/11:55	Test flight	Different altitudes over Munich
OMO-07	16/07	10:00/12:40	Test flight	Different altitudes over Munich
OMO-08	21/07	09:02/12:28	Transfer flight from Oberpfaffenhofen to Paphos and sampling of Asian Monsoon outflow over Cyprus	Oberpfaffenhofen – Paphos
OMO-09	25/07	05:53/11:08	Measurements over the Mediterranean Sea	Different altitudes over the Mediterranean Sea
OMO-10	28/07	06:01/13:59	Sampling of Asian Monsoon outflow at different altitudes over the Mediterranean Sea	Different altitudes over the Mediterranean Sea
OMO-11	01/08	05:50/14:35	Transfer flight from Paphos to Gan	Paphos – Bahrain – Gan
OMO-12	06/08	02:00/06:40	Sampling of polluted air trapped within Asian monsoon anticyclone over the Arabian Sea	Gan – Bahrain
OMO-13	06/08	07:45/12:55	Sampling of polluted air trapped within Asian monsoon anticyclone over the Arabian Sea	Bahrain – Gan
OMO-14	08/08	07:30/11:24	Sampling of Asian monsoon outflow over the Indian Ocean at different altitudes	Gan – Sri Lanka – Gan
OMO-15	09/08	01:50/06:30	Sampling of polluted air trapped within Asian monsoon anticyclone over the Arabian Sea	Gan – Bahrain
OMO-16	09/08	07:40/12:35	Sampling of polluted air trapped within Asian monsoon anticyclone over the Arabian Sea	Bahrain – Gan
OMO-17	10/08	04:50/09:35	Transfer flight and sampling of polluted air trapped within Asian monsoon anticyclone over the Arabian Sea	Gan – Bahrain
OMO-18	10/08	10:55/14:30	Transfer flight from Bahrain to Paphos and sampling of polluted air over Egypt	Bahrain – Paphos
OMO-19	13/08	06:01/14:54	Sampling Asian monsoon outflow over Saudi Arabia and Oman	Cyprus – Oman – Cyprus
OMO-20	15/08	05:50/15:10	Sampling Asian monsoon outflow over Saudi Arabia and Oman	Paphos – Oman – Paphos
OMO-21	18/08	06:16/15:10	Sampling Asian monsoon outflow over Egypt, Saudi Arabia, UAE, and Oman	Paphos – Egypt – Saudi Arabia –UAE – Oman – Saudi Arabia – Egypt – Paphos
OMO-22	23/08	06:00/12:30	Sampling of Asian monsoon outflow over Egypt and background measurements over Greece	Paphos – Egypt – Greece – Paphos
OMO-23	25/08	06:10/14:35	Sampling of Asian monsoon outflow over Egypt and sampling the volcanic plume from Mount Etna	Paphos – Egypt – Mount Etna – Paphos
OMO-24	27/08	08:38/14:32	Transfer flight from Paphos to Oberpfaffenhofen	Paphos – Mount Etna – Oberpfaffenhofen

Table 3.6: HALO instrumental payload for OMO Asia. PeRCA: Peroxy Radical Chemical Amplification; CRDS: Cavity Ring-Down Spectroscopy; LIF: Laser Induced Fluorescence; HVS: High Volume Sampler; GC-C-IRMS: Gas Chromatography Combustion Isotope Ratio Mass Spectrometry; PTR-MS: Proton-Transfer-Reaction Mass Spectrometer; CI-ITMS: Chemical Ionisation Ion Trap Mass Spectrometry; GC-MS: Gas chromatography-mass spectrometry analysis; DOAS: Differential Optical Absorption Spectrometry; CPC: Condensation Particle Counting.

Trace gas-in situ measurements				
Species/parameters	Acronym	Institution	Technique/Instrument	Reference
$RO_2^* = HO_2 + \sum RO_2$	PeRCEAS	Univ. Bremen	PeRCA + CRDS	George et al., 2020
OH, HO_2, NO_2	HORUS	MPIC Mainz	LIF	Martinez et al., 2010, Marno et al., 2020
OH, HO_2	Air LIF	FZ Jülich	LIF	
VOC/C isotope ratios	MIRAH	Univ. Wuppertal	HVS/GC-C-IRMS	Wintel et al., 2013
OVOC	HKMS	KIT Karlsruhe	PTR-MS	Brito and Zahn, 2011
O_3	FAIRO	KIT Karlsruhe	UV-Photometry/ Chemiluminescence	Zahn et al., 2012
CO, HCHO, CO_2, CH_4	TRISTAR	MPIC Mainz	TDLAS	Schiller et al., 2008, Tadic et al., 2017
Total Peroxides, H_2O_2	HYPHOP	MPIC Mainz	Liquid face reaction/ Florescence	Hottmann et al., 2020
None methyl VOC	MGC	MPIC Mainz		
NO, NO_y	AENEAS	DLR-IPA	Chemiluminescence/ Gold converter	Ziereis et al., 2004
SO_2, HCOOH	CI-ITMS	DLR-IPA	CI-ITMS	Speidel et al., 2007
Trace gas- remote sensing measurements				
NO_2, HONO, BrO, CH_2O, $C_2H_2O_2$, $C_3H_4O_2$, SO_2, IO	mini-DOAS	Univ. Heidelberg	DOAS / UV-nIR; 2D optical spectrometer	Hüneke et al. 2017
Aerosol measurements				
Particle size distribution/number concentration	CPC	DLR-IPA	CPC	
Other parameters				
Spectral actinic flux density (up/down) Photolysis frequencies	HALO-SR	FZ Jülich	CCD spectro-radiometry	Bohn and Lohse, 2017
Basic aircraft data	BAHAMAS	DLR -FX	various	Mallaun et al., 2015

The data from the following model simulations provided to the OMO community were also used during the analysis presented in this study.

- The Lagrangian particle dispersion model FLEXPART version 9.2 beta (Stohl et al., 1998) was used to derive the origin of the air masses sampled during the flights. The model is driven by

European Centre for Medium-Range Forecasts (ECMWF) operational data with a horizontal resolution of 1° × 1° and a vertical resolution of 137 levels between 1013.25 and 0.01 hPa.

- The fully coupled chemistry-climate model ECHAM/MESSy Atmospheric Chemistry (EMAC), which consists of the general circulation model ECHAM5 (fifth generation of the European Center HAMburg model, Roeckner et al., 2006) and the Modular Earth Submodel System (MESSy, Jöckel et al., 2005, 2010), was used to model different trace gases measured during the flights. A horizontal resolution of 2.8° × 2.8° and a vertical resolution of a hybrid pressure grid between the surface and 0.01 hPa were used for the simulations.

More information about the model simulation and the dataset is given in Lelieveld et al., 2018; Tomsche et al., 2019 and appendix A-IV.

3.2.2 PeRCEAS Operating Conditions During OMO Asia

PeRCEAS successfully measured RO_2^* in 17 out of 19 mission flights during OMO Asia. The detector configuration used in OMO Asia was similar to that described in Horstjann et al., 2014, which does not have a beam camera and pico motors for identifying and correcting misalignments without removing the detectors from the HALO rack. As a result, RO_2^* data from the mission flights in which one of the detectors was miss-aligned are not available, as in the case of OMO-19 and OMO-20.

DUALER I with AB as Detector I and FH as Detector II were deployed during all the mission flights except in OMO-19 and OMO-24. In the mission flight OMO-19, AB as Detector I and FR as Detector II was deployed. Similarly, in mission flight OMO-20, FR as Detector I and FH as Detector II were deployed. The measurement conditions and the corresponding eCL determined from laboratory calibrations for OMO Asia are given in Table 3.7. The eCL_{mix} is used for the retrieval of RO_2^* from ΔNO_2 measurements. The mixing ratio of the reagent gas CO was kept constant at 9 %, irrespective of the measurement conditions.

Table 3.7: eCL obtained experimentally for the measurement conditions during OMO Asia. eCL_{HO_2} and eCL_{mix} are determined for pure HO_2 and a 1:1 mixture of $HO_2:CH_3O_2$. The number concentration of NO is calculated at 298 K.

Altitude (m)	Sample flow (ml min^{-1})	Inlet pressure (hPa)	NO (μmole mole^{-1})	[NO] (molecules cm^{-3})	Reactor 1		Reactor 2	
					eCL_{HO_2}	eCL_{mix}	eCL_{HO_2}	eCL_{mix}
Up to 10000	1000	160	15	5.83×10^{13}	51	40	53	41
Between 10000 and 12000	500	80	30	5.8×10^{13}	30	24	32	26
above 12000	300	60	30	4.4×10^{13}	28	23	29	26

As described in section 3.1.2, depending upon the amount of reagent gas NO added to the inlet, the eCL dependency on $[H_2O]$ varies. Figure 3.19 shows the ambient $[H_2O]$ versus $[H_2O]$ inside the DUALER plot for OMO Asia measurements. Even though the reduced pressure in the inlet reduces $[H_2O]$, it is still significant enough to affect the eCL. Therefore the eCL was corrected using Eq. 3.10 described in section 3.1.2.

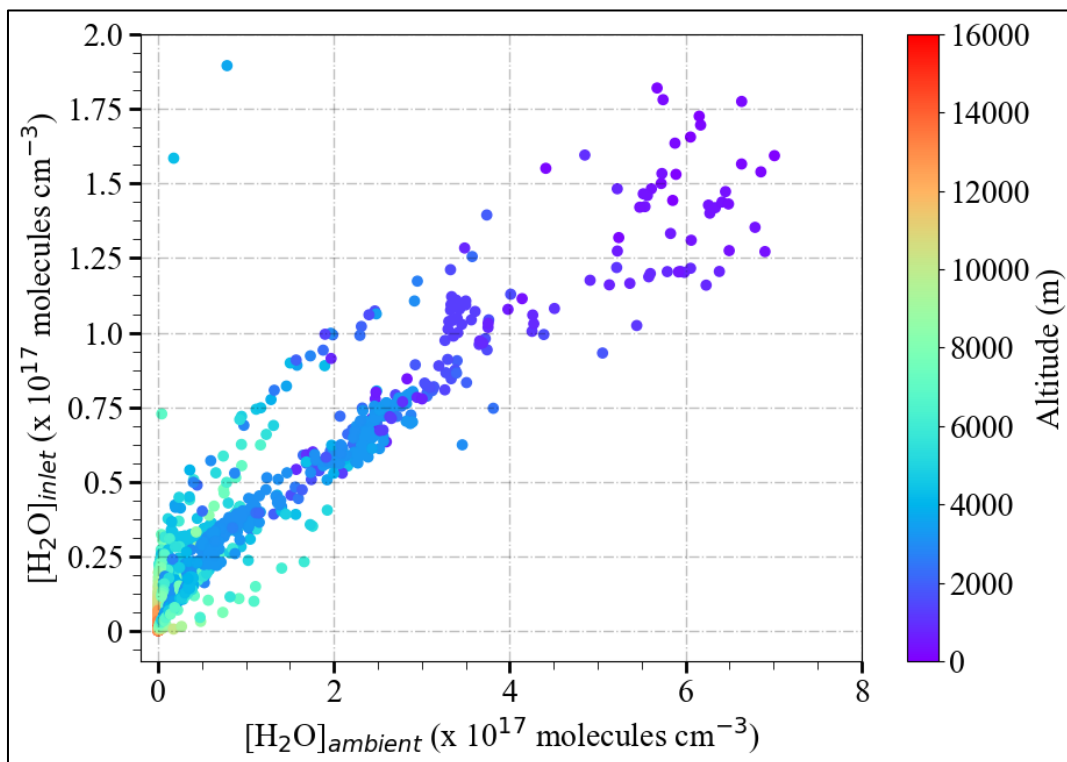Figure 3.19: Ambient $[H_2O]$ versus $[H_2O]$ measured in DUALER during OMO Asia colour coded with altitude.

3.2.3 EMeRGe Campaigns

The EMeRGe is a project of the Priority research program of the DFG to investigate the atmospheric processes using HALO. The overarching objective is to improve the current understanding of the photochemical and heterogeneous processing of outflows from **m**ajor **p**opulation **c**entres (MPCs) and their atmospheric impact on a regional to global scale. Two **i**ntensive **o**perational **p**eriods (IOPs) were carried out to investigate selected European and Asian MPC outflows to achieve the scientific goals. The European field experiment took place from 10 to 28 July 2017 during the European summer, focusing on the study of active plume processing close to emission sources. The field experiment in Asia took place from 10 March to 9 April 2018 during the spring inter-monsoon period and investigated plume processing from Southeast Asian MPCs.

A total of 180 HALO flight hours were successfully made during the IOPs. Measurements at different altitudes downwind and upwind of the target MPCs were made to investigate the impact of mixing long-range transport of biomass burning and mineral dust with fresh emissions. The emission sources of the species measured onboard HALO were identified with the help of backward

trajectories. The origin and history of the plumes probed at each point of the flight track are traced by using highly-resolved backward trajectories calculated by the kinematic trajectory model FLEXTRA 5.0 (Stohl et al., 1995, 1999) and dispersion calculations of CO enhancement caused by the selected MPC outflow over the CO background by using the NOAA (National Oceanic and Atmospheric Association) HYSPLIT (Hybrid Single Particle Lagrangian Integrated Trajectories, https://www.arl.noaa.gov/hysplit/) model. FLEXTRA uses the **E**uropean **C**entre for **M**edium-Range **W**eather **F**orecasts (ECMWF) operational data set ERA5 meteorological data at 0.25° horizontal resolution. Trajectories are started every 10 minutes of flight time and reach back 10 days. The HYSPLIT was also driven by the ECMWF forecast (0-11 hours forecast, 12-hourly update, interpolated at 0.1° horizontally, 137 vertical model levels, 1-hourly output). The CO emission rates were taken from the EDGAR HTAP V2 emission inventory (http://edgar.jrc.ec.europa.eu/htap_v2/). More details about the model simulations used in this study are given in appendix A-IV.

Ground-based and satellite measurements during the IOPs were also synergistically combined with the airborne measurements to improve the understanding of the emission sources and the transport pathways. More details about the EMeRGe mission can be found elsewhere (Andrés Hernández et al., 2022, https://doi.org/10.5194/acp-22-5877-2022).

For EMeRGe in Asia, the Weather Research and Forecasting (WRF) version 3.7.1 (Skamarock et al., 2008) coupled with the Community Multiscale Air Quality (CMAQ) version 5.0.2 (the United States Environmental Protection Agency, 2014, http://doi.org/10.5281/zenodo.1079898; Byun and Schere, 2006) model was used to calculate different trace gases concentration along the flight tracks. The regional-scale air pollution with a horizontal resolution of 45 km and 27 vertical layers between 1013.25 hPa and 50 hPa was simulated by WRF/CMAQ model. The sixth-generation CMAQ aerosol module (AERO6) and the Statewide Air Pollution Research Center version 07 (SAPRC-07) were used as aerosol and air chemistry mechanisms. The fixed anthropogenic emissions were taken from the monthly data of Hemispheric Transport of Air Pollution (HTAP) version 2.2 with a 0.25° × 0.25° resolution (Janssens-Maenhout et al., 2015) for 2010. The Global Fire Emissions Database (GFED) version 4.1 was used for the monthly emissions from biomass burning. The Model of Emissions of Gases and Aerosols from Nature (MEGAN) v2.1 was used for biogenic emissions, and the AeroCom database was used to account for the aerosol emission. More details about the model simulation are given in appendix A-IV.

Table 3.8: HALO instrumental payload for EMeRGe. PeRCA: Peroxy Radical Chemical Amplification; CRDS: Cavity Ring-Down Spectroscopy; HVS: High Volume Sampler; GC-C-IRMS: Gas Chromatography Combustion Isotope Ratio Mass Spectrometry; PTR-MS: Proton-Transfer-Reaction Mass Spectrometer; AT-BS: Adsorption Tube and Bag air Sampler; TD-GC-MS: Thermal Desorption Gas Chromatography and Mass Spectrometry; CI-ITMS: Chemical Ionisation Ion Trap Mass Spectrometry; GC-MS: Gas chromatography-mass spectrometry analysis; PAN: Peroxyacetyl nitrate; $\delta^{13}C(CH_4)$: Isotopic signature of methane; PFC: Perfluorinated carbon chemicals; DOAS: Differential Optical Absorption Spectrometry; ToF-AMS: Time of Flight- Aerosol Mass Spectrometry; SP2: Single Particle Soot Photometry; CCNC: Cloud Condensation Nucleus Counting; MI: Multi Impactor for aerosol off-line analysis; CPC: Condensation Particle Counting; DMA: Differential Mobility Analysis; OPC: Optical Particle Counting; PSAP: Particle Soot Absorption Photometry.

Trace gas-in situ measurements				
Species/parameters	Acronym	Institution	Technique/Instrument	Reference
$RO_2^* = HO_2 + \sum RO_2$	PeRCEAS	Univ. Bremen	PeRCA + CRDS	George et al., 2020
VOC/C isotope ratios	MIRAH	Univ. Wuppertal	HVS/GC-C-IRMS	Wintel et al., 2013
OVOC	HKMS	KIT Karlsruhe	PTR-MS	Brito and Zahn, 2011
O_3	FAIRO	KIT Karlsruhe	UV-Photometry/ Chemiluminescence	Zahn et al., 2012
O_3, CO	AMTEX	DLR-IPA	UV-Photometry/ VUV-Fluorimetry	Gerbig et al., 1996
NO, NO_y	AENEAS	DLR-IPA	Chemiluminescence/ Gold converter	Ziereis et al., 2004
SO_2, HCOOH	CI-ITMS	DLR-IPA	CI-ITMS	Speidel et al., 2007
a) CO_2 and CH_4 b) PAN c) $\delta^{13}C(CH_4)$	CATS	DLR-IPA	a) CRDS b) GC-MS c) GC-IRMS	Chen et al., 2010 Volz-Thomas et al., 2001 Fisher et al., 2006
PFC tracer	PERTRAS	DLR-IPA	AT-BS/TD-GC-MS	Ren et al., 2015
Trace gas- remote sensing measurements				
NO_2, HONO, BrO, CH_2O, $C_2H_2O_2$, $C_3H_4O_2$, SO_2, IO	mini-DOAS	Univ. Heidelberg	DOAS / UV-nIR; 2D optical spectrometer	Hüneke et al., 2017
NO_2, CH_2O, $C_2H_2O_2$, H_2O, SO_2, BrO, O_3	HAIDI	Univ. Heidelberg	DOAS / 3x2D-imaging spectrometers	General et al., 2014
Aerosol measurements				
Particle composition	C-ToF-AMS	MPIC Mainz & Univ. Mainz	ToF-AMS, OPC	Schulz et al., 2018
BC, CCN, microscopic properties	CCN-Rack	MPIC Mainz	SP2 CCNC, MI	Holanda et al., 2020 Wendisch et al., 2016
Particle size distribution/number concentration	AMETYST	DLR-IPA	CPC, OPC, PSAP, DMA	Andreae et al., 2018
Other parameters				
Spectral actinic flux density (up/down) Photolysis frequencies	HALO-SR	FZ Jülich	CCD spectro- radiometry	Bohn and Lohse, 2017
Basic aircraft data	BAHAMAS	DLR -FX	various	Mallaun et al., 2015

In addition to the measurement of RO_2^* from PeRCEAS, other in-situ and remote-sensing measurements and basic aircraft data from HALO are also used in this study. Details of the corresponding dataset from the instruments listed in Table 3.8 are given in appendix A-III. Concerning the data obtained by the remote-sensing instruments, the miniDOAS retrieves the Slant Column Density (SCD) of the target gas and a scaling gas (O_4) towards the horizon at the flight altitude. From this, concentration and mixing ratios of the targeted gas within the line of sight are estimated using RT modelling (Stutz et al., 2017; Hüneke et al., 2017; Kluge et al., 2020; Rotermund et al., 2021). The HAIDI instrument retrieves SCDs below the aircraft. The SCDs from HAIDI are then converted to mixing ratios using the corresponding geometric Air Mass Factor (AMF) under a well-mixed target gas layer assumption. As a result of this assumption, the calculated mixing ratios for HAIDI target gases are lower limits and close to the actual values while flying within and close to a well-mixed boundary layer. Despite the differences in sampling volume and temporal and spatial resolution in the in-situ and remote sensing measurement techniques, the concentration of common and related species obtained are in reasonable agreement (Schumann, 2020).

3.2.4 EMeRGe in Europe

The main scientific goals of EMeRGe in Europe were the identification of individual emission signatures in MPC plumes over Europe, investigation of processing in MPC pollution outflows, and the assessment of the relative importance of MPCs as sources of pollution over Europe. In this context, the European megacities London and Paris, Benelux/ Ruhr metropolitan area, Po Valley, Rome, Madrid, and Barcelona were taken as target MPCs.

A total of 53 HALO flight hours were carried out in 7 mission flights (Figure 3.20) to investigate the target MPC outflows under the most favourable conditions. All HALO flights started from the DLR base in Oberpfaffenhofen, southwest of Munich in Germany. To measure outflows from the target MPCs, 60 % of the EMeRGe flights over Europe were done below 3000 m. Dedicated vertical profiling was made in the upwind and downwind of the target MPCs with three stable flight levels (FLs). The flights are named E-EU-FN, where E stands for EMeRGe, EU for Europe, and FN represents two digits for the flight number. Table 3.9 summarises the flight time and the target MPC outflows investigated by HALO. More details about the EMeRGe in Europe IOP can be found elsewhere (Andrés Hernández et al., 2022).
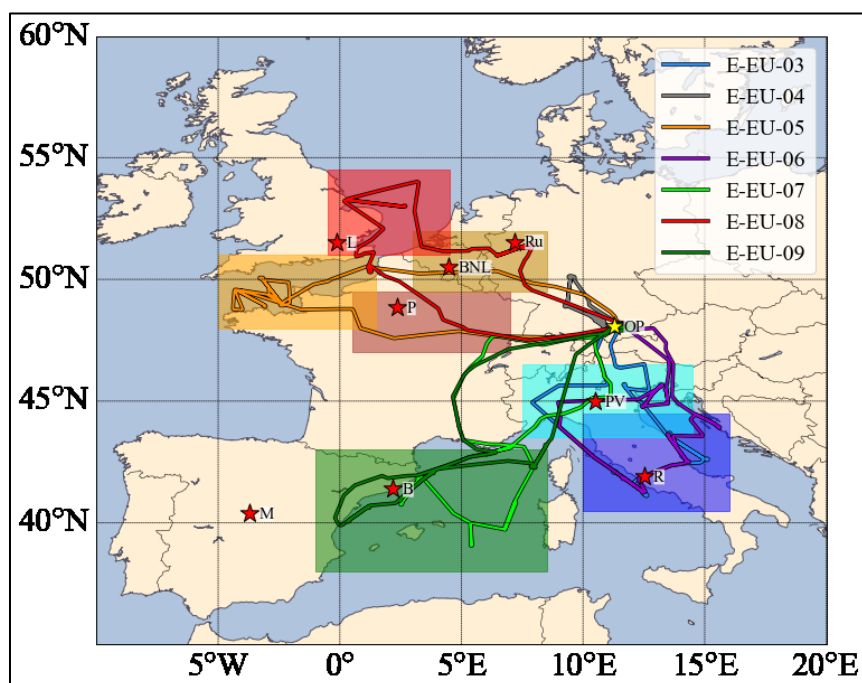
Figure 3.20: HALO flight tracks during the EMeRGe campaign in Europe on 11, 13, 17, 20, 24, 26 and 28 July 2017 (E-EU-03 to E-EU-09, respectively, colour coded). The specific flight times are presented in Table 3.9. MPC target areas are colour coded by shading, and distinctive locations/regions are marked with red stars, M: Madrid, B: Barcelona, P: Paris, L: London; BNL: BeNeLux, Ru: Ruhr area, PV: Po Valley, R: Rome. The position of the HALO base at DLR in Oberpfaffenhofen (OP) is also indicated by a yellow star for reference. (Figure source: adapted from Andrés Hernández et al., 2022).

Table 3.9: Details of the HALO flights carried out in Europe during EMeRGe.

Flight number	Day/ Month	Start/End time (UTC)	MPC emission and transport target	Other features
E-EU-03	11/07	10:00/16:30	Rome, Po Valley; convection over Alps and Apennines	Mineral dust from Northern Africa, Fires in Southern Italy.
E-EU-04	13/07	10:40/15:00	Central Europe; Intercontinental transport	HALO-FAAM blind comparison; Canada fires
E-EU-05	17/07	10:30/18:30	London, BNL/Ruhr, English Channel, and Central Europe	FAAM flight over London
E-EU-06	20/07	09:00/17:30	Rome, Po Valley; convection over Alps and Apennines	Mineral dust from Northern Africa; Fires in Southern Italy and Croatia
E-EU-07	24/07	09:45/18:15	Po Valley, South France, Barcelona; west Mediterranean	Dust transport from Northern Africa, fires in Southern Europe
E-EU-08	26/07	07:45/15:20	London, BNL/Ruhr, Paris, English Channel, and Central Europe	PFC tracer releases London., Wuppertal
E-EU-09	28/07	10:00/18:30	Po Valley, South France, Madrid, Barcelona, and West Mediterranean	Fires in Southern France and Portugal

3.2.5 PeRCEAS Operating Conditions During EMeRGe in Europe

PeRCEAS successfully measured RO_2^* in all the seven mission flights. DUALER I with AB as Detector I and FR as Detector II were deployed during the IOP in Europe. The inlet was kept at 300 hPa for the measurements done up to 6000 m. To keep the $\Delta P > 100$ hPa, all the measurements above 6000 m were made with 200 hPa inlet pressure. Other measurement conditions used were 500 ml min^{-1} sample flow, 9 % reagent gas CO, and 30 μmole mole^{-1} reagent gas NO. The eCL determined from laboratory calibrations for EMeRGe in Europe measurement conditions are given in Table 3.10. The eCL_{mix} is used for the retrieval of RO_2^* from ΔNO_2 measurements. The measurement conditions selected for this study give different sensitivities for HO_2 and RO_2 (section 3.1.2) with $\alpha = 0.52$ and 0.65. If the ratio of HO_2:RO_2 changes to 3:1, then the RO_2^* results in a 10 % overestimation of $HO_2 + RO_2$. Similarly, a HO_2:RO_2 ratio of 1:3 results in a 10 % underestimation. Considering the 16 % uncertainty from the laboratory calibrations, the maximum uncertainty of RO_2^* is 26 % for the HO_2:RO_2 ratio between 3:1 and 1:3 for the measurements during EMeRGe in Europe. This uncertainty is below the in-flight uncertainty of the PeRCEAS instrument. The uncertainty coming from the variation of the HO_2:RO_2 ratio is not included in the error calculation of the RO_2^* measurements but has been explicitly discussed during the analysis in section 4.1.11.

Table 3.10: eCL obtained experimentally for the measurement conditions during EMeRGe in Europe. eCL_{HO_2} and eCL_{mix} are the chain length determined for pure HO_2 and a 1:1 mixture of HO_2:CH_3O_2, respectively. The number concentration of NO is calculated at 298 K.

Inlet pressure (hPa)	NO mixing ratio (μmole mole^{-1})	[NO] (molecules cm^{-3})	Reactor 1		Reactor 2		α
			eCL_{HO_2}	eCL_{mix}	eCL_{HO_2}	eCL_{mix}	
200	30	1.46×10^{14}	51 ± 8	37 ± 6	45 ± 7	34 ± 5	0.65
300	30	2.19×10^{14}	47 ± 7	36 ± 5	40 ± 6	33 ± 5	0.52

As described in section 3.1.2, the eCL dependency on $[H_2O]$ varies depending upon the amount of reagent gas NO added to the inlet. Figure 3.21 shows the ambient $[H_2O]$ versus $[H_2O]$ inside the DUALER plot for EMeRGe in Europe measurements. Even though the reduced pressure in the inlet reduces $[H_2O]$, it is still significant enough to affect the eCL. Therefore the eCL was corrected using Eq. 3.10.
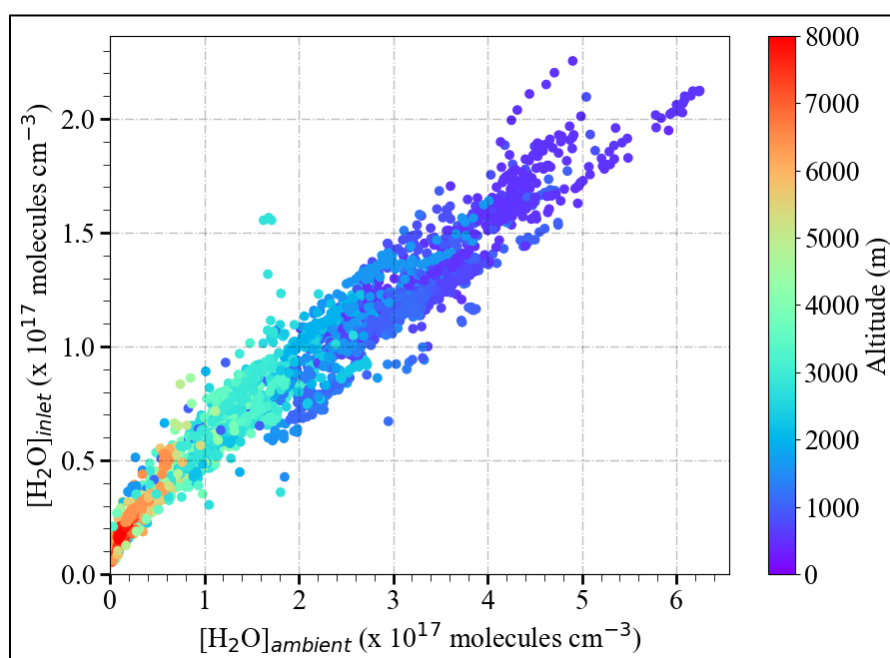
Figure 3.21: Ambient [H_2O] versus [H_2O] measured in DUALER during EMeRGe in Europe, colour coded with altitude.

3.2.6 EMeRGe in Asia

The main scientific goals of EMeRGe in Asia were: the identification of individual emission signatures in the outflows from selected East Asian MPCs, the investigation of long-range transport and transformation of pollution outflows from China to the Yellow and the East China Sea, the characterisation of the transport of outflows from selected MPCs, and the assessment of the relative importance of MPCs as sources of pollution over the West Pacific, especially of Taiwan. Based on these scientific goals, Bangkok, Manila, Taipei, Tainan, the Pearl River Delta region, the Yangtze River Delta region, and South Japan were taken as target MPCs. Tainan in Taiwan was selected as the HALO base for the mission.

A total of 127 HALO flight hours were carried out in 18 flights during EMeRGe in Asia. The flights are named E-AS-FN, where E stands for EMeRGe, AS for Asia, and FN represents two digits for the flight number. Six out of the 18 flights were transfer flights from Oberpfaffenhofen, Germany, to Tainan, Taiwan and back. Transfer to one direction was divided into three flights due to the measurement restrictions over India. The flights E-AS-01 and E-AS-16 were transfer flights between Oberpfaffenhofen and Abu Dhabi with measurements over the Mediterranean region and Arabian Peninsula (Figure 3.22). During the E-AS-02 and E-AS-15 transfer flights between Abu Dhabi and Pattaya, Thailand, airborne measurement was not permitted. The flight tracks of the transfer flight between Pattaya and Tainan (E-AS-03 and E-AS-14) and other mission flights are shown in Figure 3.23. Even under constraints like flight permission and maximum range of HALO, dedicated vertical profiling was made in the regions expected to have target MPCs outflow signatures with at least three stable flight levels.
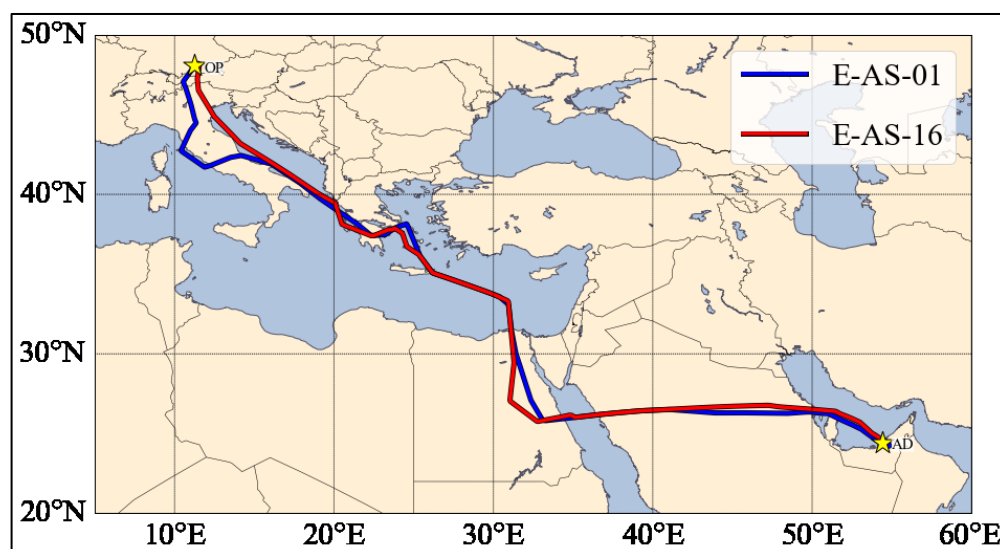
Figure 3.22: HALO transfer flight tracks from Oberpfaffenhofen to Abu Dhabi (in blue) and back (in red) during the EMeRGe campaign in Asia. OP: Oberpfaffenhofen, AD: Abu Dhabi.
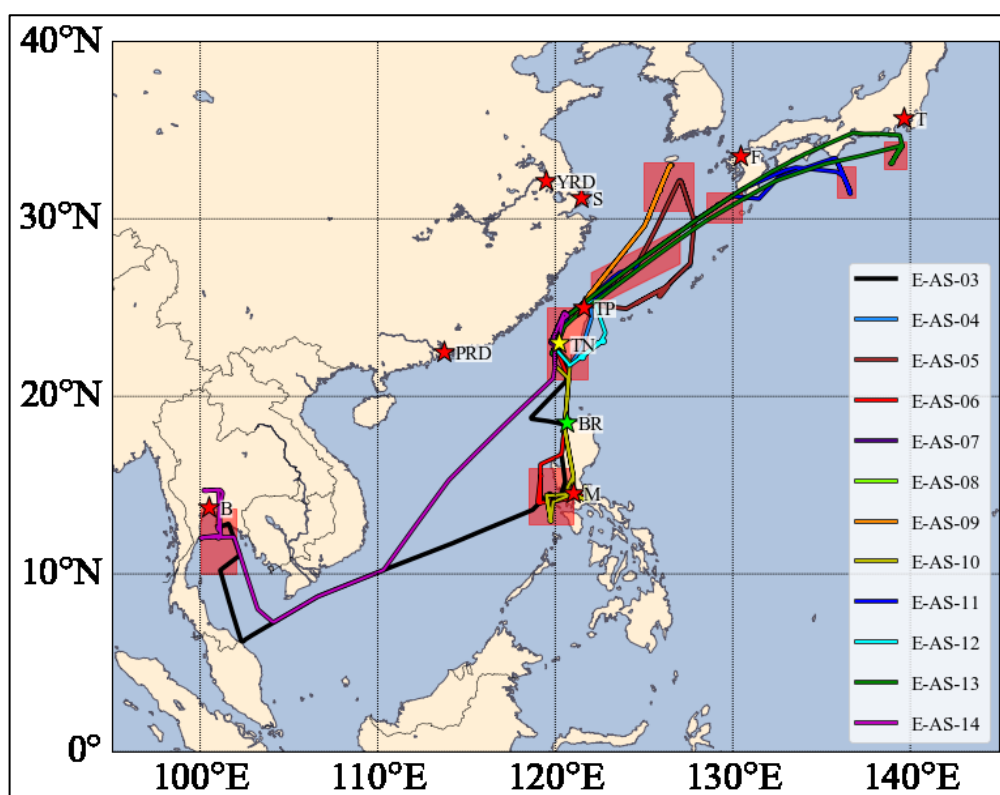

Figure 3.23: HALO flight tracks during the EMeRGe campaign in Asia. The red shaded areas show the regions with target MPC outflow signatures calculated using the HYPLIT dispersion model. Distinctive target MPC locations/regions are marked with red stars, B: Bangkok, M: Manila, TP: Taipei, PRD: Pearl River Delta region, YRD: Yangtze River Delta region, S: Shanghai, F: Fukuoka, T: Tokyo. The position of the HALO base at Tainan (TN) and the **T**otal **C**arbon **C**olumn **O**bserving **N**etwork (TCCON) station at Burgos (BR) are marked with yellow and green stars, respectively.

Table 3.11: Details of the HALO flights carried out in Asia during EMeRGe. FR: flight route, OP: Oberpfaffenhofen, YRD: Yangtze River Delta, PRD: Pearl River Delta, TCCON: Total Carbon Column Observing Network.

Flight Number	Day/ Month	Start/End time (UTC)	MPC emission and transport targets	Other mission objectives
E-AS-01	10/03	07:38/15:32	Rome and Athens	Transfer flight from OP to Abu Dhabi
E-AS-02	11/03	06:02/11:51	None	No permission for measurements; transit flight from Abu Dhabi to Pattaya over India
E-AS-03	12/03	04:05/11:19	Bangkok and Manila	Transfer flight from Pattaya to Tainan. Overflight at TCCON station at Burgos
E-AS-04	17/03	01:09/09:45	Outflow from China over East China Sea	None
E-AS-05	19/03	08:24/08:28	Outflow from Shanghai and YRD region	Impact of outflow from YRD on Taipei in the afternoon
E-AS-06	19 – 20/03	23:47/06:37	Manila	Tracer experiment
E-AS-07	22/03	30:46/09:31	Taipei, Tainan and outflow from China over the East China Sea	Tracer experiment
E-AS-08	24/03	01:00/09:52	Outflow from China over the East China Sea and Taiwan	None
E-AS-09	26/03	00:24/09:26	Outflow from China over the East China Sea and Taiwan	None
E-AS-10	27 – 28/03	23:53/08:32	Manila and PRD region	Tracer experiment
E-AS-11	30/03	00:02/09:26	Outflow from YRD and Fukuoka	None
E-AS-12	03/04	00:25/06:25	Taipei and Tainan	Long transported biomass burning in higher altitudes
E-AS-13	04/04	00:26/09:24	Outflow from Japan	None
E-AS-14	07/04	01:02/08:42	Outflow from Laos, Cambodia, Vietnam, Thailand and Bangkok	Transfer flight from Tainan to Pattaya. Tracer experiment released from Nanjing China.
E-AS-15	08/04	04:16/11:14	None	No permission for measurements; transfer flight from Pattaya to Abu Dhabi over India
E-AS-16	09/04	06:00/14:44	Saudi Arabia, Nile Valley, Cairo, Crete, Greece and Munich	Transfer flight from Abu Dhabi to OP.

3.2.7 PeRCEAS Operating Conditions During EMeRGe in Asia

During the IOP of EMeRGe in Asia, PeRCEAS successfully measured RO_2^* in 13 out of the 14 measurement flights. During the preparation of the mission flight E-AS-04, one of the magnetic valves in the inlet broke down and could not be fixed before the flight. Due to this mechanical problem, the RO_2^* measurements from this flight are not of sufficient quality for the analysis.

DUALER II with FR as Detector I and FH as Detector II was deployed during this IOP. For the measurements done up to 6000 m, 350 and 300 hPa inlet pressure were used. To keep the $\Delta P > 100$ hPa, all the measurements above 6000 m were made with 200 hPa inlet pressure. 500 ml min^{-1} sample flow and 9 % reagent gas CO were used in all the measurement flights. Unlike EMeRGe in Europe, a constant NO number concentration of 3.28×10^{14} molecules cm^{-3} (45 µmole $mole^{-1}$ at 300 hPa and 298 K) was used throughout the mission. The corresponding eCL determined from laboratory calibrations are given in Table 3.12. The eCL_{mix} is used for the retrieval of RO_2^* from ΔNO_2 measurements. The measurement conditions used in this study lead to different sensitivities for HO_2 and RO_2 (section 3.1.2) with $\alpha = 0.40$. If the ratio of $HO_2:RO_2$ changes to 3:1, then the RO_2^* results in a 16 % overestimation of $HO_2 + RO_2$. Similarly, a $HO_2:RO_2$ ratio of 1:3 results in a 16 % underestimation. Considering the 16 % uncertainty from the laboratory calibrations, the maximum uncertainty of RO_2^* is 32 % for the $HO_2:RO_2$ ratio between 3:1 and 1:3 for the measurements during EMeRGe in Asia. The uncertainty coming from the variation of the $HO_2:RO_2$ ratio is not included in the error calculation of the RO_2^* measurements but has been explicitly discussed during the analysis in sections 4.1.3, 4.1.5, 4.1.6, and 4.1.7.

Table 3.12: eCL obtained experimentally for the measurement conditions during EMeRGe in Asia. eCL_{HO_2} and eCL_{mix} are determined for pure HO_2 and a 1:1 mixture of $HO_2:CH_3O_2$, respectively. The number concentration of NO is calculated at 298 K.

Inlet pressure (hPa)	NO mixing ratio (µmole $mole^{-1}$)	[NO] (molecules cm^{-3})	Reactor 1		Reactor 2	
			eCL_{HO_2}	eCL_{mix}	eCL_{HO_2}	eCL_{mix}
350	39	3.28×10^{14}	48	32	48	33
300	45	3.28×10^{14}	37	29	37	29
200	60	3.28×10^{14}	30	23	30	23

Figure 3.24 shows the ambient $[H_2O]$ versus $[H_2O]$ inside the DUALER for the measurements during EMeRGe in Asia. The reduced $[H_2O]$ in the inlet due to the low pressure in the inlet and the [NO] reagent gas used makes the eCL independent of inlet $[H_2O]$ during EMeRGe in Asia.

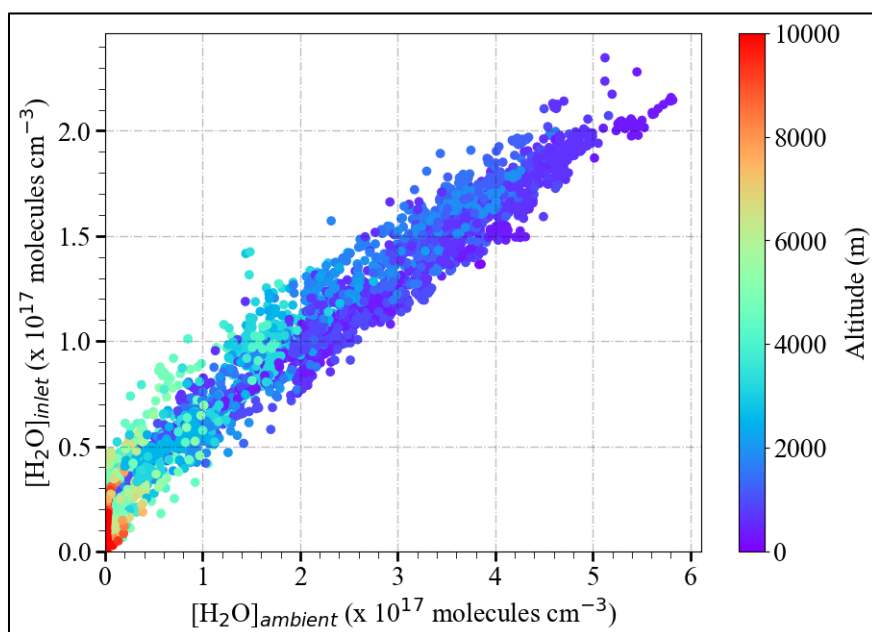Figure 3.24: Ambient [H$_2$O] versus [H$_2$O] measured in DUALER during EMeRGe in Asia colour coded with altitude.

<div style="text-align: right;">

4

</div>

<div style="text-align: center;">

Results and Discussion

</div>

This chapter presents the RO_2^* measurements ($RO_{2\ m}^*$) and the analysis of their sources and sinks using the knowledge of photochemistry in the air masses measured during the OMO Asia and EMeRGe campaigns. The chapter begins with the description of the $RO_{2\ m}^*$ from EMeRGe in Asia campaign. The $RO_{2\ m}^*$ and their analysis from OMO Asia are presented at the end of the chapter.

4.1 Tropospheric Fast Photochemistry During EMeRGe

The relation of $RO_{2\ m}^*$ with precursor mixing ratios and photolysis frequencies is investigated in this section to understand the main chemical mechanisms controlling the RO_2^* concentrations in the air masses measured during the EMeRGe IOPs. Subsequently, the $RO_{2\ m}^*$ is compared with RO_2^* calculated ($RO_{2\ c}^*$), assuming a **p**hotostationary **s**teady-**s**tate (PSS) for RO_2^*. A detailed analysis of the outflows from Manila, Taiwan, and the Yangtze River Delta region are presented to illustrate the main physical and chemical mechanisms involved in RO_2^* formation and losses under different chemical and physical regimes. Then the upper limit for [OH] and O_3 production rate (P_{O_3}) expected during EMeRGe in Asia are also calculated from $RO_{2\ m}^*$. In addition, a comparison between EMeRGe in Asia and Europe is made to identify the differences and similarities in RO_2^* production and losses between both case studies.

4.1.1 Airborne RO_2^* Measurements

RO_2^* mixing ratios up to 100 pmole mole^{-1} were measured during EMeRGe IOP in Asia (see 3.2.6). Figure 4.1 shows the $RO_{2\ m}^*$ as a function of altitude and latitude. Typically, the RO_2^* mixing ratios observed above 7000 m were ≤ 25 pmole mole^{-1}, which agrees with results from previous airborne campaigns from different parts of the world (Faloona et al., 2000; Tan et al., 2001; Green et al., 2002; Cantrell et al., 2003a; Ren et al., 2008, 2012; Martinez et al., 2010; Commane et al., 2010; Stone et al., 2011; Hornbrook et al. 2011). The highest values were observed below 4000 m between 9° to 11° East and 14° to 16° east. These measurements were made in the outflows of Bangkok and Manila over the sea. In previous airborne campaigns in different parts of the world, $HO_2 + RO_2 > 80$ pmole mole^{-1} (Cantrell et al., 2003a, Hornbrook et al., 2011) were reported in PBL. In other studies where only HO_2 was measured, HO_2 up to 60 pmole mole^{-1} were reported during the measurements below 5000 m (Tan et al., 2001; Ren et al., 2008, 2012; Martinez et al., 2010; Commane et al., 2010; Stone et al., 2011; Hornbrook et al. 2011). Since the physical conditions and chemical compositions during these campaigns and EMeRGe are different more comparison is not feasible.
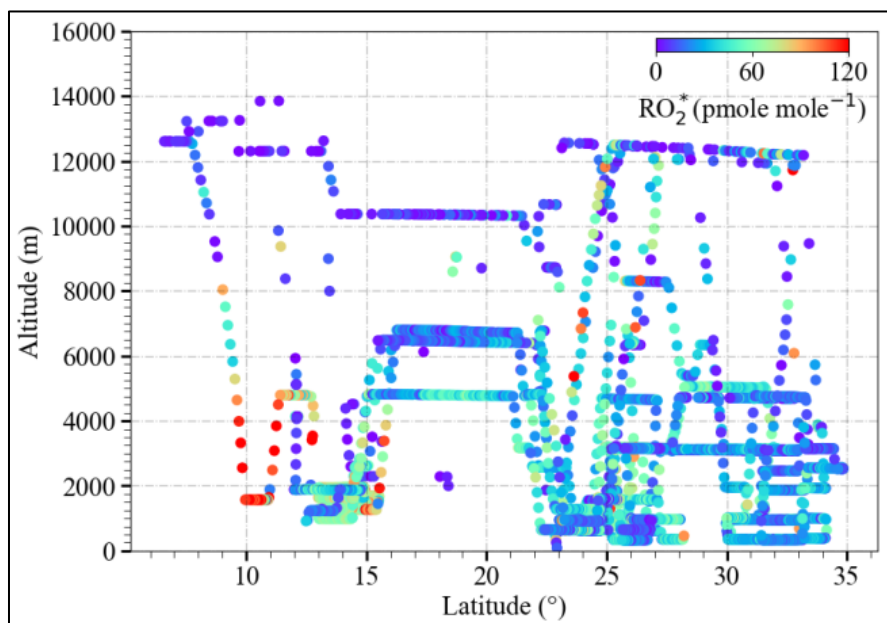
Figure 4.1: RO_2^* mixing ratios measured during EMeRGe in Asia as a function of latitude and altitude.

Figure 4.2 shows the $RO_{2\ m}^*$ from E-AS-06, E-AS-08, and E-AS-12 over the flight tracks as exemplary results of the flight routes carried out during the IOP. Similar plots for the rest of the flights from EMeRGe in Asia are given in appendix A-I. Higher RO_2^* mixing ratios were typically observed at altitudes below 2000 m close to the target MPCs. This indicates the effect of the MPC outflows on the regional photochemistry. A more detailed analysis of the measurements from these flights is given in sections 4.1.5 to 4.1.7.

The origin and composition of the air sampled during the eleven flights over Southeast Asia considered in this study were very heterogeneous. The air masses measured were influenced by emissions from MCPs and their surroundings, emissions from the forest, dust events, and sometimes biomass burning. The variations in RO_2^* depend on insolation and chemical composition, particularly on the abundance of precursors. Provided that insolation conditions and a sufficient number of key participating precursors are comparable, the RO_2^* production should be independent of the air mass origin due to the fast photochemistry involved. Thus, the RO_2^* variability and its production rates through precursor photolysis give an insight into the photochemical activity of the air masses probed. Figure 4.3 shows the RO_2^* vertical profiles averaged for the EMeRGe flights over Southeast Asia in 500 m altitude bins. The error bars are standard errors (i.e. $\pm$ 1σ standard deviation of the frequency distribution of measured RO_2^* in an altitude bin). As the altitude of the flights was mostly kept below 5000 m during the campaign, the vertical profiles are somewhat biased. Furthermore, they result from averaging different flights and are intended to merely indicate the variability of the composition of the measured air masses during the campaign.
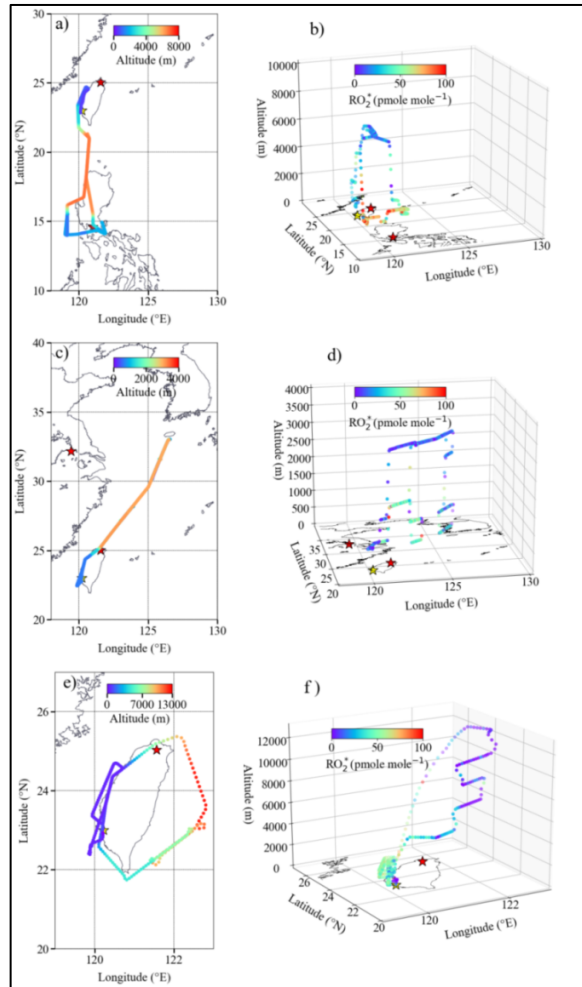
Figure 4.2: Examples of $RO_{2\,m}^{*}$ obtained in the EMeRGe campaign in Asia. The left panel shows the flight tracks colour-coded with flight altitude, and the right panel shows the 3D view of the corresponding flight track colour-coded with RO_2^{*} mixing ratios. Plot a) and b) show the E-AS-06 flight; plot c) and d) show the E-AS-08 flight; plot e) and f) show the E-AS-12 flight. Red stars indicate the targets MPC Taipei, Manila, and Yangtze River Delta, and the yellow star indicates the HALO base in Tainan.
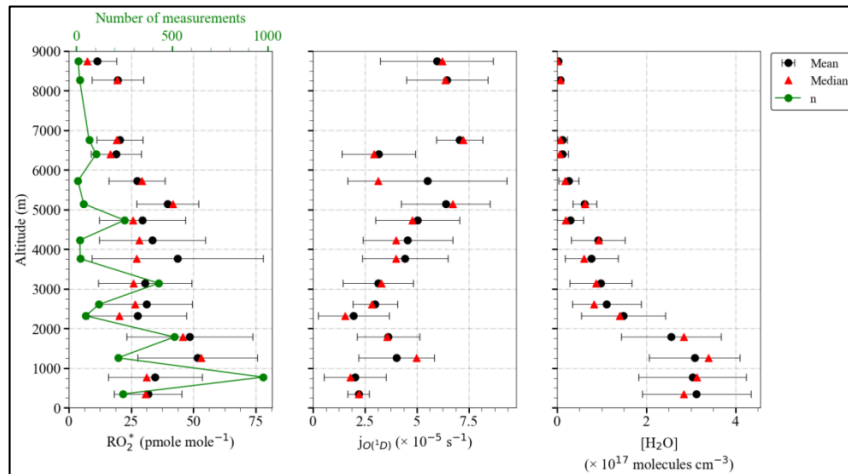
Figure 4.3: Averaged vertical profiles of a) RO_2^{*}, b) $j_{O(^1D)}$ and c) $[H_2O]$ observations during EMeRGe over Southeast Asia. The measurements are binned over 500 m altitude. The error bars are standard errors of each bin. Median values and the number of individual measurements of each bin are additionally plotted.

Most of the EMeRGe measurements below 3000 m were carried out in the outflow of MPCs which are expected to contain a signi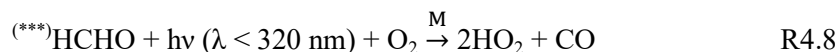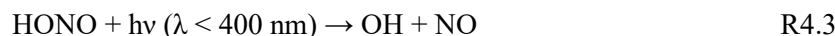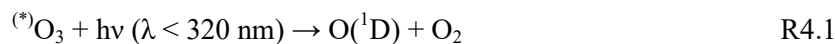ficant amount of RO_2^* precursors. As expected, the H_2O content in the air masses decreases steadily with the altitude. The slight increases in H_2O at 4250 m and 6250 m bins are associated with measurements under stormy conditions. The photolysis frequencies (j values) generally increase with altitude as expected but show high variability due to the frequent cloudy conditions encountered during the measurements. The variations in photolysis frequencies and the RO_2^* precursors concentrations make the interpretation of the averaged RO_2^* vertical profiles challenging. The investigation of the underlying photochemistry requires a joint analysis of the $RO_2^*{}_m$ and the RO_2^* production rates.

4.1.2 RO_2^* Production Rates

The production rate of the sum of OH and RO_2^* was calculated using onboard measurements of their precursors and photolysis frequencies to identify their primary sources. For this, the $P_{OH+HO_2+\Sigma RO_2}$ can be calculated by considering the following reactions:
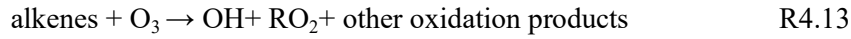
$^{(*)}O_3 + h\nu\ (\lambda < 320\ nm) \rightarrow O(^1D) + O_2$ R4.1

$O(^1D) + H_2O \rightarrow 2OH$ R4.2a

$^{(**)}O(^1D) + O_2 \rightarrow O(^3P) + O_2$ R4.2b

$^{(**)}O(^1D) + N_2 \rightarrow O(^3P) + N_2$ R4.2c

$HONO + h\nu\ (\lambda < 400\ nm) \rightarrow OH + NO$ R4.3

$H_2O_2 + h\nu\ (\lambda < 320\ nm) \rightarrow 2OH$ R4.4

$OH + O_3 \rightarrow HO_2 + O_2$ R4.5

$OH + CO + O_2 \rightarrow HO_2 + CO_2$ R4.6

$OH + CH_4 + O_2 \rightarrow CH_3O_2 + H_2O$ R4.7

$^{(***)}HCHO + h\nu\ (\lambda < 320\ nm) + O_2 \xrightarrow{M} 2HO_2 + CO$ R4.8

$^{(****)}CH_3CHO + h\nu\ (\lambda < 320\ nm) + O_2 \xrightarrow{M} CH_3O_2 + HO_2 + CO$ R4.9
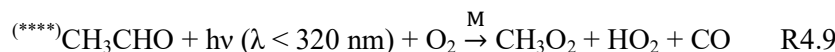
(*) The O_3 photolysis has a second channel, $O_3 + h\nu\ (\lambda < 320\ nm) \rightarrow O(^3P) + O_2$. Only the photolysis frequency for R4.1 is used in the calculation.

(**) Reactions R4.2b and R4.2c do not produce OH or RO_2^*.

(***) The HCHO photolysis has a second channel, $HCHO + h\nu\ (\lambda < 320\ nm) \rightarrow H_2 + CO$. Only the photolysis frequency for R4.8 is used in the calculation.

(****) The CH_3CHO photolysis has a second channel, $CH_3CHO + h\nu\ (\lambda < 320\ nm) \rightarrow CH_4 + CO$. Only the photolysis frequency for R4.9 is used in the calculation.

$$^{(*****)}CH_3C(O)CH_3 + h\nu + 2O_2 \xrightarrow{M} CH_3C(O)O_2 + CH_3O_2 \qquad \text{R4.10a}$$

$$CH_3C(O)CH_3 + h\nu + 2O_2 \xrightarrow{M} 2CH_3O_2 + CO \qquad \text{R4.10b}$$

$$CHOCHO + h\nu + 2O_2 \xrightarrow{M} 2HO_2 + 2CO \qquad \text{R4.11}$$

$$VOCs + OH \rightarrow OH + HO_2 + RO_2 \text{ and other oxidation products} \qquad \text{R4.12}$$

$$alkenes + O_3 \rightarrow OH + RO_2 + \text{ other oxidation products} \qquad \text{R4.13}$$
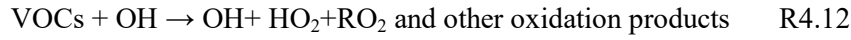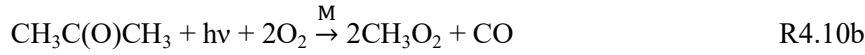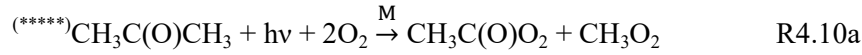
If OH produced from reactions R4.2a, R4.3, and R4.4 are assumed to be converted entirely to RO_2^* through reactions R4.5, R4.6, R4.7, and R4.12, then, based on the above reactions, $P_{OH+HO_2+\Sigma RO_2}$ is expressed as:

$$P_{OH+HO_2+\Sigma RO_2} =$$
$$2j_{4.1}[O_3] \frac{k_{4.2a}[H_2O]}{k_{4.2a}[H_2O]+k_{4.2b}[O_2]+k_{4.2c}[N_2]} + j_{4.3}[HONO] + 2j_{4.4}[H_2O_2] + 2\sum_i j_i [OVOC_i] +$$
$$\sum k_{O_3+alkenes}[O_3][alkenes] \qquad \text{Eq. 4.1}$$

As stated in section 2.5, HO_2 and RO_2 are not speciated but retrieved as RO_2^* by the PeRCEAS instrument. To a good approximation, this is the total sum of peroxy radicals that convert NO to NO_2. Hence, Eq. 4.1 is accordingly modified to calculate the RO_2^* production rate ($P_{RO_2^*}$) using the onboard measurements during EMeRGe. Based on the results from previous airborne campaigns (Tan et al., 2001 and Cantrell et al., 2003b), the contribution from the photolysis of H_2O_2 and other peroxides are expected to be negligible for the measurement conditions in EMeRGe. VOC photolysis has been assumed to dominate as a source of RO_2^* over the ozonolysis of alkenes. The most abundant and reactive OVOCs were considered as the surrogate for all VOC measurements. Thus:

$$P_{RO_2^*} = 2j_{4.1}[O_3] \frac{k_{4.2a}[H_2O]}{k_{4.2a}[H_2O]+k_{4.2b}[O_2]+k_{4.2c}[N_2]} + j_{4.3}[HONO] + 2j_{4.8}[HCHO] + 2j_{4.9}[CH_3CHO] +$$
$$2(j_{4.10a} + j_{4.10b})[CH_3COCH_3] + 2j_{4.11}[CHOCHO] \qquad \text{Eq. 4.2}$$

The HCHO, CHOCHO, and HONO measurements for the calculation of $P_{RO_2^*}$ are taken from the data provided by miniDOAS. The miniDOAS retrieves the **S**lant **C**olumn **D**ensity (SLD) of the target species towards the horizon at the flight altitude. The SLDs are then converted to mixing ratios using the corresponding **A**ir **M**ass **F**actor (AMF) and the total number concentration calculated at the flight altitude. During the mission flights E-AS-03, E-AS-07, E-AS-12, and E-AS-14, the miniDOAS instrument malfunctioned, and no measurements were available. Measurements from these four flights and all other data points with missing measurements of trace gases and photolysis frequencies used in Eq. 4.2 are excluded from the following analysis for consistency.

$^{(*****)}$To simplify the calculation, the $CH_3C(O)O_2$ produced is treated as a CH_3O_2 molecule in the calculation.

Figure 4.4 shows the variation of the fractional contribution of each RO_2^* precursor included in Eq. 4.2 with altitude. The data have been classified according to $P_{RO_2^*} < 0.06$ pmole mole^{-1} s^{-1} (4.4a), $0.06 < P_{RO_2^*} < 0.8$ pmole mole^{-1} s^{-1} (4.4b), and $P_{RO_2^*} > 0.8$ pmole mole^{-1} s^{-1} (4.4c). For 87 % of the measurements applies $0.06 < P_{RO_2^*} < 0.8$ pmole mole^{-1} s^{-1} while the rest of the data are equally distributed in the other two $P_{RO_2^*}$ ranges. The data in each group were binned over 500 m always when available. The vertical variation of selected precursor mixing ratios and photolysis frequencies are detailed in Figures 4.5a to 4.5f.

$P_{RO_2^*} < 0.06$ pmole mole^{-1} s^{-1} is associated with measurements under cloudy conditions or towards the sunset with significantly lower photolysis frequencies. In this range, the highest contribution to the RO_2^* production (85 %) comes from the sum of HCHO, CHOCHO, and HONO photolysis. The contribution from the O_3 photolysis followed by the reaction with H_2O (R4.1 and R4.2a) is < 15 %.

In the range $0.06 < P_{RO_2^*} < 0.8$ pmole mole^{-1} s^{-1}, the highest contribution to the RO_2^* production (≥ 30 %) comes from the O_3 photolysis followed by the reaction with H_2O due to the high H_2O loading in the air masses probed during EMeRGe in Asia. Only in altitude bins with a number of measurements < 10, the O_3 photolysis contribution is less than 30 %. The HCHO, CHOCHO, and HONO photolysis contributions ranged from 15% to 30%, 10 to 20%, and 20% to 40%, respectively. The sum of these three sources exceeds the contribution from the O_3 photolysis in most of the altitude bins in the $0.06 < P_{RO_2^*} < 0.8$ pmole mole^{-1} s^{-1} range.
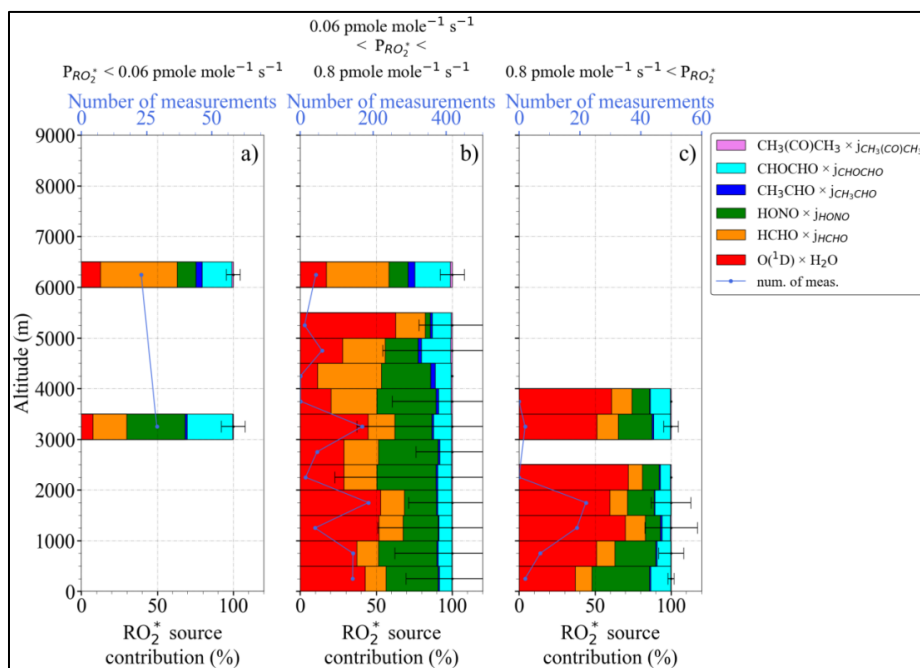

Figure 4.4: Variation of total $P_{RO_2^*}$ and fractional precursor contributions with altitude, as calculated by Eq. 4.2, for a) $P_{RO_2^*} < 0.06$ pmole mole^{-1} s^{-1}, b) 0.06 pmole mole^{-1} s^{-1} $< P_{RO_2^*} < 0.8$ pmole mole^{-1} s^{-1}, and c) $P_{RO_2^*} > 0.8$ pmole mole^{-1} s^{-1}.

As can be seen in Figure 4.4, the $P_{RO_2^*} > 0.8$ pmole mole^{-1} s^{-1} is mainly calculated in air masses measured below 3000 m with HCHO > 600 pmole mole^{-1}, indicating high precursor mixing ratios and good insolation with $j_{O(^1D)} > 3 \times 10^{-5}$ s^{-1}. These measurements were done in pollution plumes. The O_3 photolysis gives the major contribution to the RO_2^* production (≥ 50 %) in this $P_{RO_2^*}$ range. The contribution from HONO photolysis is between 10 % and 40 %. In contrast to other $P_{RO_2^*}$ ranges, the HCHO and CHOCHO photolysis contribute < 15 %. The contribution of CH$_3$CHO and CH$_3$C(O)CH$_3$ photolysis in all the $P_{RO_2^*}$ ranges are < 5 % and negligibly small.
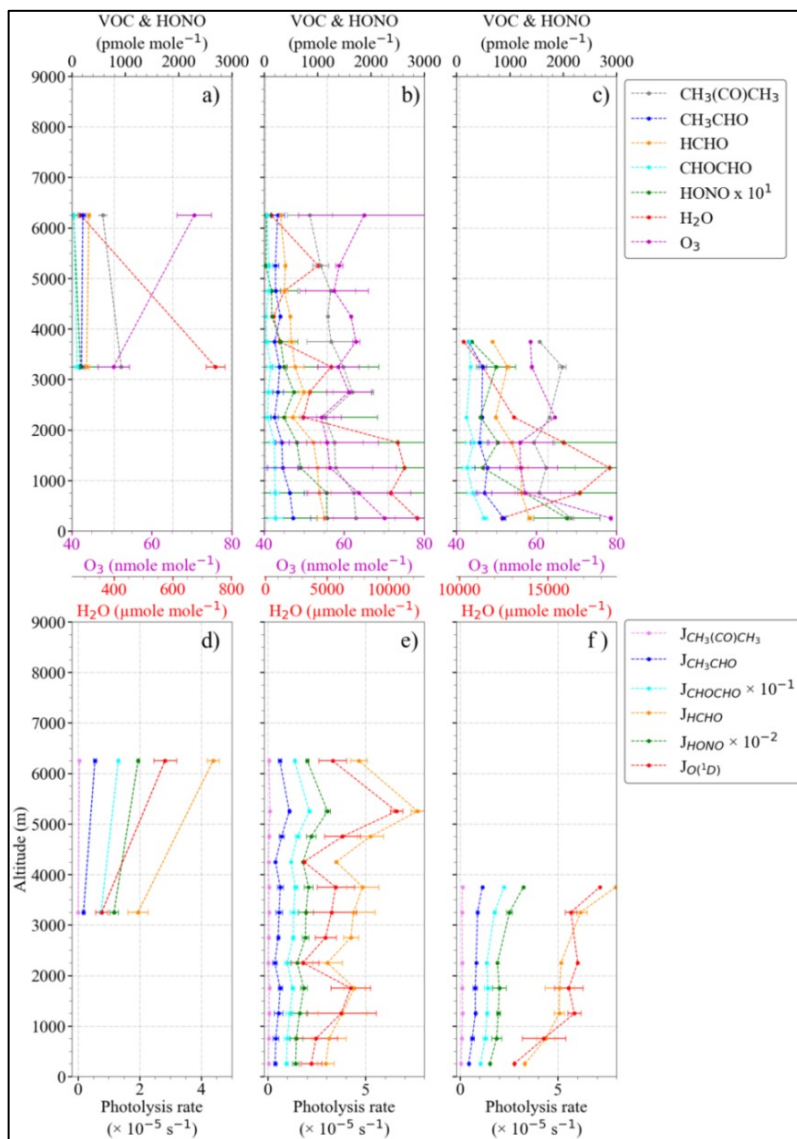
Figure 4.5: Vertical variation of: a) to c) precursor mixing ratios; d) to f) photolysis frequencies for the corresponding $P_{RO_2^*}$ bin shown in Figure 4.4. Note the change in the scale of [H$_2$O] for a) b) and c)

In previous airborne campaigns, Tan et al. (2001) and Cantrell et al. (2003b) reported a reduction of the fractional contribution of the reaction of O(^{1}D) with H$_2$O as the $P_{RO_2^*}$ value decreased. At very low $P_{RO_2^*}$ values (< 0.03 pmole mole^{-1} s^{-1}), the sum of all other production terms exceeded the fraction from the O(^{1}D) + H$_2$O term. Then H$_2$O$_2$ and VOCs photolysis dominated in $P_{RO_2^*}$. In the case

of the EMeRGe measurements over Southeast Asia, only 7 % of $P_{RO_2^*}$ remains below 0.06 pmole mole^{-1} s^{-1} where the fraction from the $O(^1D) + H_2O$ term < 15 %. Hence, the H_2O_2 and VOC photolysis not considered in Eq. 4.2 are expected to have a minor contribution to the production of RO_2^*.

The relation of the $RO_{2\ m}^*$ with $P_{RO_2^*}$ and the amount of precursors has been further investigated in Figure 4.6. Figure 4.6a shows the averaged vertical profile of all measured RO_2^* mixing ratios, colour-coded with the calculated $P_{RO_2^*}$. Small circles show the 1-minute measurements binned with $P_{RO_2^*}$ up to 0.8 pmole mole^{-1} s^{-1} in 0.1 pmole mole^{-1} s^{-1} intervals. All the values above 0.8 pmole mole^{-1} s^{-1} were binned to 0.8 pmole mole^{-1} s^{-1}. Larger circles in the figure result from further binning the small circles over 500 m altitude steps. The error bars are the standard errors of each altitude bin. For the sake of representativeness and comparability, the number of measurements in each altitude bin are shown in figure 4.6b. Higher RO_2^* were observed below 3000 m; both $P_{RO_2^*}$ and RO_2^* starts to decrease with altitude, as expected. The latter is related to the decrease in H_2O and other RO_2^* precursor concentrations with altitude. In previous airborne campaigns in various parts of the world, RO_2^* vertical distributions showed a local maximum between 1500 and 4000 m, as reported by Tan et al. (2001), Cantrell et al. (2003a, 2003b), Ren et al. (2008), Andrés-Hernández et al. (2009), Commane et al. (2010), Martinez et al. (2010), and Stone et al. (2011). For the measurements over Southeast Asia during EMeRGe, this local maximum is more evident for measurements with $P_{RO_2^*} \geq$ 0.5 pmole mole^{-1} s^{-1}.
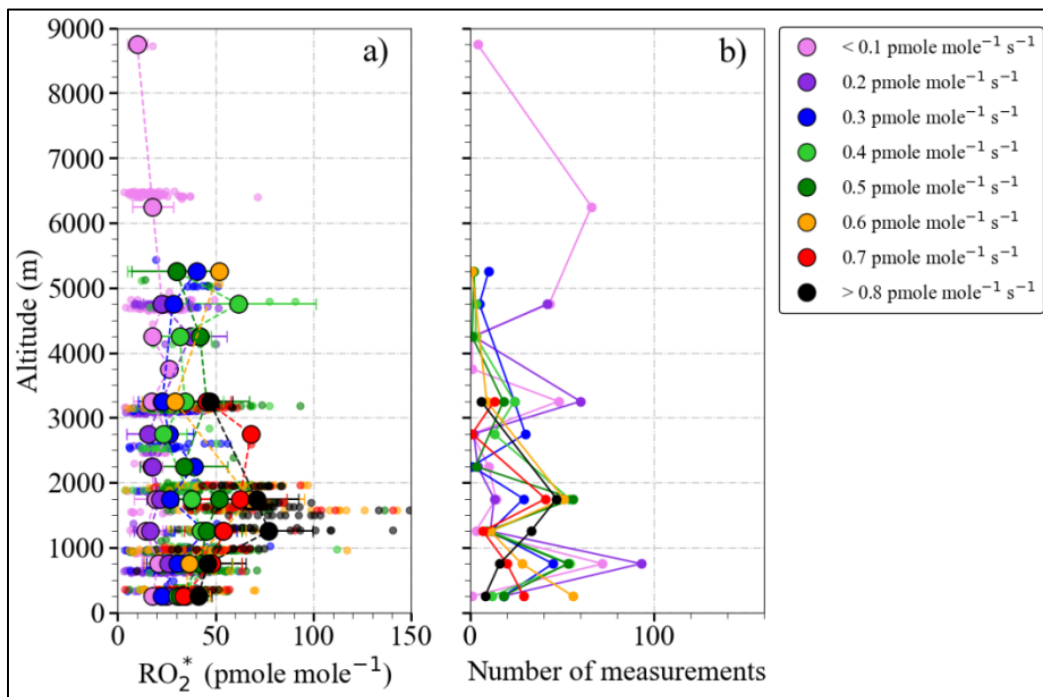

Figure 4.6: a) Vertical averaged distribution of $RO_{2\ m}^*$ colour-coded with $P_{RO_2^*}$, b) the number of measurements in each altitude bin. The small circles are 1-minute individual measurements binned with $P_{RO_2^*}$ values in 0.1 pmole mole^{-1} s^{-1} intervals. Larger circles result from a further binning over 500 m altitude.

4.1.3 PSS Approximation

The relation between $RO_2^*{}_m$ and $P_{RO_2^*}$ is further investigated to identify the dominant RO_2^* loss process in the air masses investigated. Under most ambient conditions in the troposphere, RO_2^* are short-lived, and RO_2^* reactions dominate over the transport. Consequently, pseudo-steady-state conditions prevail, and the RO_2^* production and loss rates are balanced. i.e.

$$P_{RO_2^*} = D_{RO_2^*} \qquad \text{Eq. 4.3}$$

If the interconversion reactions between OH and RO_2^* cancel out in the balance and the OH – RO_2^* interconversion reactions dominate over the OH – NO_x reactions, then the total sum of OH + HO_2 + ΣRO_2, which to a good approximation is the RO_2^* measured by PeRCEAS, can be calculated by solving Eq. 4.3.

If only $RO_2^* - RO_2^*$ reactions are considered as the dominant loss processes, then Eq. 4.3 leads to Eq. 4.4.

$$2j_{4.1}[O_3]\frac{k_{4.2a}[H_2O]}{k_{4.2a}[H_2O]+k_{4.2b}[O_2]+k_{4.2c}[N_2]} + j_{4.3}[HONO] + 2(j_{4.10a} + j_{4.10b})[CH_3COCH_3] +$$
$$2j_{4.8}[HCHO] + 2j_{4.9}[CH_3CHO] + 2j_{4.11}[CHOCHO] = 2k_{RO_2^*}[RO_2^*]^2 \qquad \text{Eq. 4.4}$$

where $k_{RO_2^*}$ represents an effective RO_2^* self-reaction rate coefficient.

Consequently, the RO_2^* mixing ratios are expected to correlate with the square root of the $P_{RO_2^*}$ calculated. Figure 4.7 shows the relationship between the $RO_2^*{}_m$ and $\sqrt[2]{P_{RO_2^*}}$. The $RO_2^*{}_m$ and $\sqrt[2]{P_{RO_2^*}}$ are correlated and increase with the photolysis frequency of O_3 $(j_{O(^1D)})$. However, the weak correlation observed indicates the presence of other dominant loss processes and/or missing production terms in the $P_{RO_2^*}$ calculation. Apart from this, $RO_2^*{}_m$ versus $\sqrt[2]{P_{RO_2^*}}$ assumes a constant value for the effective RO_2^* self-reaction rate constant, $k_{RO_2^*}$ in Eq. 4.4, which cannot capture changes related to changes in the HO_2 to RO_2 ratio in the air mass.

The measurements over the Gulf of Thailand close to Bangkok and the South China Sea close to Manila were made in a polluted air mass with $j_{O(^1D)} > 5 \times 10^{-5}$. This is also reflected in the higher $P_{RO_2^*}$ and RO_2^* values observed around 15°N (figure 4.7b). The low $RO_2^*{}_m$ and $\sqrt[2]{P_{RO_2^*}}$ with $j_{O(^1D)} > 5 \times 10^{-5}$ corresponds to measures done at altitudes above 7000 m with low RO_2^* precursor concentration.
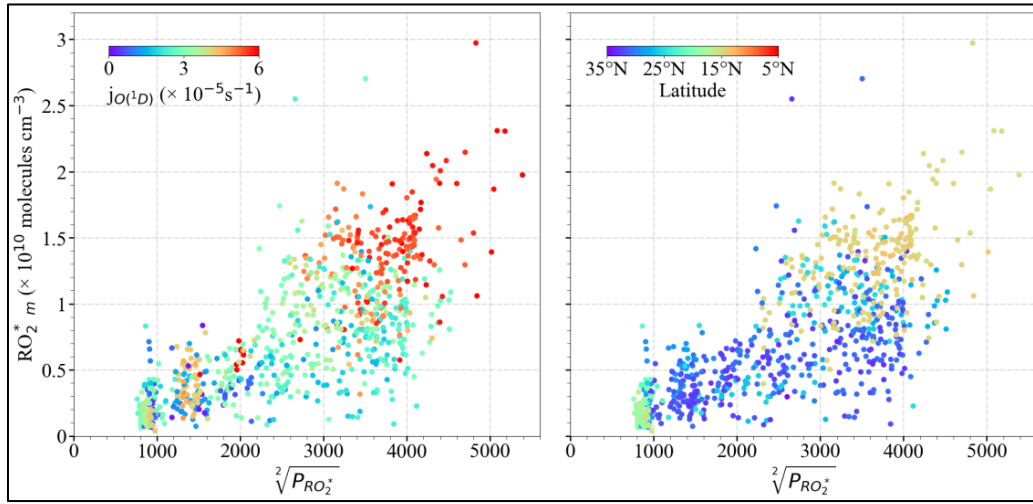
Figure 4.7: $RO_2{}^*{}_m$ vs $\sqrt[2]{P_{RO_2^*}}$ colour-coded with: a) $j_{O(^1D)}$ and b) latitude

$RO_2{}^*$ losses during the IOP were further investigated by considering: i) $RO_2{}^* - RO_2{}^*$, ii) $OH - NO_x$ and iii) HO_2 heterogeneous reactions.

i) $RO_2{}^* - RO_2{}^*$ reactions

Eq. 4.4 is a quadratic equation of $[RO_2^*]$ in the form

$$ax^2 + c = 0 \qquad\qquad \text{Eq. 4.5}$$

where $a = -2k_{RO_2^*}$ and $c = P_{RO_2^*}$.

The solution of Eq. 4.4 is given by

$$[RO_2^*]_c = \sqrt[2]{P_{RO_2^*} \big/ 2k_{RO_2^*}} \qquad\qquad \text{Eq. 4.6}$$

The second solution gives negative values for $[RO_2{}^*]$, therefore has no physical meaning. As a first approach, if the $RO_2{}^*$ is assumed to consist only of HO_2, i.e. $RO_2{}^* = HO_2$, then $k_{RO_2^*} \approx k_{HO_2+HO_2}$. The $k_{HO_2+HO_2}$ has a pressure independent bimolecular channel and a pressure-dependent termolecular channel. Both these channels have a dependence on ambient H_2O concentration due to the formation of weakly-bonded and reactive $HO_2 \cdot H_2O$ complexes (Hochanadel et al., 1972, Hamilton, 1975, Hamilton and Lii, 1977, Cox and Burrows, 1979, DeMore, 1979, Lii et al., 1981, Sander et al., 1982, Andersson et al., 1988, Stone and Rowley, 2005, English et al., 2008, Tang et al., 2010, and Burkholder et al., 2019). Therefore, the overall rate coefficient is the sum of the bimolecular and termolecular components corrected for water dependency. i.e.,

$$k_{HO_2+HO_2} = (1.4 \times 10^{-12} + 4.6 \times 10^{-32} \times [M])[1 + 1.4 \times 10^{-21}\,[H_2O]\,e^{(2200/T)}] \quad \text{Eq. 4.7}$$

where M is the total number of molecules.

Figure 4.8 shows the 1-minute $RO_2{}^*{}_m$ (small circles) and the average of the binned values over 10 pmole mole^{-1} $RO_2{}^*$ intervals (large circles) versus the calculated $RO_2{}^*$ ($RO_2{}^*{}_c$) using Eq. 4.6. The 1-

minute data are colour-coded with onboard measurement of NO. The error bars are the standard error of each bin. The slope of the linear regression (solid line) is 0.78 (R^2= 0.95), and the y-axis intercept is -9.69 pmole mole^{-1}.
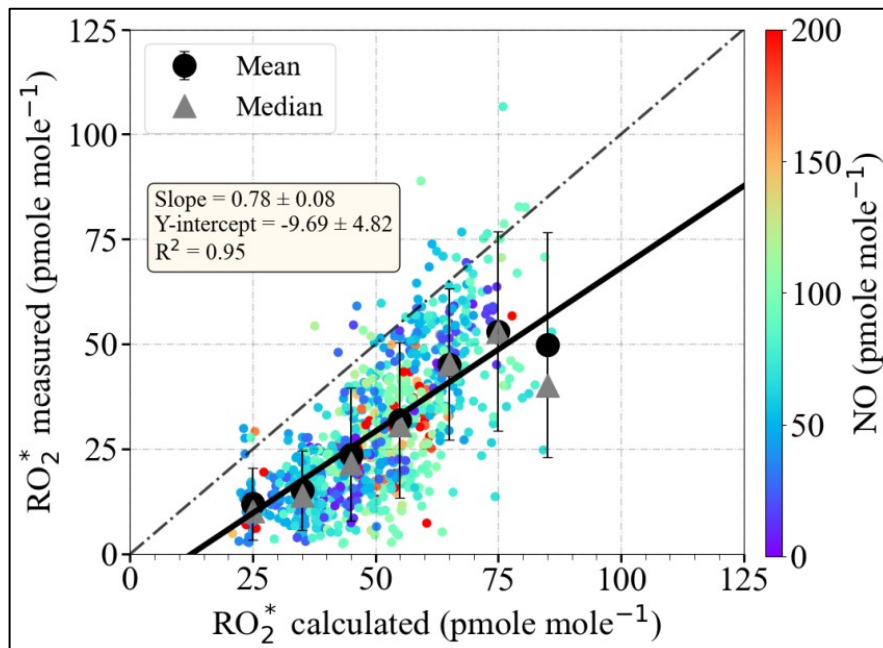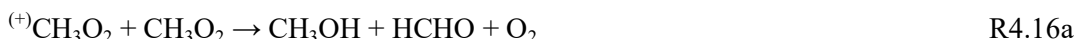

Figure 4.8: $RO_2^*{}_m$ versus $RO_2^*{}_c$ using Eq. 4.6. The HO_2:RO_2 ratio is assumed to be 1. The 1-minute (small circles), average (large circles) and median (triangles) of binned measurements over 10 pmole mole^{-1} $RO_2^*{}_c$ intervals are shown. The data are colour-coded with NO. The error bars indicate the standard error of each bin. The linear regression for the binned values (solid line) and the 1:1 relation (dashed line) are also depicted for reference.

Despite the approximations made in this analysis for the production and loss processes, the RO_2^* mixing ratios calculated from Eq. 4.6 are in reasonable agreement with the measurements. Overall $RO_2^*{}_m$, as indicated by the fit parameters, is overestimated. Overestimation indicates missing loss processes and/or overestimation of the production rate in Eq. 4.2. In addition, Eq. 4.4 and thereby Eq. 4.6 only considers the HO_2 self-reaction as a loss mechanism and neglects all other reactions resulting in the loss of RO_2^*. Therefore, Eq. 4.4 was modified to incorporate the following reactions in the calculation of RO_2^*:

a) OH, RO and RO_2^* loss reactions

$$HO_2 + HO_2 \rightarrow H_2O_2 + O_2 \hspace{3cm} \text{R4.14}$$

$$HO_2 + CH_3O_2 \rightarrow CH_3OOH + O_2 \hspace{2cm} \text{R4.15}$$

$$^{(+)}CH_3O_2 + CH_3O_2 \rightarrow CH_3OH + HCHO + O_2 \hspace{1cm} \text{R4.16a}$$

$$OH + HO_2 \rightarrow H_2O + O_2 \hspace{3cm} \text{R4.17}$$

$$^{(++)}OH + OH \xrightarrow{M} H_2O_2 \hspace{3cm} \text{R4.18a}$$

$$^{(++)}OH + OH \rightarrow H_2O + O(^3P) \hspace{2.5cm} \text{R4.18b}$$

(+) The CH_3O_2 self-reaction has a second channel (R4.16b) with a relative product yield, $\frac{k_{4.16b}}{k_{4.16a}} = (26.2 \pm 6.6)\, e^{(-1130 \pm 240)/T}$.

(++) The sum of $k_{4.18a}$ and $k_{4.18b}$ is taken as the effective rate coefficient for OH self-reaction.

$$OH + NO \xrightarrow{M} HONO \qquad\qquad\qquad\qquad\qquad R4.19$$

$$^{(+++)}OH + NO_2 \xrightarrow{M} HONO_2 \qquad (85\% \text{ to } 95\%) \qquad\qquad R4.20a$$

$$^{(+++)}OH + NO_2 \xrightarrow{M} HOONO \qquad (5\% \text{ to } 15\%) \qquad\qquad R4.20b$$

$$^{(++++)}HO_2 + NO_2 \xrightarrow{M} HO_2NO_2 \qquad\qquad\qquad\qquad R4.21$$

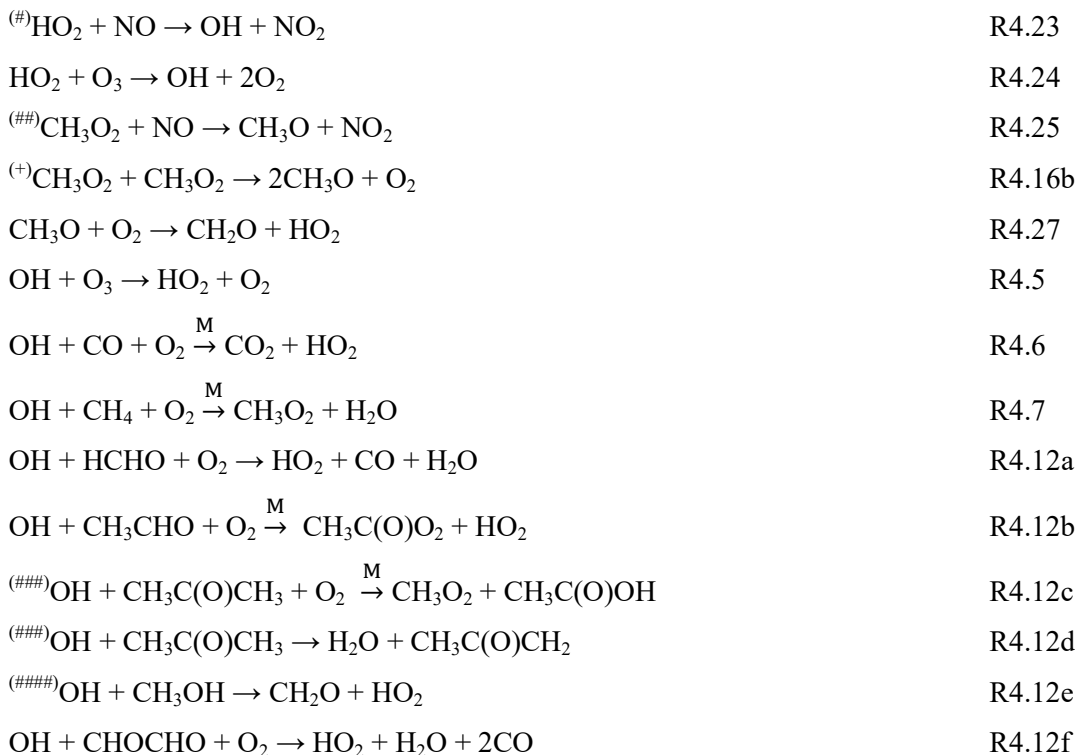$$^{(+++++)}CH_3O + NO \xrightarrow{M} CH_3ONO \qquad\qquad\qquad\qquad R4.22$$

b) OH, RO and RO_2^* interconversion reactions

$$^{(\#)}HO_2 + NO \rightarrow OH + NO_2 \qquad\qquad\qquad\qquad R4.23$$

$$HO_2 + O_3 \rightarrow OH + 2O_2 \qquad\qquad\qquad\qquad R4.24$$

$$^{(\#\#\#)}CH_3O_2 + NO \rightarrow CH_3O + NO_2 \qquad\qquad\qquad\qquad R4.25$$

$$^{(+)}CH_3O_2 + CH_3O_2 \rightarrow 2CH_3O + O_2 \qquad\qquad\qquad\qquad R4.16b$$

$$CH_3O + O_2 \rightarrow CH_2O + HO_2 \qquad\qquad\qquad\qquad R4.27$$

$$OH + O_3 \rightarrow HO_2 + O_2 \qquad\qquad\qquad\qquad R4.5$$

$$OH + CO + O_2 \xrightarrow{M} CO_2 + HO_2 \qquad\qquad\qquad\qquad R4.6$$

$$OH + CH_4 + O_2 \xrightarrow{M} CH_3O_2 + H_2O \qquad\qquad\qquad\qquad R4.7$$

$$OH + HCHO + O_2 \rightarrow HO_2 + CO + H_2O \qquad\qquad\qquad R4.12a$$

$$OH + CH_3CHO + O_2 \xrightarrow{M} CH_3C(O)O_2 + HO_2 \qquad\qquad R4.12b$$

$$^{(\#\#\#)}OH + CH_3C(O)CH_3 + O_2 \xrightarrow{M} CH_3O_2 + CH_3C(O)OH \qquad R4.12c$$

$$^{(\#\#\#)}OH + CH_3C(O)CH_3 \rightarrow H_2O + CH_3C(O)CH_2 \qquad\qquad R4.12d$$

$$^{(\#\#\#\#)}OH + CH_3OH \rightarrow CH_2O + HO_2 \qquad\qquad\qquad R4.12e$$

$$OH + CHOCHO + O_2 \rightarrow HO_2 + H_2O + 2CO \qquad\qquad R4.12f$$

To account for the variation of $k_{RO_2^*}$ due to changes in the HO_2 and the $\sum RO_2$ composition in the air mass, Eq. 4.4 is modified by introducing HO_2 to RO_2^* ratios, represented by δ ($\delta = [HO_2]/[RO_2^*]$). In addition, CH_3O_2 reactions were taken as a surrogate for all RO_2 reactions to reduce the complexity of the calculations. Thus, Eq. 4.4 is modified to become Eq. 4.8.

(+++) The rate coefficient of R4.20a is used as the effective rate coefficient for the $OH + NO_2$ reaction.

(++++)The HO_2NO_2 made from the $HO_2 + NO_2$ reaction is assumed to undergo photolysis to produce $HO_2 + NO_2$ or $OH + NO_3$. For the purpose of the present work, the $HO_2 + NO_2$ reaction is taken as a null cycle.

(+++++) The $CH_3O + NO$ has another set of products, i.e. $CH_3O + NO \rightarrow CH_2O + HNO$ with a rate coefficient $< 8 \times 10^{-12}$ $cm^3 molecules^{-1}s^{-1}$.

(#) The $HO_2 + NO$ reaction has another channel producing HNO_3. The probability of this channel is less than 1%.

(##) The $CH_3O_2 + NO$ reaction has another channel producing CH_3NO_2. The probability of this channel is less than 0.5%.

(###) For simplicity, only R4.12c is considered in the derivation to account for the $CH_3C(O)CH_3$ oxidation by OH.

(####) Reaction R4.12e has two channels that result in the same product under Earth's atmospheric conditions (Burkholder et al., 2019)

$$2j_{4.1}[O_3]\beta + j_{4.3}[HONO] + 2j_{4.8}[HCHO] + 2j_{4.9}[CH_3CHO] + 2j_{4.10a}[CH_3C(O)CH_3]$$
$$+ 2j_{4.10b}[CH_3C(O)CH_3] + 2j_{4.11}[CHOCHO]$$
$$= 2k_{4.15}\delta(1-\delta)[RO_2^*]^2 + 2k_{4.16}\left((1-\delta)[RO_2^*]\right)^2 + 2k_{4.14}(\delta[RO_2^*])^2$$

Eq. 4.8

where β is the effective yield of OH in the reaction of O(^{1}D) with H_2O and is given by:

$$\beta = \left(\frac{k_{4.2a}[H_2O]}{k_{4.2a}[H_2O] + k_{4.2b}[O_2] + k_{4.2c}[N_2]}\right)$$

By solving Eq. 4.8 for $[RO_2^*]$, Eq. 4.9, is obtained.

$$[RO_2^*]_c = \sqrt[2]{P_{RO_2^*}\Big/2k_{RO_2^*}}$$

Eq. 4.9

where

$$k_{RO_2^*} = (k_{4.15}\delta(1-\delta) + k_{4.16}(1-\delta)^2 + k_{4.14}\delta^2)$$

Eq. 4.10

and $P_{RO_2^*}$ is the RO_2^* production rate given by Eq. 4.2.

A detailed derivation of Eq. 4.8 and Eq. 4.10 are given in Appendix A-II.

Figure 4.9 shows the $RO_2{^*}_m$ versus $RO_2{^*}_c$ from Eq. 4.8 colour-coded with the NO mixing ratios. $RO_2{^*}_m$ and $RO_2{^*}_c$ are retrieved and calculated, respectively for $\delta = 1$, i.e., $RO_2^* = HO_2$ and $\delta = 0.5$, i.e., $HO_2 = RO_2$. The corresponding eCL given in Table 3.12 is used to convert the ΔNO_2 measurements from PeRCEAS to $RO_2{^*}_m$. The small circles represent 1-minute $RO_2{^*}_m$, while the large circles are the average of measurements binned over 10 pmole mole^{-1} $RO_2{^*}_c$ intervals.

Even though figure 4.9.b shows more spread than figure 4.9.a, the general agreement and the overestimation of $RO_2{^*}_m$ do not change significantly in both cases, as indicated by the fit parameters (Table 4.1). This is due to the increase in both $RO_2{^*}_m$ and $RO_2{^*}_c$ resulting from the reduction of eCL and $k_{RO_2^*}$, respectively while reducing the δ. This implies that the correlation between $RO_2{^*}_m$ and $RO_2{^*}_c$ is independent of HO_2 to RO_2 ratio under the assumptions made in this study. The general overestimation indicates missing loss processes and/or overestimation of production rates in Eq. 4.8.
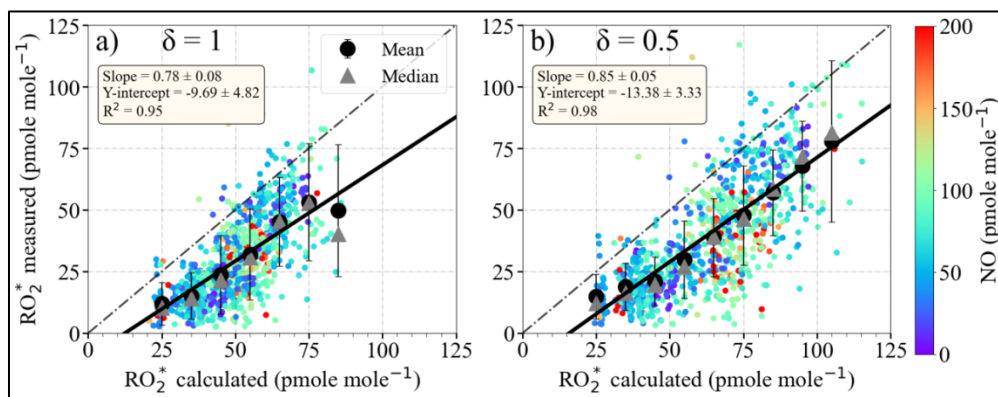
Figure 4.9: $RO_2^*{}_m$ versus $RO_2^*{}_c$ using Eq. 4.8 for a) $\delta = 1$, b) $\delta = 0.5$ ($\delta = [HO_2]/[RO_2^*]$) by assuming only OH, RO and $RO_2^* – RO_2^*$ loss reactions. The 1-minute (small circles) data, average (large circles) and median (triangles) of the binned measurements over 10 pmole mole^{-1} $RO_2^*{}_c$ intervals are shown. The error bars indicate the standard error of each bin. The linear regression for the binned values (solid line) and the 1:1 relation (dashed line) are also depicted for reference.

The CH_3O_2 self-reaction (R4.16) rate coefficient is an order of magnitude smaller than the HO_2 self-reaction (R4.14) and $HO_2 – CH_3O_2$ reaction rate coefficients expected in the troposphere. As a result, the loss of RO_2^* in Eq. 4.8 reduces as the fraction of CH_3O_2 increases, i.e. when the value of δ decreases. Due to the pressure and $[H_2O]$ dependencies of the HO_2 self-reaction, the effective RO_2^* self-reaction rate constant ($k_{RO_2^*}$) also depends on the pressure and $[H_2O]$. As the pressure and $[H_2O]$ decrease with altitude, $k_{RO_2^*}$ also decreases with altitude. The altitude dependency decreases with a decrease in HO_2 to RO_2 ratio as the RO_2 self-reaction and $HO_2 – RO_2$ reactions are bimolecular and have no dependency on $[H_2O]$. Figure 4.10 shows the variation of $k_{RO_2^*}$ with altitude and water number concentration measured during the EMeRGe flights over Southeast Asia for two HO_2 to CH_3O_2 ratios, i.e. for $\delta = 1$ and $\delta = 0.5$. For $\delta = 1$, $k_{RO_2^*}$ is higher than that for $\delta = 0.5$ at altitudes below 10000 m due to the higher HO_2 self-reaction rate coefficient. Above 10000 m, the $k_{RO_2^*}$ for $\delta = 1$ keeps on decreasing while that of $\delta = 0.5$ reaches the value of $HO_2 – RO_2$ reactions rate coefficient and stays constant. This causes the $k_{RO_2^*}$ for $\delta = 1$ to be smaller than that for $\delta = 0.5$ above 10000 m.
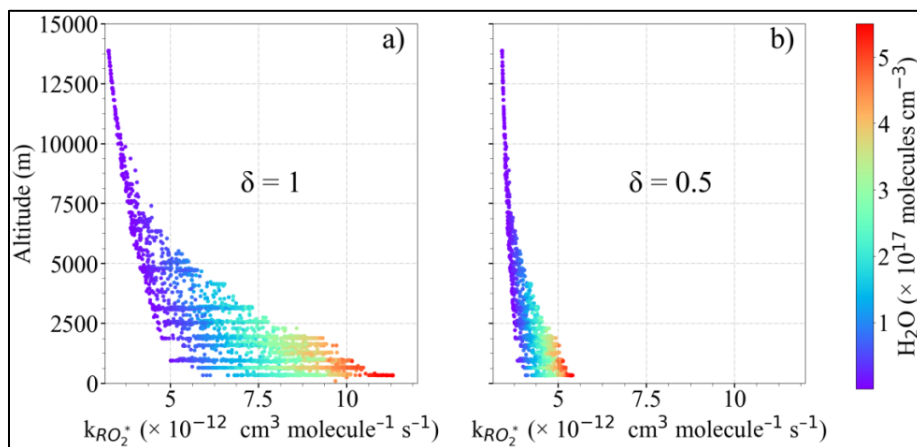

Figure 4.10: Vertical distribution of the effective RO_2^* self-reaction rate constant, $k_{RO_2^*}$, calculated using Eq. 4.10 for: a) $\delta = 1$ and b) $\delta = 0.5$ ($\delta = [HO_2]/[RO_2^*]$). The data are colour-coded with H_2O number concentration.

ii) OH – NO$_x$ reaction

The RO$_2^*{}_m$ in Figure 4.8 were calculated assuming the radical interconversion between OH, RO and RO$_2^*$ occurs without losses, and the limiting case of [OH] << [HO$_2$+ RO$_2$] with low [NO] and [NO$_2$]. Furthermore, VOC oxidation processes were not considered as a source of RO$_2^*$. The effect of these approximations was investigated by extending Eq. 4.8 with interconversion processes between OH, CH$_3$O and RO$_2^*$, and the OH and CH$_3$O reactions with NO$_x$ forming HONO, HNO$_3$, and organic nitrites. CH$_4$ and the OVOCs such as HCHO, CH$_3$CHO, CHOCHO, CH$_3$OH, and CH$_3$C(O)CH$_3$ measured onboard HALO were taken as surrogates for the dominant VOC RO$_2^*$ precursors through oxidation processes.

$$(2j_{4.1}[O_3]\beta + j_{4.3}[HONO])(1 - \rho) + 2j_{4.8}[HCHO] + 2j_{4.9}[CH_3CHO] + 2(j_{4.10a} + j_{4.10b})[CH_3C(O)CH_3] + 2j_{4.11}[CHOCHO] - \delta[RO_2^*](k_{4.23}[NO] + k_{4.24}[O_3])\rho -$$
$$\left(2k_{4.16b}((1 - \delta)[RO_2^*])^2 + k_{4.25}(1 - \delta)[RO_2^*][NO]\right)\left(\frac{k_{4.22}[NO]}{(k_{4.22}[NO] + k_{4.26}[O_2])}\right) - 2k_{4.15}\delta(1 - \delta)[RO_2^*]^2 -$$
$$2k_{16a}((1 - \delta)[RO_2^*])^2 - 2k_{4.14}(\delta[RO_2^*])^2 = 0 \qquad \text{Eq. 4.11}$$

ρ is the HONO and HNO$_3$ formation efficiency of the OH + NO$_x$ reaction and is given by

$$\rho = $$
$$\frac{k_{4.19}[NO] + k_{4.20}[NO_2]}{(k_{4.6}[CO] + k_{4.7}[CH_4] + k_{4.12a}[HCHO] + k_{4.12b}[CH_3CHO] + k_{4.12c}[CH_3C(O)CH_3] + k_{4.12d}[CH_3OH] + k_{4.12e}[CHOCHO] + k_{4.5}[O_3] + k_{4.19}[NO] + k_{4.20}[NO_2])}$$

$(1 - \rho)$ is the OH to RO$_2^*$ conversion efficiency. δ is the HO$_2$ to RO$_2^*$ ratio and varies between 1 and 0. The detailed derivation of Eq. 4.11 and the rate coefficients used are given in Appendix A-II. The solution of Eq. 4.11 is given by:

$$[RO_2^*] = \frac{-(-L_{RO_2^*}) - \sqrt[2]{(-L_{RO_2^*})^2 - 4(-2k_{RO_2^*})P_{RO_2^*}}}{2(-2k_{RO_2^*})} \qquad \text{Eq. 4.12}$$

where $k_{RO_2^*}$ is the effective RO$_2^*$ self-reaction rate coefficient, $L_{RO_2^*}$ is the linear RO$_2^*$ loss through HONO, HNO$_3$, and organic nitrites formation, and $P_{RO_2^*}$ is the RO$_2^*$ production rate given by Eq. 4.2.

$$k_{RO_2^*} = \left(\left(k_{4.16b}\left(\frac{k_{4.22}[NO]}{(k_{4.22}[NO] + k_{4.26}[O_2])}\right)\right) + k_{16a}\right)(1 - \delta)^2 + k_{4.15}\delta(1 - \delta) + k_{4.14}\delta^2\right) \qquad \text{Eq. 4.13}$$

$$L_{RO_2^*} = \left(\delta(k_{4.23}[NO] + k_{4.24}[O_3])\rho + \left(\frac{k_{4.22}[NO]}{(k_{4.22}[NO] + k_{4.26}[O_2])}\right)k_{4.25}(1 - \delta)[NO]\right) \qquad \text{Eq. 4.14}$$

When

$$k_{4.19}[NO] + k_{4.20}[NO_2] << k_{4.12a}[HCHO] + k_{4.12b}[CH_3CHO] + k_{4.12c}[CH_3C(O)CH_3] + k_{4.12d}[CH_3OH] + k_{4.12e}[CHOCHO], \text{ then } \rho \approx 0.$$

Figure 4.11 shows the 1-minute RO$_2^*{}_m$ (small circles) and the average of binned measurements over 10 pmole mole^{-1} RO$_2^*{}_c$ intervals (large circles) versus RO$_2^*{}_c$ using Eq. 4.11 for $\delta = 1$ and $\delta = 0.5$. The fit parameters from the linear regression (solid line) of the averaged bin values are given in Table

4.1. The difference between the $RO_2{}^*{}_c$ using Eq. 4.8 and Eq. 4.11 are negligible, indicating the loss through the $HO_2 - HO_2$ and $HO_2 - CH_3O_2$ reactions were higher than the loss through HONO, HNO_3, and organic nitrites formation for the measurements considered in this study. As described in section 4.1.2, measurements with insufficient trace gas or photolysis frequency data for calculating $RO_2{}^*$ using Eq. 4.11 are excluded from the current analysis. Some of the excluded data points had NO > 500 pmole mole^{-1}, where the $RO_2{}^*$ loss through HONO, HNO_3, and organic nitrites formation is expected to dominate. As a result, the data presented in Figure 4.10 is partially biased. An example, the importance of considering $RO_2{}^*$ loss through HONO, HNO_3, and organic nitrites under NO > 500 pmole mole^{-1} is given in section 4.1.5.
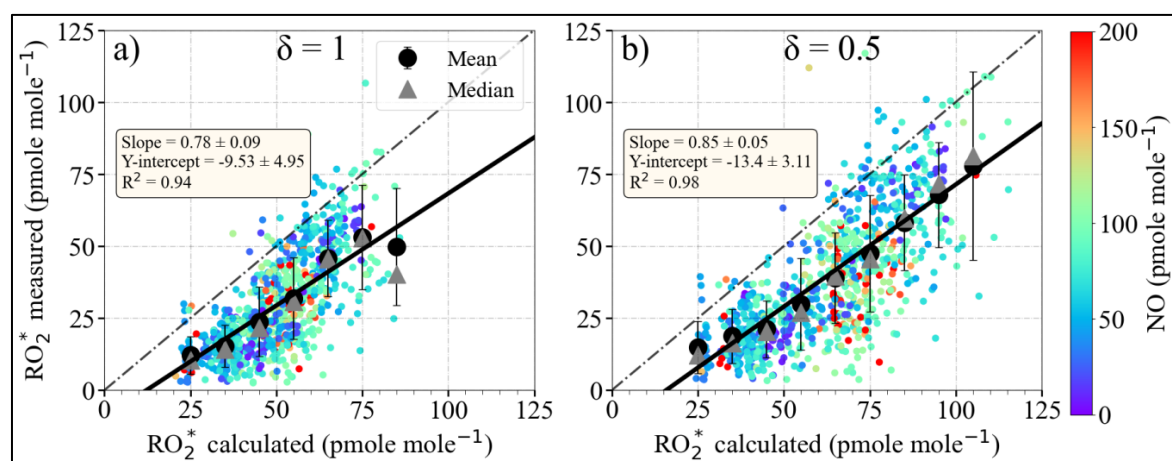

Figure 4.11: $RO_2{}^*{}_m$ versus $RO_2{}^*{}_c$ using Eq. 4.11 for a) $\delta = 1$ and b) $\delta = 0.5$ ($\delta = [HO_2]/[RO_2^*]$). The data are colour-coded with NO. $RO_2{}^*{}_m$ (small circles), average (large circles) and median (triangles) of the binned $RO_2{}^*{}_m$ over 10 pmole mole^{-1} $RO_2{}^*{}_c$ intervals are shown. The error bars indicate the standard error of each bin. The linear regression for the binned values (solid line) and the 1:1 relation (dashed line) are also depicted for reference.

Table 4.1: Fit parameters from figures 4.8, 4.9, 4.11, 4.12, 4.14, 4.16, and 4.32. The data using methylglyoxal (MGL) are discussed on page 84. $HONO_{CMAQ}$: HONO modelled using the CMAQ model; $RO_2{}^*{}_{c_{SS3}}$: estimated using HONO concentration modelled by the CMAQ model and $\gamma = 0$.

The PSS formula to calculate $RO_2{}^*$	$HO_2:CH_3O_2$	Plot number	δ	slope	y-intercept (pmole mole^{-1})	R^2
Eq. 4.8	1:0	4.8, 4.9a	1	0.78 ± 0.08	-9.69 ± 4.82	0.95
	1:1	4.9b	0.5	0.85 ± 0.05	-13.38 ± 3.33	0.97
Eq. 4.11	1:0	4.11a, 4.12a	1	0.78 ± 0.09	-9.53 ± 4.95	0.94
	1:1	4.11b, 4.12c	0.5	0.85 ± 0.05	-13.40 ± 3.11	0.98
Eq. 4.16	1:0	4.12b	1	0.98 ± 0.18	-6.96 ± 6.56	0.92
	1:1	4.12d, 4.14, 4.16a, 4.32b	0.5	0.91 ± 0.11	-2.12 ± 5.11	0.94
Eq. 4.16 with MGL	1:1	4.16b	0.5	0.86 ± 0.13	-7.95 ± 6.97	0.91
Eq. 4.16 with $\gamma = 0.08$	1:1	4.32a	0.5	0.95 ± 0.07	-13.05 ± 4.31	0.97
Eq. 4.16 with $\gamma = 0$ and $HONO_{CMAQ}$	1:1	4.32c	0.5	0.93 ± 0.09	-5.50 ± 5.92	0.93
Eq. 4.16 ($RO^*{}_c$ vs $RO_2{}^*{}_{c_{SS3}}$)	1:1	4.32d	0.5	0.98 ± 0.09	4.17 ± 4.80	0.95

iii) Heterogeneous reactions of HO$_2$ on aerosol surface

As mentioned in section 2.3, the HO$_2$ is removed by heterogeneous reactions in the presence of aerosol. To account for the heterogeneous loss mechanism, a first-order rate coefficient k_{het} is calculated from the measured aerosol surface area using Eq. 4.15.

$$k_{het} = \frac{\omega\gamma}{4}[ASA] \qquad\qquad \text{Eq. 4.15}$$

where ω is the mean molecular speed of HO$_2$ (ω = 43725 cm s^{-1} at 298 K) and γ is the aerosol uptake coefficient (γ = 0.24 is used in this work, as recommended by Taketani et al., 2012 for semi-urban/regional-scale air pollution). The total aerosol surface area concentration, ASA, is calculated from the Optical Particle Counter (OPC) measurements. The Sky-OPC in the C-ToF-AMS instrument measures the number concentration of particles classified in 21 bins of the particle sizes from 250 nm to 7500 nm. A bimodal lognormal function with fixed widths for fine and coarse modes is fitted over the size distribution to extrapolate the size up to 150 nm. By assuming a spherical shape for the particles, the total aerosol surface area is calculated using the method described in Heintzenberg (1994).

To account for heterogeneous loss, Eq. 4.11 is modified by adding the heterogeneous loss term as:

$$(2j_{4.1}[O_3]\beta + j_{4.3}[HONO])(1 - \rho) + 2j_{4.8}[HCHO] + 2j_{4.9}[CH_3CHO] +$$
$$2(j_{4.10a} + j_{4.10b})[CH_3C(O)CH_3] + 2j_{4.11}[CHOCHO] - k_{het}\delta[RO_2^*] - \delta[RO_2^*] (k_{4.23}[NO] +$$
$$k_{4.24}[O_3])\rho - (2k_{4.26}((1 - \delta)[RO_2^*])^2 - k_{4.25}(1 - \delta)[RO_2^*][NO]) \left(\frac{k_{4.22}[NO]}{(k_{4.22}[NO] + k_{4.27}[O_2])}\right) -$$
$$2k_{4.15}\delta (1 - \delta)[RO_2^*]^2 - 2k_{4.14}\delta[RO_2^*]^2 = 0 \qquad \text{Eq. 4.16}$$

This in turn modifies $L_{RO_2^*}$, Eq. 4.14 as:

$$L_{RO_2^*} = - \left(\delta k_{het} + \delta(k_{4.23}[NO] + k_{4.24}[O_3])\rho + \left(\frac{k_{4.22}[NO]}{(k_{4.22}[NO] + 4.26[O_2])}\right) k_{4.25}(1 - \delta)[NO]\right)$$

$$\text{Eq. 4.17}$$

Eq. 4.17, together with Eq. 4.13 and Eq. 4.2 are substituted in Eq. 4.12 to calculate the RO$_2$*. Figure 4.12 shows the RO$_2$*$_m$ versus RO$_2$*$_c$ without and with considering heterogeneous loss mechanism for δ = 1 and δ = 0.5. The data are colour-coded with the total aerosol surface area concentration calculated from the Sky-OPC measurements. The last two binned values in Figure 4.12b and 4.12d are not considered for the linear fit calculation since the number of data points in those bins are less than 20. The correlation between the RO$_2$*$_m$ and RO$_2$*$_c$ improves significantly after including the heterogeneous loss mechanism in the analytical equation, as shown by the fit parameters. The negative y-intercept might be coming from the uncertainties in the RO$_2$* production and loss terms calculation and/or the measurements down below the LOD$_{RO_2^*}$ of PeRCEAS. The RO$_2$*$_c$ with ASA > 4 × 10^{-6} cm^2 cm^{-3} (OPC > 800 cm^{-3}) reduces significantly by introducing the heterogeneous loss mechanism, which improves the overall correlation. Since the value of γ varies depending on the phase, relative humidity, and the type of components in the particle (Mozurkewich et al., 1987;

Hanson, 1992; Gershenzon et al., 1995; Bedjanian et al., 2005; Remorov et al., 2002; Thornton and Abbatt, 2005; Taketani et al., 2008, 2009, 2010), a sensitivity study on the dependence of $RO_2^*{}_c$ on γ was made (section 4.1.8). In addition, the relative importance of the heterogeneous loss processes under different chemical conditions and physical regimes is discussed in sections 4.1.5 to 4.1.7. Even though the slope is very close to 1 (0.91), a systematic overestimation is still present for $RO_2^*{}_m < 25$ pmole mole^{-1} with total aerosol surface area concentration (ASA) $< 1 \times 10^{-6}$ cm^2 cm^{-3} (particle number concentration < 100 cm^{-3}) and $NO_x < 150$ pmole mole^{-1} (Figure 4.14).
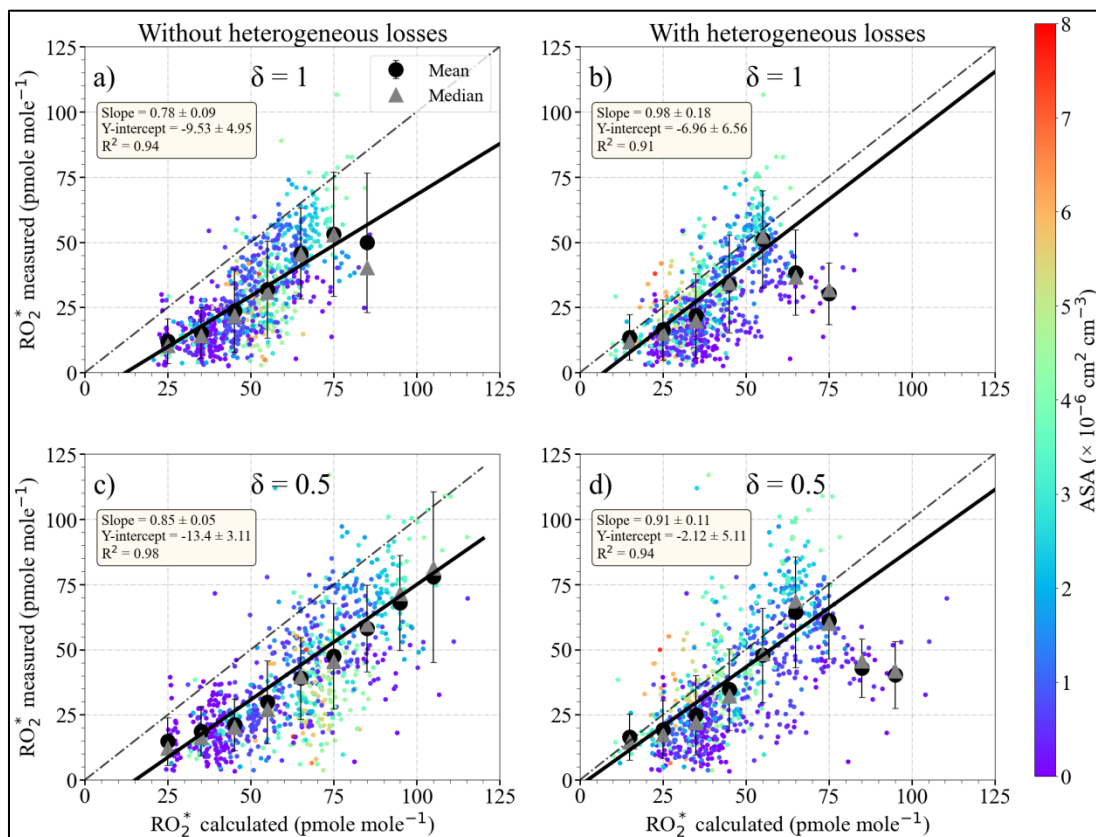
Figure 4.12: $RO_2^*{}_m$ versus $RO_2^*{}_c$ for a) and b) $\delta = 1$; c) and d) $\delta = 0.5$ ($\delta = [HO_2]/[RO_2^*]$) without (a, c) and with (b, d) HO_2 losses on the aerosol surface. The data are colour-coded with total aerosol surface area concentration (ASA). $RO_2^*{}_m$ (small circles), average (large circles) and median (triangles) of the binned $RO_2^*{}_m$ over 10 pmole mole^{-1} $RO_2^*{}_c$ are shown. The error bars indicate the standard error of each bin. The linear regression for the binned values (solid line) and the 1:1 relation (dashed line) are also depicted for reference.

The contribution of different loss processes to the total RO_2^* loss rate ($D_{RO_2^*}$) is estimated by substituting RO_2^* in Eq. 4.16 with $RO_2^*{}_m$. During the substitution, $RO_2^*{}_m$ is assumed to be the sum of an equal amount of HO_2 and CH_3O_2, i.e. $\delta = 0.5$. Figure 4.13 shows the variation of $RO_2^*{}_m$ observed during EMeRGe in Asia as a function of latitude and altitude and the calculated contribution of $HO_2 + HO_2$ reaction, $HO_2 + RO_2$ reaction, $RO_2 + RO_2$ reaction, $OH + NO$ reaction, $OH + NO_2$ reaction, and HO_2 uptake on aerosol to $D_{RO_2^*}$. For the calculation, CH_3O_2 is taken as the surrogate for all RO_2.
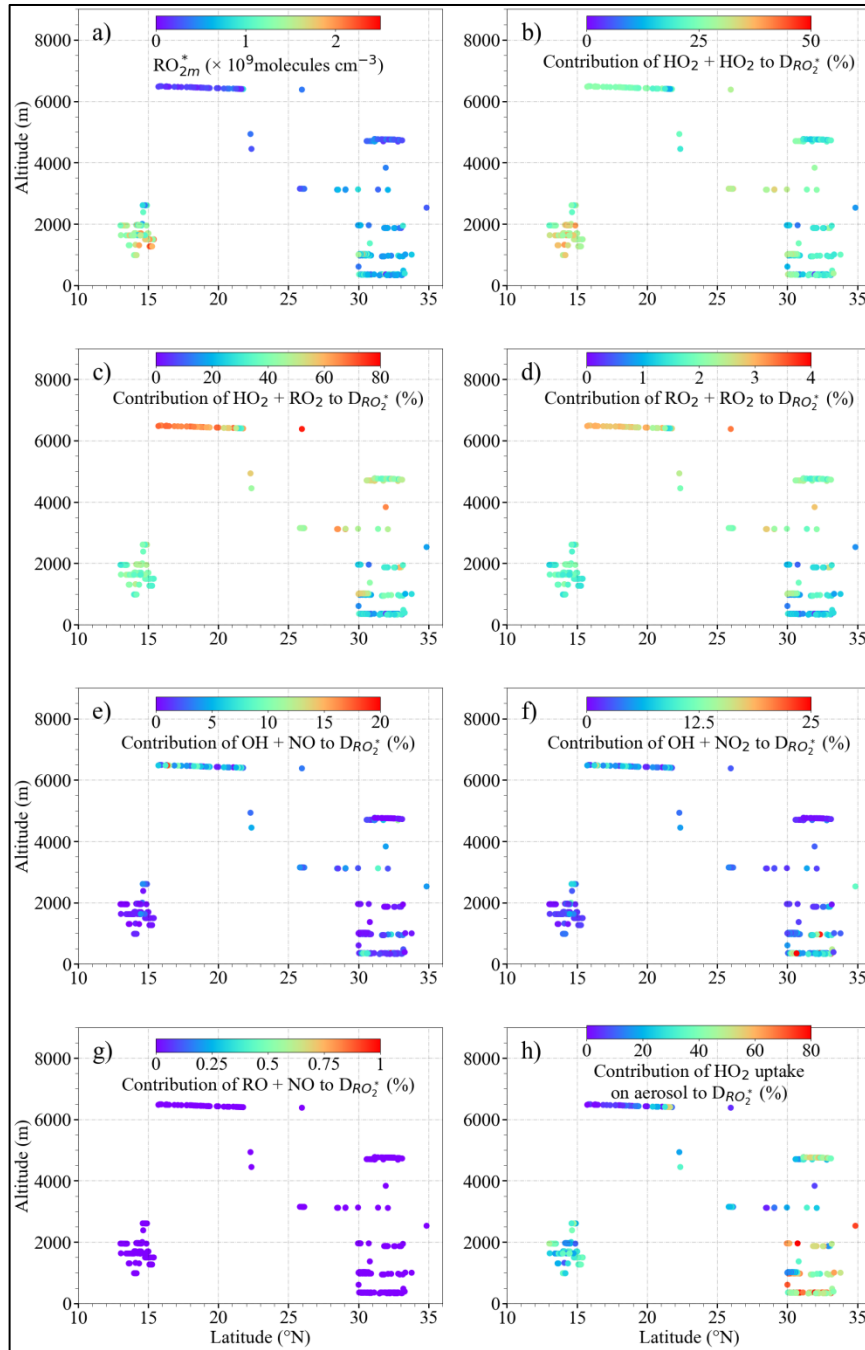
Figure 4.13: Plot of: a) [RO_2^*]; RO_2^* loss contribution from b) HO_2 + HO_2 reaction, c) HO_2 + RO_2 reaction, d) RO_2 + RO_2 reaction, e) OH + NO reaction, f) OH + NO_2 reaction, and h) HO_2 uptake on aerosol as a function of latitude and altitude.

The HO_2 + RO_2 reaction has the highest contribution to the total $D_{RO_2^*}$ and it reaches up to 75 % and remains above 25 % in most of the conditions encountered. The contribution from HO_2 + HO_2 reaction also remains above 20 % in most cases and reaches up to 50 % during the measurements in the PBL under sunny conditions. Due to the higher pressure dependency of $k_{HO_2+HO_2}$, the loss through the HO_2 + HO_2 reaction decreases with altitude. On the other hand, the RO_2 + RO_2 reaction contributes < 2 % to the $D_{RO_2^*}$ due to the lower reaction rate coefficient than HO_2 + RO_2 and HO_2 +

HO_2. In general, for the measurements of EMeRGe in Asia, the $HO_2 + RO_2$ and $HO_2 + HO_2$ reactions were the main loss process of RO_2^*.

The contribution from the OH + NO reaction forming HONO remained below 20 % for all the cases investigated except for the measurements near Taiwan with $NO_x > 8 \times 10^{12}$ molecules cm^{-3} (shown in section 4.1.6). The OH + NO_2 reaction forming HNO_3 also remained below 25 % for all the cases investigated. Since there were no NO_2 measurements available near Taiwan, the loss rate through HONO formation is not calculated. The reaction between RO + NO forming organic nitrites contributes < 2 % to $D_{RO_2^*}$. The small contribution from the OH + NO and OH + NO_2 reactions compared to the $HO_2 + RO_2$ and $HO_2 + HO_2$ reactions is the reason for the negligible difference between $RO_2^*{}_c$ calculated using Eq. 4.9 and 4.12. During EMeRGe in Asia, the loss through the HO_2 uptake on aerosol is generally below 30 % but reaches up to 60 % in air masses with ASA > 7×10^{-6} cm^2 cm^{-3} (OPC > 1400 particles cm^{-3}) for $\gamma = 0.24$. The loss through the HO_2 uptake on aerosol > 50 % in figure 4.13 is calculated for ASA > 5×10^{-6} cm^2 cm^{-3} (OPC > 1000 particles cm^{-3}) over the East China Sea. A detailed discussion on these measurements and a sensitivity study on γ are given in sections 4.1.7 and 4.1.8.

The air masses with ASA < 1×10^{-6} cm^2 cm^{-3} (particle number concentration < 100 particles cm^{-3}) and $NO_x < 150$ pmole $mole^{-1}$ were measured above 4000 m during the IOP in Asia. Under these conditions, the $HO_2 - HO_2$ and $HO_2 - RO_2$ reactions are the dominant RO_2^* loss processes. So the overestimation of $RO_2^*{}_m$ by $RO_2^*{}_c$ under these conditions might be due to the underestimation in $k_{RO_2^*}$, the OH loss reactions (OH $- HO_2$ and OH self-reaction) that are not considered in Eq. 4.16 and/or the overestimation of the production rate.

The correlation between the $RO_2^*{}_m$ and $RO_2^*{}_c$ is further investigated by considering different physical and chemical regimes. Figure 4.14 shows the $RO_2^*{}_m$ versus $RO_2^*{}_c$ using Eq. 4.16 for $\delta = 0.5$ colour-coded with $j_{O(^1D)}$, the mixing ratio of the sum of selected OVOCs as a surrogate for the dominant VOC precursors, $\Sigma VOCs$, ($\Sigma VOCs = HCHO + CH_3CHO + CHC(O)CH_3 + CHOCHO + CH_3OH$), the mixing ratio of NO_x, and the flight altitude. As the miniDOAS instrument has no measurements available in flights altitudes above 6000 m, those measurements are not considered in the correlation study in figure 4.14. As a result, the maximum altitude is set to 6000 m. The $RO_2^*{}_c$ overestimate (up to 4 times) the measured values at altitudes above 4000 m. Neither the accuracy nor the $LOD_{RO_2^*}$ of PeRCEAS can explain this discrepancy completely. These measurements were associated with $j_{O(^1D)} > 3 \times 10^{-5}$ s^{-1}, indicating high insolation. The mixing ratio of $NO_x < 150$ pmole $mole^{-1}$ indicates the absence of fresh emissions, and the $\Sigma VOCs$ mixing ratio remains < 2 nmole $mole^{-1}$. The overestimation might come from the overestimation of production rates and/or underestimation of the loss processes. The RO_2^* loss reactions (OH self-reaction and OH $- HO_2$ reaction) excluded from Eq. 4.16 might significantly contribute to the total overestimation under this chemical

composition. Even though the lower VOC loading indicates the $HO_2:RO_2$ in these air masses might be higher than 1:1, i.e., $\delta > 0.5$, the variation does not affect the correlation between $RO_2{}^*_m$ and $RO_2{}^*_c$ (see Figure 4.9).

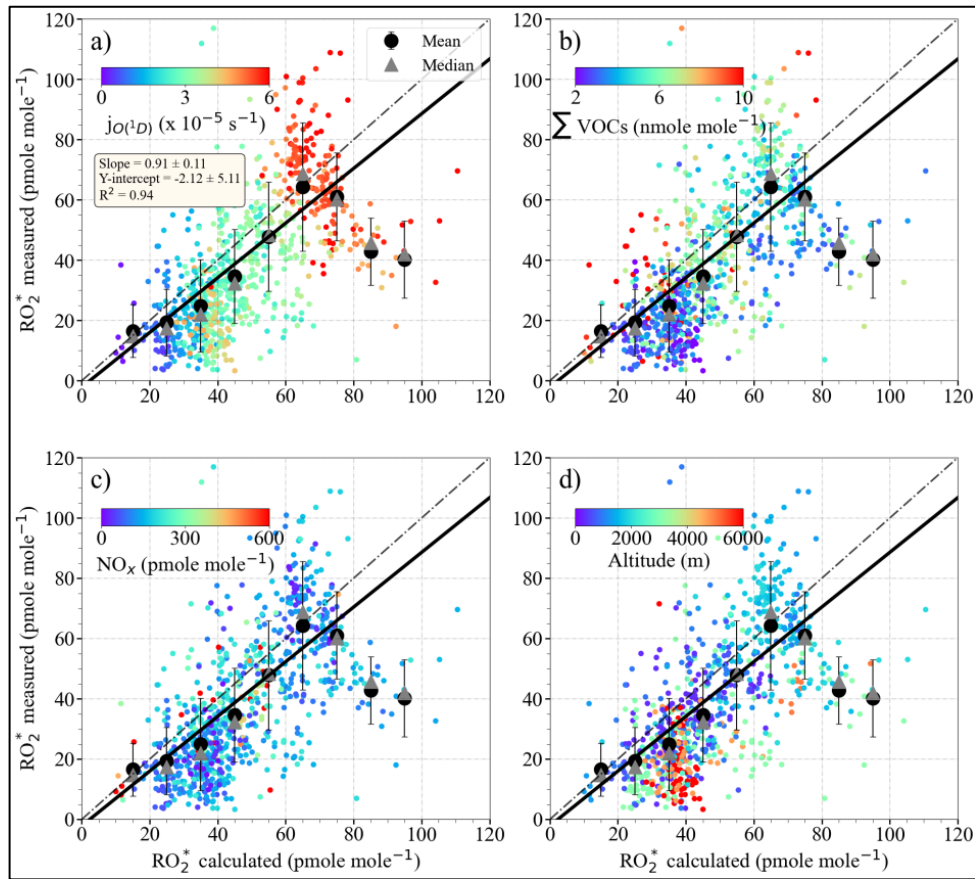Figure 4.14: $RO_2{}^*_m$ versus $RO_2{}^*_c$ using Eq. 4.16 for $\delta = 0.5$ ($\delta = [HO_2]/[RO_2^*]$). The data are colour-coded with: a) $j_{O(^1D)}$, b) mixing ratio of $\Sigma VOCs$, being $\Sigma VOCs = HCHO + CH_3CHO + CHC(O)CH_3 + CHOCHO + CH_3OH$, c) NO_x mixing ratio, and d) altitude. $RO_2{}^*_m$ (small circles), the average (large circles) and the median (triangles) of the binned $RO_2{}^*_m$ over 10 pmole mole^{-1} $RO_2{}^*_c$ intervals are shown. The error bars indicate the standard error of each bin. The linear regression for the binned values (solid line) and the 1:1 relation (dashed line) are also depicted for reference.

In addition to this, the spatial and temporal differences in the in-situ measurements (O_3, NO, H_2O, CO, CH_4, CH_3CHO, CH_3OH, and $CH_3C(O)CH_3$) with respect to remote sensing observations (NO_2, HCHO, CHOCHO, and HONO) used in Eq. 4.16 might partly contribute to the overestimation observed in Figure 4.14. Although the temporal evolution reasonably agrees, as shown for HCHO in Figure 4.15, these instruments have different air sampling volumes and do not perfectly overlap in coverage. This may occasionally lead to significant differences depending on the location of the pollutant layers with respect to HALO. In addition, PTR-MS measurements of HCHO might include interferences from molecular fragments of other compounds in the sample air (Inomata et al., 2008). Further details about the accuracy and comparability of the instrumentation on board during the campaign can be found elsewhere (Schumann, 2020).
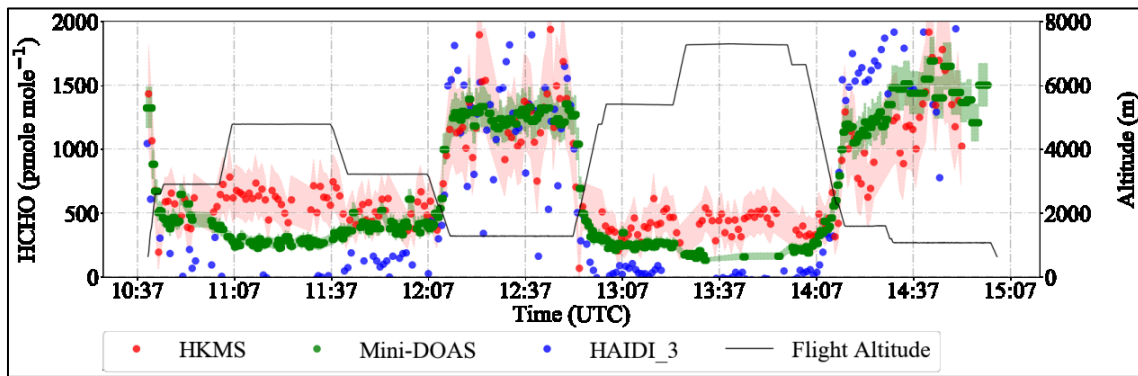
Figure 4.15: Example of a time series of HCHO obtained from remote sensing (HAIDI in blue and miniDOAS in green) and in-situ (HKMS in red) instruments during the flight E-EU-04. The shaded region shows $\pm 1\sigma$ uncertainties of the HKMS and miniDOAS instruments. HAIDI_3 stands for the data retrieved from the third spectrometer of HAIDI. The HALO altitude is depicted in black.

The effect of including methylglyoxal ($CH_3C(O)C(O)H$) photolysis as an RO_2^* source in Eq. 4.16 was investigated by using the $CH_3C(O)C(O)H^*$ measurements provided by the miniDOAS instrument. The $CH_3C(O)C(O)H^*$ measured is the sum of $CH_3C(O)C(O)H$ and a fraction of other substituted dicarbonyls (mainly 2,3-butanedione, $C_3H_6O_2$), with visible absorption spectra similar to that of $CH_3C(O)C(O)H$. For the calculation, $CH_3C(O)C(O)H$ was assumed to be half of $CH_3C(O)C(O)H^*$ as recommended by Zarzana et al. (2017) and Kluge et al. (2020). Figure 4.16 shows the comparison between the $RO_2^*{}_m$ and $RO_2^*{}_c$ without and with $CH_3C(O)C(O)H$ (where $CH_3C(O)C(O)H = \frac{CH_3C(O)C(O)H^*}{2}$) photolysis. As can be seen in the figure and the fit parameters, the spread and the overestimation increase when the RO_2^* production from $CH_3C(O)C(O)H$ is considered. The influence of $CH_3C(O)C(O)H$ is evident in data points with $CH_3C(O)C(O)H > 500$ pmole mole^{-1}. This indicates that the ½ factor might be too inaccurate depending on the composition of the air masses, and $CH_3C(O)C(O)H$ photolysis was not included in the RO_2^* calculations to avoid an unknown variable source of inaccuracies.
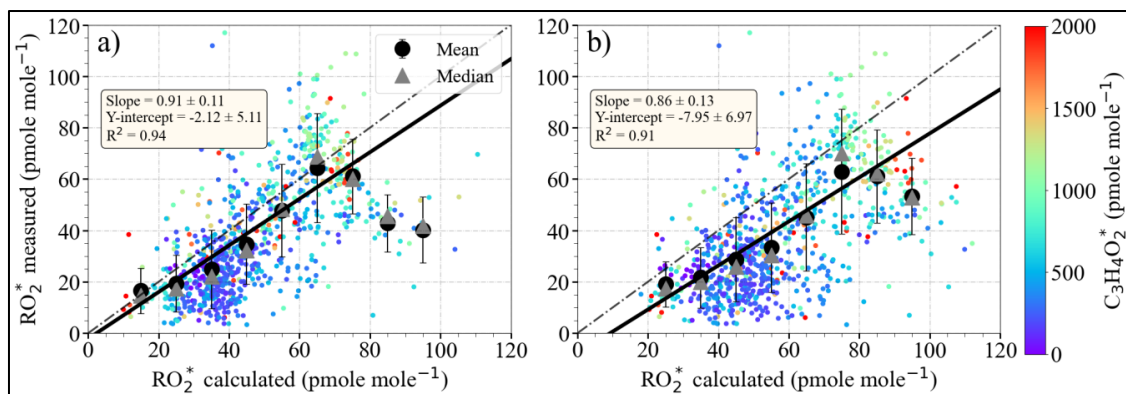
Figure 4.16: $RO_2^*{}_m$ versus $RO_2^*{}_c$ using Eq. 4.16 for $\delta = 0.5$ ($\delta = [HO_2]/[RO_2^*]$) a) without and b) with RO_2^* production from $CH_3C(O)C(O)H$. The data are colour-coded with the $CH_3C(O)C(O)H^*$ mixing ratio. $RO_2^*{}_m$ (small circles), average (large circles) and the median (triangles) of binned $RO_2^*{}_m$ over 10 pmole mole^{-1} $RO_2^*{}_c$ intervals are shown. The error bars indicate the standard error of each bin. The linear regression for the binned values (solid line) and the 1:1 relation (dashed line) are also depicted for reference.

In summary, the correlation study between $RO_2{}^*{}_m$ and $RO_2{}^*{}_c$ shows that the $RO_2{}^* - RO_2{}^*$ reactions (HO_2 self-reaction and $HO_2 - RO_2$ reactions) dominate the $RO_2{}^*$ loss processes in the air masses investigated with $NO < 200$ pmole mole^{-1} and ASA $< 4 \times 10^{-6}$ cm^2 cm^{-3} (particle number concentration < 800 cm^{-3}). Due to the pressure and [H_2O] dependency of the HO_2 self-reaction, the loss through the $HO_2 - HO_2$ reaction decreases with altitude. For the measurements considered in the PBL, the loss contribution from the HO_2 uptake on aerosol is estimated to be < 30 %, except for the measurements in the East China Sea with ASA $> 4 \times 10^{-6}$ cm^2 cm^{-3} (particle number concentration > 800 cm^{-3}). Similarly, the $RO_2{}^*$ loss through the HONO and HNO_3 formation was < 20 %, except for the measurements near Taiwan with $NO_x > 8 \times 10^{12}$ molecules cm^{-3}. $RO_2{}^*{}_c$ overestimates $RO_2{}^*{}_m$ for the measurement above 4000 m with $RO_2{}^*{}_m < 25$ pmole mole^{-1}. The overestimation might be coming from the $RO_2{}^*$ loss reactions (OH self-reaction and OH $- HO_2$ reaction) excluded from Eq. 4.16 and the overestimation of the $RO_2{}^*$ precursor measurements. Further studies of the $RO_2{}^*$ precursors are still necessary to pinpoint the cause of this overestimation. The correlation between $RO_2{}^*{}_m$ and $RO_2{}^*{}_c$ is independent of δ, i.e. of the HO_2 to $RO_2{}^*$ ratio, since both $RO_2{}^*{}_m$ and $RO_2{}^*{}_c$ vary in the same manner as δ under the assumptions made in this study.

4.1.4 Error Estimation of the PSS Calculation

The uncertainty of the $RO_2{}^*{}_c$ is estimated from the uncertainty of the measurement used in Eq. 4.16. An accuracy or precision estimate of the measurements is given in the data files by the corresponding instrument group. During EMeRGe, the maximum uncertainty of photolysis frequencies was < 10 % and was highest during the measurements with a low solar zenith angle ($< 15°$). The O_3 uncertainty remains around 2.5 % and increases up to 4 % during altitude changes. The $CH_3C(O)CH_3$ and the CH_3CHO measurements from the HKMS instrument have an uncertainty between 10 % and 15 %, between 20 % and 60 %, respectively. Since the relative contribution of CH_3CHO photolysis in $RO_2{}^*{}_c$ is < 5 %, the higher relative error of CH_3CHO has negligible importance in the uncertainty of $RO_2{}^*{}_c$.

The NO_2 and HCHO measurements from the miniDOAS instrument have an uncertainty of 20 % for the data considered in this study. The uncertainty of CHOCHO from the miniDOAS instrument is between 20 % and 30 %. HONO measurements from miniDOAS have the highest uncertainty compared to all other measurements and are between 20 % and 60 %. For those datasets without uncertainty estimates, the relative uncertainty is calculated from the corresponding detection limit, a, and the additive relative error, r, as $\Delta y = a + r\,y$ (Schumann 2020). The measurement uncertainties for NO, CO, ambient pressure, ambient temperature, and H_2O volume mixing ratio were calculated using this method with the values given in Table 4.2.

The uncertainty of $RO_2{}^*{}_c$ resulting from the error propagation of the measurement uncertainties mentioned above in Eq. 4.16 is 15 % to 20 %. Even though this uncertainty cannot

completely explain the difference between $RO_2^*{}_m$ and $RO_2^*{}_c$, it might reduce the differences observed between $RO_2^*{}_m$ and $RO_2^*{}_c$ in particular cases.

In addition to the higher uncertainty, i.e. 20 % to 60 %, the measured HONO concentration was significantly higher (more than 100 times) than the expected values in the free troposphere from known gas-phase reactions, as indicated by comparisons with model simulations. Up to the submission of this work, no known physical or chemical mechanisms resulting in higher HONO production in the free troposphere have been identified by the instrument group responsible for the HONO measurements (Benjamin Schreiner and Prof. Klaus Pfeilsticker, private communication). A sensitivity study of the $RO_2^*{}_c$ dependency on HONO measurements is presented in sections 4.1.5 to 4.1.8 to investigate the effect of a potential HONO overestimation.

The contribution from the uncertainties of the first-order reaction rate constants is ≤ 5 % to the total uncertainty. The uncertainties on the second-order reaction rate constants are estimated using the reported error in the rate constants and the uncertainty of the pressure and temperature measurements. The contribution from these estimated uncertainties of the second-order reaction rate constants was also ≤ 5 % to the total uncertainty of $RO_2^*{}_c$. The relative importance of each measurement and its uncertainty on $RO_2^*{}_c$ under different physical conditions and chemical compositions are further discussed in sections 4.1.5 to 4.1.7.

Table 4.2: Detection limit, a, and additive relative error, r, used to estimate the instrumental uncertainty. NA: not available.

Instrument	Parameter	Unit	a	r
AMTEX	CO	nmole mole^{-1}	1.3	2.4 %
AENEAS	NO	nmole mole^{-1}	0.003	11 %
AENEAS	NO$_y$	nmole mole^{-1}	0.035	10 %
BAHAMAS	Static pressure	hPa	0.3	NA
BAHAMAS	Temperature	K	0.5	NA
BAHAMAS	H$_2$O	µmole mole^{-1}	NA	10 %

4.1.5 Special Case Study: Manila

During the flights E-AS-06 on 20.03.2018 and E-AS-10 on 28.03.2018, both upwind and downwind measurements were made close to Manila under similar physical conditions. These measurements near Manila were studied in detail to understand the chemical processes involved in RO_2^* production and losses close to the source with NO < 200 pmole mole^{-1}. The flights took place under mostly clear sky conditions favouring RO_2^* production.

Flight E-AS-06

Figure 4.17 shows the 2D and zoom-in 3D representation of the flight pattern near Manila from E-AS-06. The flight tracks are colour-coded with: a) altitude; b) $RO_2^*{}_m$, c) CO; and d) NO.

Vertical profiling was made in the upwind and downwind of Manila to distinguish Manila outflow from the background. Different flight legs near Manila are marked with letters A to K. At point A, HALO reached north of Manila and descended to 2700 m. The forecasting predicted wind blows from east to west over Manila. At point B, HALO descended to 1650 m and made the upwind measurements in four flight legs at two altitudes, i.e., at 1650 m between B–C and C–D and 2000 m between D–E and E–F over the east side of Manila. HALO reached the predicted Manila outflow region over the west coast at point H and made altitude profiling at 1700 m, 1500 m, and 1270 m between H–I, I–J, and J–K, respectively. Both CO and NO mixing ratios measured on the west side of Manila were higher than those measured on the east side. This indicates the presence of fresh emission plumes during the measurements on the west side. FLEXTRA backward trajectories indicate that air masses measured during the flight legs over the west coast were transported over Manila in the PBL before reaching the sampling point. Therefore, the sampled air masses are expected to contain emissions from Manila.

The CO and NO mixing ratio reached up to 200 nmole mole^{-1} and 100 pmole mole^{-1} during the measurements on the west side of Manila between J–K at 1270 m. These were the highest values encountered during measurements near Manila. $RO_2{}^*{}_m \geq 100$ pmole mole^{-1} was observed during this period and was also the highest mixing ratio measured during E-AS-06. The pollution plumes observed between H–I and I–J at 1700 m and 1500 m were more to the south than the plume observed between J–K at 1270 m. Inside the plume between H–I and I–J, CO was less than 200 nmole mole^{-1}, while the NO mixing ratio was similar to the value observed in the flight leg J–K.
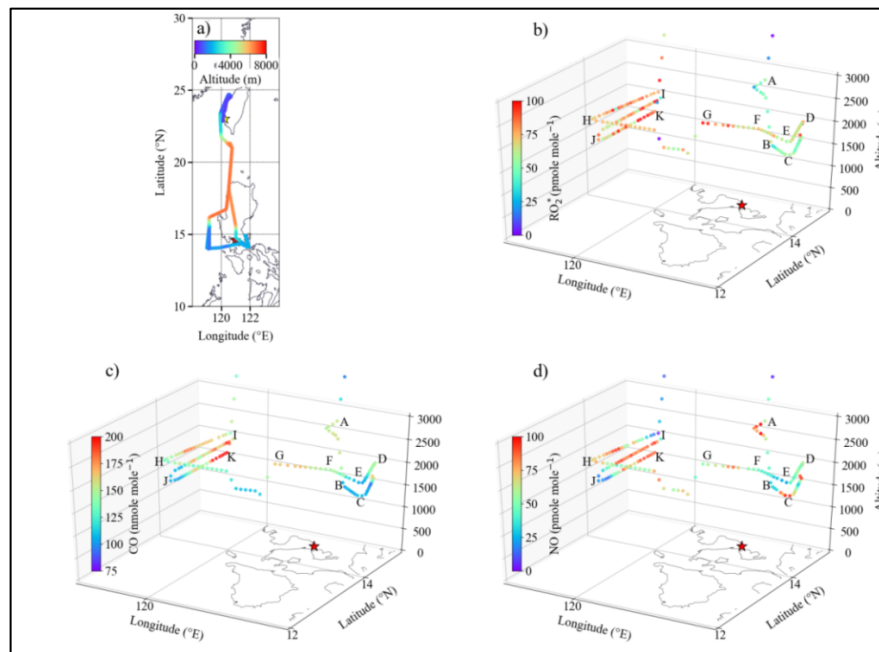

Figure 4.17: E-AS-06 flight on 20.03.2018 a) flight tracks colour-coded with flight altitude and zoom-in 3D view of the flight track near Manila colour-coded with b) $RO_2{}^*{}_m$, c) CO, and d) NO mixing ratios. Stars indicate the target MPC Manila (red) and the HALO base in Tainan (yellow). Different flight legs near Manila are also marked with letters from A to K.

Figure 4.18 shows the variation of $RO_2^*{}_m$, $RO_2^*{}_c$, other trace gas measurements, and photolysis frequencies along the flight track near Manila from flight E-AS-06. Different flight legs are marked with vertical lines and letters (A to K). Panel e) in figure 4.19 shows the HYSPLIT modelled CO enhancement over the background concentration due to emissions originating from Manila. In addition, based on HYSPLIT simulations, the measurements expected to contain emissions from Manila are highlighted with grey vertical spans.

During the upwind measurements on the east side of Manila, HALO encountered three different pollution layers. The first layer was measured between A–B at 27000 m. According to FLEXTRA trajectories, the air masses measured were transported over the land in the PBL north of Manila. The second layer was measured between B–D at an altitude of 1650 m. The air mass was transported in the PBL over the Philippine Sea. As a result, $[H_2O]$ reaches up to 4×10^{17} molecules cm^{-3}. The third layer was measured between D–F at an altitude of 2000 m, which was also transported in the PBL over the Philippine Sea and contained local emissions from the land. During the measurements in the first and second layer, i.e. between A–D, the $RO_2^*{}_m$ is around 50 pmole $mole^{-1}$, and the $RO_2^*{}_c$ value agrees very well with $RO_2^*{}_m$ during this period. Between D–F, i.e. in the third layer, $RO_2^*{}_m$ increases to 70 pmole $mole^{-1}$. The increase in $RO_2^*{}_m$ is correlated with the increase in the photolysis frequency and $\sum$VOCs. As shown in figure 4.19, during the upwind measurements, the contribution from the $O(^1D)$ reaction with H_2O to the total RO_2^* production is around 60 %. The HCHO photolysis contributes around 20 %, while the CHOCHO and HONO photolysis contribute < 10 %. The estimated total RO_2^* loss rate ($D_{RO_2^*}$) shows that the loss rate is dominated by the $HO_2 - RO_2$ and $HO_2 - HO_2$ reactions and is between 70 % and 90 %. The RO_2^* loss through the HO_2 uptake on aerosol and HONO and HNO_3 formation are < 20 % and < 10 %, respectively. The contribution from $RO_2 - RO_2$ reactions and $RO - NO$ reactions are < 2 %.

As shown in Figure 4.18, VOCs, NO_2, NO_y mixing ratios and $[H_2O]$ also increase simultaneously with CO and NO downwind of Manila. NO_y, CH_3OH, CH_3CHO, and $CH_3C(O)CH_3$ reach 3; 5.8; 1.15; and 3.8 nmole $mole^{-1}$, respectively, during the measurements between J–K. The enhancement in the trace gas measurements agrees with the HYSPLIT modelled CO enhancement. The $RO_2^*{}_c$ do not capture the enhancement in $RO_2^*{}_m$ within the plumes. This might be due to the complex chemistry inside the plume, which cannot be represented by Eq. 4.16. The RO_2^* source contribution from the $O(^1D)$ reaction with H_2O increases from 60 % to 75 % in downwind measurements, and the HCHO photolysis contribution remains between 15 % and 20 %. The CHOCHO photolysis and HONO photolysis contribution also remain < 10 % throughout the period. In the downwind measurements, the contribution of $HO_2 - RO_2$ and $HO_2 - HO_2$ reactions to $D_{RO_2^*}$ reaches $\leq$ 80 %, and the contribution from HO_2 uptake on aerosol increases up to 30 % inside the pollution plume. The contribution of HONO and HNO_3 formation to $D_{RO_2^*}$ remains < 10 %, as the NO does not show any enhancement above 100 pmole $mole^{-1}$ (Figure 4.18). The difference between the

total RO_2^* production and loss rates is within the standard errors estimated from the measurement uncertainty indicating that the relevant processes in RO_2^* production and loss are considered in the Eq.4.16. A significant difference between production and destruction is observed during pressure fluctuation.
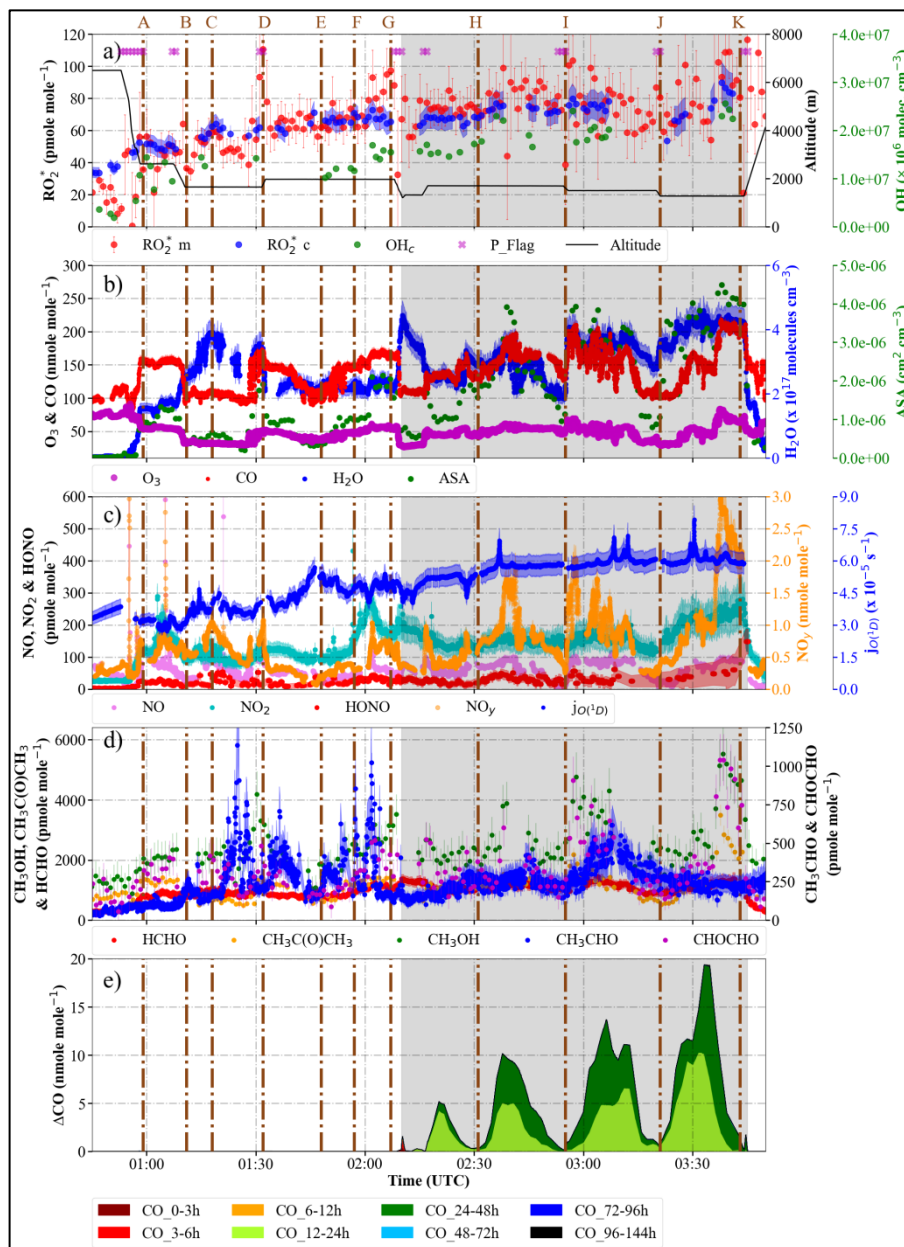
Figure 4.18: Variation of $RO_2^*{}_m$ and $RO_2^*{}_c$, selected RO_2^* precursors and $j_{O(^1D)}$ measurements along the flight track near Manila from E-AS-06. a) $RO_2^*{}_m$, $RO_2^*{}_c$ using Eq. 4.16, OH calculated (OH_c) using Eq. 4.18 discussed in section 4.1.7, and flight altitude. The P_flag indicates RO_2^* measurements affected by dynamical pressure variations in the inlet. b) O_3 and CO mixing ratios, $[H_2O]$, and ASA (total aerosol surface area concentration). c) NO, NO_2, HONO, NO_y mixing ratios and $j_{O(^1D)}$. d) HCHO, CH_3CHO, CH_3OH, CHOCHO and $CH_3C(O)CH_3$ mixing ratios. e) HYSPLIT model results in CO enhancement over background concentration due to emissions originating from the target MPCs Manila (02-04h UTC). The error bars show the standard error of the measurements. Based on HYSPLIT simulations, the measurements expected to contain the emission from Manila are highlighted with grey vertical spans. Different flight legs near Manila are also marked with vertical lines and letters from A to K.

Figure 4.19: Variation of $RO_2^*{}_m$ and $RO_2^*{}_c$, $RO_2^*{}_{CMAQ}$ (sum of $HO_2{}_{CMAQ}$, $CH_3O_2{}_{CMAQ}$, and RO_2 C $_{CMAQ}$ modelled using the CMAQ. RO_2 C $_{CMAQ}$ is the organic peroxy radical other than CH_3O_2 that converts NO to NO_2), RO_2^* production and loss contribution from each term in Eq. 4.16 along the flight track near Manila from E-AS-06. a) $RO_2^*{}_m$, $RO_2^*{}_c$, $RO_2^*{}_{CMAQ}$ ($HO_2{}_{CMAQ}$ + $CH_3O_2{}_{CMAQ}$ + RO_2 C $_{CMAQ}$, where RO_2 C is the sum of organic peroxy radicals other than that convert NO to NO_2) and flight altitude. The P_flag indicates RO_2^* measurements affected by dynamical pressure variations in the inlet. b) RO_2^* source contribution from R4.1, R4.3, R4.8, R4.9, R4.10, and R4.11. c) RO_2^* loss contribution from R4.14 ($D_{HO_2+HO_2}$), R4.15 ($D_{HO_2+RO_2}$), R4.16 ($D_{RO_2+RO_2}$), R4.19 (D_{OH+NO}), R4.20 (D_{OH+NO_2}), R4.22 (D_{RO+NO}), and HO_2 uptake on aerosol (D_{het}). d) difference between the total production ($P_{RO_2^*}$) and loss ($D_{RO_2^*}$) rate with standard errors estimated from the measurement uncertainty. e) percentage of HO_2, CH_3O_2, and RO_2 converting NO to NO_2 other than CH_3O_2 modelled using the CMAQ model in $RO_2^*{}_{CMAQ}$. Based on HYSPLIT simulations, the measurements expected to contain the emission from Manila are highlighted with grey vertical spans. Different flight legs near Manila are also marked with vertical lines and letters from A to K.
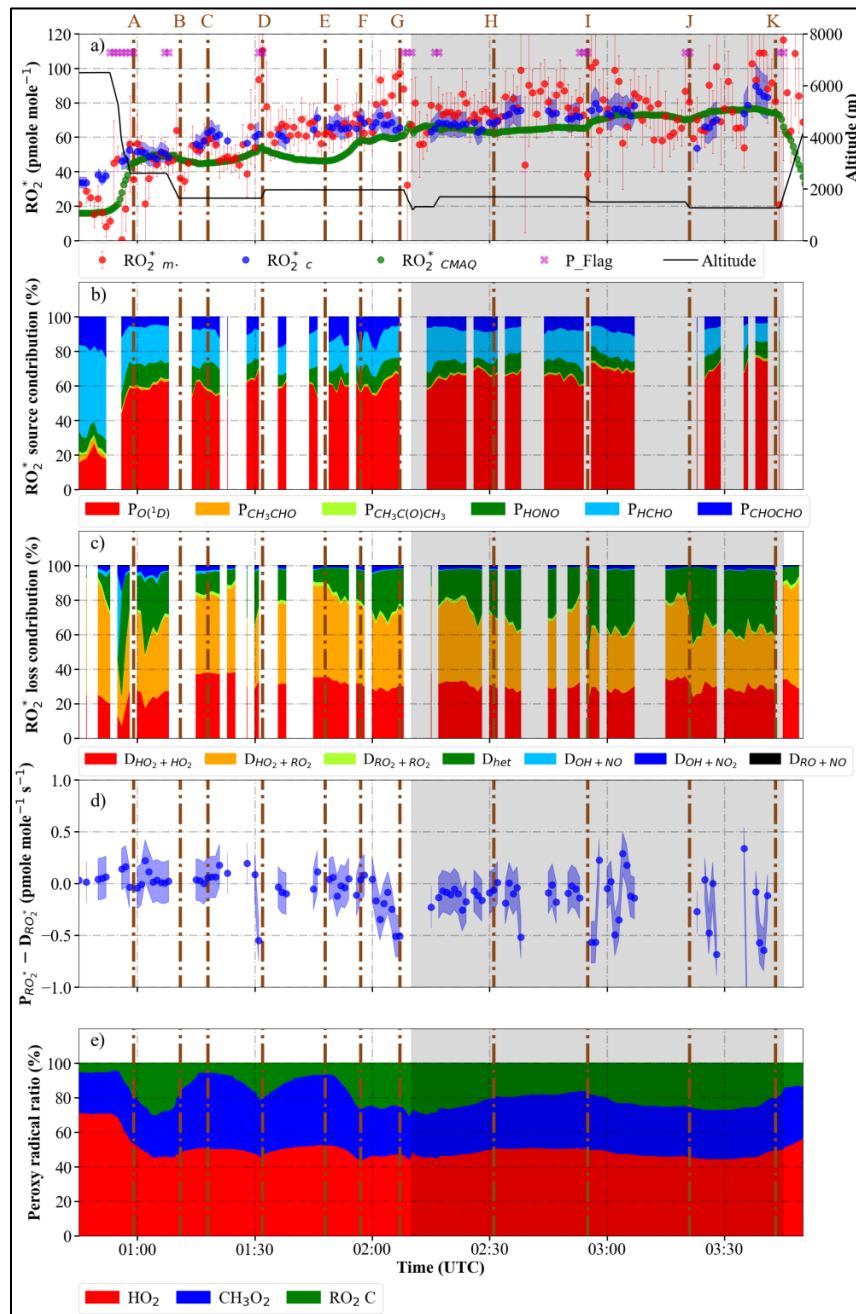
The RO_2^* calculated from the CMAQ model as the sum of peroxy radicals that convert NO to NO_2 ($RO_2^*{}_{CMAQ} = HO_2{}_{CMAQ} + CH_3O_2{}_{CMAQ} + RO_2 C{}_{CMAQ}$, where $RO_2 C$ are organic peroxy radicals which convert NO to NO_2), shows good agreement with $RO_2^*{}_c$, but fails to capture the variations in $RO_2^*{}_m$ inside the plumes (figure 4.19). As the model entirely relies on emission inventories and the chemical transport mechanism to estimate the RO_2^* precursors and other trace gases, the underestimations of $RO_2^*{}_m$ might be due to the underestimation of RO_2^* precursors or NO_x in the plumes. A detailed study comparing the $RO_2^*{}_m$ and the CMAQ model result is beyond the scope of this study. On the other hand, the HO_2 to RO_2^* ratio calculated from the CMAQ results is around 50 % for both upwind and downwind measurements and is in reasonable agreement with the assumption used to retrieve $RO_2^*{}_m$ and $RO_2^*{}_c$. The uncertainty in $RO_2^*{}_m$ from the variations in the HO_2:RO_2 ratio due to different sensitivities for HO_2 and RO_2 (section 3.2.7) is expected to be < 5 % as the calculated ratio from CMAQ remains around 50 %.

In summary, during the measurement near Manila, in both upwind and downwind measurements, the RO_2^* production is dominated by the $O(^1D)$ reaction with H_2O and the RO_2^* loss is dominated by the $HO_2 - RO_2$ and $HO_2 - HO_2$ reactions. The uncertainty of $RO_2^*{}_c$ calculated from the uncertainties of the measurements used in Eq. 4.16 is around 20 %, and $RO_2^*{}_m$ and $RO_2^*{}_c$ agree within the uncertainties except inside the pollution plumes. Even though the HONO measurements uncertainty is higher than 60 %, the contribution to the $RO_2^*{}_c$ uncertainty is < 10 % since the HONO contribution to the RO_2^* production remains less than 10 % over the period considered.

Flight E-AS-10

Figure 4.20 shows the 2D and zoom-in 3D representation of the flight track near Manila from flight E-AS-10. The flight tracks are colour-coded with: a) altitude; b) $RO_2^*{}_m$, c) CO; and d) NO. As can be seen from the flight tracks, E-AS-10 made a similar flight pattern to E-AS-06 with vertical profiling on both upwind and downwind of Manila to distinguish Manila outflow from the background. Different flight legs near Manila are marked with letters A to K. FLEXTRA backward trajectories indicate that the measured air masses over the west side of Manila were transported over Manila in the PBL before reaching the sampling point.
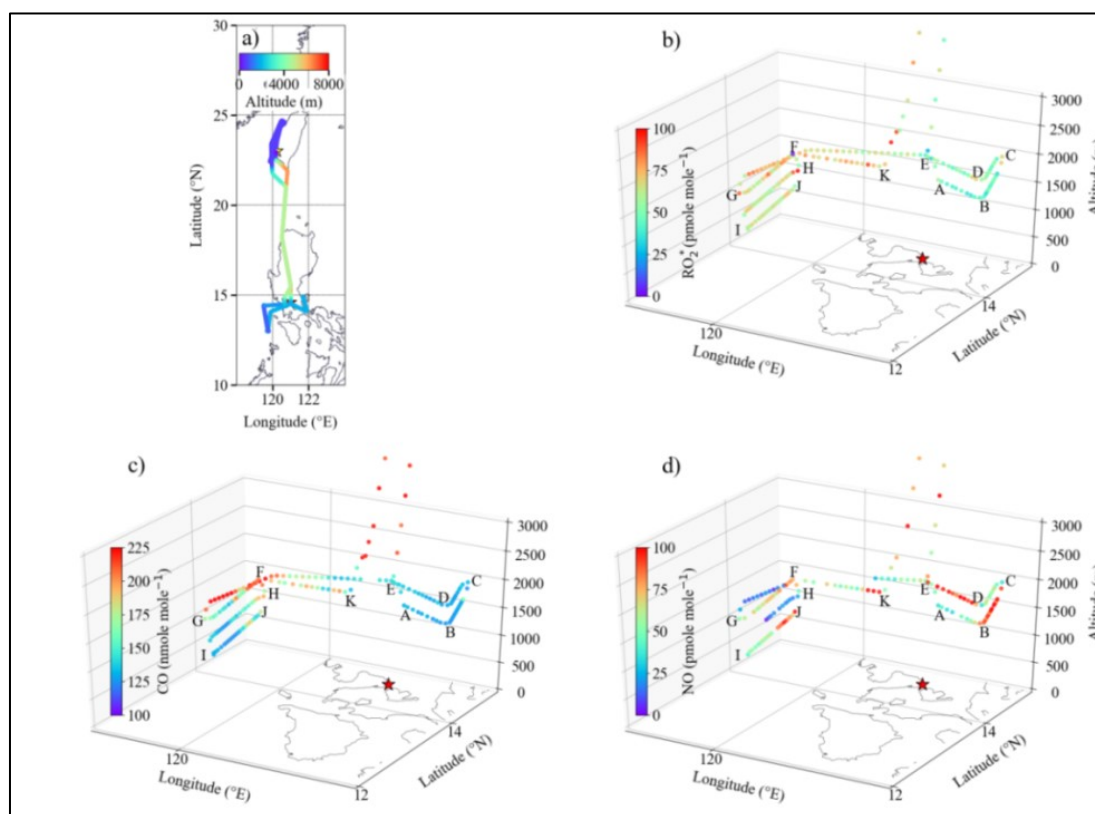
Figure 4.20: E-AS-10 flight on 28.03.2018 a) flight tracks colour-coded with flight altitude and zoom-in 3D view of the flight track near Manila colour-coded with b) $RO_2{}^*{}_m$, c) CO, and d) NO mixing ratios. Stars indicate the target MPC Manila (red) and the HALO base in Tainan (yellow). Different flight legs near Manila are also marked with letters from A to K.

Similarly to flight E-AS-06, the forecasting predicted wind blow from east to west over Manila. At point A, HALO descended to 1500 m for upwind measurements on the east side of Manila. Between A–B and B–C, upwind measurements were made at 1500 m. At point C, HALO ascended to 2000 m and repeated the upwind measurements between C–D and D–E at 2000 m. At point F, HALO reached the predicted outflow region and made altitude profiling over the west coast at 2000, 1600, 1300, and 1000 m between the points F–G, G–H, H–I, and I–J, respectively. From point J, HALO ascended to 1650 m and flew towards Manilla till K. From K, HALO ascended to 5000 m and flew back to Taiwan. Unlike flight E-AS-06, only the CO mixing ratio was enhanced during the measurements over the west coast compared to the measurements over the east coast. Even though the air masses were expected to contain emission signatures of Manila according to FLEXTRA backward trajectories, NO measurements indicate flight E-AS-10 has less amount of NO_x than in flight E-AS-06. As a result, $RO_2{}^*{}_m \leq 80$ pmole mole^{-1} is observed in flight E-AS-10 even though the photolysis frequency and $[H_2O]$ are comparable with those from E-AS-06.

Figure 4.21 shows the variation of $RO_2{}^*{}_m$, $RO_2{}^*{}_c$, other trace gas measurements, and photolysis frequencies along the flight track near Manila from E-AS-10. Different flight legs are marked with vertical lines and letters (A to K). Panel e) in Figure 4.21 shows the HYSPLIT modelled CO enhancement over the background concentration due to emissions originating from Manila. In

addition, based on HYSPLIT simulations, the measurements expected to contain emissions from Manila are highlighted with grey vertical spans.

The upwind measurements were made in a single layer as indicated by the stable mixing ratio of O_3 and CO of 50 and 130 nmole mole^{-1}, respectively, throughout the measurements. According to FLEXTRA backward trajectories, the upwind measurement in both 1500 (A–B and B–C) and 2000 m (C–D and D–E) altitudes were influenced by local emissions from the land. The NO mixing ratio of 100 pmole mole^{-1} observed during the measurements between B–C and D–E indicates the presence of fresh emissions from the east coast. The $RO_2^*{}_m$ was around 40 to 60 pmole mole^{-1} throughout the upwind measurement. The high variations in the $j_{O(^1D)}$ between A–B, B–C, and C–D indicates the presence of clouds above the aircraft. Precisely at these positions, CHOCHO and HONO measurements from the remote sensing instrument miniDOAS show enhancements and reach up to 5 nmole mole^{-1} and 150 pmole mole^{-1}, respectively, where all the other in-situ trace gas measurements show a stable value. The peak in the measurements from the remote sensing instruments might be an artefact coming from the mixing ratio retrieval under cloudy conditions. On the other hand, the NO_2 measurement from the miniDOAS remains stable at around 150 pmole mole^{-1}. Due to the increases in CHOCHO and HONO, the contribution from their photolysis in the production rate increases from 10 % to 15 % and 15 % to 30 %, respectively, under cloudy conditions (figure 4.22). As a result, $RO_2^*{}_c$ overestimate $RO_2^*{}_m$ by 40 to 50 pmole mole^{-1}. As shown in Figure 4.22, the $O(^1D)$ reaction with H_2O contributes more than 50 % to the total production rate, and HCHO photolysis contributes around 15 % for the upwind measurements. The $HO_2 - RO_2$ and $HO_2 - HO_2$ reactions were the main loss process of RO_2^* and are > 80 % of the total. The loss through HO_2 uptake on aerosol and HONO and HNO_3 formation is < 10 %. The difference between the RO_2^* production and loss rates varies around 0.5 pmole mole^{-1} s^{-1}. This also confirms that the RO_2^* production is overestimated in the upwind measurements.

In the downwind measurements of Manila, three different pollution layers were encountered. The first layer was observed during the measurement above 1500 m, i.e. between F–G at an altitude of 2000 m and between G–H at an altitude of 1650 m. During this period, CO increases up to 250 nmole mole^{-1} and remains above 200 nmole mole^{-1}. The VOC mixing ratios and the ASA also increase during this period. On the other hand, the NO mixing ratio remains < 40 pmole mole^{-1}. Due to the enhancement in the RO_2^* precursors (e.g. VOCs), $RO_2^*{}_m$ reaches up to 80 pmole mole^{-1} and remains above 60 pmole mole^{-1}. The second layer was observed during the measurement between H–I at an altitude of 1300 m. All trace gas measurements except RO_2^* and NO_2 have stable and similar values to the upwind measurements during this flight leg. $RO_2^*{}_m$ remains stable around 60 pmole mole^{-1}, which is 20 pmole mole^{-1} higher than the upwind measurements. This increase might be due to the higher and stable photolysis frequencies under the clear sky observed during this period. The third layer was observed between I–J at 1000 m. All the trace gases show an enhancement near point J, indicating the

presence of a pollution plume. Inside the plume, $RO_2{^*}_m$ reaches 75 pmole mole^{-1}. During the measurements between J–K, the in-situ measurements indicate the presence of a pollution plume. According to FLEXTRA and HYSPLIT model results, these were also Manila outflow. Due to the increase in VOCs, the $RO_2{^*}_m$ reaches up to 80 pmole mole^{-1}. HYSPLIT showed four times smaller CO enhancement in E-AS-10 than in E-AS-06. In contrast, the CO, O_3, H_2O, NO, NO_2, and NO_y mixing ratios were similar in E-AS-06 and E-AS-10. The HONO measurements in E-AS-10 are around 20 pmole mole^{-1} higher than that in E-AS-06. On the other hand, the $\sum$VOCs were almost 1 nmole mole^{-1} smaller during E-AS-10 than during E-AS-06 near Manila. This might be the reason for the 20 pmole mole^{-1} lower $RO_2{^*}_m$ observed during E-AS-10 compared to E-AS-06.

Even though $RO_2{^*}_c$ has better agreement with $RO_2{^*}_m$ for downwind measurements than for upwind measurements in flight E-AS-10, short-term variations in the pollution plume are not captured by $RO_2{^*}_c$. The contribution from the $RO_2{^*}$ sources considered in Eq. 4.16 remains almost similar in the upwind and downwind measurements. The O_3, HCHO, CHOCHO, and HONO photolysis contribute around 60 %, 20 %, 10 %, and 10 %, respectively. Outside the pollution plumes, the overall loss contributions are similar to that of upwind measurements. Inside the pollution plumes, the contribution from the HO_2 uptake on aerosol increases up to 40 % due to increased aerosol loading. As a result, the loss through $HO_2 - RO_2$ and $HO_2 - HO_2$ reactions reduces to 60 % inside the pollution plumes. The HONO and HNO_3 formation contribution to the $RO_2{^*}$ loss remains < 10 %, as the NO mixing ratio was $\leq$ 100 pmole mole^{-1} during the measurement near Manila (Figure 4.21). The uncertainty of $RO_2{^*}_c$ calculated from the uncertainties of the measurements used in Eq. 4.16 is around 20 % throughout the flight. In the downwind measurements, the difference between the total $RO_2{^*}$ production and loss rates is within the uncertainties indicating that the relevant processes in $RO_2{^*}$ production and loss are considered in Eq. 4.16.
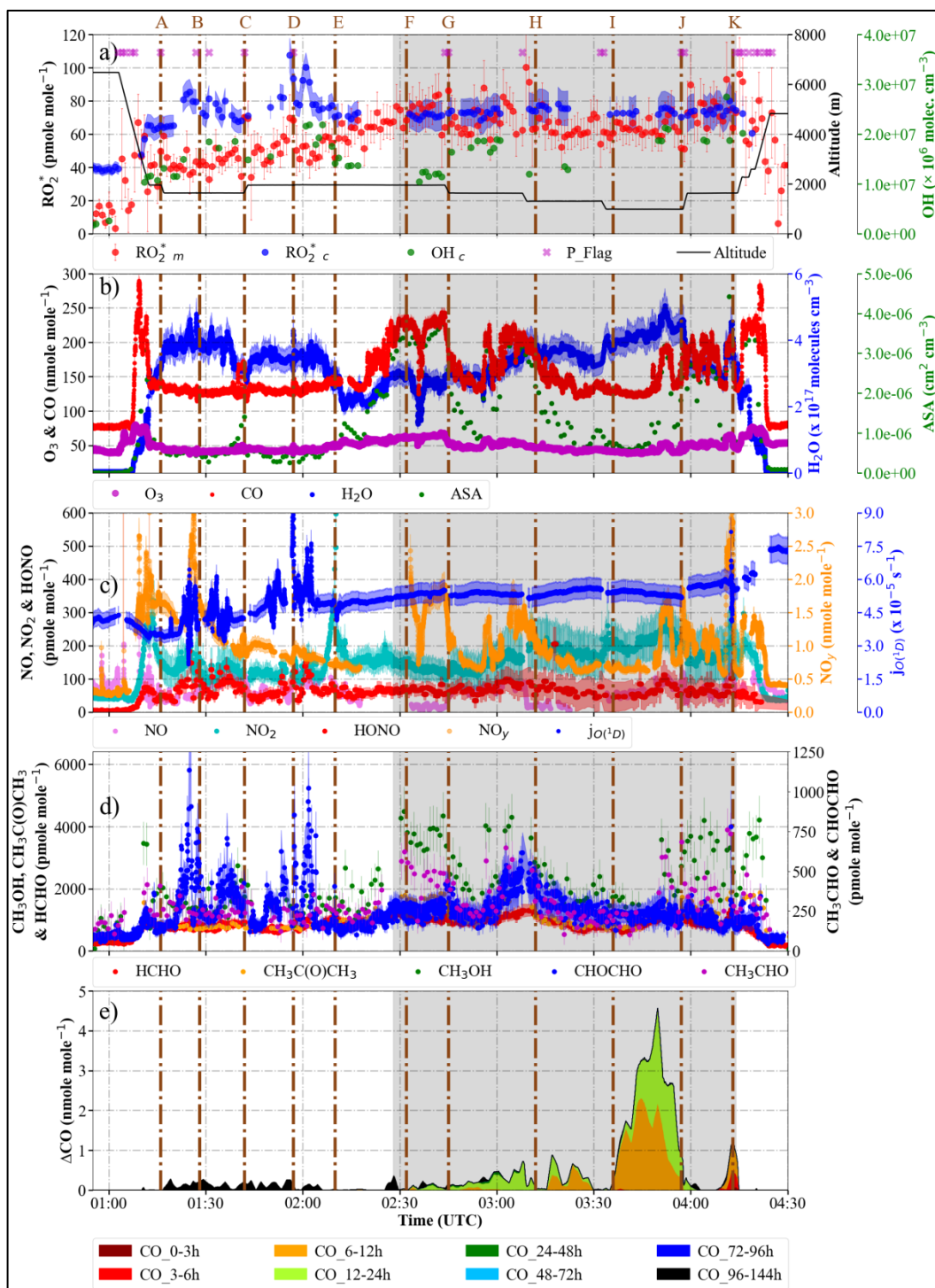
Figure 4.21: Variation of $RO_2^*{}_m$ and $RO_2^*{}_c$, selected RO_2^* precursors and $j_{O(^1D)}$ along the flight track near Manila from E-AS-10. a) $RO_2^*{}_m$, $RO_2^*{}_c$ using Eq. 4.16, OH_c using Eq. 4.18 discussed in section 4.1.7, and flight altitude. The P_flag indicates RO_2^* measurements affected by dynamical pressure variation in the inlet. b) O_3 and CO mixing ratios together with H_2O and ASA (total aerosol surface area concentration). c) NO, NO_2, HONO, NO_y mixing ratios and $j_{O(^1D)}$. d) HCHO, CH_3CHO, CH_3OH, CHOCHO and $CH_3C(O)CH_3$ mixing ratios measurements. e) HYSPLIT model results of CO enhancement over background concentration due to emissions originating from the target MPC Manila (02:25-04:15 UTC). The error bar shows the standard error of the measurements. Based on HYSPLIT simulations, the measurements expected to contain the emission from Manila are highlighted with grey vertical spans. Different flight legs near Manila are also marked with vertical lines and letters from A to K.
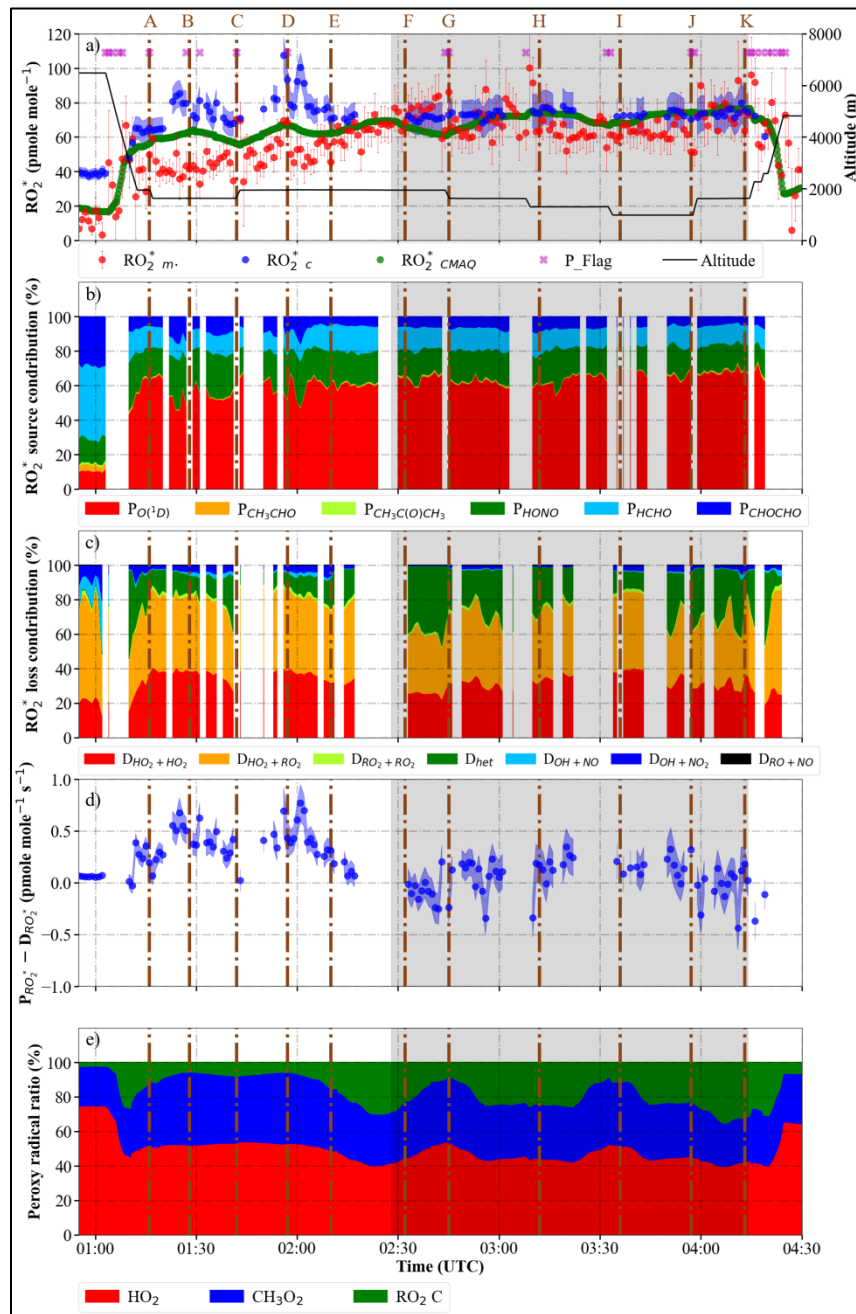
Figure 4.22: Variation of $RO_2^*{}_m$ and $RO_2^*{}_c$, $RO_2^*{}_{CMAQ}$ (sum of $HO_2{}_{CMAQ}$, $CH_3O_2{}_{CMAQ}$, and RO_2 C $_{CMAQ}$ modelled using the CMAQ. RO_2 C $_{CMAQ}$ is the organic peroxy radical other than CH_3O_2 that converts NO to NO_2), RO_2^* production and loss contribution from each term in Eq. 4.16 along the flight track near Manila from E-AS-10. a) $RO_2^*{}_m$, $RO_2^*{}_c$, $RO_2^*{}_{CMAQ}$ ($HO_2{}_{CMAQ}$ + $CH_3O_2{}_{CMAQ}$ + RO_2 C $_{CMAQ}$, where RO_2 C is the sum of organic peroxy radicals other than that convert NO to NO_2) and flight altitude. The P_flag indicates RO_2^* measurements affected by dynamical pressure variations in the inlet. b) RO_2^* source contribution from R4.1, R4.3, R4.8, R4.9, R4.10, and R4.11. c) The contribution of R4.14 ($D_{HO_2+HO_2}$), R4.15 ($D_{HO_2+RO_2}$), R4.16 ($D_{RO_2+RO_2}$), R4.19 (D_{OH+NO}), R4.20 (D_{OH+NO_2}), R4.22 (D_{RO+NO}), and HO_2 uptake on aerosol (D_{het}) to RO_2^* loss. d) the difference between the total production ($P_{RO_2^*}$) and destruction ($D_{RO_2^*}$) rate with standard errors estimated from the measurement uncertainty. e) ratio of HO_2, CH_3O_2, and RO_2 converting NO to NO_2 other than CH_3O_2 modelled using the CMAQ model. Based on HYSPLIT simulations, the measurements expected to contain the emission from Manila are highlighted with grey vertical spans. Different flight legs near Manila are also marked with vertical lines and letters from A to K.

$RO_2^*{}_{CMAQ}$ model shows good agreement with $RO_2^*{}_c$ and fails to calculate the short-term variations observed in $RO_2^*{}_m$ inside the plumes. In addition, upwind $RO_2^*{}_m$ is 50 % overestimated between points A–C, where the local clouds reduced the photolysis frequencies, which are not accounted for in the model. The HO_2 to RO_2^* ratio calculated from the model results is around 50 % during upwind and downwind measurements. Under this HO_2 to RO_2^* ratio, the uncertainty from the HO_2 to RO_2 ratio variations on $RO_2^*{}_m$ due to different sensitivities for HO_2 and RO_2 (section 3.2.7) is expected to be < 5 %.

In summary, the photolysis frequencies and trace gases like VOCs and H_2O observed during the upwind measurements in both E-AS-06 and E-AS-10 were similar. As a result, the $RO_2^*{}_m$ observed during the upwind measurements of Manila in both flights was similar, around 50 pmole mole^{-1}. On the other hand, $RO_2^*{}_c$ overestimated $RO_2^*{}_m$ during the upwind measurements in E-AS-10 due to the uncertainties in the remote sensing instruments under cloudy conditions. During upwind measurements under cloud-free conditions in E-AS-06, $RO_2^*{}_c$ agrees reasonably well with $RO_2^*{}_m$. Similarly, $RO_2^*{}_{CMAQ}$ values are closer to $RO_2^*{}_m$ and $RO_2^*{}_c$ in E-AS-06 than in E-AS-10. The overestimation of $RO_2^*{}_m$ by $RO_2^*{}_{CMAQ}$ in-flight E-AS-10 is attributed to the overestimation of photolysis frequencies by the model under cloudy conditions. This indicates the necessity of constraining the model with onboard measurements. In both flights, E-AS-10 and E-AS-06, the $RO_2^*{}_m$ is higher in downwind than upwind Manila. As mentioned earlier, $\sum$VOCs were almost 1 nmole mole^{-1} smaller during the downwind measurements of flight E-AS-10 compared to E-AS-06. As a result, the $RO_2^*{}_m$ observed in pollution plumes during E-AS-10 is 20 pmole mole^{-1} smaller than that observed during E-AS-06. The underestimation of $RO_2^*{}_m$ by $RO_2^*{}_c$ downwind Manila is higher for E-AS-06, where $\sum$VOCs are also higher. This indicates that the processes considered in Eq. 4.16 are not adequate to represent the RO_2^* production from VOCs inside the pollution plums. $RO_2^*{}_{CMAQ}$ in the downwind measurements of both flights agrees well with the $RO_2^*{}_c$ but fails to capture short-term variations of $RO_2^*{}_m$ inside the pollution plume. A 20 % increase in $RO_2^*{}_m$ is observed in the downwind measurements from both flights. This is attributed to increased RO_2^* production due to the increase in OVOCs in the downwind measurements.

During the measurements in both E-AS-06 and E-AS-10, the RO_2^* production was primarily dominated by the O_3 photolysis during upwind and downwind measurements. The HCHO photolysis contribution was around 20 % in both flights. The RO_2^* loss was mainly through the $HO_2 - RO_2$ and $HO_2 - HO_2$ reactions in both upwind and downwind measurements. The RO_2^* loss through HO_2 uptake on aerosol was < 20 % during measurements outside pollution plumes and reached up to 40 % inside pollution plumes.

4.1.6 Special Case Study: Taiwan

The measurements during flight E-AS-12 on 03.04.2018 around Taiwan were made to investigate the outflow from Taiwan and the impact of long-range transport from other target East

Asian MPCs on the air quality of Taiwan. Several flight legs were carried out on the east and west coast of Taiwan for upwind and downwind measurements, respectively. The measurements from the west coast of Taiwan were investigated in detail to understand the RO_2^* production and losses close to emission sources with NO > 800 pmole mole^{-1}.

Figure 4.23 shows the 2D and zoom in 3D representation of the flight legs below 2000 m of E-AS-12 colour-coded with: a) altitude; b) $RO_2^*{}_m$, c) CO; and d) NO. The flight took place under mostly clear sky conditions with some high clouds above the aircraft. As mentioned in section 4.1.2, the miniDOAS measurements were not available during this flight due to instrumental malfunction. As a result, the production rate and the $RO_2^*{}_c$ presented in this section do not include HONO, HCHO, and CHOCHO photolysis. The NO_2 used in Eq. 4.16 is taken from the HAIDI measurements. According to the FLEXTRA back trajectories, the measurements below 1000 m over the west coast were mainly in the PBL. On the other hand, the measurements over the east coast were made in the free troposphere from 5000 m to 12500 m.
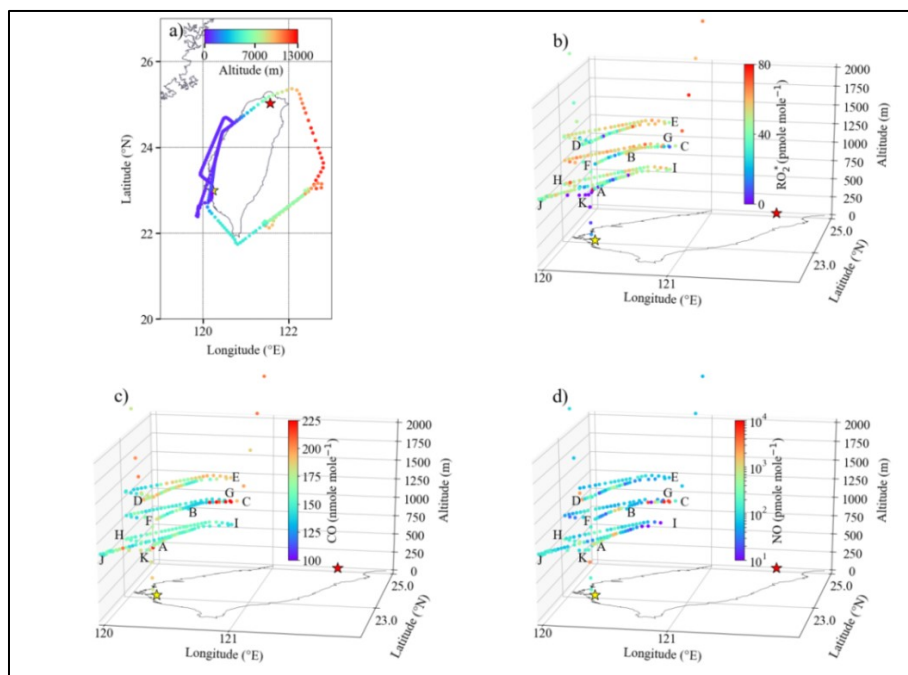
Figure 4.23: E-AS-12 flight on 03.04.2018: a) flight tracks colour-coded with flight altitude and zoom-in 3D view of the flight track on the west coast of Taiwan colour-coded with b) $RO_2^*{}_m$, c) CO, and d) NO mixing ratios. Stars indicate the target MPC Taipei (red) and the HALO base in Tainan (yellow). Different flight legs are also marked with letters from A to K.

The flight took off at 00:25 UTC and flew towards the north over the west coast of Taiwan. Between A–B, HALO flew at 650 m and between B–C at 1000 m. According to FLEXTRA and HYSPLIT model simulations, air masses sampled during these flight legs were expected to contain pollution from China and Taiwan. Between A–B, distinct pollution plumes were measured as indicated by the variations observed in CO, NO, NO_y, and ASA (Figure 4.24). The CO, NO, and NO_y reach up to 300, 6, and 11 nmole mole^{-1}, respectively, inside the plume near B. The high NO mixing ratio indicates the presence of regional emissions from Taiwan. The ASA is > 2×10^{-6} cm^2 cm^{-3} during

this period. The low-resolution OVOCs measurements also show enhancement between A–B. The $CH_3C(O)CH_3$, CH_3OH, and CH_3CHO mixing ratios reach up to 2, 4, and 1 nmole mole^{-1}, respectively, inside the plume. This indicates a high amount of RO_2^* precursors. As this flight leg was in the morning, around 08:30 h local time, $j_{O(^1D)} \leq 1.5 \times 10^{-5}$ s^{-1}. As a result of low photolysis frequencies and NO > 500 pmole mole^{-1}, $RO_2^*{}_m$ < 50 pmole mole^{-1} during this flight leg. $RO_2^*{}_m$ decreases to 20 pmole mole^{-1} inside the plume near B even though the [H_2O], OVOCs, and photolysis frequencies do not vary significantly. The decrease in $RO_2^*{}_m$ is due to the loss of OH and RO as non-reactive nitrogen species during the interconversion under a high amount of NO_x (NO = 6 nmole mole^{-1}). As shown in figure 4.25, during this time, the formation of HONO, HNO_3, and organic nitrites dominates the loss of RO_2^*. O_3, on the other hand, was < 50 nmole mole^{-1} and increased to 50 nmole mole^{-1} as HALO moved from A to B. As HALO ascended to 1000 m and flew from B–C, a different pollution layer was encountered with lower and more stable CO, NO, NO_y mixing ratios, and ASA than the previous flight leg. The lower NO and ASA reduced the RO_2^* losses. The reduced RO_2^* losses and increases in the photolysis frequencies resulted in $RO_2^*{}_m \geq 60$ pmole mole^{-1} even though the [H_2O] and OVOCs were less than the previous flight leg. Near point C, CO, NO, and NO_y mixing ratios increase to 1200, 43, and 60 nmole mole^{-1}, respectively. This indicates the presence of a fresh urban pollution plume. Even though the $CH_3C(O)CH_3$, CH_3CHO and CH_3OH remained stable around 1.6, 0.5, and 2.4 nmole mole^{-1}, respectively, the $RO_2^*{}_m$ decreased to 40 pmole mole^{-1} inside the plume. This is due to the loss of OH and RO as HONO, HNO_3, and organic nitrites during the interconversion. As indicated by the background CO enhancement from the HYSPLIT model, outflow from Taipei aged between 24 to 144 hours was expected between points A and C. At point C, where HALO started to ascend, all trace gas mixing ratios increased. According to the onboard measurements, the wind was flowing towards the north at this point. This indicates that the air mass measured was transported over Taipei. The HYSPLIT results also indicate the presence of Taipei outflow as HALO moves to the east side of Taiwan around Taipei. During this time, O_3 and $RO_2^*{}_m$ reach 100 nmole mole^{-1} and 80 pmole mole^{-1}, respectively.

The $RO_2^*{}_c$ between A–C underestimates the $RO_2^*{}_m$ up to 50 %. This is attributed to the RO_2^* production from HCHO, CHOCHO, and HONO photolysis not being considered in the calculation due to missing measurements. As the photolysis of these RO_2^* precursors takes place at a longer wavelength than that for O_3, the relative importance of HCHO, CHOCHO, and HONO photolysis is expected to be higher in the morning due to a higher solar zenith angle. The difference between the total RO_2^* production and destruction rates also indicates missing production rates. The additional RO_2^* source contributions calculated using the HCHO and HONO estimated from the CMAQ model result in an additional RO_2^* source of 50 % (Figure 4.25b). This confirms that missing measurements of HCHO and HONO cause the underestimation of $RO_2^*{}_m$ by $RO_2^*{}_c$. $RO_2^*{}_{CMAQ}$ also underestimates $RO_2^*{}_m$ during flight legs between A–C. The underestimation is mainly due to the overestimation of NO_x and underestimation of VOCs by the model during this period. The loss of RO_2^* outside the

pollution plume was dominated by the $HO_2 - RO_2$ and $HO_2 - HO_2$ reactions. RO_2^* loss inside the pollution plumes was through HONO and HNO_3 formation. The HO_2 to RO_2^* ratio calculated from the model results is < 60 % during the measurements between A–C. This indicates that the uncertainty in $RO_2^*{}_m$ from the HO_2 to RO_2^* ratio due to different sensitivities for HO_2 and RO_2 (section 3.2.7) is around 8 % to 10 %.
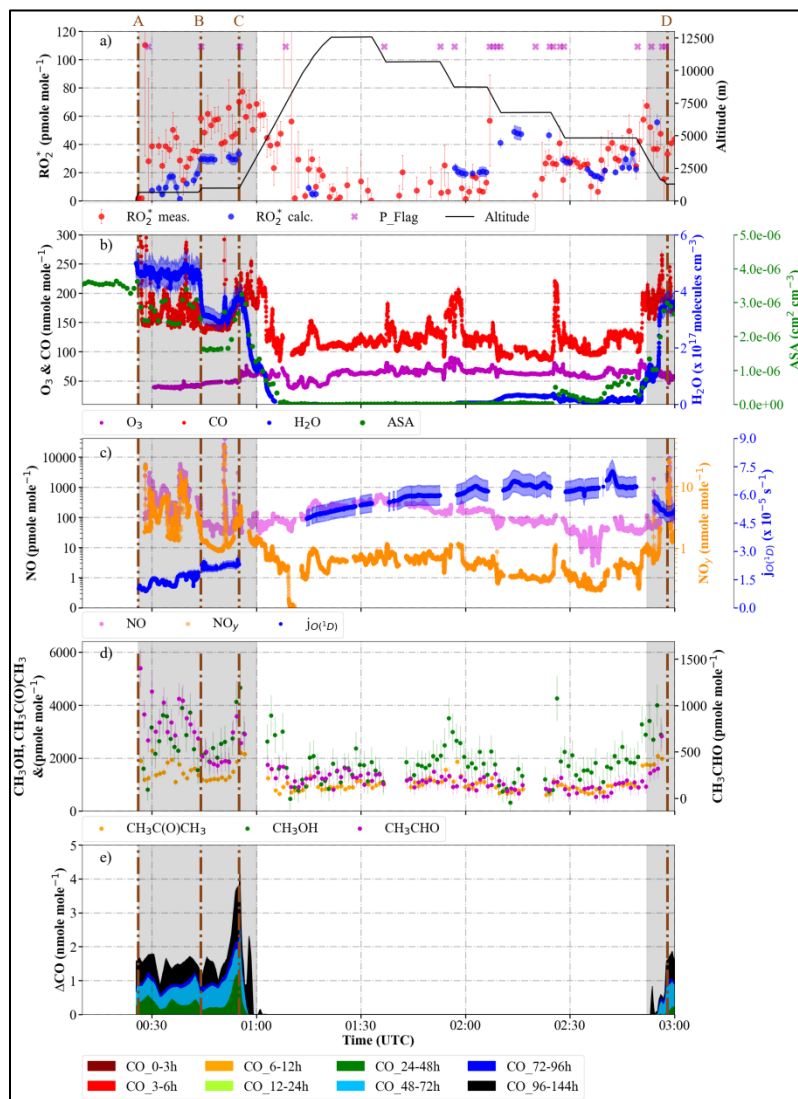
Figure 4.24: Variation of $RO_2^*{}_m$ and $RO_2^*{}_c$, selected RO_2^* precursors and $j_{O(^1D)}$ along the flight track of E-AS-12 from take-off till 03:00. a) $RO_2^*{}_m$, $RO_2^*{}_c$ using Eq. 4.16, OH_c using Eq. 4.18 discussed in section 4.1.7, and flight altitude. The P_flag indicates RO_2^* measurements affected by dynamical pressure variation in the inlet. b) O_3 and CO mixing ratios together with H_2O and ASA (total aerosol surface area concentration). c) NO, NO_y mixing ratios, and $j_{O(^1D)}$. The scale of NO and NO_y is in logarithmic scale to account for the variations during the flight. d) HCHO, CH_3CHO, CH_3OH, CHOCHO and $CH_3C(O)CH_3$ mixing ratios measurements. e) HYSPLIT model results in CO enhancement over background concentration due to emissions originating from the target MPCs Taipei (00:15-01:00 and 03:00-06:30 UTC). The error bars show the standard error of the measurements. Based on HYSPLIT simulations, the measurements expected to contain the emission from Taiwan are highlighted with grey vertical spans. Different flight legs in the boundary layer are also marked with vertical lines and letters from A to D.

Figure 4.25: Variation of $RO_2^*{}_m$ and $RO_2^*{}_c$, $RO_2^*{}_{CMAQ}$ (sum of $HO_2{}_{CMAQ}$, $CH_3O_2{}_{CMAQ}$, and RO_2 C_{CMAQ} modelled using the CMAQ. RO_2 C_{CMAQ} is the organic peroxy radical other than CH_3O_2 that converts NO to NO_2), RO_2^* production and loss contribution from each term in Eq. 4.16 along the flight track of E-AS-12 from take-off till 03:00. a) $RO_2^*{}_m$, $RO_2^*{}_c$, $RO_2^*{}_{CMAQ}$ ($HO_2{}_{CMAQ}$ + $CH_3O_2{}_{CMAQ}$ + RO_2 C_{CMAQ}, where RO_2 C is the sum of organic peroxy radicals other than that convert NO to NO_2) and flight altitude. The P_flag indicates RO_2^* measurements affected with dynamical pressure variation in the inlet. b) RO_2^* source contribution from R4.1, R4.9, and R4.10. The additional RO_2^* source contributions from R4.3 and R4.8 calculated using HONO and HCHO estimated using the CMAQ model are also shown as the contribution above 100 %. c) The contribution of R4.14 ($D_{HO_2+HO_2}$), R4.15 ($D_{HO_2+RO_2}$), R4.16 ($D_{RO_2+RO_2}$), R4.19 (D_{OH+NO}), R4.20 (D_{OH+NO_2}), R4.22 (D_{RO+NO}), and HO_2 uptake on aerosol (D_{het}) to RO_2^* loss. d) the difference between the total production ($P_{RO_2^*}$) and destruction ($D_{RO_2^*}$) rate with standard errors estimated from the measurement uncertainty. e) ratio of HO_2, CH_3O_2, and RO_2 converting NO to NO_2 other than CH_3O_2 modelled using the CMAQ model. Based on HYSPLIT simulations, the measurements expected to contain the emission from Taiwan are highlighted with grey vertical spans. Different flight legs in the boundary layer are also marked with vertical lines and letters from A to D.
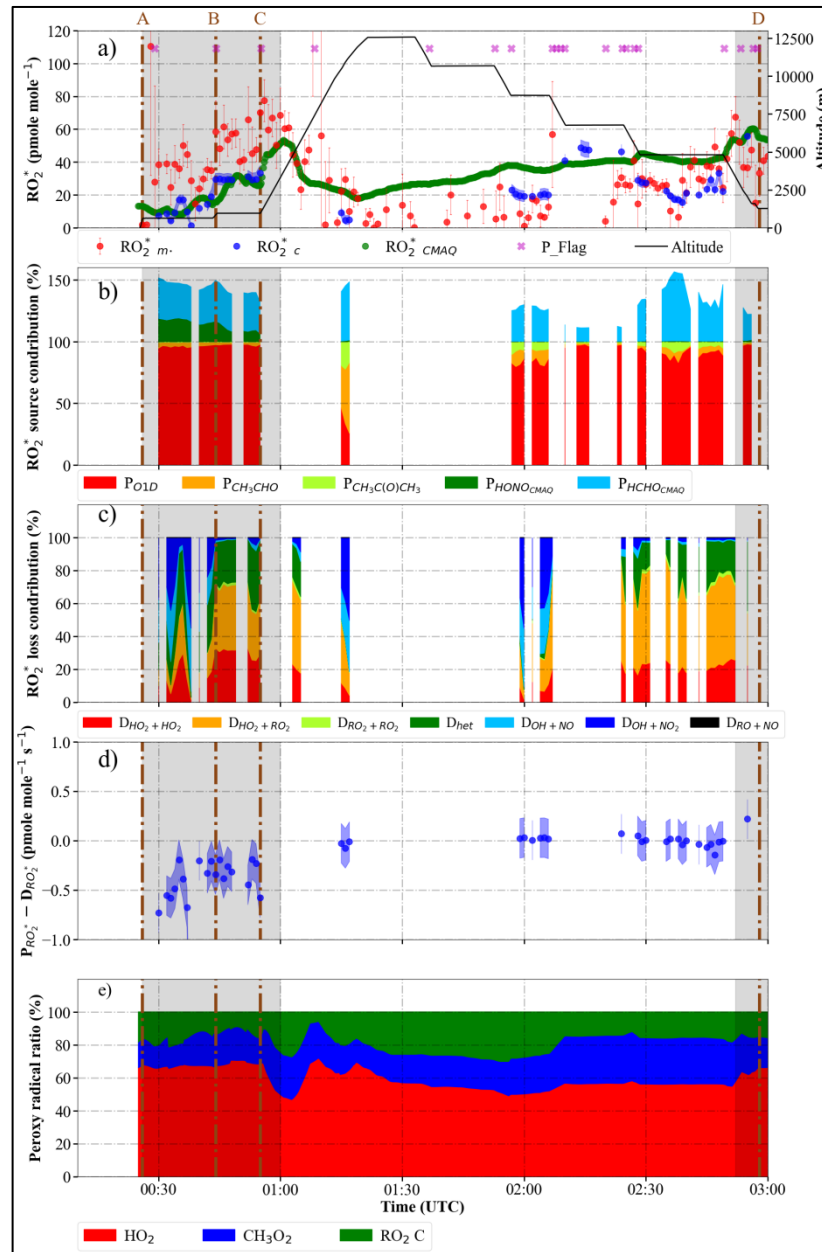
From point C to D, HALO made five flight legs over the east coast at 12500, 10600, 8700, 6700, and 4800 m. The altitudes above 10000 m were made for background measurements. During the measurements above 5000 m between C–D over the east coast of Taiwan, the $RO_2^*{}_m$ was below 20 pmole mole^{-1} and most of the time close to the detection limit of PeRCEAS. The RO_2^* calculated from the CMAQ model overestimates $RO_2^*{}_m$ up to four times during this period. More detailed sensitivity studies are necessary to understand the reason for this overestimation, which is beyond the scope of this work. As the ASA was close to zero, the contribution of the heterogeneous reaction of HO_2 to the total RO_2^* loss was negligibly small. The loss through the $HO_2 - RO_2$ and $HO_2 - HO_2$ reactions is also small due to the lower RO_2^* mixing ratio and the pressure dependency of the $HO_2 - HO_2$ reaction. $RO_2^*{}_c$ is not available during the measurements at 12500 and 10600 m due to missing trace gas measurements.

At point D, HALO reached the west coast of Taiwan south of Tainan and descended to 1300 m. From D to J, HALO made shuttles at 1300 (D–E and E–F), 950 (F–G and G–H), and 650 m (H–I and I–J) over the west coast of Taiwan, measuring the outflow in three different layers. HALO flew north between D–E over the sea. At point D, the mixing ratio of CO, NO, NO_y, and OVOCs increased, indicating air masses containing urban pollution (Figure 4.26). The NO mixing ratio reaches up to 10 nmole mole^{-1}. Despite the elevated concentrations of RO_2^* precursors, the $RO_2^*{}_m$ remains below 20 pmole mole^{-1} due to the high NO (10 nmole mole^{-1}) and ASA ($> 3 \times 10^{-6}$ cm^2 cm^{-3}). As HALO flew out of the plume, there were some clouds, as indicated by the variations in the $j_{O(^1D)}$. The lower photolysis frequencies and higher ASA ($> 3 \times 10^{-6}$ cm^2 cm^{-3}) made $RO_2^*{}_m < 50$ pmole mole^{-1} even outside the plume where NO was below 500 pmole mole^{-1}. As HALO flew from D–E, the trace gas mixing ratios were relatively stable in the first half and increased in the second half except $RO_2^*{}_m$. The $RO_2^*{}_m$ was relatively stable at 60 pmole mole^{-1} during this period. The stable $RO_2^*{}_m$ is attributed to the simultaneous increase in RO_2^* production from VOCs and loss through the heterogeneous reactions of HO_2. HALO flew southwards from E–F at the same altitude as D–E but mainly over land. As HALO flew from E to F, all the trace gas mixing ratios and ASA decreased to the value observed in the first half of D–E. This indicates HALO flew out of the pollution outflow. In the second half of E–F, all measurements except $RO_2^*{}_m$ increased, indicating the presence of pollution outflow. Considering the geolocation and the wind direction, this might be the same pollution outflow layer observed near point D. The ASA reached a value $> 4 \times 10^{-6}$ cm^2 cm^{-3}. The higher NO (< 2 nmole mole^{-1}) and ASA resulted in higher RO_2^* losses. Higher RO_2^* loss and the reduction in photolysis frequencies due to clouds resulted in a reduction of $RO_2^*{}_m$ to 40 pmole mole^{-1} during this period.

At point F, HALO descended to 950 m and flew northwards through the same path of D–E. During this leg, the CO, NO, NO_y, $CH_3C(O)CH_3$, CH_3OH, and CH_3CHO mixing ratios were around 130, 0.1, 0.6, 1.7, 1.9, 0.3 nmole mole^{-1} and did not change significantly. These were the lowest values observed on the west side of Taiwan and were similar to the upwind measurements made at 4800 m on

the southeast side of Taiwan. The HYSPLIT simulations also predict that the air mass measured between F–G was older than 48 hours. The $RO_2^*{}_m$, on the other hand, increased due to the higher $[H_2O]$ and was above 60 pmole mole^{-1} between F–G. From point G, HALO starts to fly southwards through the same path of E–F. Near point G, all the trace gases except $RO_2^*{}_m$ increased. CO, NO, NO_y, O_3, $CH_3C(O)CH_3$, CH_3OH, and CH_3CHO reached 700, 10, 30, 80, 3.5, 3.8, and 0.6 nmol mole^{-1}, respectively. The increase in NO and ASA effectively increased RO_2^* loss and reduced the $RO_2^*{}_m$ to 10 pmole mole^{-1}. As HALO flew towards H, all the measurements were similar to that of the previous flight leg and did not change significantly during the first half. In the second half of the flight leg between G–H, the trace gas and ASA show an increase similar to that observed in the second half of the flight leg between E–F. This indicates that the same outflow layer between E–F is again observed between G–H. $RO_2^*{}_m$ decreases during this period due to the increased NO and lower photolysis frequencies due to clouds above HALO.

At point H, HALO descended to 650 m and flew towards the north in the same path as D–E and F–G. During the flight between H-I, all the measurements except $RO_2^*{}_m$ were similar to those observed between F–G. This indicates that the same outflow layer was observed between F–G at 950 m and H–I at 650 m. $RO_2^*{}_m$ was around 40 to 60 pmole mole^{-1} during the flight leg H–I, 10 to 20 pmole mole^{-1} smaller than during F–G. This is due to the decrease in the photolysis frequencies towards the evening. At point I, HALO started to fly towards the South in the same path as E–F and G–H. The NO and NO_y mixing ratios have high variability during this flight leg, indicating the presence of distinct pollutions. The NO and NO_y mixing ratios reach up to 2 and 10 nmole mole^{-1}, respectively, in two plumes encountered at the middle of the flight leg I–J. CO and O_3 mixing ratios also increased from 130 to 175 and 40 to 60 nmole mole^{-1}, respectively. The CH_3CHO mixing ratio reaches 1.3 nmole mole^{-1} at the middle of the flight leg. The $RO_2^*{}_m$ mixing ratio of 50 pmole mole^{-1} decreased below 20 pmole mole^{-1} during the NO peaks due to increased RO_2^* losses. From point J, HALO flew towards Tainan and landed at the base.

The slow decrease of $RO_2^*{}_m$ from D–J is well correlated to the decrease in the $j_{O(^1D)}$. The $RO_2^*{}_c$ captures the temporal variations but underestimates $RO_2^*{}_m$ by 10 % to 30 % at different flight legs. The production of RO_2^* in Eq. 4.16 is mainly from O_3 photolysis, as the HCHO, CHOCHO, and HONO photolysis were not included in the production rate calculation. The RO_2^* production from the photolysis of HCHO and HONO calculated using the CMAQ model result indicates the underestimation results from the missing production terms in the calculation (Figure 4.27).
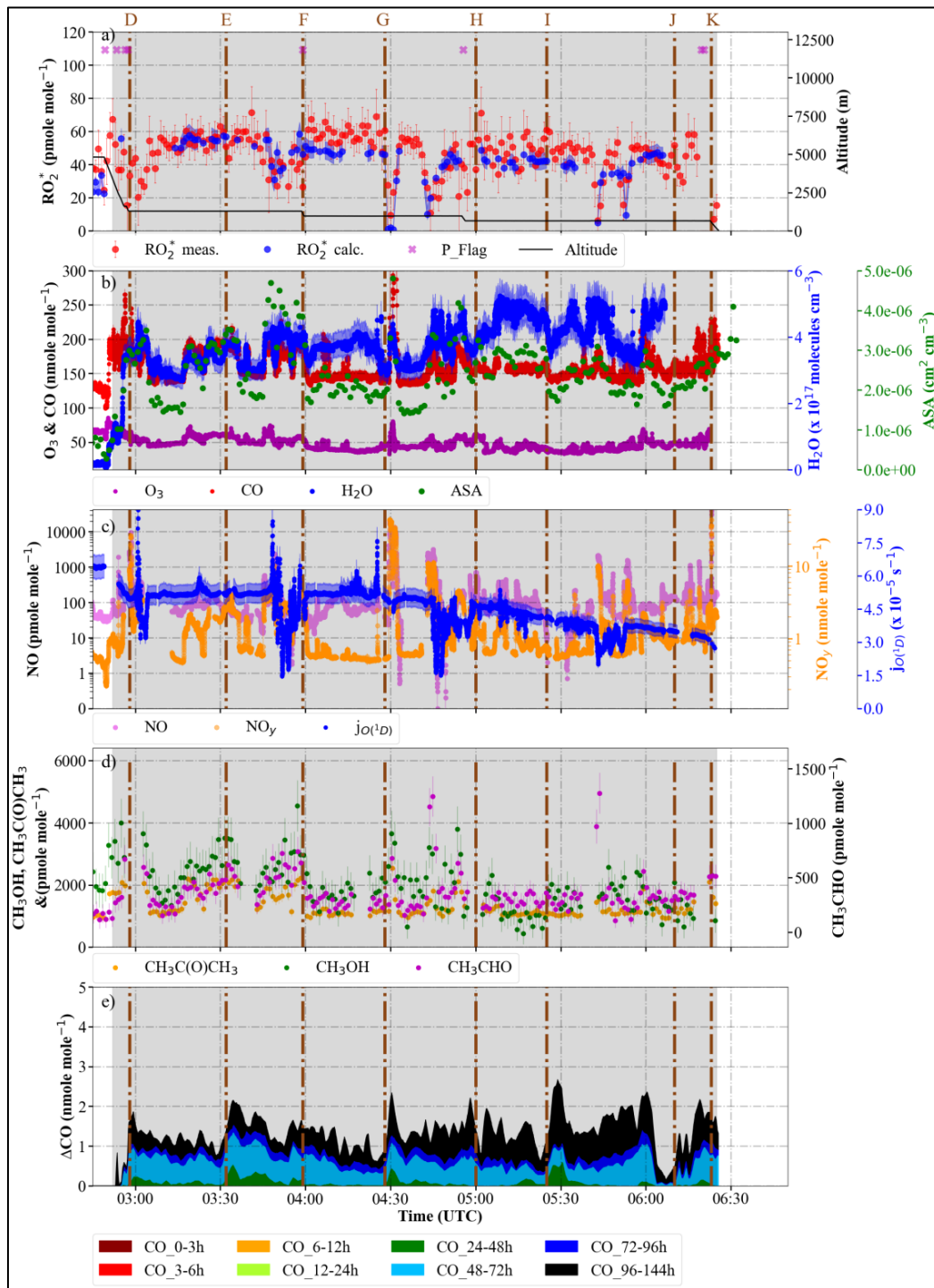
Figure 4.26: Variation of $RO_2^*{}_m$ and $RO_2^*{}_c$, selected RO_2^* precursors and $j_{O(^1D)}$ along the flight track of E-AS-12 from 02:45 UTC till landing. a) $RO_2^*{}_m$, $RO_2^*{}_c$ using Eq. 4.16, OH_c, and flight altitude. The P_flag indicates RO_2^* measurements affected by dynamical pressure variation in the inlet. b) O_3 and CO mixing ratios together with H_2O and ASA (total aerosol surface area concentration). c) NO, NO_y mixing ratios, and $j_{O(^1D)}$. The scale of NO and NO_y is in logarithmic scale to account for the variations during the flight. d) HCHO, CH_3CHO, CH_3OH, CHOCHO and $CH_3C(O)CH_3$ mixing ratios measurements. e) HYSPLIT model results in CO enhancement over background concentration due to emissions originating from the target MPCs Taipei (00:15-01:00 and 03:00-06:30 UTC). The error bars show the standard error of the measurements. Based on HYSPLIT simulations, the measurements expected to contain the emission from Taiwan are highlighted with grey vertical spans. Different flight legs in the boundary layer are also marked with vertical lines and letters from D to K.

Figure 4.27: Variation of $RO_2^*{}_m$ and $RO_2^*{}_c$, $RO_2^*{}_{CMAQ}$ (sum of $HO_2{}_{CMAQ}$, $CH_3O_2{}_{CMAQ}$, and RO_2 C $_{CMAQ}$ modelled using the CMAQ. RO_2 C $_{CMAQ}$ is the organic peroxy radical other than CH_3O_2 that converts NO to NO_2), RO_2^* production and loss contribution from each term in Eq. 4.16 along the flight track of E-AS-12 from 02:45 till landing. a) $RO_2^*{}_m$, $RO_2^*{}_c$, $RO_2^*{}_{CMAQ}$ ($HO_2{}_{CMAQ}$ + $CH_3O_2{}_{CMAQ}$ + RO_2 C $_{CMAQ}$, where RO_2 C is the sum of organic peroxy radicals other than that convert NO to NO_2) and flight altitude. The P_flag indicates RO_2^* measurements affected with dynamical pressure variation in the inlet. b) RO_2^* source contribution from R4.1, R4.9, and R4.10. The additional RO_2^* source contributions from R4.3 and R4.8 calculated using HONO and HCHO estimated using the CMAQ model are also shown as the contribution above 100 %. c) The contribution of R4.14 ($D_{HO_2+HO_2}$), R4.15 ($D_{HO_2+RO_2}$), R4.16 ($D_{RO_2+RO_2}$), R4.19 (D_{OH+NO}), R4.20 (D_{OH+NO_2}), R4.22 (D_{RO+NO}), and HO_2 uptake on aerosol (D_{het}) to RO_2^* loss. d) the difference between the total production ($P_{RO_2^*}$) and destruction ($D_{RO_2^*}$) rate with standard errors estimated from the measurement uncertainty. e) ratio of HO_2, CH_3O_2, and RO_2 converting NO to NO_2 other than CH_3O_2 modelled using the CMAQ model. Based on HYSPLIT simulations, the measurements expected to contain the emission from Taiwan are highlighted with grey vertical spans. Different flight legs in the boundary layer are also marked with vertical lines and letters from D to K.
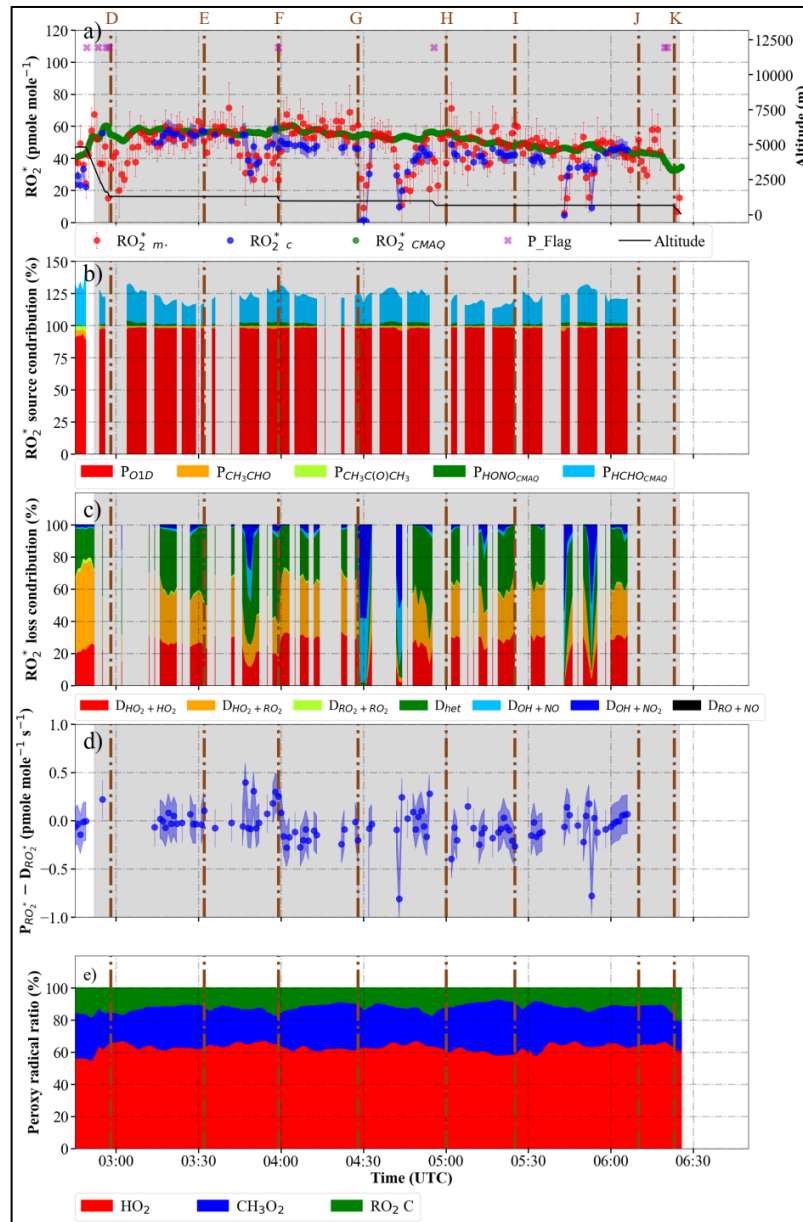
The relative uncertainty of $RO_2{}^*{}_c$ remains < 15 % during this period since the miniDOAS measurements with higher uncertainty than the in-situ measurements are not included in the calculation. In the pollution plumes, the $RO_2{}^*$ loss was mainly through the formation of HONO, HNO3, and organic nitrites due to the high amount of NO_x (NO > 2 pmole mole^{-1}). The loss of HO_2 uptake on aerosol has a relative contribution of up to 40 % when ASA > 4 × 10^{-6} cm^2 cm^{-3}. The loss through the $RO_2{}^* - RO_2{}^*$ reactions is around 60 % outside the pollution plumes and < 40 % inside the pollution plumes. Even though the production from HONO, HCHO, and CHOCHO photolysis is not included in the $RO_2{}^*$ production, the difference between the $RO_2{}^*$ production and destruction rates is small compared to the measurements on the west coast in the morning (Figure 4.25). This indicates that the contribution from the missing production terms is smaller in the measurement between D–K compared to the measurements between A–D in the morning. Since the missing precursor mixing ratios estimated by the CMAQ model and the [H_2O] measurements in both cases, i.e., measurements between A–D and D–K, are comparable, this effect comes from the higher dependency of $j_{O(^1D)}$ on solar zenith angle compared to other photolysis frequencies considered in Eq. 4.16. The HO_2 to $RO_2{}^*$ ratio calculated from the model results is < 60 % during the measurements between A–C. This indicates that the uncertainty in $RO_2{}^*{}_m$ from the HO_2 to $RO_2{}^*$ ratio due to different sensitivities for HO_2 and RO_2 (section 3.2.7) is around 8 % to 10 %.

Even though the $RO_2{}^*{}_{CMAQ}$ has an excellent agreement with the $RO_2{}^*{}_m$ for measurements below 5000 m, the model fails to reproduce the short-term decreases in $RO_2{}^*{}_m$ caused by the increases in NO and ASA and decrease in the photolysis frequencies due to clouds above HALO. This indicates the necessity of constraining the model calculation by onboard measurements for accounting the influence of local pollution events and physical conditions in the $RO_2{}^*$ production and losses. On the other hand, the CMAQ model overestimates $RO_2{}^*{}_m$ at altitudes above 5000 m. This might be due to the underestimation of NO at these altitudes. A more detailed sensitivity study is required to address this issue.

The measurements on the west coast of Taiwan show that under high NO (NO > 800 pmole mole^{-1}), $RO_2{}^*$ are mainly lost through the OH – NO_x reactions forming HONO and HNO$_3$ during the OH and $RO_2{}^*$ interconversion. As a result, the $RO_2{}^*$ mixing ratio decreases to < 20 pmole mole^{-1} in these pollution plumes, irrespective of the precursor mixing ratio. The loss through HO_2 uptake on aerosol also has a higher contribution (> 30 %) in the air masses with ASA > 3 × 10^{-6} cm^2 cm^{-3}.

4.1.7 Special Case Study: Yangtze River Delta

The measurements over the East China Sea from flight E-AS-08 on 24.03.2018 are studied in detail to understand the $RO_2{}^*$ production and loss processes in the outflow far from the emission source. The flight legs considered were carried out to investigate the transported outflow from the Yangtze River Delta region, which is expected to be more processed and mixed than the outflows

considered in the previous case studies. Unlike other case studies, the measurements were made under lower insolation conditions ($j_{O(^1D)} < 2 \times 10^{-5} \text{ s}^{-1}$).

Figure 4.28 shows the 2D and zoom in 3D representation of the flight over the East China Sea colour-coded with: a) altitude; b) $RO_2^*{}_m$; c) CO; d) NO. Vertical profilings were made over the areas predicted to have outflow from the Yangtze River Delta region. FLEXTRA backward trajectories and HYSPLIT CO enhancements indicate that the measured air masses during the flight leg presented below were transported from the Yangtze River delta region and Beijing. Unlike previous special case studies, cloudy conditions dominated during flight E-AS-08, which significantly reduced the RO_2^* production from the photolysis of precursors. As a result, $RO_2^*{}_m$ stayed below 50 pmole mole^{-1} throughout the flight. During the measurements below 1000 m, HALO intercepted three pollution plumes as indicated by the two CO enhancements between B–C and C–D, and one NO enhancement between B–C.
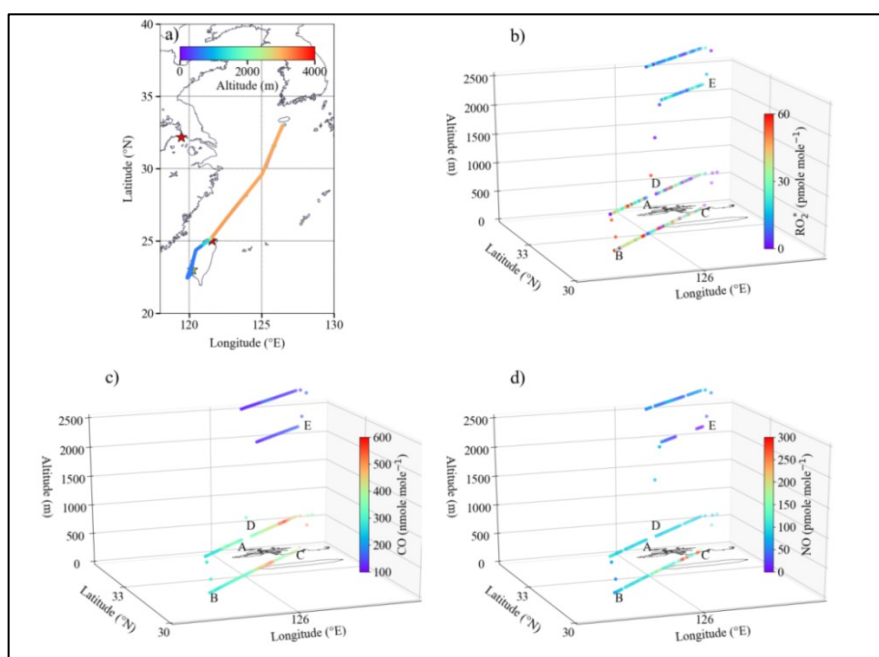
Figure 4.28: E-AS-08 flight on 24.03.2018 a) flight tracks colour-coded with flight altitude and zoom-in 3D view of the flight track over the East China Sea colour-coded with b) $RO_2^*{}_m$, c) CO, and d) NO mixing ratios. Different flight legs are also marked with letters from A to E.

Figure 4.29 shows the time series of measurements over the East China Sea during E-AS-08. At point A, HALO reached the predicted transport pathway of the outflow from the Yangtze River Delta region. HALO descended to 950 m and flew towards the south till point B. As HALO descends, CO, O_3, NO, NO_2, HONO, NO_y, HCHO, $CH_3C(O)CH_3$, CH_3OH, CH_3CHO, and CHOCHO increased to 330, 80, 0.10, 0.10, 0.16, 5.2, 0.35, 0.90, 2.5, 5, 0.70, and 0.35 nmole mole^{-1}, respectively. This indicates the presence of a pollution outflow layer. According to the FLEXTRA analysis, these air masses were transported through the PBL over the Yangtze River delta region. Since the RO_2^* loss processes increase with NO and particle number concentration, $RO_2^*{}_m$ was around 20 pmole mole^{-1} in the first half of the flight leg, even with the increased amount of RO_2^* precursors. As the ASA

decreased by 50 % towards the end of the flight leg, $RO_2^*{}_m$ increased to 40 pmole mole^{-1}, even though the precursor and photolysis frequencies did not change significantly during the flight leg. This indicates that the lower $RO_2^*{}_m$ during the first half of the flight leg is due to higher heterogeneous losses of HO_2 on the aerosol surface.

At point B, HALO descends to 340 m and flies towards the north. During the first half of flight leg B–C, the $\sum$VOCs, NO, and ASA remained similar to the values in the previous flight leg. Even though the [H_2O] increased, the photolysis frequencies decreased. As a result, $RO_2^*{}_m$ remained around 40 pmole mole^{-1}. At the beginning of the second half of B–C, CO, NO_y, O_3, $CH_3C(O)CH_3$, CH_3OH, and CH_3CHO had an enhancement of 200, 6, 15, 1.80, 3, 1 nmole mole^{-1}, respectively, nearly doubling the mixing ratios for 12 minutes. The ASA showed a similar pattern and enhanced to 6×10^{-6} cm^2 cm^{-3}. The NO and NO_2 were also enhanced to 300 and 50 pmole mole^{-1} but only for < 3 minutes. [H_2O], on the other hand, decreased. This indicates the presence of a distinct pollution layer. The $j_{O(^1D)}$, remained $\leq 2 \times 10^{-5}$ s^{-1} and $RO_2^*{}_m \leq 40$ pmole mole^{-1}. The observed NO, NO_2, and [HO_2] enhancements towards the end of the flight leg indicate a second pollution layer with a fresh emission signature. FLEXTRA analysis indicates that the airmass in the second pollution layer has been in contact with the marine PBL layer shortly before reaching the sampling point. As this part of the East China Sea is one of the busiest shipping areas, the short-term variations in NO and NO_2 mixing ratios might originate from ship emissions. CO, OVOCs, and ASA are lower compared to the previous plume. During the flight leg B–C, the $RO_2^*{}_m$ pattern agrees with the photolysis frequency variations and decreases from 40 to 20 nmole mole^{-1} as $j_{O(^1D)}$ decreases from 3×10^{-5} to 2×10^{-5} s^{-1}.

From point C, HALO ascended to 940 m and flew towards the south till point D. During the first half of the flight leg C–D, HALO encountered a pollution plume as indicated by the enhancement in CO, $CH_3C(O)CH_3$, CH_3CHO, CH_3OH, and particle number concentration. The $j_{O(^1D)}$, remained < 2 $\times 10^{-5}$ s^{-1} and $RO_2^*{}_m < 40$ pmole mole^{-1}. At point D, HALO ascended to 2500 m, and all the measurements decreased to the similar value observed before point A at 3000 m. The $RO_2^*{}_m$ remained below 20 pmole mole^{-1}. At point E, HALO ascended to 3000 m and flew towards Taiwan.

The oxidation VOCs not considered in the RO_2^* calculation might have a negligible contribution due to high CO (CO > 300 nmole mole^{-1}) and the chemical transformation during the long transport. As a result, the $RO_2^*{}_c$ is in good agreement with $RO_2^*{}_m$ within the calculated error throughout the period considered. The small difference between the total RO_2^* production and destruction indicates that the PSS assumption considered in this study is robust enough to calculate the RO_2^* in the processed pollution outflows. As shown in Figure 4.30, O_3 and HONO photolysis have a similar contribution of 30 % to 40 % to the total production rate. This is due to the lower photolysis frequency of O_3 under cloudy conditions than that of HONO.
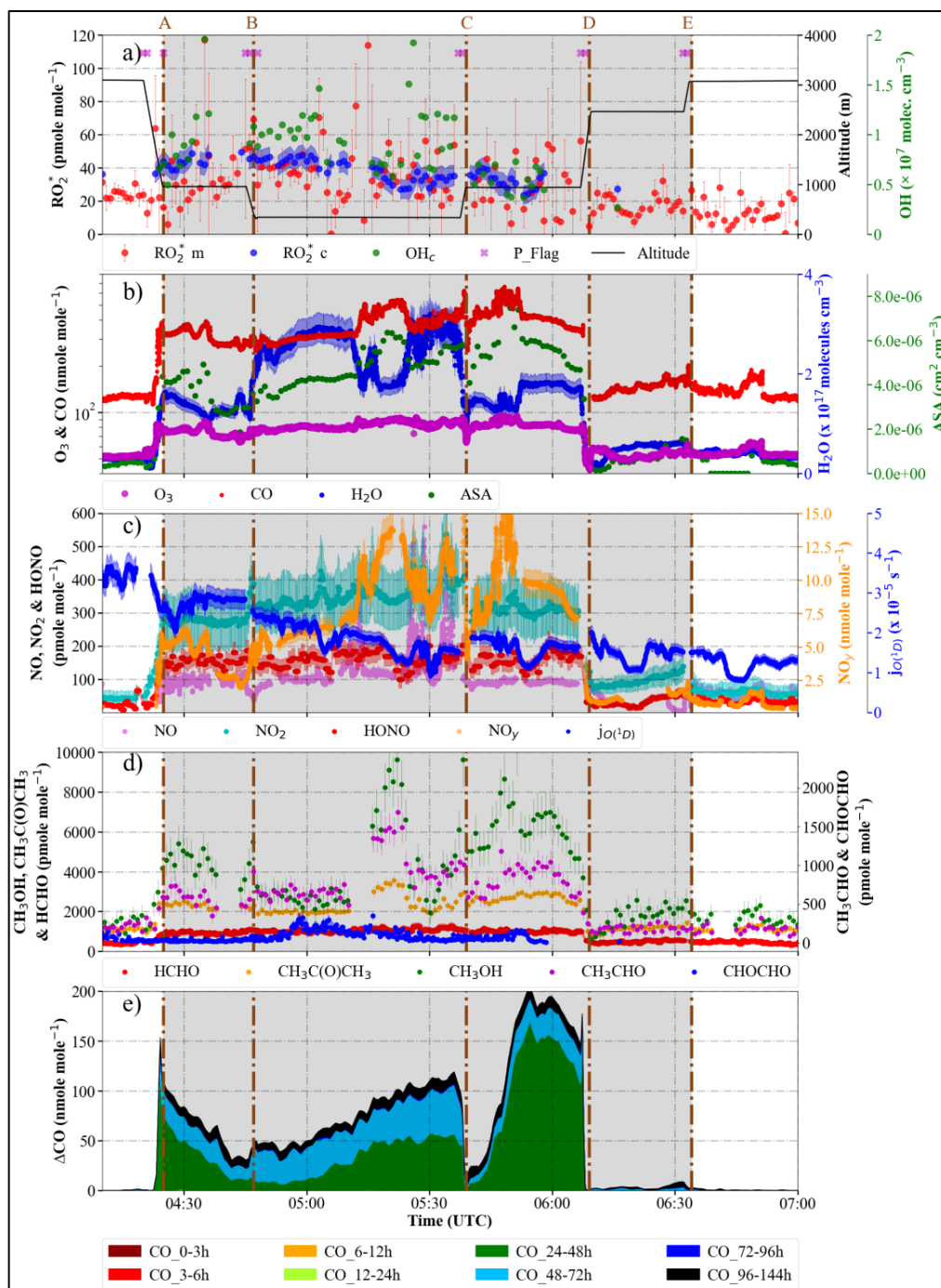
Figure 4.29: Variation of $RO_2^*{}_m$ and $RO_2^*{}_c$, selected RO_2^* precursors and $j_{O(^1D)}$ along the flight track of E-AS-08. a) $RO_2^*{}_m$, $RO_2^*{}_c$ using Eq. 4.16, OH_c, and flight altitude. The P_flag indicates RO_2^* measurements affected by dynamical pressure variation in the inlet. b) O_3 and CO mixing ratios together with H_2O and ASA (total aerosol surface area concentration). The CO and O_3 are on a logarithmic scale to account for the variations in CO during the flight. c) NO, NO_y mixing ratios, and $j_{O(^1D)}$. d) HCHO, CH_3CHO, CH_3OH, CHOCHO and $CH_3C(O)CH_3$ mixing ratios measurements. e) HYSPLIT modelled CO enhancement over background concentration due to emissions originating from the target MPCs Yangtze River delta region and Beijing (04:25-06:25 UTC). The error bars show the standard error of the measurements. Based on HYSPLIT simulations, the measurements expected to contain the emission from the Yangtze River Delta region and Beijing are highlighted with grey vertical spans. Different flight legs in the boundary layer are also marked with vertical lines and letters from A to E.
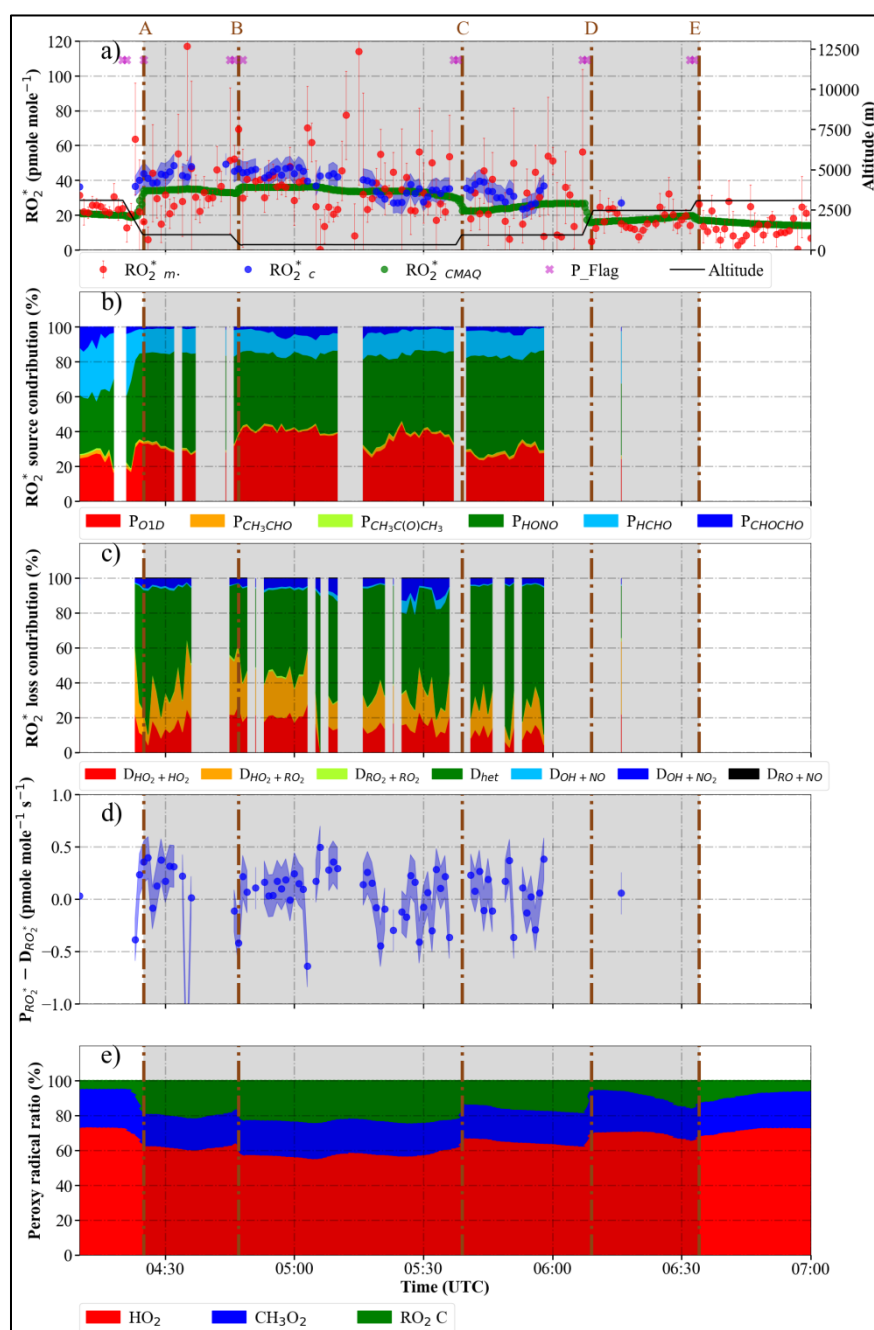
Figure 4.30: Variation of $RO_2^*{}_m$ and $RO_2^*{}_c$, $RO_2^*{}_{CMAQ}$ (sum of $HO_2{}_{CMAQ}$, $CH_3O_2{}_{CMAQ}$, and RO_2 C $_{CMAQ}$ modelled using the CMAQ. RO_2 C $_{CMAQ}$ is the organic peroxy radical other than CH_3O_2 that converts NO to NO_2), RO_2^* production and loss contribution from each term in Eq. 4.16 along the flight track of E-AS-08. a) $RO_2^*{}_m$, $RO_2^*{}_c$, $RO_2^*{}_{CMAQ}$ ($HO_2{}_{CMAQ}$ + $CH_3O_2{}_{CMAQ}$ + RO_2 C $_{CMAQ}$, where RO_2 C is the sum of organic peroxy radicals other than that convert NO to NO_2) and flight altitude. The P_flag indicates RO_2^* measurements affected by dynamical pressure variations in the inlet. b) RO_2^* source contribution from R4.1, R4.3, R4.8, R4.9, R4.10, and R4.11. c) The contribution of R4.14 ($D_{HO_2+HO_2}$), R4.15 ($D_{HO_2+RO_2}$), R4.16 ($D_{RO_2+RO_2}$), R4.19 (D_{OH+NO}), R4.20 (D_{OH+NO_2}), R4.22 (D_{RO+NO}), and HO_2 uptake on aerosol (D_{het}) to RO_2^* loss. d) the difference between the total production ($P_{RO_2^*}$) and destruction ($D_{RO_2^*}$) rate with standard errors estimated from the measurement uncertainty. e) ratio of HO_2, CH_3O_2, and RO_2 converting NO to NO_2 other than CH_3O_2 modelled using the CMAQ model. Based on HYSPLIT simulations, the measurements expected to contain the emission from the Yangtze River Delta region and Beijing are highlighted with grey vertical spans. Different flight legs in the boundary layer are also marked with vertical lines and letters from A to E.

The RO_2^* loss processes were dominated (> 50 %) by the HO_2 uptake on aerosol due to the higher ASA (> 4×10^{-6} cm^2 cm^{-3}). As the NO mixing ratio was < 100 pmole mole^{-1} most of the time, the loss through HONO and HNO_3 formation was < 20 %. Due to the lower RO_2^* mixing ratio, the loss contribution from the $HO_2 - RO_2$ and $HO_2 - HO_2$ reactions was < 50 %. The RO_2^* estimated from the CMAQ model has an excellent agreement with both $RO_{2~m}^*$ and $RO_{2~c}^*$. The RO_2^* calculated from the CMAQ model consists of 60 % to 70 % HO_2, 20 % to 25 % CH_3O_2, and 20 to 10 % other RO_2. This indicates that the uncertainty in $RO_{2~m}^*$ from the HO_2 to RO_2^* ratio due to different sensitivities for HO_2 and RO_2 (section 3.2.7) is expected to be between 8 % and 10 %. In the next section, the sensitivity study on the radical production by HONO photolysis and the radical loss by aerosol uptakes on $RO_{2~c}^*$ in these flight legs has been further investigated.

4.1.8 The Effect of Aerosol Uptake Coefficient on $RO_{2~c}^*$

The heterogeneous uptake coefficient, γ, depends upon the phase, relative humidity and compounds present in the aerosol. The presence of transition metal ions (Cu and Fe) in the aerosol acts as catalysts for the heterogeneous uptake of HO_2 and thereby increases γ (Jacob, 2000). Previous studies using aerosol produced in the laboratory reported γ values between 10^{-5} to unity (Tan et al., 2020). As a result, previous ground-based studies used different values (0.25 in Kanaya et al. 2009, 0.2 in Li et al. 2019) to explain the possible HO_2 loss through the uptake on aerosol in the North China Plain. Based on the measurements and budget analysis of OH, HO_2 and RO_2, Tan et al., 2020 suggested that the $\gamma \geq 0.2$ is too large for the North China Plain and proposed a value of 0.08. Due to this lower γ, HO_2 uptake on aerosol did not play any significant role in determining peroxy radical concentrations during the measurements made in 2014 presented in Tan et al., 2020. Since the metal ion components in the aerosol were not measured during the EMeRGe campaign, it is not possible to estimate the actual value of γ in the measured air masses. Therefore, $\gamma = 0.24$, the average value recommended by Taketani et al., 2012 for studying semi-urban/regional scale air pollution based on direct measurement of aerosol uptake coefficient at two sits in North China plain, is used in this study.

A sensitivity study on $RO_{2~c}^*$ was carried out to investigate the role of HO_2 uptake on aerosol in the RO_2^* budget. $RO_{2~c}^*$ was estimated for $\gamma = 0$, 0.08 and 0.24 using the EMeRGe in Asia dataset. Figure 4.31 shows the $RO_{2~m}^*$ and $RO_{2~c}^*$ over the East China Sea from flight E-AS-08. In addition to RO_2^* calculated using $\gamma = 0.24$, four more values of $RO_{2~c}^*$ were estimated. These comprise the following: $RO_{2~c_{SS1}}^*$, which is calculated using the measured HONO concentrations and $\gamma = 0.08$; $RO_{2~c_{SS2}}^*$, which is calculated using the measured HONO concentrations and $\gamma = 0$; $RO_{2~c_{SS3}}^*$, which is calculated using the modelled HONO concentrations from the CMAQ and $\gamma = 0$; $RO_{2~c_{SS4}}^*$, which is calculated using the modelled HONO concentrations from the CMAQ and $\gamma = 0.24$. During the measurements over the East China Sea, HO_2 uptake on aerosol, for an assumed uptake coefficient of 0.24, contributes ≥ 60 % to the total RO_2^* loss. As a result, if the γ is reduced to 0.08 ($RO_{2~c_{SS1}}^*$ in

figure 4.31) or to 0 ($RO_2^*{}_{c_{ss2}}$ in figure 4.31), then $RO_2^*{}_m$ is significantly overestimated, as shown in figure 4.31.
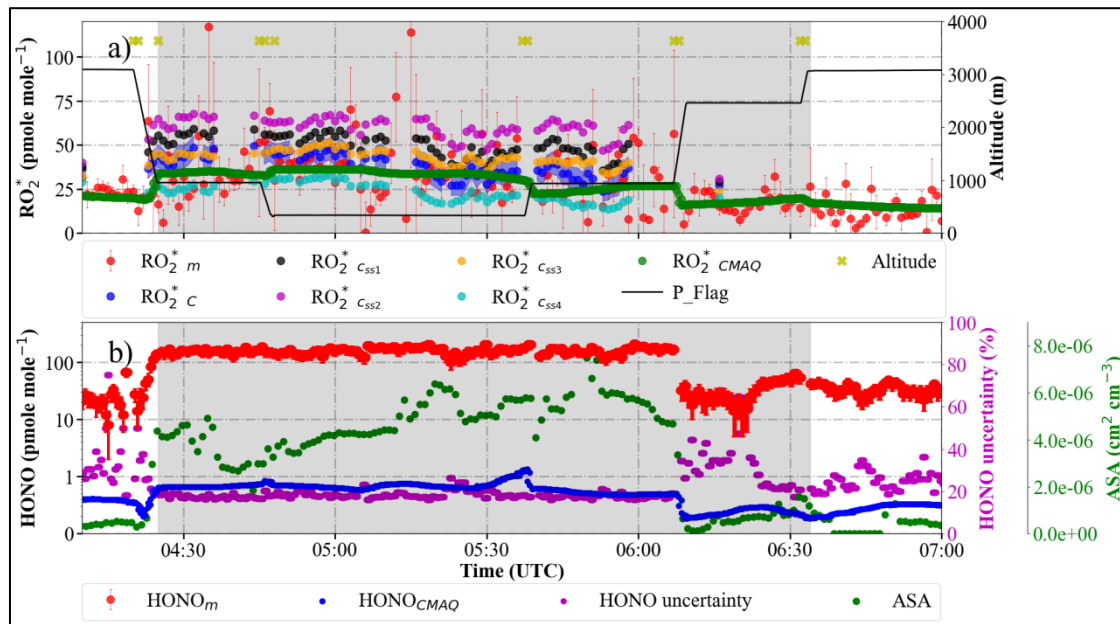
Figure 4.31: Values of $RO_2^*{}_m$ and $RO_2^*{}_c$, $RO_2^*{}_{CMAQ}$ (sum of $HO_{2\,CMAQ}$, $CH_3O_{2\,CMAQ}$, and RO_2 C $_{CMAQ}$ modelled using the CMAQ. RO_2 C $_{CMAQ}$ is the organic peroxy radical other than CH_3O_2 that converts NO to NO_2) along the flight track of E-AS-08. a) $RO_2^*{}_m$, $RO_2^*{}_c$, $RO_2^*{}_{c_{ss1}}$, $RO_2^*{}_{c_{ss2}}$, $RO_2^*{}_{c_{ss3}}$, $RO_2^*{}_{c_{ss4}}$, and flight altitude. $RO_2^*{}_{c_{ss1}}$: calculated using the measured HONO concentrations and $\gamma = 0.08$; $RO_2^*{}_{c_{ss2}}$: calculated using the measured HONO concentrations and $\gamma = 0$; $RO_2^*{}_{c_{ss3}}$: calculated using the modelled HONO concentrations by CMAQ and $\gamma = 0$; $RO_2^*{}_{c_{ss4}}$: calculated using the modelled HONO concentrations using CMAQ and $\gamma = 0.24$. The HO_2:RO_2 ratio is assumed to be 0.5. The P_flag indicates RO_2^* measurements affected by dynamical pressure variations in the inlet. b) HONO measured, HONO from the CMAQ model, HONO measurement uncertainty, and ASA (total aerosol surface area concentration). Based on HYSPLIT simulations, the measurements expected to contain the emission from the Yangtze River Delta region and Beijing are highlighted with grey vertical spans.

Figure 4.32 shows the correlation between $RO_2^*{}_m$ and different $RO_2^*{}_c$ determined using either the HONO concentrations measured by miniDOAS or those predicted by the CMAQ model and a range of γ values for all the measurements from EMeRGe in Asia considered in this study. Except for the measurement over the East China Sea, in most of the measurements considered in this study, even with a γ of 0.24, the contribution of HO_2 uptake on aerosol to total RO_2^* loss is < 30 %. As a result, reducing γ to 0.08, as suggested by Tan et al., 2020, yields a good agreement between $RO_2^*{}_m$ and $RO_2^*{}_c$ within the calculated errors (Figure 4.32a). However, $RO_2^*{}_m$ is overestimated when the γ is reduced during the measurements over the East China Sea, where aerosol number concentration and ASA are high (ASA > 4×10^{-6} cm^2 cm^{-3}, OPC > 800 particle cm^{-3}). The relative humidity during these measurements was > 60 %, higher than those reported by Tan et al., 2020, during the measurements in the North China plain. Thus the value of γ > 0.08 is feasible for this measurement condition.

On the other hand, the HONO measurements from miniDOAS were significantly higher than the CMAQ model results and the values reported by previous studies in the free troposphere (Ye et al.,

2018). The source of this large daytime HONO is not yet identified. In addition, most of the HONO measurements from EMeRGe also have relatively high uncertainty ($\geq$ 50 %). As mentioned in section 4.1.2, the RO_2^* production from HONO photolysis is between 10 % and 40 %. The higher contribution from HONO photolysis ($\approx$ 40 %) to the total RO_2^* production is observed in the air masses with higher particle number concentration (> 800 particles cm^{-3}).
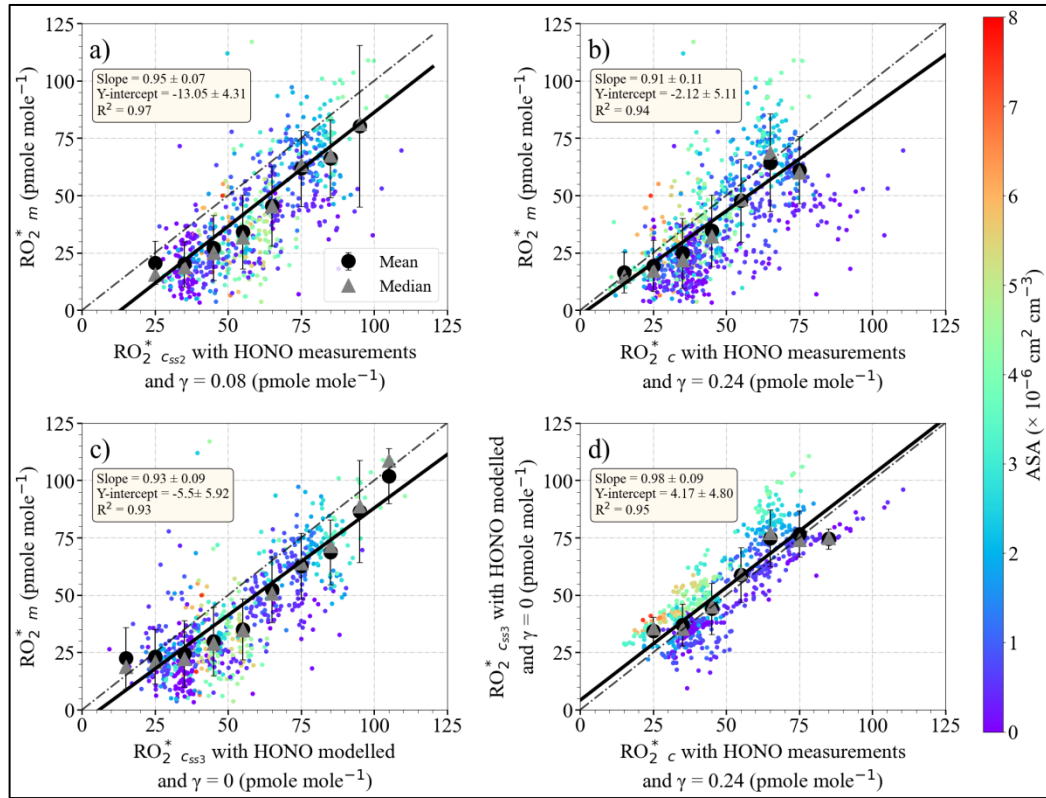
Figure 4.32: Plot of $RO_2^*{}_m$ versus $RO_2^*{}_c$ for a) using the measured HONO concentrations and $\gamma = 0.08$ ($RO_2^*{}_{c_{ss1}}$); b) using the measured HONO concentrations and $\gamma = 0.24$ ($RO_2^*{}_c$); c) using the modelled HONO concentrations by CMAQ and $\gamma = 0$ ($RO_2^*{}_{c_{ss3}}$). d) $RO_2^*{}_c$ versus $RO_2^*{}_{c_{ss3}}$. The data are colour-coded with ASA (total aerosol surface area concentration). 1-minute data (small circles), average (large circles) and median (triangles) of 1-minute data binned over the X-axis (10 pmole $mole^{-1}$) are shown. The error bars indicate the standard error of each bin. The linear regression for the binned values (solid line) and the 1:1 relation (dashed line) are also depicted for reference. The $HO_2:RO_2$ ratio is assumed to be 1:1.

In the PSS estimate of $RO_2^*{}_c$ during the measurement over the East China Sea, the photolysis from the measured HONO results in a large OH and thereby large RO_2^* source, compared to that from the photolysis of the much lower HONO concentration modelled by the CMAQ. Due to the lower HONO concentration from the CMAQ model simulation, the effect of HO_2 uptake on aerosol is not necessary (i.e. $\gamma = 0$) for a good agreement between $RO_2^*{}_c$ and $RO_2^*{}_m$ when the modelled HONO is used in Eq. 4.16 ($RO_2^*{}_{c_{ss3}}$ in Figure 4.31 and Figure 4.32c). This is also why the RO_2^* estimated using the CMAQ model agrees reasonably well with $RO_2^*{}_m$ even though the model does not include any HO_2 uptake on aerosol. Including the HO_2 uptake on aerosol with $\gamma = 0.24$ while using the modelled HONO in Eq. 4.16 results in an underestimation of $RO_2^*{}_m$ ($RO_2^*{}_{c_{ss4}}$ in figure 4.31). Since the higher

contribution from HONO photolysis ($\approx$ 40 %) to the total $RO_2{}^*$ production is observed in the air masses with higher particle number concentration (> 800 particles cm^{-3}), the $RO_2{}^*$ calculated using HONO measurements and $\gamma = 0.24$ is in good agreement with the $RO_2{}^*$ calculated using HONO modelled by the CMAQ model and $\gamma = 0$ (Figure 4.32d). Higher $RO_2{}^*$ production contribution from HONO and higher $RO_2{}^*$ loss contribution from HO_2 uptake on aerosol are observed during the measurements from the flights E-AS-08 and E-AS-09.

$RO_2{}^*$ budget analysis for the measurements made below 2000 m from the two flights (E-AS-08 and E-AS-09) made over the East China Sea during EMeRGe in the Asia campaign indicates that the HO_2 uptake on aerosol estimated for $\gamma = 0.24$ dominates the $RO_2{}^*$ loss processes in these airmasses. As mentioned in section 4.1.7, these airmasses were transported from the Yangtze River Delta region over the ocean. This indicates the influence of aerosol loading on $RO_2{}^*$ and thereby in the O_3 production in China, as previously reported by Li et al., 2019. Further measurement studies of the fresh and transported emission from the polluted urban agglomerations, such as the Yangtze River Delta region, are still necessary to support this result. Other measurements close to the East Asian MPCs (Manila and Taipei) show a loss of $RO_2{}^*$ from HO_2 uptake on aerosol < 30 %, and $\gamma = 0.08$ is enough to get a good agreement between $RO_2{}^*{}_m$ and $RO_2{}^*{}_c$ within the expected uncertainties.

4.1.9 OH Estimation

An equation similar to Eq. 4.16 is formulated to estimate the upper limit of OH concentration from the onboard measurements of precursors and photolysis frequencies. Eq. 4.18 is obtained by considering the OH production reactions (R4.1 to R4.3, R4.23 and R.4.24), loss reactions (R4.5 to R4.7; R4.17 to 4.20, and R4.12), and PSS for OH.

$$2j_{4.1}[O_3]\beta + j_{4.3}[HONO] + k_{4.23}[HO_2][NO] + k_{4.24}[HO_2][O_3] - [OH](k_{4.6}[CO] + k_{4.7}[CH_4] +$$
$$k_{4.12a}[HCHO] + k_{4.12b}[CH_3CHO] + k_{4.12c}[CH_3C(O)CH_3] + k_{4.5}[O_3] + k_{4.19}[NO] +$$
$$k_{4.20}[NO_2] + k_{4.17}[HO_2]) - 2(k_{4.18a} + k_{4.18b})[OH]^2 = 0 \qquad \text{Eq. 4.18}$$

Assuming $\delta = 0.5$, i.e. $[HO_2] = 0.5 \times [RO_2{}^*]$, the OH in the air masses probed during EMeRGe in Asia is calculated by solving the quadratic equation:

$$[OH] = \frac{L_{OH} - \sqrt[2]{L_{OH}^2 + 4\cdot(-2k_{OH})\cdot P_{OH}}}{2\cdot(-2k_{OH})} \qquad \text{Eq. 4.19}$$

where P_{OH} represents the OH production

$$P_{OH} = 2 J_{4.1}[O_3]\frac{k_{4.2a}[H_2O]}{k_{4.2a}[H_2O] + k_{4.2b}[O_2] + k_{4.2c}[N_2]} + J_{4.3}[HONO] + 0.5\left(k_{2.23}[RO_2^*][NO] +\right.$$
$$\left. k_{2.24}[RO_2^*][O_3]\right) \qquad \text{Eq. 4.20}$$

L_{OH} the OH loss processes,

$$L_{OH} = -(k_{4.17}[RO_2^*] + k_{4.19}[NO] + k_{4.20}[NO_2] + k_{4.6}[CO] + k_{4.7}[CH_4] + k_{4.5}[O_3] +$$
$$k_{4.12a}[HCHO] + k_{4.12b}[CH_3CHO] + k_{4.12c}[CH_3C(O)CH_3]) \qquad \text{Eq. 4.21}$$

and $k_{OH} = k_{4.18a} + k_{4.18b}$.

The OH calculated from Eq. 4.19 assuming $\delta = 0.5$ is higher than the OH concentration reported in the previous airborne (Crawford et al., 1999; Tan et al., 2001) and ground-based measurements (Mihelcic et al., 2003; Kanaya et al., 2007, 2012; Hofzumahaus et al., 2009; Elshorbany et al., 2012; Lu et al., 2012, 2013; Tan et al., 2017, 2018; Whalley et al., 2018, 2021; Michelle et al., 2020) in different urban environments. This indicated that the limited number of OVOCs measurements available for the EMeRGe data set is insufficient to calculate the OH reactivity. The overestimation of OH agrees with the underestimation of $RO_2{}^*{}_m$ in air masses with a high amount of OVOCs ($\sum$VOCs > 7 nmole mole^{-1}) as the missing OH – OVOCs reactions in Eq. 4.16 should reduce ρ (the OH loss during the OH – $RO_2{}^*$ interconversion) and thereby increase the $RO_2{}^*{}_c$. Due to the direct reaction of OH with most of the gases emitted in the atmosphere, OH budget calculations in air masses of complex chemistry are challenging and require the experimental determination of the OH reactivity, as described by Tan et al. 2019 and Whalley et al., 2021.

4.1.10 O$_3$ Production Rate

The contribution of $RO_2{}^*$ to the O$_3$ formation rate (P_{O_3}) was calculated for the EMeRGe Asia dataset by using the reaction of $RO_2{}^*$ with NO as in previous studies of urban environments (e.g. Kleinman et al., 1995; Volz-Thomas et al., 2003; Mihelcic et al., 2003; Cantrell et al., 2003b; and references herein).

$$P_{O_3} = k_{RO_2^* + NO}[RO_2^*][NO] \qquad \text{Eq. 4.22}$$

where $k_{RO_2^* + NO}$ is the effective rate coefficient calculated assuming $\delta = 0.5$ in the same way as in Eq. 4.16.

Figure 4.33 shows the mean P_{O_3} calculated using the $RO_2{}^*{}_m$ (red circles) and $RO_2{}^*{}_c$ using Eq. 4.16 as a function of NO (blue circles). The measurements are binned into 50 bins over NO in the logarithmic scale from 10 to 10000 pmole mole^{-1} and from 5×10^7 to 3.5×10^{10} molecules cm^{-3} in Figures 4.32a and 4.32b, respectively. The coloured area shows the standard error of each bin. Up to 500 pmole mole^{-1} NO, the P_{O_3} calculated using the $RO_2{}^*{}_m$ and $RO_2{}^*{}_c$ agree well within the standard deviation of the bins. For higher NO concentrations, the P_{O_3} calculated from $RO_2{}^*{}_c$ remains lower than that calculated from the $RO_2{}^*{}_m$. The deviation is due to the underestimation of $RO_2{}^*{}_c$ inside the plumes with a high NO mixing ratio (> 500 pmole mole^{-1}) as mentioned in the previous sections.
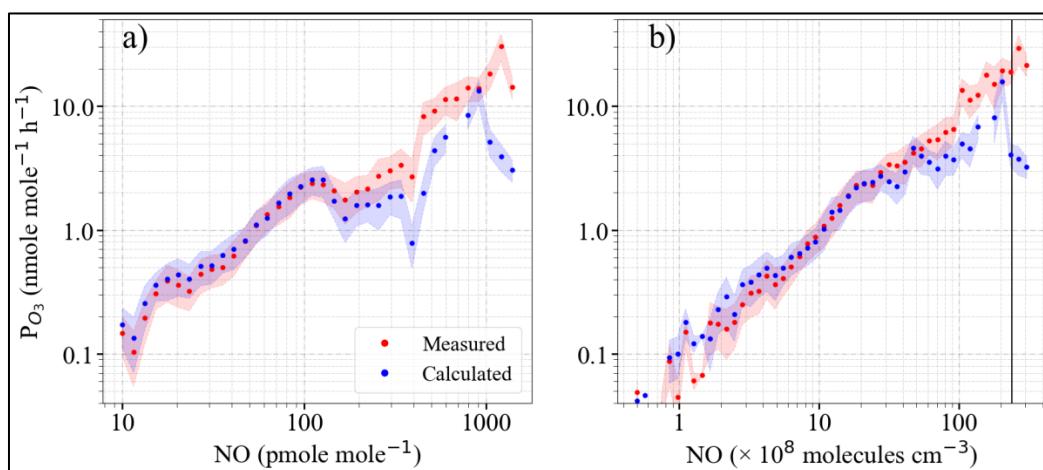
Figure 4.33: O_3 production calculated from $RO_2^*{}_m$ (red dots) and $RO_2^*{}_c$ (blue dots) versus: a) NO mixing ratio; b) NO number concentration. The 1-minute measurements are binned into 50 bins over NO in the logarithmic scale a) from 10 to 10000 pmole mole^{-1} and b) from 5×10^7 to 3.5×10^{10} molecules cm^{-3}. The shaded area shows the standard error of each bin. For comparison with ground-based measurements, the number concentration corresponding to 1 nmole mole^{-1} NO at 1000 hPa and 298K has been marked by the solid black line in b).

Similar P_{O_3} values have been reported for ground-based measurements in polluted areas such as Wangdu (Tan et al., 2017) and Beijing (Whalley et al., 2021) in the same range of RO_2^* and NO mixing ratios. In a previous work, Whalley et al. (2018) calculated P_{O_3} about an order of magnitude lower for NO < 1 nmole mole^{-1} (2.45×10^{10} molecules cm^{-3} at 1000 hPa and 298K) for observations in central London where the measured RO_2^* was < 15 pmole mole^{-1}.

During the measurement considered for the P_{O_3} calculation over Southeast Asia, NO remained < 300 pmole mole^{-1} (approximately $< 1 \times 10^{10}$ molecules cm^{-3}) in 95% of the measurements. Similar values of ozone production rates were reported in other ground-based modelling studies in China for urban environments with NO < 1 nmole mole^{-1} (Tan et al., 2017; Whalley et al., 2021) and the sum of peroxy radicals > 80 pmole mole^{-1}. This confirms the capabilities of the PSS-based analytical equation Eq. 4.16 for the simulation of airborne RO_2^* measurements. Since Eq. 4.22 only take into consideration NO and RO_2^* measurements, similar P_{O_3} is expected for measurements with similar NO and RO_2^* values irrespective of other physical and chemical parameters in the PBL and free troposphere.

4.1.11 Comparison of Results from Asia and Europe

As the target MPCs in Europe were situated closer to each other than those in Asia, all the measurement flights in Europe were made close to the MPCs during EMeGRe in Europe. As a result, the NO mixing ratio was generally higher in the outflow plumes encountered in Europe compared to Asia. On the other hand, the photolysis frequencies and the measurement altitude were comparable between Asia and Europe. So the results from Asia are compared with the results from Europe to identify the similarities and differences in RO_2^* production and loss processes.

RO_2^* mixing ratios up to 120 pmole mole^{-1} were measured during the EMeRGe campaign in Europe, as shown in Figure 4.34. As shown in Figure 4.34b, 60 % of the measurements were made below 3000 m during EMeRGe in Europe. Typically, higher mixing ratios were observed in southern than northern Europe. This is due to the higher insolation and temperatures present during the measurements over southern Europe, favouring the active photochemistry.
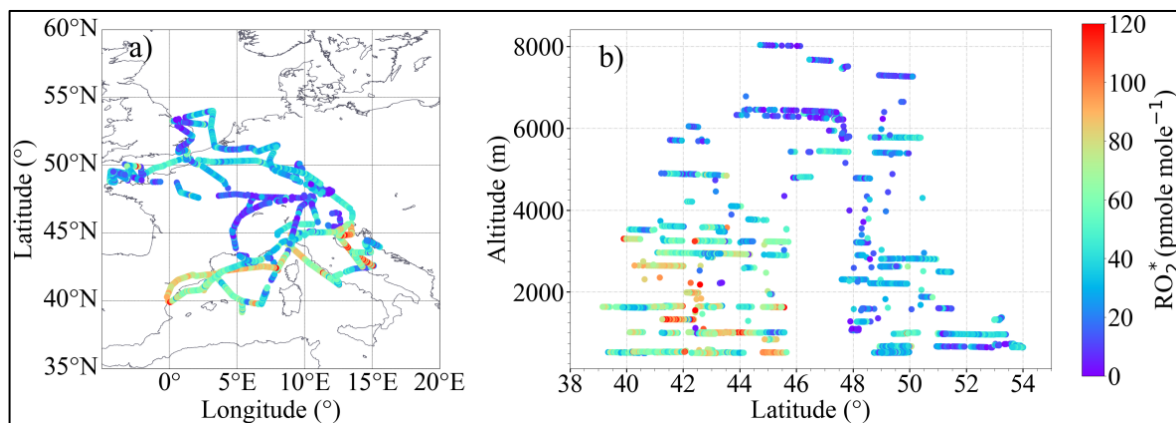
Figure 4.34: RO_2^* measured during EMeRGe in Europe a) over the flight tracks, b) as a function of latitude and altitude.

Figure 4.35 shows the averaged vertical profile of $RO_2^*{}_m$, colour-coded with the $P_{RO_2^*}$ calculated for both EMeRGe in Asia and Europe. Similarly to the measurements in Asia, the averaged vertical profiles obtained from Europe are also partly biased by the large number of measurements below 3000 m. The vertical profile of $RO_2^*{}_m$ from EMeRGe in Europe measurements is similar to the EMeRGe in Asia measurements (Figure 4.6), with higher RO_2^* mixing ratios observed below 3000 m and a local maximum observed between 1500 and 4000 m for $P_{RO_2^*} \geq 0.5$ pmole mole^{-1} s^{-1}. Above 3000 m both $P_{RO_2^*}$ and RO_2^* starts to decrease with altitude.

Figure 4.36 shows the variation with the altitude of the fractional contribution of each RO_2^* precursor included in Eq. 4.2 for EMeRGe Asia and Europe. The data are classified into three groups according to $P_{RO_2^*}$ to show the lowest, most common, and highest ranges encountered during the campaigns. The data in each group are binned over 500 m always when available.

The vertical variation of the precursor mixing ratios and photolysis frequencies used to calculate the fractional contributions in Figure 4.36 for Asia are shown in Figures 4.5a to 4.5f and Europe in figure 4.37a to 4.37f. Since the precursor mixing ratio and photolysis frequencies in the $P_{RO_2^*}$ ranges are comparable, the vertical profiles of the production rate contribution from each source in Eq. 4.2 are comparable in both EMeRGe in Asia and Europe. This implies that due to the fast photochemistry involved, $P_{RO_2^*}$ does not depend upon the origin of the air mass and can be calculated from the precursor mixing ratios and photolysis frequencies. In both campaigns, the main RO_2^* sources were the O_3, HCHO, CHOCHO, and HONO photolysis. The contributions of CH_3CHO and

$CH_3C(O)CH_3$ photolysis are practically negligible in EMeRGe in Asia and Europe measurement campaigns. Up to 4000 m, the O_3 photolysis has the highest contribution in both cases.
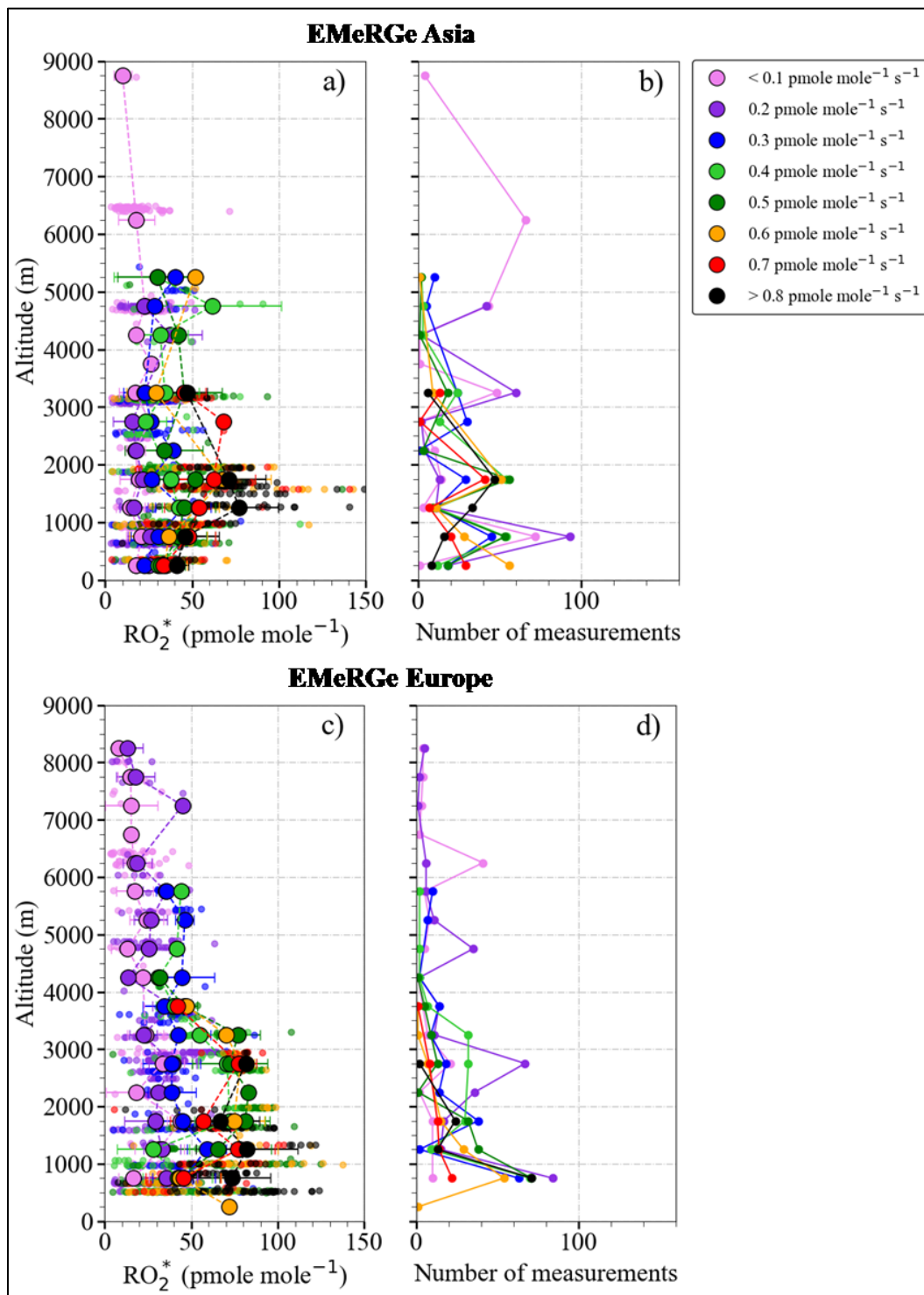
Figure 4.35: Vertical distribution of measured RO_2^* colour-coded according to $P_{RO_2^*}$ (a and c) and the number of measurements in each altitude bin (b and d) from EMeRGe in Asia and Europe. Small circles are 1-minute individual measurements binned with $P_{RO_2^*}$ values in 0.1 pmole mole^{-1} s^{-1} intervals. Larger circles result from a further binning over 500 m altitude steps. All the production rates below 0.1 pmole mole^{-1} s^{-1} and above 0.8 pmole mole^{-1} s^{-1} are binned to 0.1 pmole mole^{-1} s^{-1} and 0.8 pmole mole^{-1} s^{-1}, respectively.
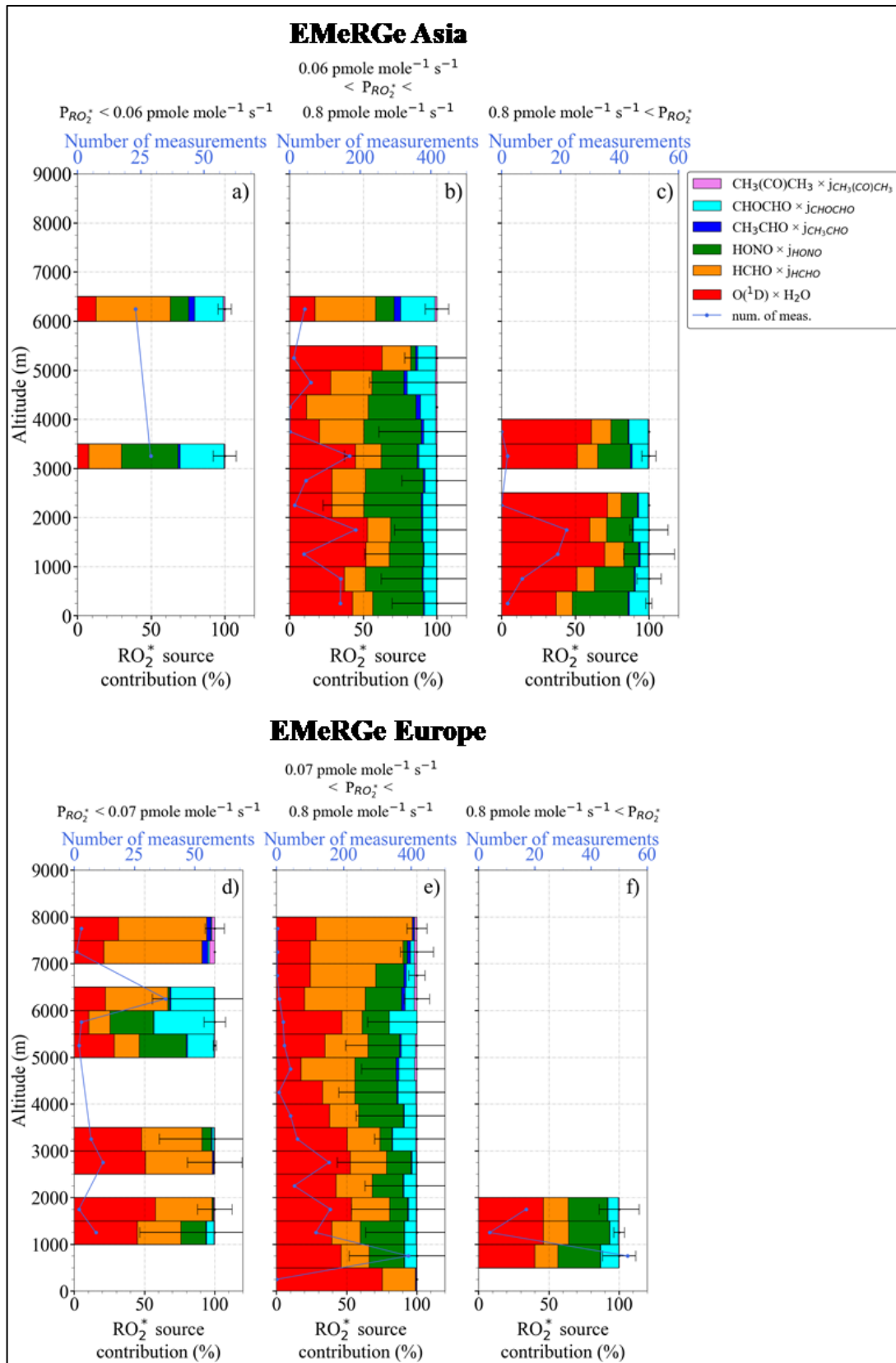
Figure 4.36: Variation of total $P_{RO_2^*}$ and fractional precursor contributions with altitude, as calculated by Eq. 4.2, from EMeRGe in Asia for: a) $P_{RO_2^*} < 0.06$ pmole mole^{-1} s^{-1}; b) 0.06 pmole mole^{-1} s^{-1} < $P_{RO_2^*} < 0.8$ pmole mole^{-1} s^{-1}; and c) $P_{RO_2^*} > 0.8$ pmole mole^{-1} s^{-1}, and Europe for: d) $P_{RO_2^*} < 0.07$ pmole mole^{-1} s^{-1}; e) 0.07 pmole mole^{-1} s^{-1} < $P_{RO_2^*} < 0.8$ pmole mole^{-1} s^{-1}; and f) $P_{RO_2^*} > 0.8$ pmole mole^{-1} s^{-1}.
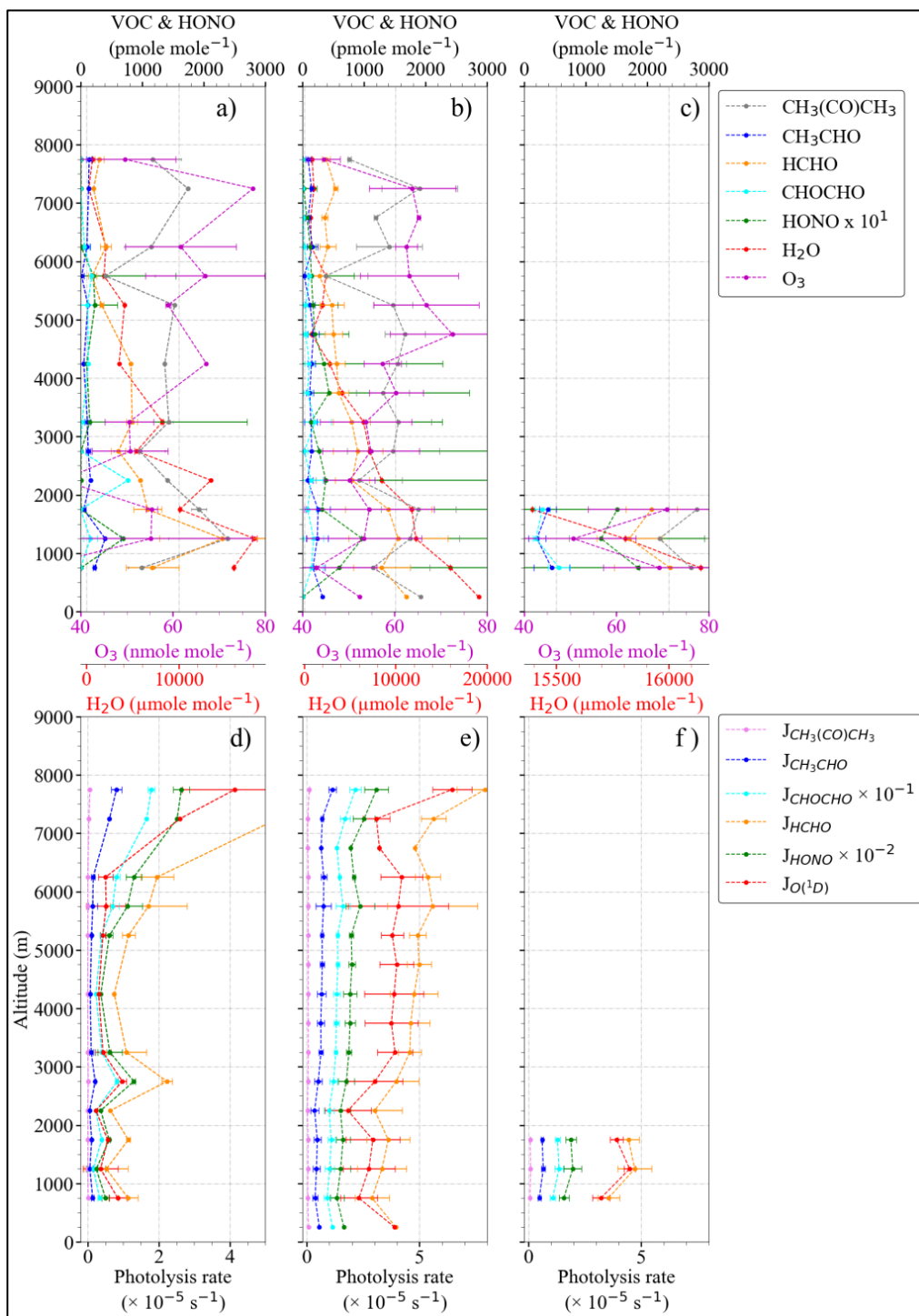
Figure 4.37: Vertical variation of: a) to c) precursor mixing ratios; d) to f) photolysis frequencies for the corresponding $P_{RO_2^*}$ bin shown in Figure 4.36 for EMeRGe in Europe.

Figure 4.38 shows the variation of $k_{RO_2^*}$ with altitude colour-coded with water number concentration measured during both EMeRGe campaigns for different HO_2 to CH_3O_2 ratios, i.e. for δ = 1 and δ = 0.5. The δ = 1 condition has a higher $k_{RO_2^*}$ than the δ = 0.5 condition and is two times higher below 2000 m in both campaigns. The decrease in $k_{RO_2^*}$ with altitude is also comparable between the two campaigns.
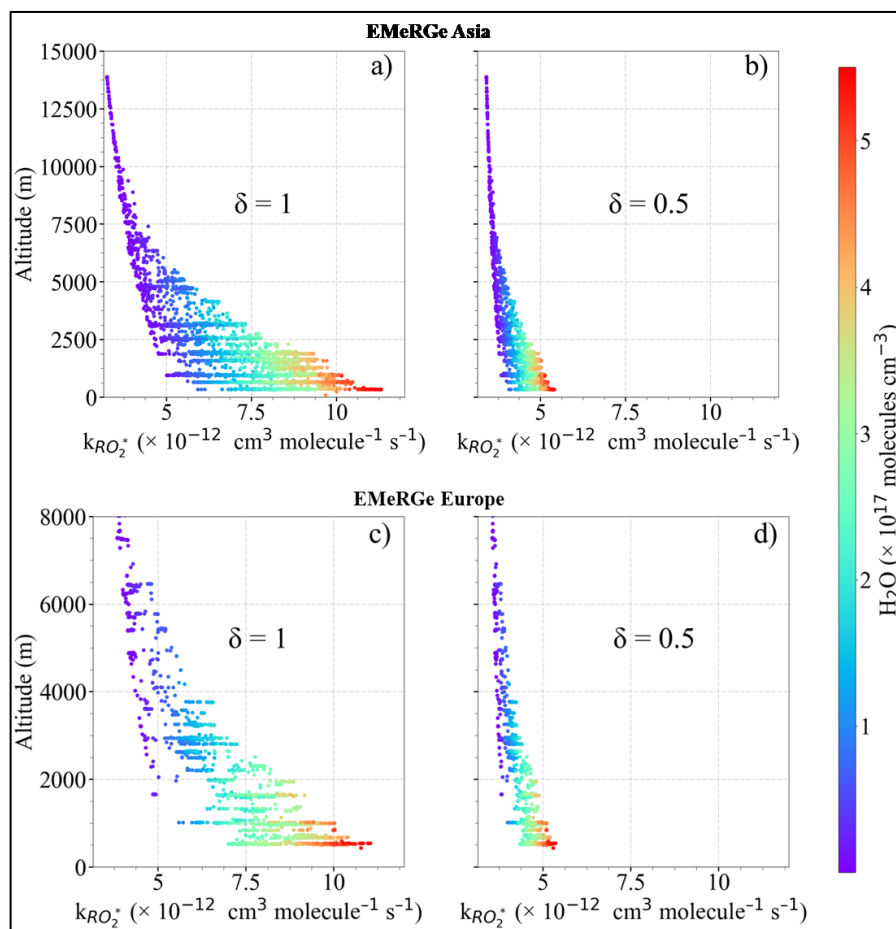
Figure 4.38: Vertical distribution of the effective RO_2^* self-reaction rate constant, $k_{RO_2^*}$, calculated using Eq. 4.15 from EMeRGe in Asia for: a) $\delta = 1$; and b) 0.5, and Europe for: c) $\delta = 1$; and d) 0.5 ($\delta = [HO_2]/[RO_2^*]$). The data are colour-coded with H_2O number concentration.

Figure 4.39 shows the variation of $RO_2^*{}_m$ observed during EMeRGe in Europe as a function of latitude and altitude and the calculated contribution of $HO_2 + HO_2$ reaction, $HO_2 + RO_2$ reaction, $RO_2 + RO_2$ reaction, $OH + NO$ reaction, $OH + NO_2$ reaction, $RO + NO$ reaction, and HO_2 uptake on aerosol to $D_{RO_2^*}$. Similar to the results observed in Asia, the highest loss contribution is from the $HO_2 + RO_2$, which reaches up to 80 %. The $HO_2 + HO_2$ reaction is also a major loss process, and the contribution to the total loss process reaches up to 50 % during the measurement below 1000 m. Due to the pressure dependency of $k_{HO_2+HO_2}$, the loss through the $HO_2 + HO_2$ reaction decreases with altitude. On the other hand, the $RO_2 + RO_2$ reaction contributes < 3 % to the $D_{RO_2^*}$ due to the lower reaction rate coefficient than $HO_2 + RO_2$ and $HO_2 + HO_2$. The contribution from the $OH + NO$ reaction forming HONO and $OH + NO_2$ reaction forming HNO_3 remained below 20 % except for the measurements near the target MPCs Po Valley, Rome, and London with $NO_x > 8 \times 10^{12}$ molecules cm^{-3}. The reaction between $RO + NO$ forming organic nitrites contributes < 1 % to $D_{RO_2^*}$. Air masses with $[NO_x] > 8 \times 10^{12}$ molecules cm^{-3} are encountered more often during EMeRGe in Europe. The loss through the HO_2 uptake on aerosol is below 10 %, even with $\gamma = 0.24$. This is due to the lower aerosol loading (ASA < 4×10^{-6} cm^2 cm^{-3} and OPC < 800 particles cm^{-3}) compared to EMeRGe in Asia and

indicates that the HO_2 uptake on aerosol during EMeRGe in Europe is negligible compared to the measurements from EMeRGe Asia.
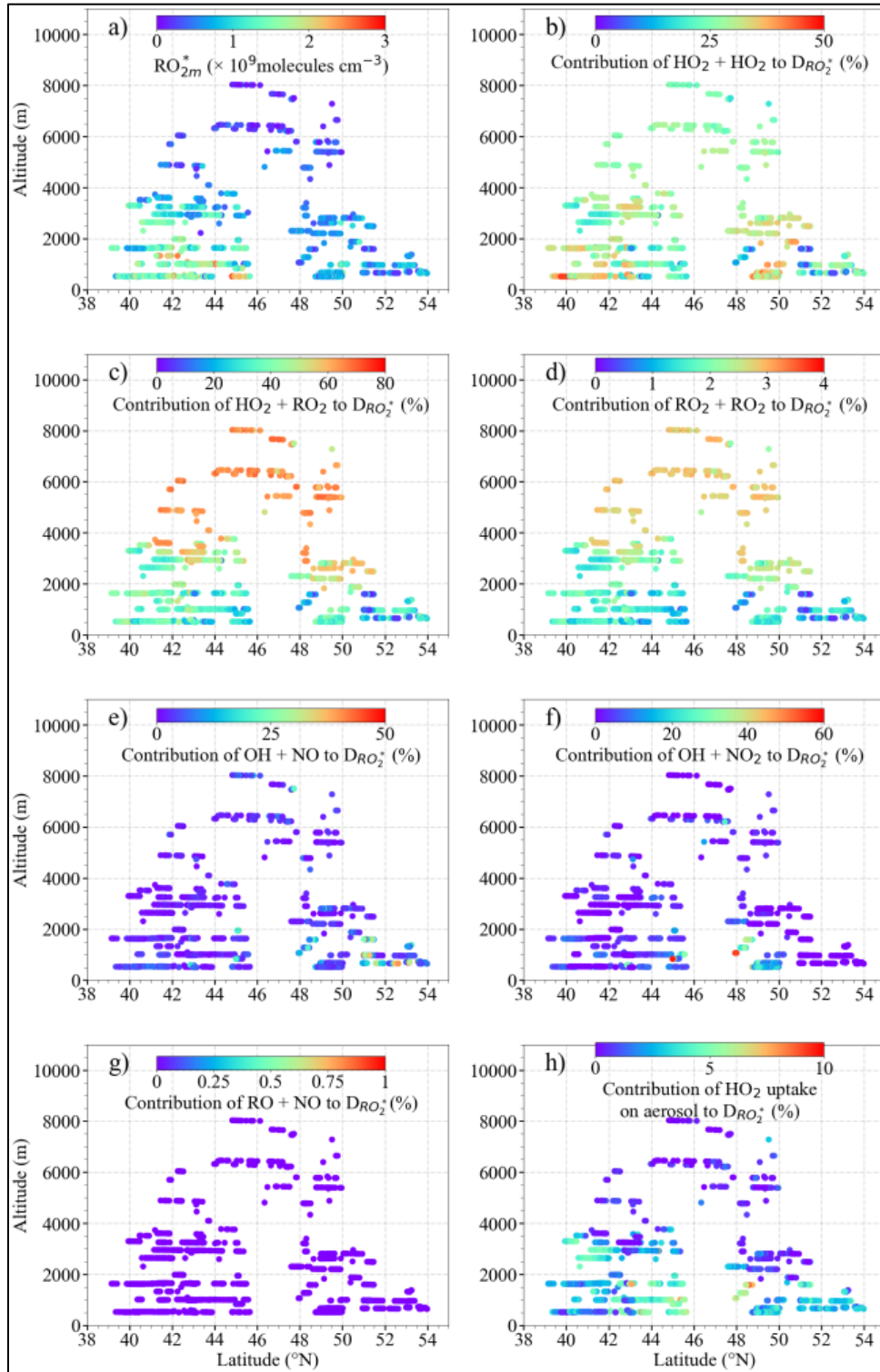
Figure 4.39: Plot of: a) $[RO_2^*]$; RO_2^* loss contribution from b) $HO_2 + HO_2$ reaction, c) $HO_2 + RO_2$ reaction, d) $RO_2 + RO_2$ reaction, e) $OH + NO$ reaction, f) $OH + NO_2$ reaction, and h) HO_2 uptake on aerosol as a function of latitude and altitude.

Figure 4.40 shows the $RO_2^*{}_m$ versus $RO_2^*{}_c$ using Eq. 4.16 for $\delta = 0.5$ colour-coded with $j_{O(^1D)}$, the $\Sigma VOCs$, NO_x, and the flight altitude. The slope of the linear regression (solid line) is 0.67 ($R^2 =$

0.96), and the y-axis intercept equals 15.87 pmole mole^{-1}. The $RO_2^*{}_c$ from the European measurements also overestimates $RO_2^*{}_m$ < 25 pmole mole^{-1} (up to 4 times). For EMeRGe in Europe, these measurements belong to altitudes above 6000 m. Similar to EMeRGe in Asia, these measurements were associated with $j_{O(^1D)}$ > 3 × 10^{-5} s^{-1}, NO$_x$ < 150 pmole mole^{-1}, and ΣVOCs mixing ratio < 2 nmole mole^{-1}. These comparisons show that Eq. 4.16 systematically overestimates $RO_2^*{}_m$ in air masses with low VOC and NO$_x$ with high photolysis frequencies. As mentioned in section 4.1.3, most of the overestimation might come from the RO_2^* loss reactions (OH self-reaction and OH – HO$_2$ reaction) excluded from Eq. 4.16 and the overestimation in the RO_2^* precursor measurements.

In summary, the O$_3$, HCHO, CHOCHO, and HONO photolysis were the dominant peroxy RO_2^* sources in the air masses investigated in both Asia and Europe. The loss through heterogeneous reactions of HO$_2$ was higher in Asia due to higher ASA compared to Europe. The loss through OH – NO$_x$ reactions was dominant in Europe as most measurements were made close to the source with NO > 500 pmole mole^{-1}. In both campaigns, the RO_2^* – RO_2^* reactions were the dominant loss process in the free troposphere with NO < 800 pmole mole^{-1} and ASA < 4 × 10^{-6} cm^2 cm^{-3}.
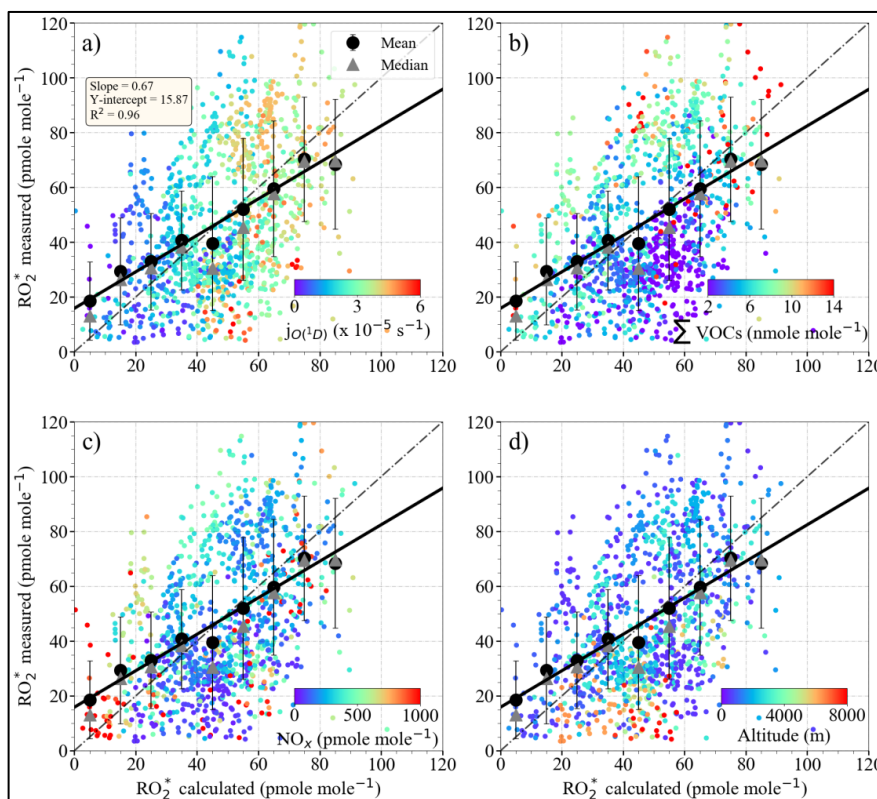
Figure 4.40: $RO_2^*{}_m$ versus $RO_2^*{}_c$ from Eq. 4.16 for δ = 0.5 (δ = [HO$_2$]/[RO$_2^*$]) for EMeRGe in Europe. The data are colour-coded with: a) $j_{O(^1D)}$, b) mixing ratio of ΣVOCs, being ΣVOCs = HCHO + CH$_3$CHO + CHC(O)CH$_3$ + CHOCHO + CH$_3$OH, c) NO$_x$ mixing ratio, and d) altitude. $RO_2^*{}_m$ (small circles), the average (large circles) and the median (triangles) of the binned $RO_2^*{}_m$ over 10 pmole mole^{-1} $RO_2^*{}_c$ intervals are shown. The error bars indicate the standard error of each bin. The linear regression for the binned values (solid line) and the 1:1 relation (dashed line) are also depicted for reference.

4.2 OMO Asia: RO_2^* in Lower Troposphere

OMO Asia offered the unique opportunity to compare the $RO_{2\ m}^*$ with the HO_2 measurements ($HO_{2\ m}$) from the AirLIF instrument. The comparison allows to check the HO_2 to RO_2 ratio in the air masses investigated and validate the 1:1 HO_2:RO_2 ratio assumed for eCL determination and thereby the RO_2^* retrieval. Additionally, comparing $RO_{2\ m}^*$ and $HO_{2\ m}$ with HO_2 modelled using the EMAC also validates these results.

More than 80 % of measurements during OMO Asia were made at an altitude above 10000 m, mainly in the upper troposphere and lower stratosphere, to intercept the transported outflow from the Indian subcontinent over the measurement area. As shown in Figure 4.41, the EMAC model results indicate that the HO_2 mixing ratios during the measurements above 10000 m were < 6 pmole mole^{-1}. Based on the PeRCEAS inlet pressure $\leq$ 80 hPa, the amount of reagent gas, NO used, and the in-flight stability of the detectors, the $LOD_{RO_2^*}$ > 15 pmole mole^{-1} for the measurements above 10000 m. As a result, during the measurements above 10000 m, the RO_2^* mixing ratio was expected to be below the detection limit of PeRCEAS.

Below 10000 m, EMAC predicts HO_2 > 20 pmole mole^{-1}, which is expected to be above the $LOD_{RO_2^*}$ (< 10 pmole mole^{-1}) of PeRCEAS at the corresponding operating conditions (160 hPa inlet pressure and 15 µmole mole^{-1} reagent gas NO).
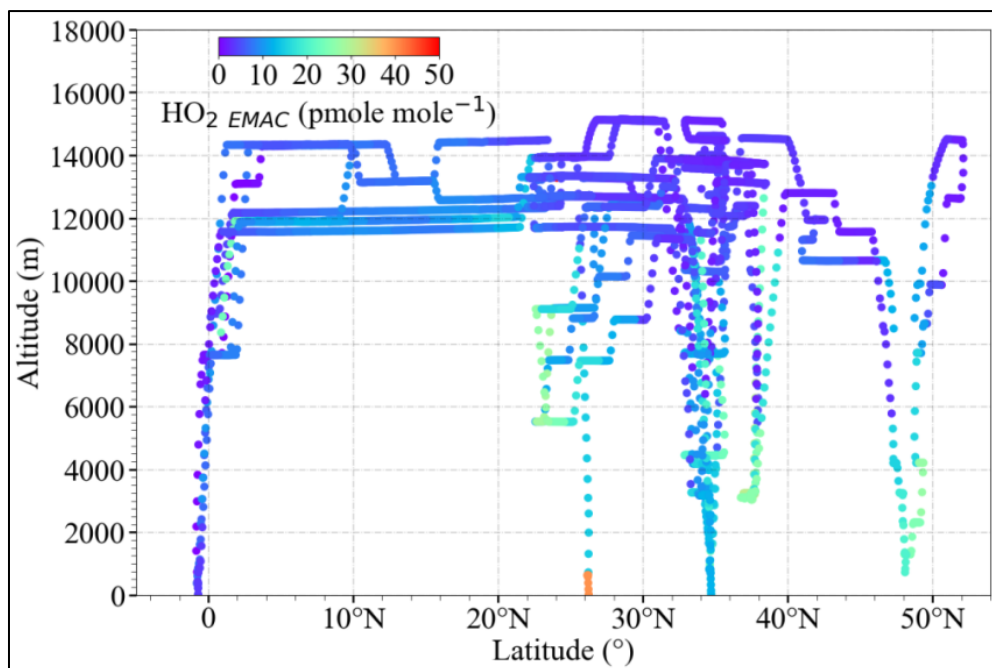
Figure 4.41: HO_2 mixing ratios calculated using EMAC model during OMO Asia as a function of latitude and altitude.

4.2.1 Case Study: Flight Over Egypt

Figure 4.42 shows the flight legs above Egypt below 10000 m from the mission flight OMO-23 on 25.08.2015 colour-coded with flight altitude. During this measurement period, HALO flew three

stable altitudes below 10000 m over the land. From point A to C, HALO flew towards the southeast in two flight legs at 9000 m and 7600 m. The flight leg between points C and D was made at 5500 m while flying southwest. FLEXPART backward trajectories indicate that the air masses measured during these flight legs were transported over the Arabian Peninsula in the PBL before reaching the sampling point and were not influenced by the Asian summer monsoon.

Figure 4.43 shows the variation of $RO_2^*{}_m$, OH and HO_2 measured using the AirLIF instrument (OH_m and $HO_{2\,m}$), and HO_2 calculated using the EMAC model ($HO_{2\,EMAC}$) together with other relevant trace gas measurements during the flight rack over Egypt from flight OMO-23. Different flight legs shown in Figure 4.42 are marked with vertical lines and letters (A to D). The gaps in the measurements correspond with missing data points. The photolysis frequency measurements were not available during these flight legs due to instrument malfunction. The variations in NO, NO_y, CO, and O_3 indicate the HALO encountered different layers between A–B. NO_y, CO, and O_3 increased to 0.6, 100, and 100 nmole mole^{-1} from A to B. NO has an enhancement of 40 pmole mole^{-1} for 8 minutes between A–B. The $HO_{2\,m}$ and $HO_{2\,EMAC}$ have similar values around 10 pmole mole^{-1}, while $RO_2^*{}_m$ varies between 10 and 20 pmole mole^{-1}. The $RO_2^*{}_m > 40$ pmole mole^{-1} near point B are measurements with pressure instabilities, as shown by the pressure flags. The $RO_2^*{}_m$, $HO_{2\,m}$, and $HO_{2\,EMAC}$ agree well within the measurement uncertainties for a 1:1 HO_2:RO_2 ratio during this flight leg. The OH_m varies around 0.25 pmole mole^{-1}.
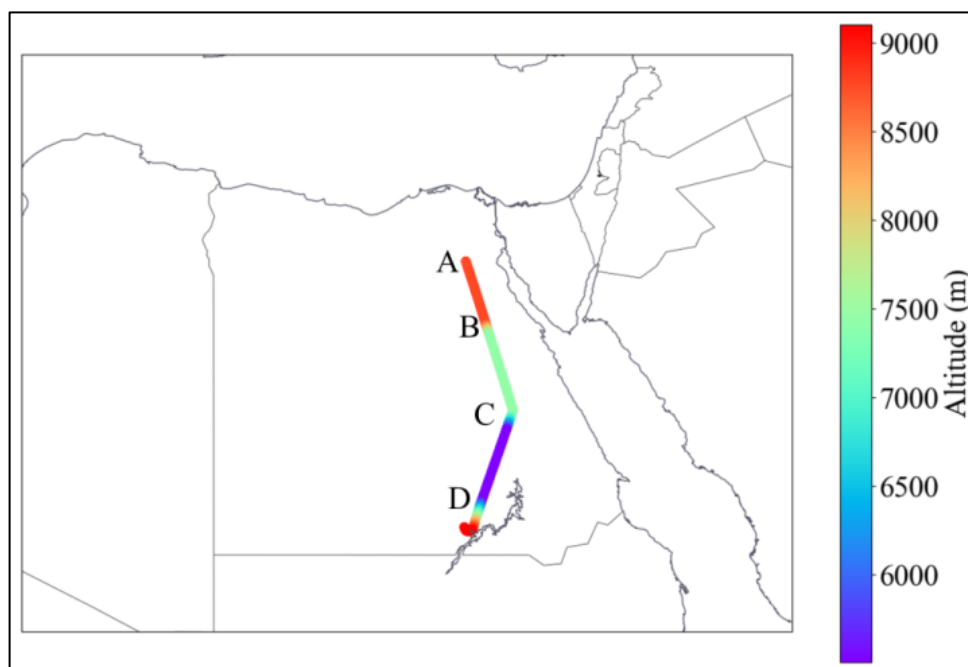
Figure 4.42: Flight legs over Egypt from flight OMO-23 on 25.08.2015. The flight track is colour-coded with flight altitude. Different flight legs are marked with letters A to D.
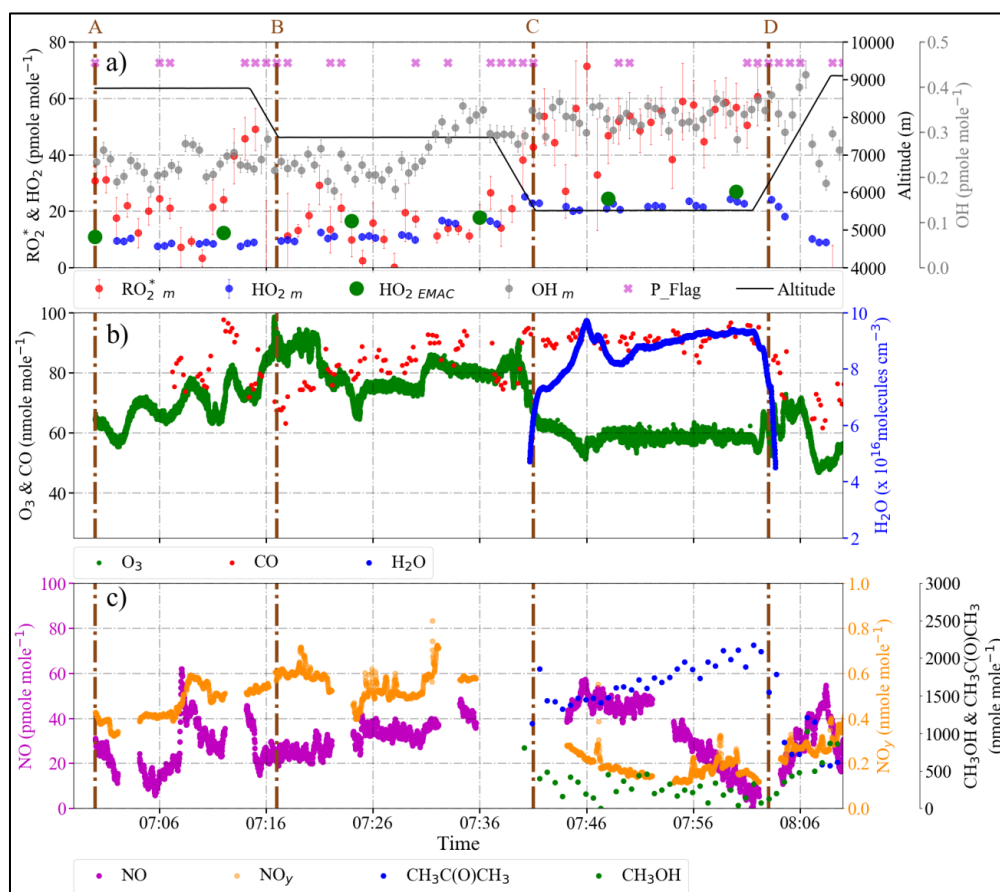
Figure 4.43: Variation of a) $RO_2^*{}_m$, OH and HO_2 measured using AirLIF instrument (OH_m and $HO_{2\ m}$), HO_2 calculated using EMAC model ($HO_{2\ EMAC}$), and flight altitude, b) O_3, CO mixing ratios and [H_2O] measured, and c) NO, NO_y, CH_3OH, and $CH_3C(O)CH_3$ mixing ratios along the EMeRGe flight OMO-23 over Egypt. The P_flag indicates RO_2^* measurements affected by dynamical pressure variation in the inlet. Different flight legs shown in Figure 4.42 are marked with vertical lines and letters from A to D.

At point B, HALO descended to 7600 m. The NO, NO_y, CO, and O_3 variations indicate HALO encountered three different layers transported over the Arabian Peninsula at altitudes above 5000 m during the flight leg B–C. The first layer has 0.6, 60, and 90 nmole mole^{-1} NO_y, CO, and O_3, respectively. The second one has ≤ 0.5, 80, and < 80 nmole mole^{-1} NO_y, CO, and O_3. The third one has ≥ 0.6, 90, 80 nmole mole^{-1} NO_y, CO, and O_3. The NO mixing ratio was around 20 to 30, 30 to 40, and > 40 pmole mole^{-1} inside the first, second, and third layers. $RO_2^*{}_m$ and $HO_{2\ m}$ were 10 pmole mole^{-1} in the first two plumes and increased to 20 pmole mole^{-1} in the third. $HO_{2\ EMAC}$ was between 15 and 20 pmole mole^{-1} during the flight leg B–C.

HALO descended to 5500 m at point C and flew towards the southwest in the flight leg C–D. The air mass measured was transported over the Arabian peninsula at altitudes below 5000 m with $<$ 0.3, 90, and 60 nmole mole^{-1} NO_y, CO, O_3. The $HO_{2\ m}$ and $HO_{2\ EMAC}$ were around 20 pmole mole^{-1} during this flight leg. $RO_2^*{}_m$ was around 50 pmole mole^{-1} which is more than two times $HO_{2\ m}$. This might result from a higher RO_2 mixing ratio in the air mass.

4.2.2 Special Case Study: Outflow from Mount Etna

Figure 4.44 shows the flight legs above the Mediterranean Sea near Mount Etna from the mission flight OMO-23 on 25.08.2015, colour-coded with flight altitude. This part of the flight was performed to measure the volcanic plume from Mount Etna. The volcanic plume was tracked during this period using the in-situ SO_2 measurements > 20 nmole $mole^{-1}$. HALO flew at an altitude of 3200 m and carried out a zigzag flight pattern, as shown in figure 4.44.
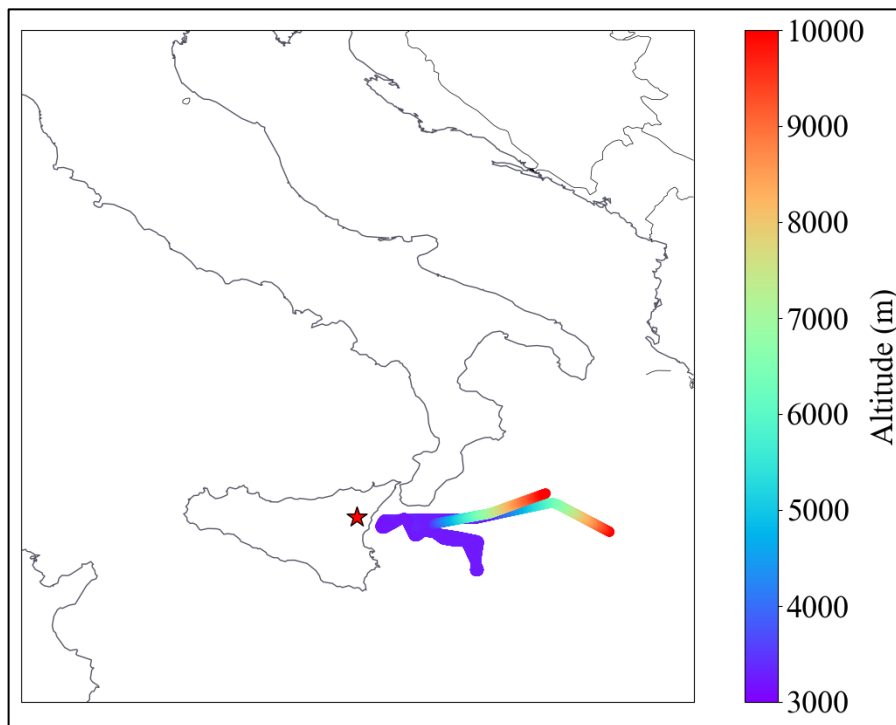
Figure 4.44: Flight legs near Mount Etna from flight OMO-23 on 25.08.2015. The flight track is colour-coded with flight altitude.

Figure 4.45 shows the variation of $RO_2{}^*{}_m$, OH_m and $HO_{2\ m}$ from the AirLIF instrument and $HO_{2\ EMAC}$ together with other relevant trace gas measurements during the flight rack near Mount Etna. The air masses with SO_2 > 20 nmole $mole^{-1}$ indicate the presence of a volcanic plume and are highlighted with grey vertical spans. The air mass with SO_2 > 20 nmole $mole^{-1}$ was encountered two times during measurements near Etna. In the volcanic plume, $HO_2/ RO_2{}^*{}_m$ changes. $RO_2{}^*{}_m$ reaches up to 120 pmole $mole^{-1}$, almost five times the $HO_{2\ m}$ and $HO_{2\ EMAC}$. The higher $RO_2{}^*{}_m$ might be due to a ClO_x (Cl + ClO + OClO) interference in the chemical amplifier, as previously reported by Perner et al., 1999 and Martinez et al., 1999 for the Arctic Tropospheric Ozone Chemistry (ARCTOC) campaigns at Ny-Ålesund. Perner et al., 1999, proposed that the chemical amplifiers using the PeRCA technique are also sensitive to ClO and OClO due to the following reactions.

$$OClO + NO \rightarrow ClO + NO_2 \hspace{4cm} \text{R4.32}$$

$$ClO + NO \rightarrow Cl + NO_2 \hspace{4.3cm} \text{R4.33}$$

$$Cl + CO \xrightarrow{M} ClCO \hspace{4.6cm} \text{R4.34}$$

$$ClCO + O_2 \xrightarrow{M} ClCO_3 \tag{R4.35}$$

$$ClCO_3 + NO \rightarrow Cl + CO_2 + NO_2 \tag{R4.36}$$

The termination of this cycle is through the wall losses and formation of nitrosyl chloride (ClNO).

$$Cl + NO \xrightarrow{M} ClNO \tag{R4.37}$$

As the interference is proportional to the amount of ClO_x present in the air mass, accurate measurements of these species and the chain length are necessary to account for the interference in the $RO_2^*{}_m$. Since ClO_x were not measured during OMO-Asia, it is impossible to calculate the possible overestimations of $RO_2^*{}_m$ in the volcanic plume.
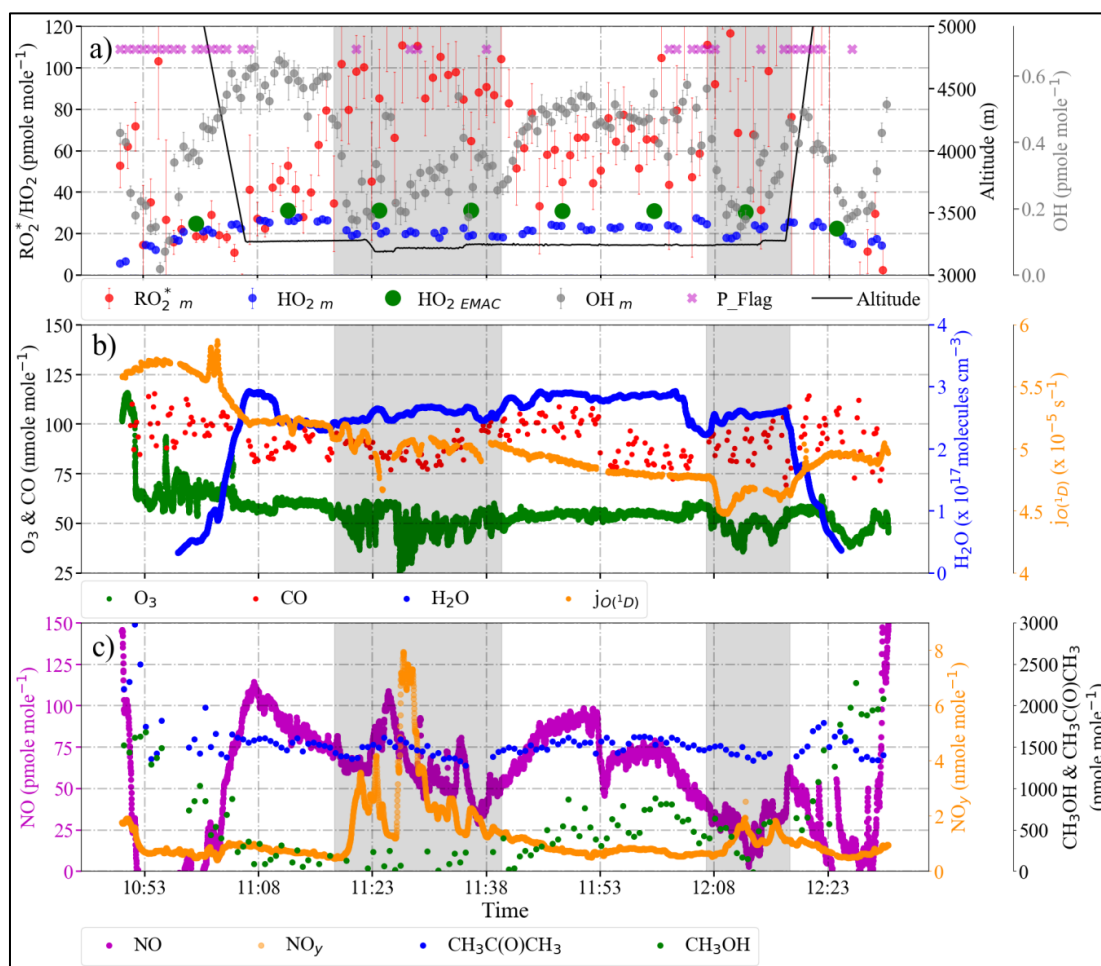
Figure 4.45: Variation of $RO_2^*{}_m$, OH and HO_2 measured using AirLIF instrument (OH_m and $HO_{2\,m}$), HO_2 calculated using EMAC model ($HO_{2\,EMAC}$), and selected RO_2^* precursors along the EMeRGe flight OMO-23 near Mount Etna. a) $RO_2^*{}_m$, $HO_{2\,m}$, OH_m, $HO_{2\,EMAC}$, and flight altitude. The P_flag indicates RO_2^* measurements affected by dynamical pressure variation in the inlet. b) O_3 and CO mixing ratios together with $[H_2O]$ and $j_{O(^1D)}$. c) NO, NO_y, CH_3OH, and $CH_3C(O)CH_3$ mixing ratios measurements. The air mass with elevated SO_2 values indicating the presence of a volcanic plume is highlighted with grey colour.

During the laboratory studies to quantify the interference, Perner et al., 1999 reported two times higher chain length for ClO than RO_2^*. Laboratory calibrations were carried out in IUP Bremen to quantify the chain length of ClO_x for the measurement conditions used during OMO-Asia in PeRCEAS. The photolysis of an HCl gas mixture in SA at 184.96 nm was used as the ClO_x source. During the experiment, the detector signal continuously deteriorated due to the hydrochloric acid formed inside the detector from the rest of the HCl gas and a small amount of the humidity coming from the additional gases, especially NO. The hydrochloric acid caused permanent damage to the high reflective mirrors and eventually damaged the NO_2 detector used. As a result, estimating the chain length for ClO_x was challenging and the subject of high experimental errors. Further laboratory studies with a different ClO_x source or a detector with mirrors protected from the sample flow with purging are necessary to determine the chain length for ClO_x for the measurement conditions used during OMO-Asia.

Outside the volcanic plume, $RO_{2\ m}^*$ is 40 to 60 pmole mole^{-1}, two times $HO_{2\ m}$ and $HO_{2\ EMAC}$. This indicates 50 % HO_2 and 50% RO_2 in $RO_{2\ m}^*$ and is similar to the measurements over Egypt.

5

Summary and Conclusion

The scientific objective of the research undertaken as part of this doctoral dissertation was to investigate and assess the current knowledge of the chemical and physical processes which control and determine the amount of peroxy radicals in the **p**lanetary **b**oundary **l**ayer (PBL) and the free troposphere. Specifically, the sum of peroxy radicals collectively known as RO_2^*. The RO_2^* is defined as the sum of HO_2 and those RO_2 that react with NO to make NO_2.

RO_2^* measurements of known accuracy are necessary prerequisites to understand its sources and sinks as well as the impact of transport and transformation on its amount. This requires a thoroughly characterised, calibrated and optimised instrument (i.e. PeRCEAS) for RO_2^* measurements. After the laboratory calibration and characterisation, a sufficient number of RO_2^* measurements must be made under various ambient conditions to represent the different air masses. In this respect, participation in three airborne measurement campaigns using HALO research aircraft provides an extensive set of data to analyse Asian and European air masses. Finally, comparing RO_2^* measurements with RO_2^* calculations using mathematical models based on currently known radical chemistry facilitates assessing the current understanding of the processes controlling the amount of RO_2^* in the troposphere.

To fulfil these requirements, the research undertaken addresses three areas.

i) Instrument Characterisation, Calibration and Optimisation

- The PeRCEAS instrument was calibrated, characterised and optimised for its deployment on HALO through laboratory studies made under atmospherically representative conditions. As a result, the dependency of the instrumental response to variations in the sample air pressure, humidity and mixing ratios of the reagent gases added to the chemical reactor of PeRCEAS was quantified. Potential interferences from ambient trace gases were investigated. The sensitivity of the HO_2 to CH_3O_2 ratio was parametrised for different operating conditions. In addition, the detection limit and reproducibility of RO_2^* measurements under controlled laboratory conditions were determined.

- The installation, testing, and monitoring of the PeRCEAS instrument before, during and after the campaigns enabled the optimisation of instrument and calibration procedures.

ii) Data Acquisition and Processing

- The customised LabVIEW™ data acquisition program was optimised using the experience from the first airborne deployment. It was extended to monitor and save key parameters such as

detector temperature, laser beam profile, and individual ring-down time for data quality assessment.

- The PeRCEAS retrieval technique and the error analysis were improved and modified to obtain an accurate RO_2^* data set with a 1- minute temporal resolution. Different routines were developed using LabVIEW™ and Python. The final analysis program developed during this doctoral study uses advanced data analysis tools like PANDAS from Python.

iii) Airborne RO_2^* Measurements and Data Analysis

- Airborne RO_2^* in-situ measurements were made using PeRCEAS onboard HALO from the PBL to the upper troposphere during the measurement campaigns OMO Asia and EMeRGe. During these campaigns, PeRCEAS successfully measured RO_2^* in 33 mission flights with a total of 275 flight hours. Onboard operations during the measurement flights, maintenance and instrument calibration after each flight were also carried out as part of the doctoral study.

- A rigorous quality assessment of the retrieved RO_2^* data set was made based on sample air temperature and humidity, operating pressure, detector temperature, and laser beam profile. The data expected to have uncertainties from these parameters were flagged. The final RO_2^* data set from OMO Asia and EMeRGe campaigns were uploaded to the HALO database to be distributed in the scientific community.

- An algebraic equation was developed to calculate the RO_2^* during campaigns assuming that the RO_2^* is in **p**hotostationary **s**teady-**s**tate (PSS). A Python routine was developed to apply this equation to the simultaneous measurements of trace gases and photolysis frequencies involved in known radical chemistry to calculate RO_2^*.

- RO_2^* measurements ($RO_{2\,m}^*$) from PeRCEAS during EMeRGe campaigns were compared with the calculated RO_2^* ($RO_{2\,c}^*$). In addition, for the Asian data set, a further comparison was made with RO_2^* estimated by using the CMAQ model. The comparisons of the $RO_{2\,m}^*$ and $RO_{2\,c}^*$ with the RO_2^* estimated by the CMAQ model were used to study the ability of CMAQ to calculate RO_2^*.

- An experimental budget analysis was performed to estimate the main loss processes of RO_2^* by introducing the RO_2^* measurements in the PSS equation.

The analysis of laboratory and campaign measurements conducted during this doctoral research led to the following conclusions.

i) Instrument Performance

- PeRCEAS was shown to be a sensitive instrument for the airborne measurement of RO_2^* in the troposphere. This is evidenced by the small **l**imit **o**f **d**etection for RO_2^* ($LOD_{RO_2^*}$), $LOD_{RO_2^*} = 6.2\times10^6$ molecules cm^{-3} (≤ 2 pmole mole^{-1} in all atmospheric conditions investigated) for a 60 s

average. Under stable laboratory conditions, PeRCEAS measurements have a relative error of 16%.

- A novel RO_2^* retrieval method delivers continuous RO_2^* measurements at a temporal resolution of 60 s during airborne measurements. This method combines both PeRCEAS channels and accounts for the errors arising from the short-term variations in the air composition during the measurement.

- Background variations in the signal within one modulation period arising from the dynamic pressure changes at the inlet, the temperature inside the aircraft, mechanical vibrations, and variation in the chemical composition are expected to increase the in-flight $LOD_{RO_2^*}$ and uncertainty of PeRCEAS measurements. Therefore, the in-flight error in the RO_2^* measurement is calculated by taking into account the uncertainty of the eCL and the background variation in the signal within one modulation period.

ii) Airborne RO_2^* Measurements

- $RO_2^*{}_m$ < 15 pmole $mole^{-1}$ was measured above 10000 m in Asia during EMeRGe and OMO campaigns. Below 10000 m, $RO_2^*{}_m$ varied between 20 and 120 pmole $mole^{-1}$ depending on the amount of water vapour (H_2O), OVOCs, NO_x, aerosol and the photolysis frequencies.

- The agreement between the RO_2^* calculated ($RO_2^*{}_c$) using the PSS assumption and the RO_2^* measured ($RO_2^*{}_m$) using PeRCEAS is generally good. The order of magnitude and short term variations of RO_2^* mixing ratios measured for most of the conditions encountered during the EMeRGe campaigns is reasonably explained by the known photochemistry described in the PSS analysis.

- Some limitations of the PSS analysis are evident inside the pollution plumes probed, where $RO_2^*{}_m$ is underestimated (< 20 %) by $RO_2^*{}_c$. The underestimation is attributed to the production of RO_2^* through OVOCs oxidation and photolysis not considered in the PSS analysis.

- The primary source of RO_2^* during the EMeRGe campaigns was the photolysis of RO_2^* precursors. This conclusion is supported by the observed correlation between $RO_2^*{}_m$ and photolysis frequencies. More specifically, O_3, HCHO, CHOCHO, and HONO photolysis were the dominant RO_2^* sources in the air masses investigated. O_3 photolysis followed by the $O(^1D) - H_2O$ reaction contributes more than 40 % to the RO_2^* production rate in the PBL and is the highest source contributor compared to other precursors. Due to the decrease in H_2O, the production rate contribution from O_3 photolysis is < 40 % in the free troposphere. As a result, other RO_2^* sources, such as the photolysis of HCHO and HONO, become more significant in the free troposphere.

- The $HO_2 - HO_2$ and $HO_2 - RO_2$ reactions are the most important loss process in air masses having NO < 800 pmole $mole^{-1}$ and aerosol ASA < 4×10^{-6} cm^2 cm^{-3} (particle number concentration < 800 particles cm^{-3}). The loss from the reaction of OH with NO and NO_2 forming HONO and HNO_3 become the dominant RO_2^* loss process for measurements with NO_x > 800

pmole mole^{-1}. In addition, for an assumed aerosol uptake coefficient of 0.24, the HO_2 uptake on aerosol becomes an important RO_2^* loss process when ASA $> 4 \times 10^{-6}$ cm^2 cm^{-3} (particle number concentration > 800 particles cm^{-3}) and NO_x mixing ratios < 800 pmole mole^{-1}.

- The RO_2^* loss rate through HO_2 uptake on aerosol is higher than the loss rate through OH reactions with NO and NO_2 during the measurements in Asia when the aerosol uptake coefficient is assumed to be ≥ 0.2. Conversely, the RO_2^* loss through the OH reaction with NO and NO_2 during the radical interconversion is more significant than the heterogeneous loss of HO_2 in the MPC outflows investigated in Europe, even with an uptake coefficient $= 0.24$. These observations are attributed to the high aerosol number concentration (> 800 particles cm^{-3}) typically observed in Asian air masses and the high NO_x (> 800 pmole mole^{-1}) and the lower particle number concentration (< 800 particles cm^{-3}) observed near European target MPCs during EMeRGe.

- $RO_2^*{}_c$ determined by the PSS assumption fails to calculate the RO_2^* accurately in the air masses with $RO_2^*{}_m < 20$ pmole mole^{-1} measured above 4000 m. The overestimation of $RO_2^*{}_m$ by $RO_2^*{}_c$ is attributed to the errors in the spatial and temporal uncertainties of the in-situ and remote sensing measurements used in the calculation and the RO_2^* loss processes (OH – OH and HO – HO_2 reactions) not considered in the PSS assumption.

- The RO_2 calculated using the CMAQ model could reproduce the amount of RO_2^* in most of the air masses investigated but fails to capture short-term variations, especially those inside the pollution plumes and under cloudy conditions. These are attributed to an underestimation of NO_x and overestimation of photolysis frequencies under cloudy conditions in the model, respectively. The agreement should improve when the model is constrained with HALO measurements.

- The RO_2 calculated using the CMAQ model agrees reasonably well with the $RO_2^*{}_c$ even though the model does not consider the loss of RO_2^* through the HO_2 uptake on aerosol. This is due to the lower production rate contribution from HONO in the model since the modelled HONO is significantly lower (more than 100 times) than the measured values from miniDOAS.

- The 1:1 HO_2:RO_2 ratio assumed for eCL determination and thus $RO_2^*{}_m$ retrieval is confirmed by the results of the CMAQ model for most of the measurements considered in this study.

- The 1:1 HO_2 to RO_2 ratio assumed generally agree with simultaneous HO_2 measurements and model calculations in the air masses sampled within OMO Asia.

- Potential interferences from ClO_x in RO_2^* obtained using PeRCEAS cannot be ruled out during the measurements in the volcanic plume of Mount Etna. $RO_2^*{}_m$ is five times higher than the HO_2 measured using AirLIF and calculated using the EMAC model in the volcanic plume.

Some of the results presented above are published in George et al., 2020; Andrés Hernández et al., 2022; and the ACPD publication George et al., 2022. In addition, it is planned to submit one paper on the measurements of RO_2^* in Asia.

List of Publications and Scientific Conferences Attended

Peer reviewed

Georg, M., Andrés-Hernández, M. D., Nenakhov, V., Liu, Y., and Burrows, J. P.: Airborne measurement of peroxy radicals using chemical amplification coupled with cavity ring-down spectroscopy: the PeRCEAS instrument, Atmos. Meas. Tech 13, 2577–2600, https://doi.org/10.5194/amt-13-2577-2020, 2020.

Andrés Hernández, M. D., Hilboll, A., Ziereis, H., Förster, E., Krüger, O. O., Kaiser, K., Schneider, J., Barnaba, F., Vrekoussis, M., Schmidt, J., Huntrieser, H., Blechschmidt, A.-M., George, M., Nenakhov, V., Harlass, T., Holanda, B. A., Wolf, J., Eirenschmalz, L., Krebsbach, M., Pöhlker, M. L., Kalisz Hedegaard, A. B., Mei, L., Pfeilsticker, K., Liu, Y., Koppmann, R., Schlager, H., Bohn, B., Schumann, U., Richter, A., Schreiner, B., Sauer, D., Baumann, R., Mertens, M., Jöckel, P., Kilian, M., Stratmann, G., Pöhlker, C., Campanelli, M., Pandolfi, M., Sicard, M., Gómez-Amo, J. L., Pujadas, M., Bigge, K., Kluge, F., Schwarz, A., Daskalakis, N., Walter, D., Zahn, A., Pöschl, U., Bönisch, H., Borrmann, S., Platt, U., and Burrows, J. P.: Overview: On the transport and transformation of pollutants in the outflow of major population centres – observational data from the EMeRGe European intensive operational period in summer 2017, Atmos. Chem. Phys., 22, 5877–5924, https://doi.org/10.5194/acp-22-5877-2022, 2022.

ACPD Publication

Georg, M., Andrés-Hernández, M. D., Nenakhov, V., Liu, Y., Bohn, B., Förster, E., Obersteiner, F., Zahn, A., Harlaß, T., Ziereis, H., Benjamin, S., Kluge, F., Bigge, K., Platt, U., Pfeilsticker, K., Schlager, H., and Burrows, J. P.: On the understanding tropospheric fast photochemistry: airborne observations of peroxy radicals during the EMeRGe campaign in Europe, Atmos. Chem. Phys. Discuss. [preprint], https://acp.copernicus.org/preprints/acp-2022-119, under revision, 2022.

Conference presentations

Poster presentation: "Airborne measurement of peroxy radicals during EMeRGe" in 14th iCACGP Quadrennial Symposium/15th IGAC Science Conference in September 2018.

Oral presentation: "Airborne measurement of peroxy radicals in polluted air masses of East Asian origin during EMeRGe" in EGU General Assembly in April 2019.

Oral presentation: "Airborne measurement of peroxy radicals in MPC outflows during EMeRGe" in IUGG General Assembly in July 2019.

Oral presentation: "Investigation of the photo-chemical activity in different MPC outflows during EMeRGe" in EGU General Assembly-Online in April 2020.
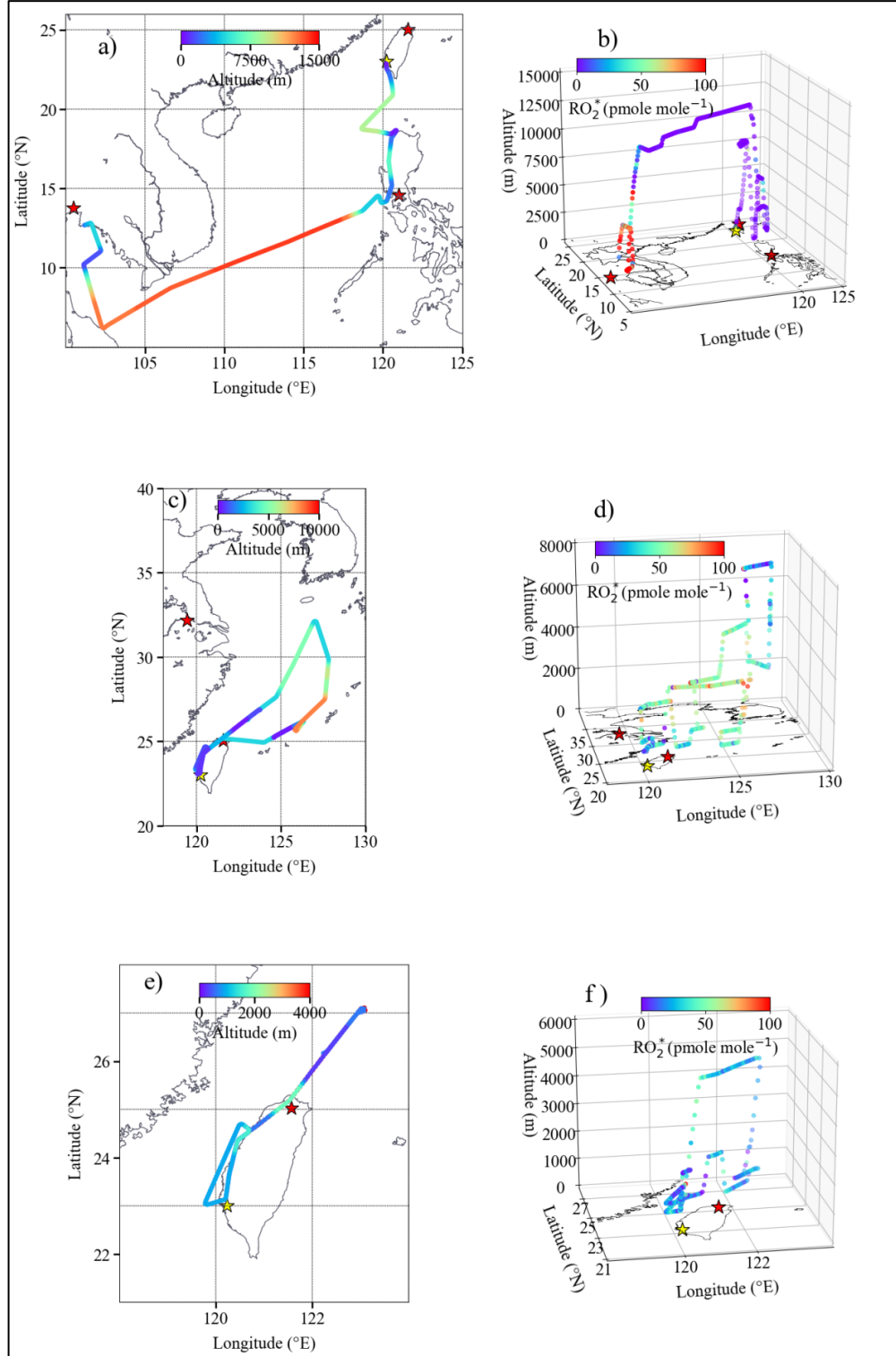
Figure A1: Examples of $RO_2^*{}_m$ obtained in the EMeRGe campaign in Asia. The left panel shows the flight tracks colour-coded with flight altitude, and the right panel shows the 3D view of the corresponding flight track colour-coded with RO_2^* mixing ratios. Plots a) and b) show the E-AS-03 flight; plots c) and d) show the E-AS-05 flight; plots e) and f) show the E-AS-07 flight. Red stars indicate the targets MPC Taipei, Bangkok, Manila, and Yangtze River Delta, and yellow indicates the HALO base in Tainan.
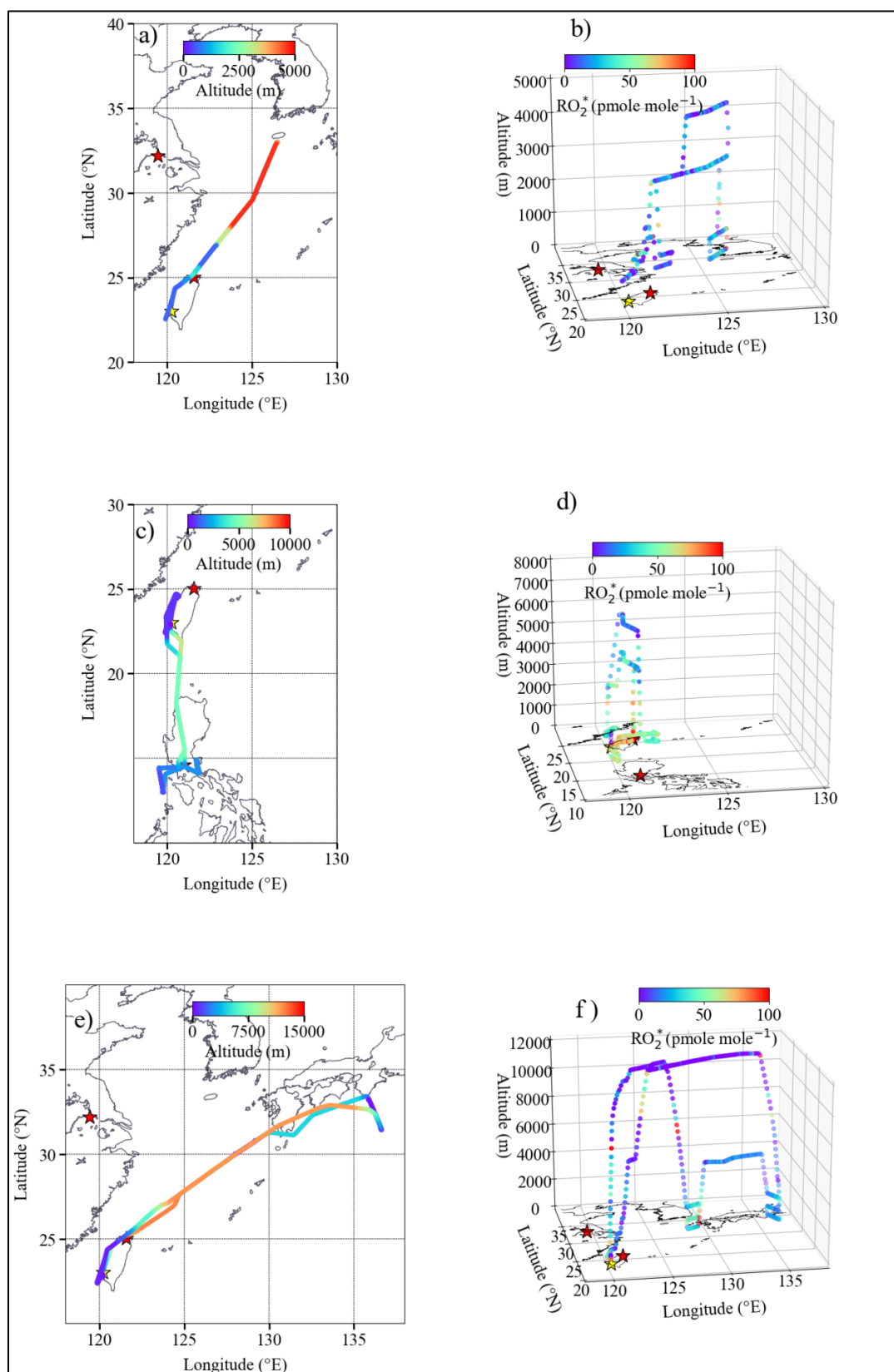
Figure A2: Examples of RO$_2^*$$_m$ obtained in the EMeRGe campaign in Asia. The left panel shows the flight tracks colour-coded with flight altitude, and the right panel shows the 3D view of the corresponding flight track colour-coded with RO$_2^*$ mixing ratios. Plots a) and b) show the E-AS-09 flight; plots c) and d) show the E-AS-10 flight; plots e) and f) show the E-AS-11 flight. Red stars indicate the targets MPC Taipei, Manila, and Yangtze River Delta, and the yellow star indicates the HALO base in Tainan.

Figure A3: Examples of $RO_2{}^*{}_m$ obtained in the EMeRGe campaign in Asia. The left panel shows the flight tracks colour-coded with flight altitude, and the right panel shows the 3D view of the corresponding flight track colour-coded with $RO_2{}^*$ mixing ratios. Plots a) and b) show the E-AS-13 flight; plots c) and d) show the E-AS-14 flight. Red stars indicate the targets MPC Taipei, Bangkok, and Yangtze River Delta, and the yellow star indicates the HALO base in Tainan.

I. Reaction and rate constants used in the current study

The temperature dependent rate constant of the bimolecular reactions is calculated using the Arrhenius expression:

$$k(T) = A \times e^{(-E/RT)}$$

Eq. A1

The low-pressure-limiting rate constants for termolecular reactions are given in the form:

$$k_0(T) = k_{0^{298}} \times (T/298)^{-n} \text{ cm}^6 \text{ molecules}^{-2} \text{ s}^{-1}$$

Eq. A2

The high-pressure-limiting rate constants for termolecular reactions are given in the form:

$$k_\infty(T) = k_{\infty^{298}} \times (T/298)^{-m} \text{ cm}^3 \text{ molecules}^{-1} \text{ s}^{-1}$$

Eq. A3

The following formula calculates the effective second-order rate constant for a given temperature and pressure (altitude) (Burkholder et al., 2019).

$$k_f(T, [M]) = \left\{ \frac{k_\infty(T) k_0(T)[M]}{k_\infty(T) + k_0(T)[M]} \right\} 0.6^{\left\{ 1 + \left[\log_{10}\left(\frac{k_0(T)[M]}{k_\infty(T)} \right) \right]^2 \right\}^{-1}}$$

Eq. A4

Where [M] is the total gas concentration.

Table A1: Reactions and corresponding rate constants taken from Burkholder et al., 2019. The radical intermediate formed during OVCO oxidation and photolysis are assumed to be converted to RO_2^*, and the oxidation reaction or the photolysis is taken as the rate-determining step.

Number	Reaction	A-Factor	E/R	k (298 K) or k_{total} (298K, 1atm)	$k_0(T) = k_{0^{298}} \times (T/298)^{-n}$		$k_\infty(T) = k_{\infty^{298}} \times (T/298)^{-m}$	
					$k_{0^{298}}$	n	$k_{\infty^{298}}$	m
R4.1	[a]O_3 + hv → O(^{1}D) + O_2							
R4.2a	O(^{1}D) + H_2O → 2OH	1.63×10^{-10}	-60	2.0×10^{-10}				

Number	Reaction	A-Factor	E/R	k (298 K) or k_{total} (298K, 1atm)	$k_0(T) =$ $k_{0^{298}} \times (T/298)^{-n}$		$k_\infty(T) =$ $k_{\infty^{298}} \times (T/298)^{-m}$	
					$k_{0^{298}}$	n	$k_{\infty^{298}}$	m
R4.2b	$O(^1D) + O_2 \rightarrow O(^3P) + O_2$	3.3×10^{-11}	-55	3.95×10^{-11}				
R4.2c	$O(^1D) + N_2 \rightarrow O(^3P) + N_2$	2.15×10^{-11}	-110	3.1×10^{-11}				
R4.3	$HONO + hv \rightarrow OH + NO$							
R4.4	$H_2O_2 + hv \rightarrow 2OH$							
R4.5	$OH + O_3 \rightarrow HO_2 + O_2$	1.7×10^{-12}	940	7.3×10^{-14}				
R4.6	$OH + CO + O_2 \xrightarrow{M} HO_2 + CO_2$			2.4×10^{-13}	6.9×10^{-33}	2.1	1.1×10^{-12}	-1.3
R4.7	[b]$OH + CH_4 + O_2 \rightarrow CH_3O_2 + H_2O$	2.45×10^{-12}	1775	6.3×10^{-15}				
R4.8	[c]$HCHO + hv + 2O_2 \rightarrow 2HO_2 + CO$							
R4.9	[d]$CH_3CHO + hv + 2O_2 \rightarrow CH_3O_2 + HO_2 + CO$							
R4.10a	[e]$CH_3C(O)CH_3 + hv + 2O_2 \rightarrow CH_3C(O)O_2 + CH_3O_2$							
R4.10b	$CH_3C(O)CH_3 + hv + 2O_2 \rightarrow 2\ CH_3O_2 + CO$							
R4.11	$CHOCHO + hv + 2O_2 \rightarrow 2HO_2 + 2CO$							
R4.12a	$OH + HCHO + O_2 \rightarrow HO_2 + CO + H_2O$	5.5×10^{-12}	-125	8.5×10^{-12}				
R4.12b	[f]$OH + CH_3CHO + O_2 \xrightarrow{M} CH_3C(O)O_2 + H_2O$	4.63×10^{-12}	-350	1.5×10^{-11}				
R4.12c	[g]$OH + CH_3C(O)CH_3 \rightarrow H_2O + CH_3C(O)CH_2$			See note				
R4.12d	$OH + CH_3OH + O_2 \rightarrow CH_2O + HO_2 + H_2O$	2.9×10^{-12}	345	9.1×10^{-13}				
R4.12e	$OH + CHOCHO + O_2 \rightarrow HO_2 + H_2O + 2CO$	1.15×10^{-11}	0	1.15×10^{-11}				
R4.13	[h]$O3 + CH_2=C(CH_3)CH=CH_2 \rightarrow products$	1.1×10^{-14}	2000	1.3×10^{-17}				

Number	Reaction	A-Factor	E/R	k (298 K) or k_{total} (298K, 1atm)	$k_0(T) = k_{0^{298}} \times (T/298)^{-n}$		$k_\infty(T) = k_{\infty^{298}} \times (T/298)^{-m}$	
					$k_{0^{298}}$	n	$k_{\infty^{298}}$	m
R4.14	$^{(i)}HO_2 + HO_2 \rightarrow H_2O_2 + O_2$	3.0×10^{-13}	-460	1.4×10^{-12}				
	$\xrightarrow{M} H_2O_2 + O_2$	$2.3 \times 10^{-33}[M]$	-920	$4.6 \times 10^{-32}[M]$	See note			
R4.15	$HO_2 + CH_3O_2 \rightarrow CH_3OOH + O_2$	4.1×10^{-13}	-750	5.2×10^{-12}				
R4.16a	$^{(j)}CH_3O_2 + CH_3O_2 \rightarrow CH_3OH + HCHO + O_2$	9.5×10^{-14}	-390	3.5×10^{-13}				
R4.16b	$CH_3O_2 + CH_3O_2 \rightarrow 2CH_3O + O_2$	9.5×10^{-14}	-390	3.5×10^{-13}				
R4.17	$OH + HO_2 \rightarrow H_2O + O_2$	4.8×10^{-11}	-250	1.1×10^{-10}				
R4.18a	$OH + OH \xrightarrow{M} H_2O_2$			6.3×10^{-12}	6.9×10^{-31}	1.0	2.6×10^{-11}	0
R4.18b	$OH + OH \rightarrow H_2O + O(^3P)$	1.8×10^{-12}	0	1.8×10^{-12}				
R4.19	$OH + NO \xrightarrow{M} HONO$			7.4×10^{-12}	7.1×10^{-31}	2.6	3.6×10^{-11}	0.1
R4.20	$OH + NO_2 \xrightarrow{M} HNO_3$			1.1×10^{-11}	1.8×10^{-30}	3.0	2.8×10^{-11}	0
R4.21	$^{(k)}HO_2 + NO_2 \xrightarrow{M} HO_2NO_2$			1.3×10^{-12}	1.9×10^{-31}	3.4	4.0×10^{-12}	0.3
R4.22	$CH_3O + NO \xrightarrow{M} CH_3ONO$			2.9×10^{-11}	2.3×10^{-29}	2.8	3.8×10^{-11}	0.6
R4.23	$^{(l)}HO_2 + NO \rightarrow OH + NO_2$	3.44×10^{-12}	-260	8.2×10^{-12}				

Number	Reaction	A-Factor	E/R	k (298 K) or k_{total} (298K, 1atm)	$k_0(T) = k_{0^{298}} \times (T/298)^{-n}$		$k_\infty(T) = k_{\infty^{298}} \times (T/298)^{-m}$	
					$k_{0^{298}}$	n	$k_{\infty^{298}}$	m
R4.24	$HO_2 + O_3 \rightarrow OH + 2O_2$	1.0×10^{-14}	490	1.9×10^{-15}				
R4.25	$^{(m)}CH_3O_2 + NO \rightarrow CH_3O + NO_2$	2.8×10^{-12}	-300	7.7×10^{-12}				
R4.26	$CH_3O + O_2 \rightarrow CH_2O + HO_2$	3.9×10^{-14}	900	1.9×10^{-15}				

(a) The O_3 photolysis has a second channel $O_3 + h\nu$ ($\lambda < 320$ nm) $\rightarrow O(^3P) + O_2$. So, only the photolysis frequency for R4.1 is used in the calculation.

(b) Reaction OH with CH_4 produces CH_3 and H_2O. The CH_3 formed further reacts with O_2 to form CH_3O_2. The formation of CH_3O_2 is assumed to be much faster than the CH_3 formation due to the high amount of O_2 present in the atmosphere. So the reaction of OH with CH_3 is taken as the rate-determining step for R4.7.

(c) The HCHO photolysis has a second channel, HCHO + $h\nu$ ($\lambda < 320$ nm) $\rightarrow H_2 + CO$. So, only the photolysis frequency for R4.8 is used in the calculation.

(d) The CH_3CHO photolysis has a second channel $CH_3CHO + h\nu$ ($\lambda < 320$ nm) $\rightarrow CH_4 + CO$. So, only the photolysis frequency for R4.9 is used in the calculation.

(e) To simplify the calculation, the $CH_3C(O)O_2$ produced is treated as a CH_3O_2 molecule during the calculation.

(f) The reaction of OH with CH_3CHO produces $CH_3C(O)$ and H_2O. The $CH_3C(O)$ formed reacts with O_2 in a three-body reaction to form $CH_3C(O)O_2$. The formation of $CH_3C(O)O_2$ is assumed to be much faster than the $CH_3C(O)$ formation due to the high amount of O_2 present in the atmosphere. So the reaction of OH with CH_3CHO is taken as the rate-determining step for R4.12b. To simplify the calculation, the $CH_3C(O)O_2$ produced is treated as a CH_3O_2 molecule during the calculation.

(g) The temperature-dependent reaction rate constant is given by: $k_{4.12c}(T) = 1.33 \times 10^{-13} + 3.82 \times 10^{-11} \times e^{(-2000/T)}$ $cm^3 molecules^{-1}s^{-1}$. $CH_3C(O)CH_2$ formed reacts with O_2 in a three-body reaction to form $CH_3C(O)CH_2O_2$. The formation of $CH_3C(O)CH_2O_2$ is assumed to be much faster than the $CH_3C(O)CH_2$ formation due to the high amount of O_2 present in the atmosphere. So the reaction of OH with $CH_3C(O)CH_3$ is taken as the rate-determining step for R4.12c. To simplify the calculation, the $CH_3C(O)CH_2O_2$ produced is treated as a CH_3O_2 molecule during the calculation.

(h) The reaction R4.13 shows an example of an ozonolysis reaction. To simplify the calculation, the ozonolysis reactions are not considered in this study.

(i) Reaction R4.14 exhibits a dependence on H_2O concentration. So the overall rate constant is given by the sum of the bimolecular component and a pressure-dependent termolecular component multiplied by the H_2O enhancement term. i.e.,

$(1.4 \times 10^{-12} + 4.6 \times 10^{-32}[M])(1 + 1.4 \times 10^{-21}[H_2O]exp^{(2200/T)})$

(j) The CH_3O_2 self-reaction has a second channel with relative product yield, $\frac{k_{4.16b}}{k_{4.16a}} = (26.2 \pm 6.6) e^{(-1130 \pm 240)/T}$

(k) The HO_2NO_2 made from the $HO_2 + NO_2$ reaction is assumed to undergo photolysis to produce $HO_2 + NO_2$ or $OH + NO_3$. The $HO_2 + NO_2$ reaction is taken as a null cycle for the present work.

(l) Note that the $HO_2 + NO$ reaction have another channel producing HNO_3. The probability of this channel is less than 1% and therefore negligible.

(m) Note that the $CH_3O_2 + NO$ reaction have another channel producing CH_3NO_2. The probability of this channel is less than 0.5% and therefore negligible.

II.   Deviation of Eq. 4.8 and Eq. 4.9

An analytical equation to calculate $RO_2{}^*$ was derived, assuming the primary source of $RO_2{}^*$ production is precursor photolysis, the loss of $RO_2{}^*$ is only through $RO_2{}^*$ – $RO_2{}^*$ reactions, and the radical interconversion reactions between OH, RO and $RO_2{}^*$ occurs without losses. Based on the results of previous airborne campaigns (Tan et al., 2001 and Cantrell et al., 2003b), the production of $RO_2{}^*$ from the photolysis of H_2O_2 and ozonolysis of alkenes were assumed to have a minor contribution and are excluded from this study. In addition, CH_3O_2 reactions were taken as a surrogate for all RO_2 reactions to reduce the complexity of the calculations.

Under these assumptions and based on the reactions in Table A1

- The rate of change of $[RO_2{}^*]$ is given by

$$\frac{d}{dt}([RO_2^*]) = \frac{d}{dt}([OH] + [CH_3O] + [HO_2] + [CH_3O_2])$$

$$\frac{d}{dt}([RO_2^*]) = 2j_{4.1}[O_3]\beta + j_{4.3}[HONO] + 2j_{4.8}[HCHO] + 2j_{4.11}[CHOCHO] + 2j_{4.9}[CH_3CHO] + 2(j_{4.10a} + j_{4.10b})[CH_3C(O)CH_3] - 2k_{4.15}[HO_2][CH_3O_2]$$
$$- 2k_{4.14}[HO_2]^2 - 2k_{4.16a}[CH_3O_2]^2$$

<div align="right">Eq. A5</div>

Where β is the fraction of $O(^1D)$ that reacts with H_2O to form OH and is given by $\beta = \left(\frac{k_{4.2a}[H_2O]}{k_{4.2a}[H_2O] + k_{4.2b}[O_2] + k_{4.2c}[N_2]}\right)$

Now substituting $[HO_2] = \delta[RO_2{}^*]$ and $[CH_3O_2] = (1-\delta)[RO_2{}^*]$ in Eq. A5

$$\frac{d}{dt}([RO_2^*]) = 2j_{4.1}[O_3]\beta + j_{4.3}[HONO] + 2j_{4.8}[HCHO] + 2j_{4.11}[CHOCHO] + 2j_{4.9}[CH_3CHO] + 2(j_{4.10a} + j_{4.10b})[CH_3C(O)CH_3] - 2k_{4.15}\delta(1-\delta)[RO_2^*]^2$$
$$- 2k_{4.16a}((1-\delta)[RO_2^*])^2 - 2k_{4.14}(\delta[RO_2^*])^2$$

Under photostationary steady-state

$$\frac{d}{dt}([RO_2^*]) = 0$$

$\Rightarrow 2j_{4.1}[O_3]\beta + j_{4.3}[HONO] + 2j_{4.8}[HCHO] + 2j_{4.11}[CHOCHO] + 2j_{4.9}[CH_3CHO] + 2(j_{4.10a} + j_{4.10b})[CH_3C(O)CH_3] = 2k_{4.15}\delta(1-\delta)[RO_2^*]^2 + 2k_{4.16a}((1-\delta)[RO_2^*])^2 + 2k_{4.14}(\delta[RO_2^*])^2$

<div align="right">Eq. A6</div>

Eq. A6 is a quadratic equation of $[RO_2{}^*]$ without a linear term. The solution is given by

$$[RO_2^*]_c = \sqrt[2]{P_{RO_2^*} \Big/ 2k_{RO_2^*}}$$

<div align="right">Eq. A7</div>

$$k_{RO_2^*} = (k_{4.15}\delta(1-\delta) + k_{4.16a}(1-\delta)^2 + k_{4.14}\delta^2)$$

$$P_{RO_2^*} = 2j_{4.1}[O_3]\beta + j_{4.3}[HONO] + 2j_{4.8}[HCHO] + 2j_{4.11}[CHOCHO] + 2j_{4.9}[CH_3CHO] + 2(j_{4.10a} + j_{4.10b})[CH_3C(O)CH_3]$$

III. Derivation of Eq. 4.11 and Eq. 4.12

If the radical interconversion and the loss of OH and CH$_3$O through the reaction with NO$_x$ during the interconversion are considered, then

- The rate of change of [OH] is given by

$$\frac{d}{dt}([OH]) = 2j_{4.1}[O_3]\beta + j_{4.3}[HONO] + k_{4.23}[HO_2][NO] + k_{4.24}[HO_2][O_3] - [OH](k_{4.6}[CO] + k_{4.7}[CH_4] + k_{4.12a}[HCHO] + k_{4.12b}[CH_3CHO] +$$
$$k_{4.12c}[CH_3C(O)CH_3] + k_{4.12d}[CH_3OH] + k_{4.12e}[CHOCHO] + k_{4.5}[O_3] + k_{4.19}[NO] + k_{4.20}[NO_2] + k_{4.17}[HO_2]) - 2(k_{4.18a} + k_{4.18b})[OH]^2$$

<div align="right">Eq. A8</div>

Under photostationary steady-state

$$\frac{d}{dt}([OH]) = 0$$

i.e.,

$$2j_{4.1}[O_3]\beta + j_{4.3}[HONO] + k_{4.23}[HO_2][NO] + k_{4.24}[HO_2][O_3] = [OH](k_{4.6}[CO] + k_{4.7}[CH_4] + k_{4.12a}[HCHO] + k_{4.12b}[CH_3CHO] + k_{4.12c}[CH_3C(O)CH_3] +$$
$$k_{4.12d}[CH_3OH] + k_{4.12e}[CHOCHO] + k_{4.5}[O_3] + k_{4.19}[NO] + k_{4.20}[NO_2] + k_{4.17}[HO_2]) - 2(k_{4.18a} + k_{4.18b})[OH]^2$$

<div align="right">Eq. A9</div>

Since the atmospheric [OH] and [HO$_2$] << [NO] and [NO$_2$], reactions R4.18 (OH – OH reaction) and R4.17 (OH – HO$_2$ reaction) are assumed to be negligible in the loss process of OH compared to the OH – NO$_x$ reactions. So Eq. A9 can be modified as:

$$[OH] = \frac{2j_{4.1}[O_3]\beta + j_{4.3}[HONO] + k_{4.23}[HO_2][NO] + k_{4.24}[HO_2][O_3]}{(k_{4.6}[CO] + k_{4.7}[CH_4] + k_{4.12a}[HCHO] + k_{4.12b}[CH_3CHO] + k_{4.12c}[CH_3C(O)CH_3] + k_{4.12d}[CH_3OH] + k_{4.12e}[CHOCHO] + k_{4.5}[O_3] + k_{4.19}[NO] + k_{4.20}[NO_2])}$$

<div align="right">Eq. A10</div>

- The rate of change of [CH$_3$O] is given by

$$\frac{d}{dt}([CH_3O]) = 2k_{4.16b}[CH_3O_2]^2 + k_{4.25}[CH_3O_2][NO] - [CH_3O](k_{4.22}[NO] + k_{4.26}[O_2])$$

Eq. A11

Under photostationarysteady state

$$\frac{d}{dt}([CH_3O]) = 0$$

$$\Rightarrow [CH_3O] = \frac{2k_{4.16b}[CH_3O_2]^2 + k_{4.25}[CH_3O_2][NO]}{(k_{4.22}[NO] + k_{4.26}[O_2])}$$

Eq. A12

- The rate of change of $[HO_2]$ is given by

$$\frac{d}{dt}([HO_2]) = 2j_{4.8}[HCHO] + j_{4.9}[CH_3CHO] + 2j_{4.11}[CHOCHO] + [OH](k_{4.6}[CO] + k_{4.5}[O_3] + k_{4.12a}[HCHO] + k_{4.12d}[CH_3OH] + k_{4.12e}[CHOCHO]) +$$
$$k_{4.26}[CH_3O][O_2] - [HO_2](k_{4.15}[CH_3O_2] + k_{4.17}[OH] + k_{4.23}[NO] + k_{4.24}[O_3]) - 2k_{4.14}[HO_2]^2$$

Since the atmospheric $[OH] \ll [NO]$ and $[NO_2]$, reaction R4.17 (OH – HO₂ reaction) is assumed to have a negligible contribution to the HO₂ loss process. So

$$\frac{d}{dt}([HO_2]) = 2j_{4.8}[HCHO] + j_{4.9}[CH_3CHO] + 2j_{4.11}[CHOCHO] + [OH](k_{4.6}[CO] + k_{4.5}[O_3] + k_{4.12a}[HCHO] + k_{4.12d}[CH_3OH] + k_{4.12e}[CHOCHO]) +$$
$$k_{4.26}[CH_3O][O_2] - [HO_2](k_{4.15}[CH_3O_2] + k_{4.23}[NO] + k_{4.24}[O_3]) - 2k_{4.14}[HO_2]^2$$

Eq. A13

- The rate of change of $[CH_3O_2]$ is given by

$$\frac{d}{dt}([CH_3O_2]) = j_{4.9}[CH_3CHO] + 2(j_{4.10a} + j_{4.10b})[CH_3C(O)CH_3] + [OH](k_{4.7}[CH_4] + k_{4.12d}[CH_3CHO] + k_{4.12c}[CH_3C(O)CH_3]) - [CH_3O_2](k_{4.15}[HO_2] +$$
$$k_{4.25}[NO]) - 2(k_{16a} + k_{16b})[CH_3O_2]^2$$

Eq. A14

- If CH_3O_2 is assumed as a surrogate for all RO₂, then the rate of change of $[RO_2^*]$ is given by

$$\frac{d}{dt}([RO_2^*]) = \frac{d}{dt}([HO_2] + [CH_3O_2])$$

$$=$$

$$2j_{4.8}[HCHO] + j_{4.9}[CH_3CHO] + 2j_{4.11}[CHOCHO] + [OH](k_{4.6}[CO] + k_{4.5}[O_3] + k_{4.12a}[HCHO] + k_{4.12d}[CH_3OH] + k_{4.12e}[CHOCHO]) + k_{4.26}[CH_3O][O_2] -$$
$$[HO_2](k_{4.15}[CH_3O_2] + k_{4.23}[NO] + k_{4.24}[O_3]) - 2k_{4.14}[HO_2]^2 + j_{4.9}[CH_3CHO] + 2(j_{4.10a} + j_{4.10b})[CH_3C(O)CH_3] + [OH](k_{4.7}[CH_4] + k_{4.12d}[CH_3CHO] +$$
$$k_{4.12c}[CH_3C(O)CH_3]) - [CH_3O_2](k_{4.15}[HO_2] + k_{4.25}[NO]) - 2(k_{16a} + k_{16b})[CH_3O_2]^2$$

Eq. A15

Since OH and CH$_3$O are not measured onboard during EMeRGe, Eq. A10 and Eq. A12 are substituted in Eq. A15 and rearranging.

$\frac{d}{dt}([RO_2^*]) =$

$2j_{4.8}[HCHO] + 2j_{4.9}[CH_3CHO] + 2j_{4.11}[CHOCHO] + 2(j_{4.10a} + j_{4.10b})[CH_3C(O)CH_3] +$

$\frac{2j_{4.1}[O_3]\beta + j_{4.3}[HONO] + k_{4.23}[HO_2][NO] + k_{4.24}[HO_2][O_3]}{(k_{4.6}[CO] + k_{4.7}[CH_4] + k_{4.12a}[HCHO] + k_{4.12b}[CH_3CHO] + k_{4.12c}[CH_3C(O)CH_3] + k_{4.12d}[CH_3OH] + k_{4.12e}[CHOCHO] + k_{4.5}[O_3] + k_{4.19}[NO] + k_{4.20}[NO_2])}(k_{4.6}[CO] +$

$k_{4.5}[O_3] + k_{4.12a}[HCHO] + k_{4.12d}[CH_3OH] + k_{4.12e}[CHOCHO] + k_{4.7}[CH_4] + k_{4.12d}[CH_3CHO] + k_{4.12c}[CH_3C(O)CH_3]) +$

$k_{4.26}\frac{2k_{4.16b}[CH_3O_2]^2 + k_{4.25}[CH_3O_2][NO]}{(k_{4.22}[NO] + k_{4.26}[O_2])}[O_2] - [CH_3O_2](k_{4.15}[HO_2] + k_{4.25}[NO]) - 2(k_{16a} + k_{16b})[CH_3O_2]^2 - [HO_2](k_{4.15}[CH_3O_2] + k_{4.23}[NO] +$

$k_{4.24}[O_3]) - 2k_{4.14}[HO_2]^2$ \hfill Eq. A16

Now substituting

$(1 - \rho) = \frac{(k_{4.6}[CO] + k_{4.5}[O_3] + k_{4.12a}[HCHO] + k_{4.12d}[CH_3OH] + k_{4.12e}[CHOCHO] + k_{4.7}[CH_4] + k_{4.12d}[CH_3CHO] + k_{4.12c}[CH_3C(O)CH_3])}{(k_{4.6}[CO] + k_{4.7}[CH_4] + k_{4.12a}[HCHO] + k_{4.12b}[CH_3CHO] + k_{4.12c}[CH_3C(O)CH_3] + k_{4.12d}[CH_3OH] + k_{4.12e}[CHOCHO] + k_{4.5}[O_3] + k_{4.19}[NO] + k_{4.20}[NO_2])}$ in Eq. A16 gives

$\frac{d}{dt}([RO_2^*]) = 2j_{4.8}[HCHO] + 2j_{4.9}[CH_3CHO] + 2j_{4.11}[CHOCHO] + 2(j_{4.10a} + j_{4.10b})[CH_3C(O)CH_3] + (2j_{4.1}[O_3]\beta + j_{4.3}[HONO] + k_{4.23}[HO_2][NO] +$

$k_{4.24}[HO_2][O_3])(1 - \rho) + k_{4.26}\frac{2k_{4.16b}[CH_3O_2]^2 + k_{4.25}[CH_3O_2][NO]}{(k_{4.22}[NO] + k_{4.26}[O_2])}[O_2] - [CH_3O_2](k_{4.15}[HO_2] + k_{4.25}[NO]) - 2(k_{16a} + k_{16b})[CH_3O_2]^2 -$

$[HO_2](k_{4.15}[CH_3O_2] + k_{4.23}[NO] + k_{4.24}[O_3]) - 2k_{4.14}[HO_2]^2$ \hfill Eq. A17

Where ρ is the HONO and HNO$_3$ formation efficiency of the OH + NO$_x$ reactions

On rearranging

$\frac{d}{dt}([RO_2^*]) = (2j_{4.1}[O_3]\beta + j_{4.3}[HONO])(1 - \rho) + 2j_{4.8}[HCHO] + 2j_{4.9}[CH_3CHO] + 2(j_{4.10a} + j_{4.10b})[CH_3C(O)CH_3] + 2j_{4.11}[CHOCHO]$

$+ {\color{red}[HO_2](k_{4.23}[NO] + k_{4.24}[O_3])(1 - \rho)} + k_{4.26}\frac{2k_{4.16b}[CH_3O_2]^2 + k_{4.25}[CH_3O_2][NO]}{(k_{4.22}[NO] + k_{4.26}[O_2])}[O_2] - {\color{red}[HO_2](k_{4.23}[NO] + k_{4.24}[O_3])}$

$- {\color{teal}k_{4.15}[HO_2][CH_3O_2]} - {\color{teal}k_{4.15}[HO_2][CH_3O_2]} - {\color{teal}(2k_{16b}[CH_3O_2]^2 + k_{4.25}[CH_3O_2][NO])} - 2k_{16a}[CH_3O_2]^2 - 2k_{4.14}[HO_2]^2$

Combining common terms indicated by the same colours gives

$$\frac{d}{dt}([RO_2^*]) =$$

$$(2j_{4.1}[O_3]\beta + j_{4.3}[HONO])(1-\rho) + 2j_{4.8}[HCHO] + 2j_{4.9}[CH_3CHO] + 2(j_{4.10a} + j_{4.10b})[CH_3C(O)CH_3] + 2j_{4.11}[CHOCHO] - [HO_2](k_{4.23}[NO] + k_{4.24}[O_3])\rho - (2k_{4.16b}[CH_3O_2]^2 + k_{4.25}[CH_3O_2][NO])\left(\frac{k_{4.22}[NO]}{(k_{4.22}[NO] + k_{4.26}[O_2])}\right) - 2k_{4.15}[HO_2][CH_3O_2] - 2k_{16a}[CH_3O_2]^2 - 2k_{4.14}[HO_2]^2$$

Eq. A18

Under steady-state

$$\frac{d}{dt}([RO_2^*]) = 0$$

$$\Rightarrow (2j_{4.1}[O_3]\beta + j_{4.3}[HONO])(1-\rho) + 2j_{4.8}[HCHO] + 2j_{4.9}[CH_3CHO] + 2(j_{4.10a} + j_{4.10b})[CH_3C(O)CH_3] + 2j_{4.11}[CHOCHO] = [HO_2](k_{4.23}[NO] + k_{4.24}[O_3])\rho + (2k_{4.16b}[CH_3O_2]^2 + k_{4.25}[CH_3O_2][NO])\left(\frac{k_{4.22}[NO]}{(k_{4.22}[NO] + k_{4.26}[O_2])}\right) + 2k_{4.15}[HO_2][CH_3O_2] + 2k_{16a}[CH_3O_2]^2 + 2k_{4.14}[HO_2]^2$$

Eq. A19

Now substituting $[HO_2] = \delta[RO_2{}^*]$ and $[CH_3O_2] = (1-\delta)[RO_2{}^*]$ in Eq. A19

$$(2j_{4.1}[O_3]\beta + j_{4.3}[HONO])(1-\rho) + 2j_{4.8}[HCHO] + 2j_{4.9}[CH_3CHO] + 2(j_{4.10a} + j_{4.10b})[CH_3C(O)CH_3] + 2j_{4.11}[CHOCHO] = \delta[RO_2^*](k_{4.23}[NO] + k_{4.24}[O_3])\rho + \left(2k_{4.16b}((1-\delta)[RO_2^*])^2 + k_{4.25}(1-\delta)[RO_2^*][NO]\right)\left(\frac{k_{4.22}[NO]}{(k_{4.22}[NO] + k_{4.26}[O_2])}\right) + 2k_{4.15}\delta(1-\delta)[RO_2^*]^2 + 2k_{16a}((1-\delta)[RO_2^*])^2 + 2k_{4.14}(\delta[RO_2^*])^2$$

Eq. A20

Eq. A20 is a quadratic equation of $[RO_2{}^*]$. The solution is given by

$$[RO_2^*] = \frac{-(-L_{RO_2^*}) - {}^2\sqrt{L_{RO_2^*}^2 - 4(-2k_{RO_2^*})P_{RO_2^*}}}{2(-2k_{RO_2^*})}$$

Eq. A21

Where

$$k_{RO_2^*} = \left(\left(k_{4.16b}\left(\frac{k_{4.22}[NO]}{(k_{4.22}[NO]+k_{4.26}[O_2])}\right) + k_{16a}\right)(1-\delta)^2 + k_{4.15}\delta(1-\delta) + k_{4.14}\delta^2\right)$$

$$L_{RO_2^*} = \left(\delta(k_{4.23}[NO] + k_{4.24}[O_3])\rho + \left(\frac{k_{4.22}[NO]}{(k_{4.22}[NO] + k_{4.26}[O_2])}\right)k_{4.25}(1-\delta)[NO]\right)$$

$$P_{RO_2^*} = (2j_{4.1}[O_3]\beta + j_{4.3}[HONO])(1-\rho) + 2j_{4.8}[HCHO] + 2j_{4.9}[CH_3CHO] + 2(j_{4.10a} + j_{4.10b})[CH_3C(O)CH_3] + 2j_{4.11}[CHOCHO]$$

- Special case I

When $k_{4.19}[NO] + k_{4.20}[NO_2] \ll k_{4.12a}[HCHO] + k_{4.12b}[CH_3CHO] + k_{4.12c}[CH_3C(O)CH_3] + k_{4.12d}[CH_3OH] + k_{4.12e}[CHOCHO]$, i.e., $\rho \approx 0$, Eq. A19 can be simplified as follows:

$$(2j_{4.1}[O_3]\beta + j_{4.3}[HONO]) + 2j_{4.8}[HCHO] + 2j_{4.9}[CH_3CHO] + 2(j_{4.10a} + j_{4.10b})[CH_3C(O)CH_3] + 2j_{4.11}[CHOCHO] = \left(2k_{4.16b}((1-\delta)[RO_2^*])^2 +$$

$$k_{4.25}(1-\delta)[RO_2^*][NO]\right)\left(\frac{k_{4.22}[NO]}{(k_{4.22}[NO]+ k_{4.26}[O_2])}\right) + 2k_{4.15}\delta(1-\delta)[RO_2^*]^2 + 2k_{16a}((1-\delta)[RO_2^*])^2 + 2k_{4.14}(\delta[RO_2^*])^2$$

Eq. A22

$L_{RO_2^*}$ and $P_{RO_2^*}$ becomes

$$L_{RO_2^*} = \left(\frac{k_{4.22}[NO]}{(k_{4.22}[NO] + k_{4.26}[O_2])}\right)k_{4.25}(1-\delta)[NO]$$

$$P_{RO_2^*} = (2j_{4.1}[O_3]\beta + j_{4.3}[HONO]) + 2j_{4.8}[HCHO] + 2j_{4.9}[CH_3CHO] + 2(j_{4.10a} + j_{4.10b})[CH_3C(O)CH_3] + 2j_{4.11}[CHOCHO]$$

- Special case II

If $\rho \approx 0$ and OH and CH$_3$O are converted to RO$_2^*$ without any losses, then Eq. A20 becomes Eq. A6 and the solution is given by Eq. A7.

Table A2: Details of the airborne measurements data set used from the OMO Asia campaign. NA: not available

Trace gas-in situ measurements						
Species/parameters	Instrument	Institution	Technique/Instrument	Version	Date of creation	Database
$RO_2^* = HO_2 + \sum RO_2$	PeRCEAS	University of Bremen	PeRCA + CRDS	01		HALO database
OH, HO_2	Air LIF	FZ Jülich	LIF	NA	2016.09.15	HALO database
$CH_3OH, CH_3C(O)CH_3$	HKMS	KIT Karlsruhe	PTR-MS	01	2016.09.14	HALO database
O_3	FAIRO	KIT Karlsruhe	UV-Photometry/ Chemiluminescence	01	2016.02.09	HALO database
NO, NO_y	AENEAS	DLR-IPA	Chemiluminescence/ Gold converter	NA	2015.10.28	HALO database
CO	TRISTAR	MPIC Mainz	TDLAS	NA	2015.07.16	HALO database
Other parameters						
Spectral actinic flux density (up/down) Photolysis frequencies	HALO-SR	FZ Jülich	CCD spectro- radiometry	01	2016.06.13	HALO database
Basic aircraft data	BAHAMAS	DLR -FX	various	01	2016.02.25	HALO database

All measurement datasets used in this study are available in the HALO database under the OMO Asia directory. The permission to access the directory is limited to the OMO partners. The dataset is available to the open community on demand. The contact person for data access is Dr Hartwig Harder, MPIC Mainz (hartwig.harder@mpic.de).

Table A3: Details of the airborne measurements dataset used from the EMeRGe in Europe campaigns.

Species/parameters	Instrument	Institution	Technique/Instrument	Data Version	Date of creation	Measure flight	Database
$RO_2^* = HO_2 + \sum RO_2$	PeRCEAS	University of Bremen	PeRCA + CRDS	04	2021.06.17	E-EU-03 to E-EU-09	HALO database
HCHO	HKMS	KIT Karlsruhe	PTR-MS	a) 03 b) 06	a) 2020.03.04 b) 2020.12.09	a) E-EU-05 b) E-EU-03,04,06 to 09	HALO database
CH_3CHO	HKMS	KIT Karlsruhe	PTR-MS	a) 03 b) 06	a) 2020.03.04 b) 2020.12.09	a) E-EU-05 b) E-EU-03,04,06 to 09	HALO database
$CH_3C(O)CH_3$	HKMS	KIT Karlsruhe	PTR-MS	a) 03 b) 06	a) 2020.03.04 b) 2020.12.09	a) E-EU-05 b) E-EU-03,04,06 to 09	HALO database
CH_3OH	HKMS	KIT Karlsruhe	PTR-MS	a) 03 b) 06	a) 2020.03.04 b) 2020.12.09	a) E-EU-05 b) E-EU-03,04,06 to 09	HALO database
O_3	FAIRO	KIT Karlsruhe	Chemiluminescence	03	2020.06.29	E-EU-03 to E-EU-09	HALO database
NO	AENEAS	DLR-IPA	Chemiluminescence/ Gold converter	02	2020.03.05	E-EU-03 to E-EU-09	HALO database
NO_y	AENEAS	DLR-IPA	Chemiluminescence/Gold converter	02	2020.03.05	E-EU-03 to E-EU-09	HALO database
CH_4	CATS	DLR-IPA	CRDS	02	2020.03.03	E-EU-03 to E-EU-09	HALO database
CO	AMTEX	DLR-IPA	UV-Photometry/ VUV-Fluorimetry	a) 02 b) 03	2020.03.18	a) E-EU-03, E-EU-05 to 09 b) E-EU-04	HALO database
(*)NO_2	mini-DOAS	University of Heidelberg	DOAS / UV-nIR; 2D optical spectrometer	01	2019.05.03	E-EU-03 to E-EU-07	HALO database
(*)HONO	mini-DOAS	University of Heidelberg	DOAS / UV-nIR; 2D optical spectrometer	a) 03 b) 02	2021.06.10	a) E-EU-03, E-EU-05 to 07 b) E-EU-04	HALO database
(*)CHOCHO	mini-DOAS	University of Heidelberg	DOAS / UV-nIR; 2D optical spectrometer	02	2021.10.30	E-EU-03 to E-EU-07	HALO database
NO_2	HAIDI	University of Heidelberg	DOAS / 3x2D-imaging spectrometers	01	2017.07.28	E-EU-08 and E-EU-09	HALO database

Species/parameters	Instrument	Institution	Technique/Instrument	Data Version	Date of creation	Measure flight	Database
Spectral actinic flux density (up/down) Photolysis frequencies	HALO-SR	FZ Jülich	CCD spectro- radiometry	02	2021.03.22	E-EU-03 to E-EU-09	HALO database
Basic aircraft data	BAHAMAS	DLR -FX	various	01	2017.10.12	E-EU-03 to E-EU-09	HALO database
Total aerosol surface area concentration (ASA)	C-ToF-AMS	MPIC Mainz	OPC	01	NA	E-EU-03 to E-EU-09	On-demand (K.Kaiser@mpic.de)

(*) There were no data available from the miniDOAS instrument for the flights E-EU-08 and E-EU-09 due to instrument malfunction.

All measurement datasets except the total aerosol surface area concentration (ASA) used in this study from EMeRGe in Europe are available in the HALO database under the EMeRGe Europe directory. The permission to access the directory is limited to the EMeRGe partners. At the time of submission of the present work, the dataset is available to the open community on demand. The contact person for data access is Dr M. D. Andrés Hernández, IUP, University of Bremen (lola@iup.physik.uni-bremen.de). The ASA data are calculated by Katharina Kaiser (K.Kaiser@mpic.de) from MPIC Mainz, and the data is available on-demand.

Table A4: Details of the airborne measurements dataset used from the EMeRGe in Asia campaigns.

Species/parameters	Instrument	Institution	Technique/Instrument	Data Version	Date of creation	Measure flight	Database
$RO_2^* = HO_2 + \sum RO_2$	PeRCEAS	University of Bremen	PeRCA + CRDS	a) 03 b) 04	a) 2021.06.17 b) 2022.02.	a) E-AS-03, 06 to 14 b) E-AS-05	HALO database
CH_3CHO	HKMS	KIT Karlsruhe	PTR-MS	05	2020.12.09	E-AS-03 to E-AS-14	HALO database
$CH_3C(O)CH_3$	HKMS	KIT Karlsruhe	PTR-MS	05	2020.12.09	E-AS-03 to E-AS-14	HALO database
CH_3OH	HKMS	KIT Karlsruhe	PTR-MS	05	2020.12.09	E-AS-03 to E-AS-14	HALO database
O_3	FAIRO	KIT Karlsruhe	Chemiluminescence	03	2020.06.23	E-AS-03 to E-AS-14	HALO database
NO	AENEAS	DLR-IPA	Chemiluminescence/ Gold converter	a) 02 b) 03	2020.03.06	a) E-AS-03 b) E-AS-05 to E-AS-14	HALO database
NO_y	AENEAS	DLR-IPA	Chemiluminescence/ Gold converter	a) 02 b) 03	2020.03.06	a) E-AS-03 b) E-AS-05 to E-AS-14	HALO database
CH_4	CATS	DLR-IPA	CRDS	01	2020.03.03	E-AS-04 to E-AS-14	HALO database

Species/parameters	Instrument	Institution	Technique/Instrument	Data Version	Date of creation	Measure flight	Database
CO	AMTEX	DLR-IPA	UV-Photometry/ VUV-Fluorimetry	02	2020.03.18	E-AS-03 to E-AS-14	HALO database
Species/parameters	Instrument	Institution	Technique/Instrument	Data Version	Date of creation	Measure flight	Database
NO$_2$	mini-DOAS	University of Heidelberg	DOAS / UV-nIR; 2D optical spectrometer	02	2019.11.07	E-AS-05, 06, 08, 09, 10, 11, 13	HALO database
HONO	mini-DOAS	University of Heidelberg	DOAS / UV-nIR; 2D optical spectrometer	04	2021.06.10	E-AS-05, 06, 08, 09, 10, 11, 13	HALO database
HCHO	mini-DOAS	University of Heidelberg	DOAS / UV-nIR; 2D optical spectrometer	03	2021.03.23	E-AS-05, 06, 08, 09, 10, 11, 13	
CHOCHO	mini-DOAS	University of Heidelberg	DOAS / UV-nIR; 2D optical spectrometer	03	2021.10.30	E-AS-05, 06, 07, 08	HALO database
Spectral actinic flux density (up/down) Photolysis frequencies	HALO-SR	FZ Jülich	CCD spectro- radiometry	02	2021.03.22	E-AS-03 to E-AS-14	HALO database
Basic aircraft data	BAHAMAS	DLR -FX	various	01	2018.06.18	E-AS-03 to E-AS-14	HALO database
Total aerosol surface area concentration (ASA)	C-ToF-AMS	MPIC Mainz	OPC	01	NA	E-AS-01, E-AS-03 to E-EU-14 and E-AS-16	On-demand (K.Kaiser@mpic.de)

All measurement datasets except the total aerosol surface area concentration (ASA) used in this study from EMeRGe in Asia are available in the HALO database under the EMeRGe Asia directory. The permission to access the directory is limited to the EMeRGe partners. At the time of submission of the present work, the dataset is available to the open community on demand. The contact person for data access is Dr M. D. Andrés Hernández, IUP, University of Bremen (lola@iup.physik.uni-bremen.de). The ASA data are calculated by Katharina Kaiser (K.Kaiser@mpic.de) from MPIC Mainz, and the data is available on-demand.

Appendix A-IV

Model description

I. FLEXPART back trajectories for OMO Asia

The origin of the air masses during the OMO Asia campaign was derived using the Lagrangian particle dispersion model FLEXPART version 9.2 beta (Stohl et al., 1998) by Laura Tomsche from the Department of Atmospheric Chemistry, Max Planck Institute for Chemistry, Mainz, Germany. The details of the model setup have been described in Tomsche et al., 2019. Briefly, the model is driven by **E**uropean **C**entre for **M**edium-Range **W**eather **F**orecasts (ECMWF) operational data with a horizontal resolution of $1° × 1°$ and a vertical resolution of 137 levels between 1013.25 and 0.01 hPa. The temporal resolution is 3 h, with analyses at 00:00, 06:00, 12:00, and 18:00 UTC and forecasts for 03:00, 09:00, 15:00, and 21:00 UTC. FLEXPART accounts for turbulence using the mean wind plus turbulent fluctuations and the mesoscale wind fluctuations (Stohl et al., 2010). The planetary boundary layer (PBL) height is parameterised following the concept of Vogelezang and Holtslag (1996) using the critical Richardson number (Stohl et al., 2010). Vertical transport is calculated using the Langevin equation (Thomson, 1987), which considers the turbulent vertical wind and its standard deviation. It also includes a decrease in the air density with height. Additional moist convection is parameterised according to Emanuel and Zivkovic-Rothman (1999). Their parameterisation builds on temperature and humidity fields to provide mass flux information (Stohl et al., 2005). Trajectories are started every 10 min along the flight tracks for air parcels, neglecting loss processes due to deposition or chemical reactions. The trajectories are calculated 10 days back in time for 10000 parcels that are initialised per release point (size: $1° × 1° × 500$ m and 1 h).

The model results are available on-demand from the OMO Asia coordination team in Max Planck Institute for Chemistry, Mainz, Germany. Contact person: Dr Hartwig Harder (hartwig.harder@mpic.de).

II. EMAC model for OMO Asia

The trace gas/aerosol concentrations and meteorological parameters during the OMO Asia campaign were modelled using the **ECHAM**/**M**ESSy **A**tmospheric **C**hemistry (EMAC) model by Andrea Pozzer and Patrick Joeckel from the Department of Atmospheric Chemistry, Max Planck Institute for Chemistry, Mainz, Germany. A detailed description of the model setup is given in Lelieveld et al., 2018; Tomsche et al., 2019. Briefly, the EMAC model consists of the general circulation model ECHAM5 (fifth generation of the **E**uropean **C**enter **HAM**burg model, Roeckner et al., 2006) and the **M**odular **E**arth **S**ubmodel **S**ystem (MESSy, Jöckel et al., 2005, 2010), which

extends the model to a fully coupled chemistry-climate model. The horizontal resolution applied is $2.8° \times 2.8°$, and the vertical resolution is determined by 90 layers on a hybrid pressure grid between 1015.25 and 0.01 hPa. The EMAC model is a hydrostatic model and the convective transport is parameterised (Tost et al., 2006; Ouwersloot et al., 2015). Indication of the vertical transport time in EMAC can be found in Krol et al. (2018), where a comparison with a model of similar complexity is also shown. The emissions are based on the Representative Concentration Pathways (RCP) 8.5 for anthropogenic activity (Van Vuuren et al., 2011) and the Global Fire Emissions Database (GFED) v3.1 for biomass burning emissions of 2015 (van der Werf et al., 2010). For methane, additional sources of wetlands in the Amazon and North American shale gas drilling were added to simulate the methane trend since 2007 (Zimmermann et al., 2018).

The EMAC model was not run in an offline chemistry-transport mode, as the radiation calculations were based on simulated greenhouse gas concentrations. The model was weakly nudged towards ECMWF ERA-Interim data (Jeuken et al., 1996) and therefore reproduced very similar dynamics to the ECMWF model (although not binary identical). The simulation is an extension of simulation RC1SD-base-10 (Jöckel et al., 2016) to cover the full OMO Asia campaign. Few changes to the original simulation have been applied (i.e. increased South Asia SO_2 emissions and reduced lightning NO_x), as described in Lelieveld et al. (2018). Although the simulation is a continuation of a well-evaluated experiment, the simulation was run from 1 March 2015 to give the SO_2 and NO_x time to balance the new emissions (i.e. 4-month spin-up time). Only the data from July/August 2015, which cover the field campaign, are used. The model results are available in the HALO database in NASA ames 1001 formate for the campaign partners. Contact person: Dr Andrea Pozzer (andrea.pozzer@mpic.de).

III.   FLEXTRA back trajectories for EMeRGe campaigns

Air mass back trajectories for the EMeRGe flights are calculated with the FLEXTRA 5.0 trajectory model developed by Stohl et al. (1999), which uses the ECMWF operational data set ERA5 meteorological data at 0.25° horizontal resolution. The model simulations were performed by the **L**aboratory for **M**odeling and **O**bservation of the **E**arth **S**ystem (LAMOS) group at IUP, University of Bremen. Trajectories are started every 10 minutes of flight time and reach back 10 days. The general content of the model output has been enhanced by adding manually other parameters after the simulations (troph, tropp, blh, sp, surf, cwc), which provide additional information over the BL conditions along the trajectory.

There are two sets of data:

1. Original trajectories of the FLEXTRA run at the ~10 min temporal resolution along the flight tracks.

2. Interpolated trajectories at a strict 5 min temporal resolution, linearly interpolated from the original trajectories. In the interpolated trajectories, the timestamps are the same for all releases/trajectories, and the temporal resolution is higher than the original trajectories.

The model results are available in the Seafile directory for the EMeRGe mission in the IUP Bremen server. The results are accessible to the EMeRGe community. Others can obtain the data on demand from the server. Contact person: Dr. M. D. Andrés Hernández (lola@iup.physik.uni-bremen.de).

IV.   HYSPLIT model for EMeRGe campaigns

The Lagrangian Particle Dispersion Model HYSPLIT (https://www.arl.noaa.gov/hysplit/hysplit/) was utilised to calculate the transport and dispersion of regional CO emissions accumulated over 6 days during EMeRGe IOPs. These values do not include accumulated background concentrations due to the much longer lifetime of CO and are thus not to be compared with absolute concentrations but rather with enhancements inside of local plumes. The model simulations were performed by Dr Robert Baumann, Institute of Atmospheric Physics, DLR, Oberpfaffenhofen, Munich, Germany (robert.baumann@dlr.de).

HYSPLIT was driven by meteorology data from the operational ECMWF forecast. For this, the initial state and first 11 hours of the forecast of successive forecast datasets (00 UTC and 12 UTC daily) were concatenated. The meteorological data has a time step of 1 hour, 137 vertical model levels, and is horizontally interpolated onto a 0.1° latitude-longitude grid for use with the HYSPLIT model.

CO emission rates were taken from EDGAR HTAP V2 emission inventory (monthly means of 2010, 0.1° resolution, http://edgar.jrc.ec.europa.eu/htap_v2/). The model provides the CO volume mixing ratio (VMR), in nmole mone^{-1}, of the whole 6-days accumulation period as well as the partial VMR in eight different age classes: 0-3h, 3-6h, 6-12h, 12-24h, 1-2d, 2-3d, 3-4d, 4-6d. The arithmetic mean age of all contributions provided is also provided. Data files for source regions that did not significantly contribute CO (i.e. VMR < 0.1 nmole mole^{-1}) along a specific flight track were removed from the data collection; hence some combinations of date and region are omitted intentionally.

The model results are available in the Seafile directory for the EMeRGe mission in the IUP Bremen server. The results are accessible to the EMeRGe community. Others can obtain the data on demand from the server. Contact person: Dr. M. D. Andrés Hernández (lola@iup.physik.uni-bremen.de).

V.   CMAQ model for EMeRGe in Asia campaign

The **W**eather **R**esearch and **F**orecasting (WRF) coupled with the **C**ommunity **M**ultiscale **A**ir **Q**uality (CMAQ) model was used to model the gas/aerosol concentrations and meteorological parameters during EMeRGe in Asia campaign. This WRF/CMAQ model included the effects of stagnation, dilution, and dispersion in both the horizontal and vertical directions. The details of the

model setup have been described in Chatani et al. (2018). The model simulations were performed by Dr Yugo Kanaya, JAMSTEC, Kanagawa, JAPAN (yugo@jamstec.go.jp).

Briefly, the WRF model version 3.7.1 (Skamarock et al., 2008), based on the National Centers for Environmental Prediction (NCEP) Final (FNL) Operational Global Analysis data (ds083.2) originating from GDAS, was coupled to the CMAQ version 5.0.2 (Byun and Schere, 2006) to simulate regional-scale air pollution with 27 vertical layers between surface and 50 hPa. Two model runs were performed with 220×170 grids/45km (East Asia) and 154×160 grids/15km (Japan) horizontal domains (Figure A1). The results from the model run for the East Asian domain were used during this study.

The sixth-generation CMAQ aerosol module (AER06) was used for the aerosol simulation, while the Statewide Air Pollution Research Center version 07 (SAPRC-07) was used for air chemistry. The wet deposition was represented with the cloud_acm_ae5 module. The boundary concentrations were derived from the climatological means of the global chemical transport CHemical Atmospheric general circulation model for the Study of atmospheric Environment and Radiative forcing (CHASER) described in Sudo et al., 2002. The fixed anthropogenic emissions were taken from the monthly data of Hemispheric Transport of Air Pollution (HTAP) version 2.2 with a $0.25° \times 0.25°$ resolution (Janssens-Maenhout et al., 2015) for 2010. The Global Fire Emissions Database (GFED) version 4.1 was used for the monthly emissions from biomass burning. The Model of Emissions of Gases and Aerosols from Nature (MEGAN) v2.1 was used for biogenic emissions, and the AeroCom database was used to account for the aerosol emission.
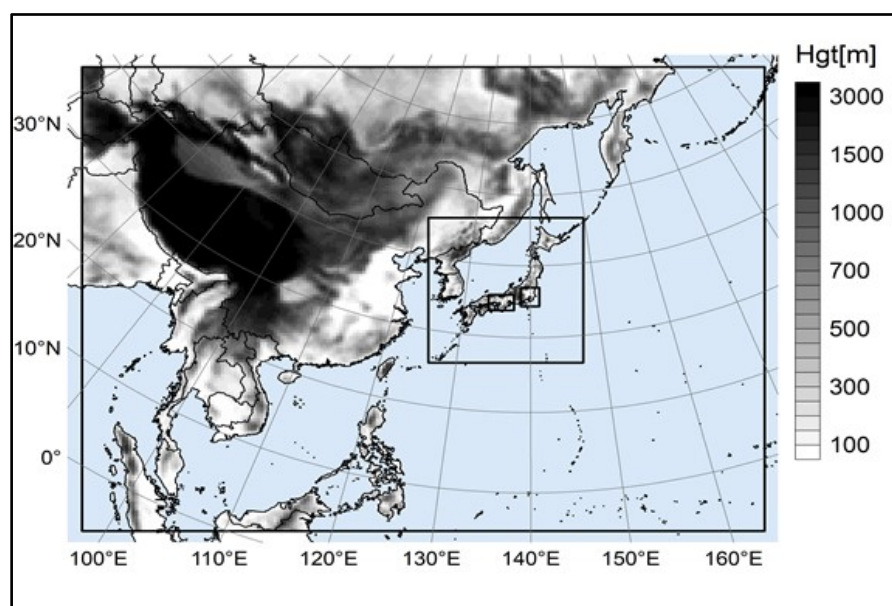

Figure A1: The domain of the different CMAQ model simulations. The results from the simulation with the largest domain covering entire East Asia were used in this study.

Table A.5: State of the art instruments for the airborne measurement of peroxy radicals. Ground-based instruments are also included for comparison.

Author	Year	Technique	eCL	LOD_{NO_2} (pmole mole^{-1})	$LOD_{RO_2^*}$ (pmole mole^{-1})	Averaging time (s)	Pressure (mbar)
Airborne instruments							
Green et al.	2002	PeRCA + Luminol	277 - 322 (3 µmole mole^{-1} NO + 7 % CO)	180	1	20	not controlled (from ground level to 7 km)
Kartal et al.	2010	PeRCA + Luminol	45 ± 7 (3 µmole mole^{-1} NO + 7.4 % CO)	130 ± 5	3 ± 2	60	200
Horstjan et al.	2014	PeRCA + OF-CEAS	110 ± 21 (6 µmole mole^{-1} NO + 9 % CO)	300	3 - 5	120	300
			55 ± 10 (6 µmole mole^{-1} NO + 9 % CO)	300	6	120	200
Hornbrook et al.	2011	PeRCIMS			2		200
Ren at al.	2012	LIF			0.1 (2σ)	60	up to 300
		PerCIMS			1 (2σ)	15	up to 300
This work		PeRCA + CRDS	100 ± 15 (10 µmole mole^{-1} NO 9 % CO) 62 ± 9 (30 µmole mole^{-1} NO 9 % CO) 38 ± 4 (45 µmole mole^{-1} NO 9 % CO)	60	< 2	60	200 to 350
Ground-based instruments							
Cantrell et al.	1984	PeRCA + Luminol	1010 (3 µmole mole^{-1} NO + 10 % CO)		0.6	300	1000
Hastie et al.	1991	PeRCA + Luminol	120 (2 µmole mole^{-1} NO + 4 % CO)	50	2	10	1000
Cantrell et al.	1993	PeRCA + Luminol	300 (3 µmole mole^{-1} NO +		< 2	60	1000

			10 % CO)				
Reiner et.al.	1997	PeRCA + IMR-MS	100		10^6 molecules cm^{-3}		1000
Burkert et al.	2001a	PeRCA + Luminol	154 ± 15 and 195 ± 10 (3 μmole mole^{-1} NO + 9% CO)	150	3 to 5 (60 to 80 % RH)	60	1000
Sadanaga et al.	2004	PeRCA + LIF	190 (3 μmole mole^{-1} NO + 10 % CO)	61	2.7 (50 % RH) 3.6 (80 % RH)	60	1000
Liu et al.	2009	PERCA + CRDS	150 ± 50 (2σ)	150 (3σ 10s)	10 (3σ)	60	1000
Wood et al.	2014	PeRCA + CAPS	168 ± 20 (3.75 μmole mole^{-1} NO 9.8 % CO)	12 (1σ 30s)	0.6 (40 % RH)	60	1000
Liu et al.	2014	PeRCA + CRDS	190		4	10	1000
Chen et al.	2016	PeRCA + IBBCEAS	91 ± 11 (7.7 μmole mole^{-1} NO 8.5 % CO)	49 and 62 for different channels	0.9 (10 % RH)	60	1000
Wood et al.	2017	ECHAMP + CAPS	25 (dry) and 17(50 % RH) (1 μmole mole^{-1} NO 2.3 % C$_2$H$_6$)	10 (1σ 45s)	1.6 (50 % RH)	90	1000
Anderson et al.	2019	ECHAMP + CAPS	23 (dry) and 12(58 % RH) (0.9 μmole mole^{-1} NO 1.3 % C$_2$H$_6$)	10 (1σ 45s)	1.6 (50 % RH)	120	1000
Edwards et al.	2003	PeRCIMS			0.4	15	200
Fush et al.	2008	LIF			0.1	60	1000
Mihelcic et al.	2003	MIESR			2	1800	1000

References

Albrecht, S. R., Novelli, A., Hofzumahaus, A., Kang, S., Baker, Y., Mentel, T., Wahner, A., and Fuchs, H.: Measurements of hydroperoxy radicals (HO2) at atmospheric concentrations using bromide chemical ionisation mass spectrometry, Atmos. Meas. Tech., 12, 891–902, https://doi.org/10.5194/amt-12-891-2019, 2019.

Allan, D. W.: Statistics of atomic frequency standards, Pr. Inst. Electr. Elect., 54, 221–230, https://doi.org/10.1109/PROC.1966.4634, 1966.

Andreae, M. O. , Afchine, A. Albrecht, R., Holanda, B. A., Artaxo, P., Barbosa, H. M. J., Borrmann, S., Cecchini, M. A., Costa, A., Dollner, M., Fütterer, D., Järvinen, E., Jurkat, T., Klimach, T., Konemann, T., Knote, C., Krämer, M., Krisna, T., Machado, L. A. T., Mertes, S.; Minikin, A. , Pöhlker, C., Pöhlker, M. L., Pöschl, U. Rosenfeld, D., Sauer, D., Schlager, H., Schnaiter, M., Schneider, J., Schulz, C., Spanu, A., Sperling, V. B., Voigt, C., Walser, A., Wang, J., Weinzierl, B., Wendisch, M. , Ziereis, H.: Aerosol characteristics and particle production in the upper troposphere over the Amazon Basin. Atmos. Chem. Phys., 18, 921–961, https://doi.org/10.5194/acp-18-921-2018, 2018.

Andersson, B. Y., Cox, R. A., Jenkin, M. E.: The effect of methanol on the self-reaction of HO_2 radicals. Int. J. Chem. Kinet., 20, 283-295, https://doi.org/10.1002/kin.550200403, 1988.

Anderson, D. C., Pavelec, J., Daube, C., Herndon, S. C., Knighton, W. B., Lerner, B. M., Roscioli, J. R., Yacovitch, T. I., and Wood, E. C.: Characterization of ozone production in San Antonio, Texas, using measurements of total peroxy radicals, Atmos. Chem. Phys., 19, 2845–2860, https://doi.org/10.5194/acp-19-2845-2019, 2019.

Andrés Hernández, M.D., Burkert, J., Reichert, L., Stöbener, D., Meyer- Arnek J., and Burrows, J.P., Dickerson, R.R., and Doddridge, B.: Marine boundary layer peroxy radical chemistry during the AEROSOLS99 campaign: measurements and analysis. Journal of Geophys. Res, 106, D18, 20,833-20,846, https://doi.org/10.1029/2001JD900113, 2001.

Andrés-Hernández, M. D., Kartal, D., Reichert, L., Burrows, J. P., Meyer Arnek, J., Lichtenstern, M., Stock, P., and Schlager, H.: Peroxy radical observations over West Africa during AMMA 2006: photochemical activity in the outflow of convective systems, Atmos. Chem. Phys., 9, 3681–3695, https://doi.org/10.5194/acp-9-3681-2009, 2009.

Andrés-Hernández, M. D., Stone, D., Brookes, D. M., Commane, R., Reeves, C. E., Huntrieser, H., Heard, D. E., Monks, P. S., Burrows, J. P., Schlager, H., Kartal, D., Evans, M. J., Floquet, C. F. A., Ingham, T., Methven, J., and Parker, A. E.: Peroxy radical partitioning during the AMMA radical

intercomparison exercise, Atmos. Chem. Phys., 10, 10621–10638, https://doi.org/10.5194/acp-10-10621-2010, 2010.

Andrés Hernández, M. D., Hilboll, A., Ziereis, H., Förster, E., Krüger, O. O., Kaiser, K., Schneider, J., Barnaba, F., Vrekoussis, M., Schmidt, J., Huntrieser, H., Blechschmidt, A.-M., George, M., Nenakhov, V., Klausner, T., Holanda, B. A., Wolf, J., Eirenschmalz, L., Krebsbach, M., Pöhlker, M. L., Hedegaard, A. B., Mei, L., Pfeilsticker, K., Liu, Y., Koppmann, R., Schlager, H., Bohn, B., Schumann, U., Richter, A., Schreiner, B., Sauer, D., Baumann, R., Mertens, M., Jöckel, P., Kilian, M., Stratmann, G., Pöhlker, C., Campanelli, M., Pandolfi, M., Sicard, M., Gomez-Amo, J. L., Pujadas, M., Bigge, K., Kluge, F., Schwarz, A., Daskalakis, N., Walter, D., Zahn, A., Pöschl, U., Bönisch, H., Borrmann, S., Platt, U., and Burrows, J. P.: Overview: On the transport and transformation of pollutants in the outflow of major population centres – observational data from the EMeRGe European intensive operational period in summer 2017, Atmos. Chem. Phys. Discuss. [preprint], https://doi.org/10.5194/acp-2021-500, Accepted manuscript, 2022.

AP ENVIRONMENTAL: https://mhsapes.weebly.com/44-45-reading.html, last access: 7 April 2021.

Ashbourn, S.F.M., Jenkin, M.E. & Clemitshaw, K.C. Laboratory Studies of the Response of a Peroxy Radical Chemical Amplifier to HO2 and a Series of Organic Peroxy Radicals. Journal of Atmospheric Chemistry 29, 233–266. https://doi.org/10.1023/A:1005992316512, 1998.

Atkinson, R. and S. Aschmann, OH radical production from the gas-phase reactions of 0 3 with a series of alkenes under atmospheric conditions, Environ. Sci. Tech. 27, 1357-63, https://doi.org/10.1021/es00044a010, 1993.

Atkinson, D. B.: Solving chemical problems of environmental importance using cavity ring-down spectroscopy, Analyst, 128, 117–125, https://doi.org/10.1039/B206699H, 2003.

Bedjanian, Y., Lelievere, S., and Le Bras, G.: Experimental Study of the Interaction of HO_2 Radicals with Soot Surface, Phys. Chem. Chem. Phys., 7, 334–341, 2005.

Berden, G. and Engeln, R.: Cavity Ring-Down Spectroscopy: Techniques and Applications, John Wiley & Sons Ltd, The Atrium, Southern Gate, Chichester, West Sussex, UK, https://doi.org/10.1002/9781444308259.fmatter, 2010.

Berndt, T., Richters, S., Jokinen, T., Hyttinen, N., Kurtén, T., Otkjær, R. V., Kjaergaard, H. G., Stratmann, F., Herrmann, H., Sipilä, M., Kulmala, M., and Ehn, M.: Hydroxyl radical-induced formation of highly oxidized organic compounds. Nat Commun 7, 13677, https://doi.org/10.1038/ncomms13677, 2016.

Boeker, E. and Van Grondelle, R.: Environmental Physics, John W. & Sons, 1994.

Bohn, B., and Lohse, I.: Calibration and evaluation of CCD spectroradiometers for ground-based and airborne measurements of actinic flux densities, Atmos. Meas. Tech., 10, 3151-3174, https://doi.org/10.5194/amt-10-3151-2017, 2017.

Brown, S.: Absorption Spectroscopy in High-Finesse Cavities for Atmospheric Studies, Chem. Rev., 103, 5219–5238, https://doi.org/10.1021/cr020645c, 2003.

Brito, J., and Zahn, A.: An unheated permeation device for calibrating atmospheric VOC measurements, Atmos. Meas. Tech., 4(10), 2143–2152, https://doi.org/10.5194/amt-4-2143-2011, 2011.

Brune, W. H., Baier, B. C., Thomas, J., Ren, X., Cohen, R. C., Pusede, S. E., Browne, E. C., Goldstein, A. H., Gentner, D. R., Keutsch, F. N., Thornton, J. A., Harrold, S., Lopez-Hilfiker, F. D., and Wennberg, P. O.: Ozone production chemistry in the presence of urban plumes, Faraday Discuss., 189, 169–189, https://doi.org/10.1039/c5fd00204d, 2016.

Burkert, J., Behmann, T., Andrés Hernández, M. D., Weissenmayer, M., Perner, D., and Burrows, J. P.: Measurements of peroxy radicals in a forested area in Portugal, Chemosphere, 3, 3327–3338, https://doi.org/10.1016/S1465-9972(01)00014-9, 2001a.

Burkert, J., Andrés Hernández, M. D., Stöbener, D., Burrows, J. P., Weissenmayer, M., and Kraus, A.: Peroxy radical and related trace gas measurement in the marine boundary layer above the Atlantic Ocean, J. Geophys. Res., 106, 5457–5477, https://doi.org/10.1029/2000JD900613, 2001b.

Burkert, J. Andrés Hernández, M. D., L. Reichert, D. Stöbener, J. Meyer- Arnek and J.P. Burrows, J.Mühle, A.Zahn, T.Carsey, RR. Dickerson and B. Doddridge, Trace gas and radical behaviour in the marine boundary layer during INDOEX 1999 J. Geophys. Res., 108, 8000, https://doi.org/10.1029/2002JD002790, 2003.

Burkholder, J. B., Sander, S. P., Abbatt, J., Barker, J. R., Huie, R. E., Kolb, C. E., Kurylo, M. J., Orkin, V. L. Wilmouth, D. M., and Wine P. H.: Chemical Kinetics and Photochemical Data for Use in Atmospheric Studies, Evaluation No. 18, JPL Publication 15-10, Jet Propulsion Laboratory, Pasadena, http://jpldataeval.jpl.nasa.gov (last access: 7 April 2020), 2015.

Burkholder, J. B., Sander, S. P., Abbatt, J., Barker, J. R., Cappa, C., Crounse, J. D., Dibble, T. S., Huie, R. E., Kolb, C. E., Kurylo, M. J., Orkin, V. L. Wilmouth, D. M., and Wine P. H.: Chemical Kinetics and Photochemical Data for Use in Atmospheric Studies, Evaluation No. 19, JPL Publication 19-5, Jet Propulsion Laboratory, Pasadena, http://jpldataeval.jpl.nasa.gov, 2019.

Byun, D. and Schere, K. L.: Review of the governing equations, computational algorithms, and other components of the Model-3 Community Multiscale Air Quality (CMAQ) modeling system, Appl. Mech. Rev., 59, 51–77, https://doi.org/10.1115/1.2128636, 2006.

Cantrell, C. A. and Stedman, D. H.: A possible technique for the measurement of atmospheric peroxy radicals, Geophys. Res. Lett., 9, 846–849, https://doi.org/10.1029/GL009i008p00846, 1982.

Cantrell, C. A., Stedman, D. H., and Wendel, G. J.: Measurement of atmospheric peroxy radicals by chemical amplification, Anal. Chem., 56, 1496–1502, https://doi.org/10.1021/ac00272a065, 1984.

Cantrell, C. A., Shetter, R. E., Lind, A. J., McDaniel, A. H., and Calvert, J. G.: An improved chemical amplifier technique for peroxy radical measurements, J. Geophys. Res, 98, 2897–2909, https://doi.org/10.1029/92JD02842, 1993.

Cantrell, C. A., Shetter, R. E., and Calvert, J. G.: Dual-inlet chemical amplifier for atmospheric peroxy radical measurements, Anal. Chem., 68, 4194–4199, https://doi.org/10.1021/ac960639e, 1996.

Cantrell, C. A., Zimmer, A., and Tyndall, G. S.: Absorption cross sections for water vapour from 183 to 193 nm, Geophys. Res. Lett., 24, 2195–2198, https://doi.org/10.1029/97GL02100, 1997a.

Cantrell, C. A., Zimmer, A., and Tyndall, G. S.: Correction to Absorption cross sections for water vapor from 183 to 193 nm, Geophys. Res. Lett., 24, 2687-2687, https://doi.org/10.1029/97GL02803, 1997b.

Cantrell, C. A., Edwards, G. D., Stephens, S., Mauldin, L., Kosciuch, E., Zondlo, M., and Eisele, F.: Peroxy radical observations using chemical ionization mass spectrometry during TOPSE, J. Geophys. Res., 108, 8371, https://doi.org/10.1029/2002JD002715, 2003a.

Cantrell, C. A., Edwards, G. D., Stephens, S., Mauldin, R.L., Zondlo. M.A., Kosciuch, E., Eisele, F. L., Shetter, R. E., Lefer, B. L., Hall, S., Flocke, F., Weinheimer, A., Fried, A., Apel, E., Kondo, Y., Blake, D. R., Blake, N. J., Simpson, I. J., Bandy, A. R., Thornton, D. C., Heikes, B. G., Singh, H. B., Brune, W. H., Harder, H., Martinez, M., Jacob, D. J., Avery, M. A., Barrick, J. D., Sachse, G. W., Olson, J. R., Crawford, J. H., and Clarke, A. D.: Peroxy radical behaviour during the Transport and Chemical Evolution over the Pacific (TRACE-P) campaign as measured aboard the NASA-3B aircraft, J. Geophys. Res., 108(D20), 8797, https://doi.org/10.1029/2003JD003674, 2003b.

Carslaw, N., Carpenter, L. J., Plane, J. M. C., Allan, B. J., Burgess, R. A., Clemitshaw, K. C., Coe, H., and Penkett, S. A.: Simultaneous observations of nitrate and peroxy radicals in the marine boundary layer, J. Geophys. Res., 102(D15), 18917– 18933, https://doi.org/10.1029/97JD00399, 1997.

Carslaw, N., Creasey, D. J., Heard, D. E., Jacobs, P. J., Lee, J. D., Lewis, A. C., Bauguitte, S., Penkett, S. A., Monks, P. S., and Salisbury, G.: Eastern Atlantic spring experiment 1997 (EASE97) 2. Comparisons of model concentrations of OH, HO2, and RO2 with measurements, J. Geophys. Res., 107, 4190, https://doi.org/10.1029/2001JD001568, 2002.

Chen H., Winderlich, J., Gerbig, C., Hoefer, A., Rella, C. W., Crosson, E. R., Van Pelt, A. D., Steinbach, J., Kolle, O., Beck, V., Daube, B. C., Gottlieb, E. W., Chow, V. Y., Santoni, G. W., and S. C. Wofsy, High-accuracy continuous airborne measurements of greenhouse gases (CO_2 and CH_4) using the cavity ring-down spectroscopy (CRDS) technique, Atmos. Mes. Tech., 3, 375-386, https://doi.org/10.5194/amt-3-375-2010, 2010.

Chen, Y., Chengqian, Y., Zhao, W., Fang, B., Xuezhe, X., Gai, Y., Lin, X., Chend, W., and Zhang, W.: Ultra-sensitive measurement of peroxy radicals by chemical amplification broadband cavity-enhanced spectroscopy, Analyst, 141, 5870, https://doi.org/10.1039/c6an01038e, 2016.

Chrobry, A.: Development and laboratory characterization of a sampling system for airborne measurements of peroxy radicals using chemical amplification, PhD thesis, Fachbereich für Physik und Elektrotechnik, University of Bremen, Germany, 2013.

Clemitshaw, K. C., Carpenter, L. J., Penkett, S. A., and Jenkin M. E.: A calibrated peroxy radical chemical amplifier for ground-based tropospheric measurements, J. Geophys. Res., 102, 25405–25416, https://doi.org/10.1029/97JD01902, 1997.

Clemitshaw, K. C.: A review of instrumentation and measurement techniques for ground-based and airborne field studies of gas-phase tropospheric chemistry, Crit. Rev. Env. Sci. Tec., 34, 1–108, https://doi.org/10.1080/10643380490265117, 2004.

Commane, R., Floquet, C. F. A., Ingham, T., Stone, D., Evans, M. J., and Heard, D. E.: Observations of OH and HO_2 radicals over West Africa, Atmos. Chem. Phys., 10, 8783–8801, https://doi.org/10.5194/acp-10-8783-2010, 2010.

Cox, R. A., Burrows, J. P.: Kinetics and mechanism of the disproportionation of HO_2 in the gas phase. J. Phys. Chem., 83, 2560-2568, https://doi.org/10.1021/j100483a002, 1979.

Crawford, J., Davis, D., Olson, J., Chen, G., Liu, S., Gregory, G., Barrick, J., Sachse, G., Sandholm, S., Heikes, B., Singh, H., and Blake, D.: Assessment of upper tropospheric HO_x sources over the tropical Pacific based on NASA GTE/PEM data: Net effect on HO_x and other photochemical parameters, J. Geophys. Res., 104, 16255–16273, https://doi.org/10.1029/1999JD900106, 1999.

Creasey, D., Heard, D. E., and Lee, J. D.: Absorption cross-section measurements of water vapour and oxygen at 185 nm. Implications for the calibration of field instruments to measure OH, HO_2 and RO_2 radicals, Geophys. Res. Lett., 27, 1651–1654, https://doi.org/10.1029/1999GL011014, 2000.

DeMore, W. B.: Reaction of HO_2 with O_3 and the effect of water vapor on HO_2 kinetics. J. Phys. Chem., 83, 1113-1118, https://doi.org/10.1021/j100472a001, 1979.

Edwards, G. D, Cantrell, C. A., Stephens, S., Hill, B., Goyea, O., Shetter, R. E., Mauldin, R. L., Kosciuch, E., Tanner, D. J., and Eisele, F. L.: Chemical Ionization Mass Spectrometer Instrument for the Measurement of Tropospheric HO_2 and RO_2, Anal. Chem. 2003, 75, 20, 5317–5327, https://doi.org/10.1021/ac034402b, 2003.

EMeRGe: http://www.iup.uni-bremen.de/emerge/home/home.html, last access: 7 April 2021.

Emmerson, K. M., Carslaw, N., Carslaw, D. C., Lee, J. D., McFiggans, G., Bloss, W. J., Gravestock, T., Heard, D. E., Hopkins, J., Ingham, T., Pilling, M. J., Smith, S. C., Jacob, M., and Monks, P. S.: Free radical modelling studies during the UK TORCH Campaign in Summer 2003, Atmos. Chem. Phys., 7, 167–181, https://doi.org/10.5194/acp-7-167-2007, 2007.

Engeln, R., Helden, G. von., Berden, G., Meijer, G.: Phase shift cavity ring-down absorption spectroscopy, Chemical Physics Letters, 262 (1–2), 105-109, https://doi.org/10.1016/0009-2614(96)01048-2, 1996.

English, A. M., Hansen, J. C., Szente, J. J., Maricq, M. M.: The effects of water vapor on the CH_3O_2 self-reaction and reaction with HO_2. J. Phys. Chem. A, 112, 9220-9228, https://doi.org/10.1021/jp800727a, 2008.

FAAM: www.faam.ac.uk, last access: 20 April 2021.

Faloona, I., Tan, D., Brun, W. H., Jaeg1é, L., Jacob D. J., Kondo, Y., Koike, M., Chatfield, R., Puesche, R., Ferry, G., Sachs, G., Vay, S., Anderso, B., Hannon, J., and Fuelber, H.: Observations of HO_x and its relationship with NO_x in the upper troposphere during SONEX, J. Geophys. Res., 105, 3771–3783, 2000.

Fiedler, S. E., Hese, A., and Ruth, A. A.: Incoherent broad-band cavity-enhanced absorption spectroscopy, Chemical Physics Letters, 371 (3–4), 284-294, https://doi.org/10.1016/S0009-2614(03)00263-X, 2003.

Fisher, R., Lowry, D., Wilkin, O., Sriskantharajah, S., and Nisbet, E. G.: High-precision, automated stable isotope analysis of atmospheric methane and carbon dioxide using continuous-flow isotope-ratio mass spectrometry, Rapid communications in mass spectrometry: RCM 2006, 20 (2), 200–208. https://doi.org/10.1002/rcm.2300, 2006.

Fleming, Z. L., Monks, P. S., Rickard, A. R., Bandy, B. J., Brough, N., Green, T. J., Reeves, C. E., and Penkett, S. A.: Seasonal dependence of peroxy radical concentrations at a Northern hemisphere marine boundary layer site during summer and winter: evidence for radical activity in winter, Atmos. Chem. Phys., 6, 5415–5433, https://doi.org/10.5194/acp-6-5415-2006, 2006a.

Fleming, Z. L., Monks, P. S., Rickard, A. R., Heard, D. E., Bloss, W. J., Seakins, P. W., Still, T. J., Sommariva, R., Pilling, M. J., Morgan, R., Green, T. J., Brough, N., Mills, G. P., Penkett, S. A., Lewis, A. C., Lee, J. D., Saiz-Lopez, A., and Plane, J. M. C.: Peroxy radical chemistry and the control of ozone photochemistry at Mace Head, Ireland during the summer of 2002, Atmos. Chem. Phys., 6, 2193–2214, https://doi.org/10.5194/acp-6-2193-2006, 2006b.

Fuchs, H., Hofzumahaus, A., and Holland, F.: Measurement of tropospheric RO2 and HO2 radicals by a laser-induced fluorescence instrument, Review of Scientific Instruments, 79, 084104, https://doi.org/10.1063/1.2968712, 2008.

Fuchs, H., Bohn, B., Hofzumahaus, A., Holland, F., Lu, K. D., Nehr, S., Rohrer, F., and Wahner, A.: Detection of HO2 by laser-induced fluorescence: calibration and interferences from RO2 radicals, Atmos. Meas. Tech., 4, 1209–1225, https://doi.org/10.5194/amt-4-1209-2011, 2011.

General Circulation of the Atmosphere: http://cimss.ssec.wisc.edu/wxwise/class/gencirc.html, last access: 7 April 2020.

General, S., Pöhler, D., Sihler, H., Bobrowski, N., Frieß, U., Zielcke, J., Horbanski, M., Shepson, P. B., Stirm, B. H., Simpson, W. R., Weber, K., Fischer, C., and Platt, U.: The Heidelberg Airborne Imaging DOAS Instrument (HAIDI) – a novel Imaging DOAS device for 2-D and 3-D imaging of trace gases and aerosols, Atmos. Meas. Tech., 7, 3459-3485, https://doi.org/10.5194/amt-7-3459-2014, 2014.

Georg, M., Andrés-Hernández, M. D., Nenakhov, V., Liu, Y., and Burrows, J. P.: Airborne measurement of peroxy radicals using chemical amplification coupled with cavity ring-down spectroscopy: the PeRCEAS instrument, Atmos. Meas. Tech 13, 2577–2600, https://doi.org/10.5194/amt-13-2577-2020, 2020.

Gerbig, C., Kley, D., Volz-Thomas, A., Kent, J., Dewey, K., and McKenna, D. S.: Fast response resonance fluorescence CO measurements aboard the C-130: Instrument characterization and measurements made during North Atlantic Regional Experiment 1993, J. Geophys. Res., 101, 29229-29238, https://doi.org/10.1029/95JD03272, 1996.

Gershenzon, Y. M., Grigorieva, V., Ivanov, A. V., and Remorov, R. G.: O_3 and OH Sensitivity to Heterogeneous Sink of HO_x and CH_3O_3 on Aerosol Particles, Faraday Discuss., 100, 83–100, 1995.

Gioli, B., Miglietta, F., Vaccari, F. P., Zaldei, A. and De Martino, B.: The Sky Arrow ERA, an innovative airborne platform to monitor mass, momentum and energy exchange of ecosystems. Annals of Geophysics. 49, https://doi.org/10.4401/ag-3159, 2009.

Green, T.J., Brough, N., Reeves, C.E., Edwards, G.D., Monks P. S., and Penkett, S.A.: Airborne measurements of peroxy radicals using the PERCA technique, J. Environ. Monitoring., 5, 75-83, https://doi.org/10.1039/B204493E, 2002.

Green, T. J., Reeves, C. E., Fleming, Z. L., Brough, N., Rickard, R. A., Bandy, B. J., Monks, P. S., and Penkett, S. A.: An improved dual channel PERCA instrument for atmospheric measurements of peroxy radicals, J. Environ. Monitor., 8, 530–536, https://doi.org/10.1039/b514630e, 2006.

Griffith, S. M., Hansen, R. F., Dusanter, S., Michoud, V., Gilman, J. B., Kuster, W. C., Veres, P. R., Graus, M., de Gouw, J. A., Roberts, J., Young, C., Washenfelder, R., Brown, S. S., Thalman, R., Waxman, E., Volkamer, R., Tsai, C., Stutz, J., Flynn, J. H., Grossberg, N., Lefer, B., Alvarez, S. L., Rappenglueck, B., Mielke, L. H., Osthoff, H. D., and Stevens, P. S.: Measurements of Hydroxyl and Hydroperoxy Radicals during CalNexLA: Model Comparisons and Radical Budgets, J. Geophys. Res.-Atmos., 121, 4211–4232, https://doi.org/10.1002/2015JD024358, 2016.

HALO, DLR: http://www.halo.dlr.de, last access: 7 April 2020.

HALO, DLR: http://www.halo.dlr.de/science/missions/omo/omo.html, last access: 7 April 2020.

Hamilton, E. J., Jr.: Water vapor dependence of the kinetics of the self-reaction of HO_2 in the gas phase. J. Chem. Phys., 63, 3682-3683, https://doi.org/10.1063/1.431772, 1975.

Hamilton, E. J., Jr., Lii, R.-R.: The dependence on H_2O and on NH_3 of the kinetics of the self-reaction of HO_2 in the gas-phase formation of $HO_2\bullet H_2O$ and $HO_2\bullet NH_3$ complexes. Int. J. Chem. Kinet., 9, 875-885, https://doi.org/10.1002/kin.550090604, 1977.

Hanke, M., J. Uecker, T. Reiner, and F. Arnold, Atmospheric peroxy radicals: ROxMAS, as new mass-spectrometric methodology for speciated measurements of HO_2 and $\sum RO_2$ and first results, Int. J. Mass Spectrom., 213, 91 – 99, https://doi.org/10.1016/S1387-3806(01)00548-6, 2002.

Hanson, D. R., Burkholder, J. B., Howard, C. J., and Ravishankara, A. R.: Measurement of hydroxyl and hydroperoxy radical uptake coefficients on water and sulfuric acid surfaces, J. Phys. Chem. A., 96, 4979–4985 doi:10.1021/j100191a046, 1992.

Hard, T. M., O'Brien, R. J., Chan, C. Y., and Mehrabzadeh, A. A.: Tropospheric free radical determination by FAGE, Environ. Scie. and Tech., 18, 768–777, https://doi.org/10.1021/es00128a009, 1984.

Hastie, D. R., Weissenmayer, M., Burrows, J. P., and Harris, G. W.: Calibrated chemical amplifier for atmospheric ROx measurements, Anal. Chem. , 63, 2048–2057, https://doi.org/10.1021/ac00018a029, 1991.

Hayman, G. D.: Numerical Model of the Calibration Source of a PERCA Instrument, AEAT-24737/20410001/001, 1997.

Heard, D.: Analytical Techniques for Atmospheric Measurement, Blackwell Publishing Ltd, Oxford, UK, 528 pp., https://doi.org/10.1002/9780470988510, 2006.

Heintzenberg, J.: Properties of the Log-Normal Particle Size Distribution, Aerosol Science and Technology, 21:1, 46-48, https://doi.org/10.1080/02786829408959695, 1994.

Herbelin, J., McKay, J., Kwok, M., Ueunten, R., Urevig, D., Spencer, D., and Benard, D.: Sensitive measurement of photon lifetime and true reflectances in an optical cavity by a phase-shift method, Appl. Opt. 19, 144-147, https://doi.org/10.1364/AO.19.000144, 1980.

Hochanadel, C. J., Ghormley, J. A., Ogren, P. J.: Absorption spectrum and reaction kinetics of the HO_2 radical in the gas phase. J. Chem. Phys., 56, 4426-4432, https://doi.org/10.1063/1.1677885, 1972.

Hofzumahaus, A., Brauers, T., Aschmutat, U., Brandenburger, U., Dorn, H. P., Hausmann, M., Heßling, M., Holland, F., PlassDulmer, C., Sedlacek, M., Weber, M., and Ehhalt, D. H.: Reply [to "Comment on 'The measurement of tropospheric OH radicals by laser-induced fluorescence spectroscopy during the POPCORN field campaign' by Hofzumahaus et al. and 'Intercomparison of tropospheric OH radical measurements by multiple folded long-path laser absorption and laser induced fluorescence' by Brauers et al."], Geophys. Res. Lett., 24, 3039–3040, https://doi.org/10.1029/97GL02947, 1997.

Hofzumahaus, A., Rohrer, F., Lu, K., Bohn, B., Brauers, T., Chang, C.-C., Fuchs, H., Holland, F., Kita, K., Kondo, Y., Li, X., Lou, S., Shao, M., Zeng, L., Wahner, A., and Zhang, Y.: Amplified trace gas removal in the troposphere, Science, 324, 1702–1704, https://doi.org/10.1126/science.1164566, 2009.

Holanda, B. A., Pöhlker, M. L., Walter, D., Saturno, J., Sörgel, M., Ditas, J., Ditas, F., Schulz, C., Franco, M. A., Wang, Q., Donth, T., Artaxo, P., Barbosa, H. M. J., Borrmann, S., Braga, R., Brito, J., Cheng, Y., Dollner, M., Kaiser, J. W., Klimach, T., Knote, C., Krüger, O. O., Fütterer, D., Lavrič, J. V., Ma, N., Machado, L. A. T., Ming, J., Morais, F. G., Paulsen, H., Sauer, D., Schlager, H., Schneider, J., Su, H., Weinzierl, B., Walser, A., Wendisch, M., Ziereis, H., Zöger, M., Pöschl, U., Andreae, M. O., and Pöhlker, C.: Influx of African biomass burning aerosol during the Amazonian dry season through layered transatlantic transport of black carbon-rich smoke, Atmos. Chem. Phys., 20, 4757–4785, https://doi.org/10.5194/acp-20-4757-2020, 2020.

Holton, J.R., Haynes, P.H., McIntyre, Douglas, A.R., Rood, R.B., and Pfister, L.: Stratosphere-troposphere exchange, Rev. Geo-phys., 33, 403-439, https://doi.org/10.1029/95RG02097, 1995.

Hornbrook, R. S., Crawford, J. H., Edwards, G. D., Goyea, O., Mauldin III, R. L., Olson, J. S., and Cantrell, C. A.: Measurements of tropospheric HO2 and RO2 by oxygen dilution modulation and chemical ionization mass spectrometry, Atmos. Meas. Tech., 4, 735–756, https://doi.org/10.5194/amt-4-735-2011, 2011.

Horstjann, M., Andrés Hernández, M. D., Nenakhov, V., Chrobry, A., and Burrows, J. P.: Peroxy radical detection for airborne atmospheric measurements using absorption spectroscopy of NO_2, Atmos. Meas. Tech., 7, 1245–1257, https://doi.org/10.5194/amt-7-1245-2014, 2014.

Hüneke, T., Aderhold, O. A., Bounin, J., Dorf, M., Gentry, E., Grossmann, K., Grooß, J. U., Hoor, P., k Jöckel, P., Kenntner, M., Knapp, M., Knecht, M., Lörks, D., Ludmann, S., Matthes, S., Raecke, R., Reichert, M., Weimar, J., Werner, B., Zahn, A., Ziereis, H., and Klaus Pfeilsticker, The novel HALO mini-DOAS instrument: inferring trace gas concentrations from airborne UV/visible limb spectroscopy under all skies using the scaling method, Atmos. Meas. Tech., 10, 4209–4234, https://doi.org/10.5194/amt-10-4209-2017, 2017.

Ianni, J. C.: Kintecus, Windows Version 6.01, available at: http://www.kintecus.com (last access: 7 April 2020), 2017.

Inomata, S., Tanimoto, H., Kameyama, S., Tsunogai, U., Irie, H., Kanaya, Y., and Wang, Z.: Technical Note: Determination of formaldehyde mixing ratios in air with PTR-MS: laboratory experiments and field measurements, Atmos. Chem. Phys., 8, 273–284, https://doi.org/10.5194/acp-8-273-2008, 2008.

Jacob, D. J.: Heterogeneous chemistry and tropospheric ozone, Atmos. Environ., 34, 2131–2159, https://doi.org/10.1016/S1352-2310(99)00462-8, 2000.

Janssens-Maenhout, G., Crippa, M., Guizzardi, D., Dentener, F., Muntean, M., Pouliot, G., Keating, T., Zhang, Q., Kurokawa, J., Wankmüller, R., Denier van der Gon, H., Kuenen, J. J. P., Klimont, Z., Frost, G., Darras, S., Koffi, B., and Li, M.: HTAP_v2.2: a mosaic of regional and global emission grid maps for 2008 and 2010 to study hemispheric transport of air pollution, Atmos. Chem. Phys., 15, 11411–11432, https://doi.org/10.5194/acp-15-11411-2015, 2015.

Jokinen, T., Sipilä, M., Junninen, H., Ehn, M., Lönn, G., Hakala, J., Petäjä, T., Mauldin III, R. L., Kulmala, M., and Worsnop, D. R.: Atmospheric sulphuric acid and neutral cluster measurements using CI-APi-TOF, Atmos. Chem. Phys., 12, 4117–4125, https://doi.org/10.5194/acp-12-4117-2012, 2012.

Junninen, H., Ehn, M., Petäjä, T., Luosujärvi, L., Kotiaho, T., Kostiainen, R., Rohner, U., Gonin, M., Fuhrer, K., Kulmala, M., and Worsnop, D. R.: A high-resolution mass spectrometer to measure atmospheric ion composition, Atmos. Meas. Tech., 3, 1039–1053, https://doi.org/10.5194/amt-3-1039-2010, 2010.

Jöckel, P., Sander, R., Kerkweg, A., Tost, H., and Lelieveld, J.: Technical Note: The Modular Earth Submodel System (MESSy) – a new approach towards Earth System Modeling, Atmos. Chem. Phys., 5, 433–444, https://doi.org/10.5194/acp-5-433-2005, 2005.

Jöckel, P., Kerkweg, A., Pozzer, A., Sander, R., Tost, H., Riede, H., Baumgaertner, A., Gromov, S., and Kern, B.: Development cycle 2 of the Modular Earth Submodel System (MESSy2), Geosci. Model Dev., 3, 717–752, https://doi.org/10.5194/gmd-3-717-2010, 2010.

Kanaya, Y., Cao, R., Akimoto, H., Fukuda, M., Komazaki, Y., Yokouchi, Y., Koike, M., Tanimoto, H., Takegawa, N., and Kondo, Y.: Urban photochemistry in central Tokyo: 1. Observed and modelled OH and HO2 radical concentrations during the winter and summer of 2004, J. Geophys. Res., 112, D21312, https://doi.org/10.1029/2007JD008670, 2007.

Kanaya, Y., Fukuda, M., Akimoto, H., Takegawa, N., Komazaki, Y., Yokouchi, Y., Koike, M., and Kondo, Y.: Urban photochemistry in central Tokyo: 2. Rates and regimes of oxidant (O3 + NO2) production, J. Geophys. Res., 113, https://doi.org/10.1029/2007JD008671, 2008.

Kanaya, Y., Hofzumahaus, A., Dorn, H.-P., Brauers, T., Fuchs, H., Holland, F., Rohrer, F., Bohn, B., Tillmann, R., Wegener, R., Wahner, A., Kajii, Y., Miyamoto, K., Nishida, S., Watanabe, K., Yoshino, A., Kubistin, D., Martinez, M., Rudolf, M., Harder, H., Berresheim, H., Elste, T., Plass-Dülmer, C., Stange, G., Kleffmann, J., Elshorbany, Y., and Schurath, U.: Comparisons of observed and modeled OH and HO2 concentrations during the ambient measurement period of the HOxComp field campaign, Atmos. Chem. Phys., 12, 2567–2585, https://doi.org/10.5194/acp-12-2567-2012, 2012.

Kartal, D.: Characterization and optimization of a dual channel PERCA for the investigation of the chemistry of peroxy radicals in the upper troposphere, PhD thesis, Fachbereich für Physik und Elektrotechnik, University of Bremen, Germany, 2009.

Kartal, D., Andrés-Hernández, M. D., Reichert, L., Schlager, H., and Burrows, J. P.: Technical Note: Characterisation of a DUALER instrument for the airborne measurement of peroxy radicals during AMMA 2006, Atmos. Chem. Phys., 10, 3047–3062, https://doi.org/10.5194/acp-10-3047-2010, 2010.

Kebabian, P. L., Herndon, S. C., and Freedman, A: Detection of Nitrogen Dioxide by Cavity Attenuated Phase Shift Spectroscopy, Analytical Chemistry, 77 (2), 724-728, https://doi.org/10.1021/ac048715y, 2005.

Kiehl, J. T. and Trenberth, K. E.: Earth's annual global mean energy budget, Bull. Am. Meteorol. Soc., 78, 197–208, https://doi.org/10.1175/1520-0477(1997)078<0197:EAGMEB>2.0.CO;2, 1997.

Kintecus: http://www.kintecus.com, last access: 7 April 2020.

Kluge, F., Hüneke, T., Knecht, M., Lichtenstern, M., Rotermund, M., Schlager, H., Schreiner, B., and Pfeilsticker, K.: Profiling of formaldehyde, glyoxal, methylglyoxal, and CO over the Amazon: normalized excess mixing ratios and related emission factors in biomass burning plumes, Atmos. Chem. Phys., 20, 12363–12389, https://doi.org/10.5194/acp-20-12363-2020, 2020.

Kukui, A., Legrand, M., Preunkert, S., Frey, M. M., Loisil, R., Gil Roca, J., Jourdain, B., King, M. D., France, J. L., and Ancellet, G.: Measurements of OH and RO2 radicals at Dome C, East Antarctica, Atmos. Chem. Phys., 14, 12373–12392, https://doi.org/10.5194/acp-14-12373-2014, 2014.

Lelieveld, J., Bourtsoukidis, E., Brühl, C., Fischer, H., Fuchs, H., Harder, H., Hofzumahaus, A., Holland, F., Marno, D., and Neumaier, M.: The South Asian monsoon – Pollution pump and purifier, Science, 6399, 270–273, https://doi.org/10.1126/science.aar2501, 2018.

Levine, I. N.: Physical Chemistry, 4th edition, McGraw-Hill, Inc., New York, 1995.

Levy II, H.: Normal Atmosphere: Large Radical and Formaldehyde Concentrations Predicted, Science 1971, Vol. 173, Issue 3992, pp. 141-143, https://doi.org/10.1126/science.173.3992.141. 1971.

Lew, M. M., Rickly, P. S., Bottorff, B. P., Reidy, E., Sklaveniti, S., Léonardis, T., Locoge, N., Dusanter, S., Kundu, S., Wood, E., and Stevens, P. S.: OH and HO$_2$ radical chemistry in a midlatitude forest: measurements and model comparisons, Atmos. Chem. Phys., 20, 9209–9230, https://doi.org/10.5194/acp-20-9209-2020, 2020.

Li, K., Jacob, D. J., Liao, H., Shen, L., Zhang, Q., and Bates K. H.: Anthropogenic drivers of 2013–2017 trends in summer surface ozone in China, Proc. Natl. Acad. Sci. U.S.A., 116, 422 −427, https://doi.org/10.1073/pnas.1812168116, 2019.

Li, X., Qi, B., Zeng, L., Zeng, L, and Tang, X. Y.: Development and deployment of an instrument for measurement of atmospheric peroxy radical by chemical amplification, Sci. China Ser. D-Earth Sci. 52, 333–340, https://doi.org/10.1007/s11430-009-0032-0, 2009.

Lii, R. R., Sauer, M. C., Jr., Gordon, S.: Temperature dependence of the gas-phase self-reaction of HO$_2$ in the presence of H$_2$O. J. Phys. Chem., 85, 2833-2834, https://doi.org/10.1021/j150619a027, 1981.

Liu, Y., Morales-Cueto, R., Hargrove, J., Medina, D., and Zhang, J.: Measurements of peroxy radicals using chemical amplification cavity ring down spectroscopy, Environ. Sci. Technol., 43, 7791–7796, https://doi.org/10.1021/es901146t, 2009.

Liu, Y. and Zhang, J.: Atmospheric Peroxy Radical Measurements Using Dual-Channel Chemical Amplification Cavity Ringdown Spectroscopy, Analytical Chemistry, 86, 5391–5398, https://doi.org/10.1021/ac5004689, 2014.

Langridge, J. M., Ball, S. M., and Jonesa, R. L.: A compact broadband cavity enhanced absorption spectrometer for detection of atmospheric NO_2 using light emitting diodes, Analyst, 8, https://doi.org/10.1039/B605636A, 2006.

Mallaun, C., Giez, A., and Baumann, R.: Calibration of 3-D wind measurements on a single engine research aircraft Atmos. Meas. Tech., 8, 3177-3196, https://doi.org/10.5194/amt-8-3177-2015, 2015.

Mao, J., Jacob, D. J., Evans, M. J., Olson, J. R., Ren, X., Brune, W. H., Clair, J. M. St., Crounse, J. D., Spencer, K. M., Beaver, M. R., Wennberg, P. O., Cubison, M. J., Jimenez, J. L., Fried, A., Weibring, P., Walega, J. G., Hall, S. R., Weinheimer, A. J., Cohen, R. C., Chen, G., Crawford, J. H., McNaughton, C., Clarke, A. D., Jaeglé, L., Fisher, J. A., Yantosca, R. M., Le Sager, P., and Carouge, C.: Chemistry of hydrogen oxide radicals (HO_x) in the Arctic troposphere in spring, Atmos. Chem. Phys., 10, 5823–5838, https://doi.org/10.5194/acp-10-5823-2010, 2010.

Marno, D., Ernest, C., Hens, K., Javed, U., Klimach, T., Martinez, M., Rudolf, M., Lelieveld, J., and Harder, H.: Calibration of an airborne HO_x instrument using the All Pressure Altitude-based Calibrator for HO_x Experimentation (APACHE), Atmos. Meas. Tech., 13, 2711–2731, https://doi.org/10.5194/amt-13-2711-2020, 2020.

Martinez, M., Harder, H., Kovacs, T. A., Simpas, J. B., Bassis, J., Lesher, R., Brune, W. H., Frost, G. J., Williams, E. J., Stroud, C. A., Jobson, B. T., Roberts, J. M., Hall, S. R., Shetter, R. E., Wert, B., Fried, A., Alicke, B., Stutz, J., Young, V. L., White, A. B., and Zamora, R. J.: OH and HO_2 concentrations, sources, and loss rates during the Southern Oxidants Study in Nashville, Tennessee, summer 1999, J. Geophys. Res.-Atmos., 108, 4617, https://doi.org/10.1029/2003jd003551, 2003.

Martinez, M., Harder, H., Kubistin, D., Rudolf, M., Bozem, H., Eerdekens, G., Fischer, H., Klüpfel, T., Gurk, C., Königstedt, R., Parchatka, U., Schiller, C. L., Stickler, A., Williams, J., and Lelieveld, J.: Hydroxyl radicals in the tropical troposphere over the Suriname rainforest: airborne measurements, Atmos. Chem. Phys., 10, 3759–3773, https://doi.org/10.5194/acp-10-3759-2010, 2010.

Mozurkewich, M., McMurry, P. H., Gupta, A., and Calvert, J. G.: Mass Accommodation Coefficient for HO_2 Radicals on Aqueous Particles, J. Geophys. Res., 92, 4163–4170, 1987.

Murphy D. M. and Fahey D. W.: Mathematical treatment of the wall loss of a trace species in denuder and catalytic converter tubes, Anal. Chem., 1987, 59, 2753–2759, https://doi.org/10.1021/ac00150a006, 1987.

Mihelcic, D., Müsgen, P., and Ehhalt, D. H.: An improved method of measuring tropospheric NO_2 and RO_2 by matrix isolation and electron spin resonance, J. Atmos. Chem., 3, 341–361, https://doi.org/10.1007/BF00122523, 1985.

Mihelcic, D., Volz-Thomas, A., Pätz, H.W. et al. Numerical analysis of ESR spectra from atmospheric samples. J. Atmos. Chem., 11, 271–297, https://doi.org/10.1007/BF00118353, 1990.

Mihelcic, D., Klemp, D., Müsgen, P. et al. Simultaneous measurements of peroxy and nitrate radicals at Schauinsland. J. Atmos. Chem.,16, 313–335, https://doi.org/10.1007/BF01032628, 1993.

Mihele, C. M. and Hastie, D. R.: The sensitivity of the radical amplifier to ambient water vapour, Geophys. Res. Lett., 25, 1911–1913, https://doi.org/10.1029/98GL01432, 1998.

Mihele, C. M., Mozurkewich, M., and Hastie, D. R.: Radical loss in a chain reaction of CO and NO in the presence of water: Implications for the radical amplifier and atmospheric chemistry, Int. J. Chem. Kinet., 31, 145–152, https://doi.org/10.1002/(SICI)1097-4601(1999)31:2<145::AID-KIN7>3.0.CO;2-M, 1999.

Mihelcic, D., Holland, F., Hofzumahaus, A., Hoppe, L., Konrad, S., Müsgen, P., Pätz, H.-W., Schäfer, H.-J., Schmitz. T., Volz-Thomas, A., Bächmann, K., Schlomski, S., Platt, U., Gezer, A., Alicke, B., and Moortgat G. K.: Peroxy radicals during BERLIOZ at Pabstthum: Measurements, radical budgets and ozone production, J. Geophys. Res., 108, 8254, https://doi.org/10.1029/2001JD001014, 2003.

Miyazaki, K., Matsumoto, J., Kato, S., and Kajii, Y.: Development of atmospheric NO analyser by using a laser-induced fluorescence NO_2 detector, Atmospheric Environment, 42, 7812-7820, https://doi.org/10.1016/j.atmosenv.2008.05.056, 2008.

Miyazaki, K., Parker, A. E., Fittschen, C., Monks, P. S., and Kajii, Y.: A new technique for the selective measurement of atmospheric peroxy radical concentrations of HO2 and RO2 using a denuding method, Atmos. Meas. Tech., 3, 1547–1554, https://doi.org/10.5194/amt-3-1547-2010, 2010.

Monks, P. S., Carpenter, L. J., Penkett, S. A., Ayers, G. P., Gillett, R. W., Galbally, I. E., and Meyer, C. P.: Fundamental ozone photochemistry in the remote marine boundary layer: the SOAPEX experiment, measurement and theory, Atmos. Environ., 32, 3647–3664, https://doi.org/10.1016/S1352-2310(98)00084-3, 1998.

Monks, P. S., Granier, C., Fuzzi, S., Stohl, A., Williams, M. L., Akimoto, H., Amann, M., Baklanov, A., Baltensperger, U., Bey, I., Blake, N., Blake, R. S., Carslaw, K., Cooper, O. R., Dentener, F., Fowler, D., Fragkou, E., Frost, G. J., Generoso, S., Ginoux, P., Grewe, V., Guenther, A., Hansson, H. C., Henne, S., Hjorth, J., Hofzumahaus, A., Huntrieser, H., Isaksen, I. S. A., Jenkin, M . E., Kaiser, J., Kanakidou, M., Klimont, Z., Kulmala, M., Laj, P., Lawrence, M. G., Lee, J. D., Liousse, C., Maione, M., McFiggans, G., Metzger, A., Mieville, A., Moussiopoulos, N. Orlandou, J. J., O'Dowd, C. D., Palmer, P. I., Parrish, D. D., Petzold, A., Platt, U., Pöschl, U., Prévôt, A. S. H., Reeves, C. E., Reimann, S., Rudich, Y., Sellegri, K., Steinbrecher, R., Simpson, D., ten Brink, H., Theloke, J., van

der Werf, G. R., Vautard, R., Vestreng, V., Vlachokostas, C., and von Glasow, R.,: Atmospheric composition changeglobal and regional air quality, Atmos. Environ., 43, 5268–5350, https://doi.org/10.1016/j.atmosenv.2009.08.021, 2009.

NASA Earth Observatory: https://earthobservatory.nasa.gov/features/EnergyBalance/page4.php, last access: 7 April 2021.

NWS, 2016: Global Circulations in NWS Jet Stream: An Online School for Weather. National Weather Service, http://www.srh.noaa.gov/jetstream/global/circ.html, 2016.

Ocean Currents: https://seos-project.eu/oceancurrents/oceancurrents-c02-s02-p01.html, last access: 7 April 2020.

O'Keefe, A. and Deacon, D. A. G.: Cavity ring-down optical spectrometer for absorption measurements using pulsed laser sources, Rev. Sci. Instrum., 59, 2544–2551, https://doi.org/10.1063/1.1139895, 1988.

Olson, J. R., Crawford, J. H., Chen, G., Brune, W. H., Faloona, I. C., Tan, D., Harder, H., and Martinez, M.: A reevaluation of airborne HO_x observations from NASA field campaigns, J. Geophys. Res. , 111, D10301, https://doi.org/10.1029/2005JD006617, 2006.

OMO, MPI: https://www.mpic.de/3599603/OMO, last access: 7 April 2020.

Paulson, S. E, Orlando, J. J.: The reactions of ozone with alkenes: An important source of HO_x in the boundary layer. Geophys Res Lett 23(25)1: 3727–3730, https://doi.org/10.1029/96GL03477, 1996.

Penkett, S. A., Monks, P. S., Carpenter, L. J., Clemitshaw, K. C., Ayers, G. P., Gillett, R. W., Galbally, I. E., and Meyer, C. P.: Relationships between ozone photolysis rates and peroxy radical concentrations in clean marine air over the Southern Ocean, J. Geophys. Res., 102(D11), 12805–12817, https://doi.org/10.1029/97JD00765, 1997.

Qi, B., Kanaya, Y., Takami, A., Hatakeyama, S. Kato, S., Sadanaga, Y., Tanimoto, H., and Kajii, Y.: Diurnal peroxy radical chemistry at a remote coastal site over the sea of Japan, J. Geophys. Res., 112, D17306, https://doi.org/10.1029/2006JD008236, 2007.

Reichert, L., Untersuchung des Wassereffektes eines Peroxyradikal-Detektors, M.S. thesis, Univ. of Bremen, Bremen, Germany, 2000.

Reichert, L., Andrés Hernández, M. D., Stöbener, D., Burkert, J., and Burrows, J. P.: Investigation of the effect of water complexes in the determination of peroxy radical ambient concentrations: implications for the atmosphere, J. Geophys. Res, 108, 4017– 4032, https://doi.org/10.1029/2002JD002152, 2003.

Reiner, T., Hanke, M., and Arnold, F.: Atmospheric peroxy radical measurements by ion molecule reaction mass spectrometry: A novel analytical method using amplifying chemical conversion to sulfuric acid, J. Geophys. Res.-Atmos., 102, 1311–1326, https://doi.org/10.1029/96JD02963, 1997.

Remorov, R. G., Gershenzon, Y. M., Molina, L. T., and Molina, M. J.: Kinetics and Mechanism of HO_2 Uptake on Solid NaCl, J. Phys. Chem. A., 106, 4558–4565, 2002.

Ren, Y., R. Baumann, H. Schlager, An airborne perfluorocarbon tracer system and its first application for a Lagrangian experiment. Atmos. Meas. Tech., 8, 69-80. https://doi.org/10.5194/amt-8-69-2015, 2015.

Ren, X., Harder, H., Martinez, M., Lesher, R. L., Oliger, A., Shirley, T., Adams, J., Simpas, J. B., and Brune, W. H.: HOX concentrations and OH reactivity observations in New York City during PMTACS-NY2001, Atmos. Environ., 37, 3627–3637, 2003.

Ren, X., Olson, J. R., Crawford, J. H., Brune, W. H., Mao, J., Long, R. B., Chen, Z., Chen, G., Avery, M. A., Sachse, G. W., Barrick, J. D., Diskin, G. S., Huey, L. G., Fried, A., Cohen, R. C., Heikes, B., Wennberg, P. O., Singh, H. B., Blake, D. R., and Shetter, R. E.: HO_x chemistry during INTEX-A 2004: Observation, model calculation, and comparison with previous studies, J. Geophys. Res., 113, D05310, https://doi.org/10.1029/2007JD009166, 2008.

Ren, X., Mao, J., Brune, W. H., Cantrell, C. A., Mauldin III, R. L., Hornbrook, R. S., Kosciuch, E., Olson, J. R., Crawford, J. H., Chen, G., and Singh, H. B.: Airborne intercomparison of HO_x measurements using laser-induced fluorescence and chemical ionization mass spectrometry during ARCTAS, Atmos. Meas. Tech., 5, 2025–2037, https://doi.org/10.5194/amt-5-2025-2012, 2012.

Ren, X., van Duin, D., Cazorla, M., Chen, S., Mao, J., Zhang, L., Brune, W. H., Flynn, J. H., Grossberg, N., Lefer, B. L., Rappenglück, B., Wong, K. W., Tsai, C., Stutz, J., Dibb, J. E., Thomas Jobson, B., Luke, W. T., and Kelley, P.: Atmospheric oxidation chemistry and ozone production: Results from SHARP 2009 in Houston, Texas, J. Geophys. Res., 118, 5770–5780, https://doi.org/10.1002/jgrd.50342, 2013.

Rissanen, M. P., Kurtén, T., Sipilä, M., Thornton, J. A., Kangasluoma, J., Sarnela, N., Junninen, H., Jørgensen, S., Schallhart, S., Kajos, M. K., Taipale, R., Springer, M., Mentel, T. F., Ruuskanen, T., Petäjä, T., Worsnop, D. R., Kjaergaard, H. G., and Ehn, M.: The Formation of Highly Oxidized Multifunctional Products in the Ozonolysis of Cyclohexene, Journal of the American Chemical Society 2014 136 (44), 15596-15606, https://doi.org/10.1021/ja507146s, 2014.

Roeckner, E., Brokopf, R., Esch, M., Giorgetta, M., Hagemann, S., Kornblueh, L., Manzini, E., Schlese, U., and Schulzweida, U.: Sensitivity of simulated climate to horizontal and vertical resolution in the ECHAM5 atmosphere model, J. Climate, 19, 3771–3791, https://doi.org/10.1175/JCLI3824.1, 2006.

Robert Carroll Weather: https://robertcarrollweather.files.wordpress.com/2014/11/agburt01_09.jpg, last access: 11 July 2021.

Rotermund, M. K., Bense, V., Chipperfield, M. P., Engel, A., Grooß, J.-U., Hoor, P., Hüneke, T., Keber, T., Kluge, F., Schreiner, B., Schuck, T., Vogel, B., Zahn, A., and Pfeilsticker, K.: Organic and inorganic bromine measurements around the extratropical tropopause and lowermost stratosphere: Insights into the transport pathways and total bromine, Atmos. Chem. Phys. Discuss. [preprint], https://doi.org/10.5194/acp-2021-202, in review, 2021.

Sadanaga, Y., Matsumoto, J., Sakurai, K., Isozaki, R., Kato, S., Nomaguchi, T., Bandow, H., and Kajii, Y.: Development of a measurement system of peroxy radicals using a chemical amplification/laser-induced fluorescence technique, Rev. Sci. Instrum., 75, 864–872, https://doi.org/10.1063/1.1666985, 2004.

Salisbury, G., P. S. Monks, S. Bauguitte, B. J. Bandy, and S. A. Penkett, A seasonal comparison of the ozone photochemistry in clean and polluted air masses at Mace Head, Ireland, J. Atmos. Chem., 41, 163–187, https://doi.org/10.1023/A:1014202229304, 2002.

Sanchez, J., Tanner, D. J., Chen, D., Huey, L. G., and Ng, N. L.: A new technique for the direct detection of HO2 radicals using bromide chemical ionization mass spectrometry (BrCIMS): initial characterization, Atmos. Meas. Tech., 9, 3851–3861, https://doi.org/10.5194/amt-9-3851-2016, 2016.

Sander, S. P.; Peterson, M.; Watson, R. T.; Patrick, R. Kinetics studies of the $HO_2 + HO_2$ and $DO_2 + DO_2$ reactions at 298 K. J. Phys. Chem., 86, 1236-1240, https://doi.org/10.1021/j100397a002, 1982.

Schiller, C. L., Bozem, H., Gurk, C., Parchatka, U., Konigstedt, R., Harris, G. W., Lelieveld, J., and Fischer, H.: Applications of quantum cascade lasers for sensitive trace gas measurements of CO, CH4, N2O and HCHO, Appl. Phys. B-Lasers O., 92, 419– 430, https://doi.org/10.1007/s00340-008-3125-0, 2008.

Schlatter, T. W.: Atmospheric Composition and Vertical Structure, Environmental Impact, Manufacturing and Operations Operational Environment, Encyclopedia of Aerospace Engineering, https://doi.org/10.1002/9780470686652.eae582, 2010.

Schultz, M., Heitlinger, M., Mihelcic, D., and Volz-Thomas, A.: Calibration source for peroxy radicals with built-in actinometry using H_2O and O_2 photolysis at 185nm, J. Geophys. Res. 100, 18811–18816, https://doi.org/10.1029/95JD01642, 1995.

Schulz, C., Schneider, J., Holanda, B. A., Appel, O., Costa, A., de Sá, S.S., Dreiling, V. Fütterer, D., Jurkat-Witschas, T., Klimach, T., Knote, C., Krämer, M., Martin, S.T., Mertes, S., Pöhlker, M.L., Sauer, D., Voigt, C., Walser, A., Weinzierl, A.B., Ziereis, H., Zöger, M., Andreae, M.O., Artaxo, P., Machado, L-A.T., Pöschl, U., Wendisch, M., and S. Borrmann, Aircraft-based observations of isoprene-epoxydiol-derived secondary organic aerosol (IEPOX-SOA) in the tropical upper troposphere over the Amazon region. Atmos. Chem. Phys., 18, 14979–15001, https://doi.org/10.5194/acp-18-14979-2018, 2018.

Schumann, U.: Measurement and model data comparisons for the HALO-FAAM formation flight during EMeRGe on 17 July 2017, https://doi.org/10.5281/zenodo.4427965, 2020.

Seinfeld, H. J. and Pandis, S. N.: Atmospheric Chemistry and Physics, Wiley & Sons 1997. ISBN: 0-471-17816-0.

Skamarok, W. C., Klemp, J. B., Dudhia, J., Gill, D. O., Barker, D. M., Duda, M. G., Huang, X. Y., Wang, W., and Powers, J. G.: A description of the Advanced Research WRF version 3, NCAR Technical Note NCAR/TN-4751STR, 2008.

Stone, D., Evans, M. J., Edwards, P. M., Commane, R., Ingham, T., Rickard, A. R., Brookes, D. M., Hopkins, J., Leigh, R. J., Lewis, A. C., Monks, P. S., Oram, D., Reeves, C. E., Stewart, D., and Heard, D. E.: Isoprene oxidation mechanisms: measurements and modelling of OH and HO_2 over a South-East Asian tropical rainforest during the OP3 field campaign, Atmos. Chem. Phys., 11, 6749–6771, https://doi.org/10.5194/acp-11-6749-2011, 2011.

Stone, D., Whalley, L. K., and Heard, D. E.: Tropospheric OH and HO_2 radicals: field measurements and model comparisons, Chemical Society Reviews, 2012, 41, 6348–6404, https://doi.org/10.1039/C2CS35140D, 2012.

Stöbener, D.: Further development of a peroxy radical source for the calibration of ambient air RO_2 measurements, M.S. thesis, University of Bremen, Germany, http://www.iup.physik.uni-bremen.de/troposphere/Publications.html, April 1999.

Speidel, M., Nau, R., Arnold, F., Schlager, H., A. Stohl, Sulfur dioxide measurements in the lower, middle and upper troposphere: Deployment of an aircraft-based chemical ionization mass spectrometer with permanent in-flight calibration, Atmospheric Environment, 41, 2427-2437, https://doi.org/10.1016/j.atmosenv.2006.07.047, 2007.

Stohl, A., Wotawa, G., Seibert, P. and Kromp-Kolb H.: Interpolation errors in wind fields as a function of spatial and temporal resolution and their impact on different types of kinematic trajectories. J. Appl. Meteor. 34, p. 2149-2165, https://doi.org/10.1175/1520-0450(1995)034<2149:IEIWFA>2.0.CO;2, 1995.

Stohl, A., Hittenberger, M., and Wotawa, G.: Validation of the Lagrangian particle dispersion model FLEXPART against largescale tracer experiment data, Atmos. Environ., 32, 4245–4264, https://doi.org/10.1016/S1352-2310(98)00184-8, 1998.

Stohl, A., Haimberger, L., Scheele, M.P. and Wernli, H.: An intercomparison of results from three trajectory models. Meteorol. Applications 8, 127-135, https://doi.org/10.1017/S1350482701002018, 1999.

Stone, D. Rowley, D. M.: Kinetics of the gas phase HO_2 self-reaction: Effects of temperature, pressure, water and methanol vapours. Phys. Chem. Chem. Phys., 7, 2156-2163, https://doi.org/10.1039/b502673c, 2005.

Stone, D., Whalley, L. K., and Heard, D. E.: Tropospheric OH and HO_2 radicals: field measurements and model comparisons, Critical Review, Chem. Soc. Rev., 41, 6348–6404, https://doi.org/10.1039/C2CS35140D, 2012.

Stutz, J., Werner, B., Spolaor, M., Scalone, L., Festa, J., Tsai, C., Cheung, R., Colosimo, S. F., Tricoli, U., Raecke, R., Hossaini, R., Chipper1180 field, M. P., Feng, W., Gao, R.-S., Hintsa, E. J., Elkins, J. W., Moore, F. L., Daube, B., Pittman, J., Wofsy, S., and Pfeilsticker, K.: A new Differential Optical Absorption Spectroscopy instrument to study atmospheric chemistry from a high-altitude unmanned aircraft, Atmos. Meas. Tech., 10, 1017 – 1042, https://doi.org/10.5194/amt-10-1017-2017, 2017.

Tadic, I., Parchatka, U., Konigstedt, R., and Fischer, H.: Inflight stability of quantum cascade laser-based infrared absorption spectroscopy measurements of atmospheric carbon monoxide, Appl. Phys. B-Lasers O., 123, 146, https://doi.org/10.1007/s00340-017-6721-z, 2017.

Taketani, F., Kanaya, Y., and Akimoto, H.: Kinetics of Heterogeneous Reactions of HO_2 Radical at Ambient Concentration Levels with $(NH_4)_2SO_4$ and NaCl Aerosol Particles, J. Phys. Chem. A., 112, 2370–2377, 2008.

Taketani, F., Kanaya, Y., and Akimoto, H.: Heterogeneous Loss of HO_2 by KCl, Synthetic Sea Salt, and Natural Seawater Aerosol Particles, Atmos. Environ., 43, 1660–1665, 2009.

Taketani, F., Kanaya, Y., and Akimoto, H.: Kinetics of HO_2 Uptake in Levoglucosan and Polystyrene Latex Particles, J. Phys. Chem. Lett., 1, 1701–1704, doi:10.1021/jz100478s, 2010.

Taketani, F., Kanaya, Y., Pochanart, P., Liu, Y., Li, J., Okuzawa, K., Kawamura, K., Wang, Z., and Akimoto, H.: Measurement of overall uptake coefficients for HO2 radicals by aerosol particles sampled from ambient air at Mts. Tai and Mang (China), Atmos. Chem. Phys., 12, 11907–11916, https://doi.org/10.5194/acp-12-11907-2012, 2012.

Tan, D., Faloona, I., Simpas, J. B., Brune, W., Olson, J., Crawford, J., Avery, M., Sachse, G., Vay, S., Sandholm, S., Guan, H.-W., Vaughn, T., Mastromarino, J., Heikes, B., Snow, J., Podolske, J., and Singh, H.: OH and HO_2 in the tropical Pacific: Results from PEMTropics B, J. Geophys. Res., 106, 32,667–32,681, https://doi.org/10.1029/2001JD900002, 2001.

Tan, Z., Fuchs, H., Lu, K., Hofzumahaus, A., Bohn, B., Broch, S., Dong, H., Gomm, S., Häseler, R., He, L., Holland, F., Li, X., Liu, Y., Lu, S., Rohrer, F., Shao, M., Wang, B., Wang, M., Wu, Y., Zeng, L., Zhang, Y., Wahner, A., and Zhang, Y.: Radical chemistry at a rural site (Wangdu) in the North China Plain: observation and model calculations of OH, HO2 and RO2 radicals, Atmos. Chem. Phys., 17, 663–690, https://doi.org/10.5194/acp-17-663-2017, 2017.

Tan, Z., Hofzumahaus, A., Lu, K., Brown, S. S., Holland, F., Huey, L. G., Kiendler-Scharr, A, Li, X., Liu, X., Ma, N., Min, K. E., Rohrer, F., Shao, M., Wahner, A., Wang, Y, Wiedensohler, A., Wu, Y., Wu, Z., Zeng, L., Zhang, Y., and Fuchs, H.: Environmental Science & Technology 54 (10), 5973-5979, https://doi.org/10.1021/acs.est.0c00525, 2020.

Tang, Y., Tyndall, G. S., Orlando, J. J.: Spectroscopic and kinetic properties of HO_2 radicals and the enhancement of the HO_2 self reaction by CH_3OH and H_2O. J. Phys. Chem. A, 114, 369-378, https://doi.org/10.1021/jp905279b, 2010.

Thalman, R. and Volkamer, R.: Inherent calibration of a blue LED-CE-DOAS instrument to measure iodine oxide, glyoxal, methylglyoxal, nitrogen dioxide, water vapour and aerosol extinction in open cavity mode, Atmos. Meas. Tech., 3, 1797–1814, https://doi.org/10.5194/amt-3-1797-2010, 2010.

The United States Environmental Protection Agency. CMAQ (Version 5.0.2) [Software], https://doi.org/10.5281/zenodo.1079898, 2014.

The United States Environmental Protection Agency, Community Multiscale Air Quality Modeling System (CMAQ), https://www.epa.gov/cmaq/chemical-process-overview, 2014.

Thornton, J. and Abbatt, J. P. D.: Measurements of HO_2 uptake to aqueous aerosol: Mass accommodation coefficients and net reactive loss, J. Geophys. Res.-Atmos., 110, D08309, https://doi.org/10.1029/2004jd005402, 2005.

Tomsche, L., Pozzer, A., Ojha, N., Parchatka, U., Lelieveld, J., and Fischer, H.: Upper tropospheric CH4 and CO affected by the South Asian summer monsoon during the Oxidation Mechanism Observations mission, Atmos. Chem. Phys., 19, 1915–1939, https://doi.org/10.5194/acp-19-1915-2019, 2019.

Vandaele, A. C., Hermans, C., Fally, S., Carleer, M., Colin, R., Mérienne, M.-F., Jenouvrier, A., and Coquart, B.: High resolution Fourier transform measurement of the NO2 visible and near-infrared

absorption cross-section: temperature and pressure effects, J. Geophys. Res., 107, 4348, https://doi.org/10.1029/2001JD000971, 2002.

Varma, R. M., Venables, D. S., Ruth, A. A., Heitmann, U., Schlosser, E., and Dixneuf, S.: Long optical cavities for open-path monitoring of atmospheric trace gases and aerosol extinction, Appl. Optics B, 48, 159–171, https://doi.org/10.1364/AO.48.00B159, 2009.

Veres, P. R., Roberts, J. M., Wild, R. J., Edwards, P. M., Brown, S. S., Bates, T. S., Quinn, P. K., Johnson, J. E., Zamora, R. J., and de Gouw, J.: Peroxynitric acid (HO_2NO_2) measurements during the UBWOS 2013 and 2014 studies using iodide ion chemical ionization mass spectrometry, Atmos. Chem. Phys., 15, 8101– 8114, https://doi.org/10.5194/acp-15-8101-2015, 2015.

Visionlearning®: https://www.visionlearning.com/en/library/Earth-Science/6/Composition-of-Earths-Atmosphere/107/reading, last access: 11 July 2021.

Volz-Thomas, A., Xueref, I., and Schmitt, R.: Automatic gas chromatograph and calibration system for ambient measurements of PAN and PPN, Environ. Sci. Poll. Res., 9, 72-76, 2001.

Wayne, R. P.: Atmospheric Chemistry, Oxford University Press, ISBN: 0-19-855571-7, 2000.

Wendisch, M., Pöschl, U., Andreae, M. O., Machado, L. A. T., Albrecht, R., Schlager, H., Rosenfeld, D., Martin, S. T., Abdelmonem, A. Afchine, A., Araùjo, A. C., Artaxo, P., Aufmhoff, H. Barbosa, H. M. J., Borrmann, S., Braga, R., Buchholz, B., Cecchini, M. A., Costa, A. Curtius, J., Dollner, M., Dorf, M., Dreiling, V., Ebert, V., Ehrlich, A., Ewald, F., Fisch, G., Fix, A., Frank, F., Fütterer, D., Heckl, C., Heidelberg, F., Hüneke, T., Jäkel, E., Järvinen, E., Jurkat, T., Kanter, S., Kästner, U., Kenntner, M., Kesselmeier, J., Klimach, T., Knecht, M., Kohl, R., Kölling, T., Krämer, M., Krüger, M., Krisna, T. C., Lavric, J. V., Longo, K., Mahnke, C., Manzi, A. O., Mayer, B., Mertes, S., Minikin, A., Molleker, S., Münch, S., Nillius, B.. Pfeilsticker, K., Pöhlker, C.. Roiger, A., Rose, D., Rosenow, D., Sauer, D., Schnaiter, M., Schneider, J., Schulz, C., de Souza, R. A. F. Spanu, A., Stock, P., Vila, D., Voigt, C., Walser, A., Walter, D., Weigel, R., Weinzierl, B., Werner, F., Yamasoe, M. A., Ziereis, H., Zinner, T., and Zöger, M.: The ACRIDICON-CHUVA campaign: Studying tropical deep convective clouds and precipitation over Amazonia using the new German research aircraft HALO, Bull. Amer. Meteorol. Soc., 97, 1885-1908, https://doi.org/10.1175/BAMS-D-14-00255, 2016.

Werle, P., Mücke, R., and Slemr, F.: The Limits of Signal Averaging in Atmospheric Trace-Gas Monitoring by Tunable Diode-Laser Absorption Spectroscopy (TDLAS), Appl. Phys. B, 57, 131–139, https://doi.org/10.1007/BF00425997, 1993.

Whalley, L. K., Stone, D., Dunmore, R., Hamilton, J., Hopkins, J. R., Lee, J. D., Lewis, A. C., Williams, P., Kleffmann, J., Laufs, S., Woodward-Massey, R., and Heard, D. E.: Understanding in situ ozone production in the summertime through radical observations and modelling studies during the

Clean air for London project (ClearfLo), Atmos. Chem. Phys., 18, 2547–2571, https://doi.org/10.5194/acp-18-2547-2018, 2018.

Whalley, L. K., Slater, E. J., Woodward-Massey, R., Ye, C., Lee, J. D., Squires, F., Hopkins, J. R., Dunmore, R. E., Shaw, M., Hamilton, J. F., Lewis, A. C., Mehra, A., Worrall, S. D., Bacak, A., Bannan, T. J., Coe, H., Percival, C. J., Ouyang, B., Jones, R. L., Crilley, L. R., Kramer, L. J., Bloss, W. J., Vu, T., Kotthaus, S., Grimmond, S., Sun, Y., Xu, W., Yue, S., Ren, L., Acton, W. J. F., Hewitt, C. N., Wang, X., Fu, P., and Heard, D. E.: Evaluating the sensitivity of radical chemistry and ozone formation to ambient VOCs and NO_x in Beijing, Atmos. Chem. Phys., 21, 2125–2147, https://doi.org/10.5194/acp-21-2125-2021, 2021.

Wintel, J., Hösen, E., Koppmann, R., Krebsbach, M., Hofzumahaus, A., and Rohrer, F.:Stable carbon isotope ratios of toluene in the boundary layer and the lower free troposphere, Atmos. Chem. Phys., 13, 11059-11071, https://doi.org/10.5194/acp-13-11059-2013, 2013.

Wikimedia: https://commons.wikimedia.org/w/index.php?curid=24648395, last access: 11 July 2021.

Wood, E. C. and Charest, J. R.: Chemical Amplification – Cavity Attenuated Phase Shift Spectroscopy Measurements of Atmospheric Peroxy Radicals, Analytical Chemistry, 86, 10266–10273, https://doi.org/10.1021/ac502451m, 2014.

Wood, E. C., Deming, B. L., and Kundu, S.: Ethane-Based Chemical Amplification Measurement Technique for Atmospheric Peroxy Radicals Environ. Sci. Technol. Lett., 4, 15–19, https://doi.org/10.1021/acs.estlett.6b00438, 2017.

Ye, C., Zhou, X., Pu, D., Stutz, J., Festa, J., Spolaor, M., Tsai, C., Cantrell, C., Mauldin III, R. L., Weinheimer, A., Hornbrook, R. S., Apel, E. C., Guenther, A., Kaser, L., Yuan, B., Karl, T., Haggerty, J., Hall, S., Ullmann, K., Smith, J., and Ortega, J.: Tropospheric HONO distribution and chemistry in the southeastern US, Atmos. Chem. Phys., 18, 9107–9120, https://doi.org/10.5194/acp-18-9107-2018, 2018.

Zahn, A., Weppner, J., Widmann, H., Schlote-Holubek, K., Burger, B., Kühner, T., Franke, H, A fast and precise chemiluminescence ozone detector for eddy flux and airborne application, Atmos. Meas. Techn., 5 (2), 363–375. https://doi.org/10.5194/amt-5-363-2012, 2012.

Zanis, P., Monks, P. S., Green, T. J., Schuepbach, E., Carpenter, L. J., Mills, G. P., Rickard, A. R., and Penkett, S. A.: Seasonal variation of peroxy radicals in the lower free troposphere based on observations from the FREE Tropospheric EXperiments in the Swiss Alps, Geophys. Res. Lett., 30, 1497, https://doi.org/10.1029/2003GL017122, 2003.

Zarzana, K. J., Min, K.-E., Washenfelder, R. A., Kaiser, J., Krawiec-Thayer, M., Peischl, J., Neuman, J. A., Nowak, J. B., Wagner, N. L., Dubè, W. P., St. Clair, J. M., Wolfe, G. M., Hanisco, T. F., Keutsch, F. N., Ryerson, T. B., and Brown, S. S.: Emissions of Glyoxal and Other Carbonyl Compounds from Agricultural Biomass Burning Plumes Sampled by Aircraft, Environ. Sci. Technol., 51, 11761–11770, https://doi.org/10.1021/acs.est.7b03517, 2017.

Ziereis, H., Minikin, A., Schlager, H., Gayet, J.F., Auriol, F., Stock, P., Baehr, J., Petzold, A., Schumann, U., Weinheimer, A., Ridley, B., and Ström, J.: Uptake of reactive nitrogen on cirrus cloud particles during INCA, Geophys. Res. Lett., 31(5), https://doi.org/10.1029/2003GL018794, 2004.

Zhu, T., Melamed, M., Parrish, D., Gauss, M., Gallardo Klenner, L., Lawrence, M., Konare, A. and Liousse, C.: Impacts of Megacities on air pollution and climate, WMO/ IGAC, GAW Report No.205, 2012

Acknowledgements

"Dream is not that which you have while sleeping. It is something that does not let you sleep."

Dr A. P. J. Abdul Kalam

Finally, the dream that kept me awake over the past years has come true. Completing this dissertation is a significant milestone in my career. On this occasion, I express my most profound sense of gratitude to my supervisor, Prof. John P. Burrows, for his mentorship, contribution, and support during this journey. Under his supervision, I had the liberty of independent thinking and, at the same time, received continuous inputs and support that helped to sharpen my ideas. I am also thankful for his everlasting moral support, exemplary work ethics, and encouragement towards novel ideas. I am incredibly grateful for the knowledge I gained from him in Atmospheric Science.

I want to express my deep and sincere gratitude to our group leader, Dr M. D. Andrés Hernández, for providing consistent feedback and inputs on my research and spending numerous hours reviewing my write-ups and for providing valuable feedback. I am grateful that I could improve my practical and analytical skills by working with her in field and laboratory experiments. I am also thankful for her moral support in my academic and personal life.

I express my sincere gratitude to my dearest friend and former colleague, Vladyslav Nenakhov, for his support during the lab and field experiments. I am also thankful for his advice and support, which made my life in Germany easier. I thank my colleagues, Yangzhuoran Liu and Wilke Thomssen, for their support throughout my research. I am forever thankful to Dr Bram Sanders and deceased Dr Andreas Hilboll for teaching the basics of the PYTHON programing language and helping me to improve my programming skills. I am also thankful to all the IUP members for their help and contributions throughout my research.

I thank the coordinators of the OMO mission and the OMO team for their valuable support during the measurements campaign. I also thank the EMeRGe community for supporting my research by providing measurement data and giving valuable comments and corrections to my publications. Heartfelt thanks to the University of Bremen, Deutsche Forschungsgemeinschaft, and Postgraduate International Programme in Physics and Electrical Engineering, University of Bremen, for providing financial support for my research.

This journey is only possible because there is a family who believes in me. The sacrifices of my parents, Mrs Mary George and the late Mr P. T. George, made me achieve this goal. They have always given me the freedom of thinking and supported my decisions throughout my life. They planted the seeds of perseverance and determination in achieving my goals. Even in their struggle with health issues, the support I received made me strive forward in completing this long PhD

journey. There is my sibling Mr Sarun George, who was a great friend and a mentor throughout my life.

Last but not least, I would like to thank my supportive wife, Mrs Sanaja Joseph, for her encouragement when the time got rough. Even though she joined my life towards the end of the PhD journey, her support and motivation helped me reach this goal against all odds.

It is an honour to pursue my PhD in an institute like IUP at the University of Bremen. The ambience, infrastructure, and profound research team add charm and make it an ideal place for research and learning. Thank you, IUP Bremen.

PhD is not the end of education but the starting point of a new life.

Midhun George

"Life is like riding a bicycle. To keep your balance, you must keep moving."

Dr Albert Einstein